PURE SCIENCES
International Journal of Kerbala

Ministry of Higher Education
and Scientific Research
University of Kerbala
College of Education for Pure Sciences

Pure Sciences International Journal of Kerbala

P S J I K

Year:2026
Volume : 3
ISSUE :9

DOAJ doi Crossref
ISSN: 2789-6188 Print
3005 -2394 Online

PURE
SCIENCES
International Journal of Kerbala

Pure Sciences International Journal of Kerbala

(PSIJK) is published in four issues annually

A quarterly peer-reviewed scientific journal issued by the College of Education for Pure Sciences at the University of Kerbala, specializing in pure sciences, accredited for the purposes of scientific promotion Pursuant to Ministerial Resolution No. **B.T 7575** Dated **14 /9 /2023**

Licensed by

Ministry of Higher Education
and Scientific Research and Scientific Research

Issued by

University of Kerbala
College of Education for Pure Sciences

2026 , Volume 3 , Issue 9
31 March 2026

Ministry of Higher Education and Scientific Research

College of Education for Pure Sciences

University of Kerbala

Print ISSN: 6188-2789

Online ISSN: 3005 -2394

Consignment Number in the Housebook and Iraqi

Documents: 2515, 2021

Postal Code: 56001

Mailbox: 232

Mobile: +964 7769920165

https://journals.uokerbala.edu.iq

Iraq - Holy Karbala

Workflow by OJS/PKP

About the Journal

The "Pure Sciences International Journal of Kerbala", published quarterly and distributed internationally by the College of Education for Pure Sciences provides a forum for publication of significant science advancements and developments in chemistry, biology, computer, physics, mathematics and interdisciplinary areas of science. All prospective authors are invited to submit their original contributions on new theoretical and applied aspects of growing research. All manuscripts submitted, including symposium papers, will be peer reviewed by qualified scholars assigned by the editorial board.

You are cordially encouraged to use this journal as a means of dissemination of information on the various facets of science and technical problems; and to impart specialized knowledge, quality and excellence to strengthen the perception of technological resources and needs of the world. The PSIJK is looking forward to receiving your assistance to working together to develop a worthwhile, high quality journal.

Aims and Scope

Pure Sciences International Journal of Kerbala is an open-access, interdisciplinary, single-blind peer-reviewed journal that consolidates research activities in the experimental and theoretical aspects of modern sciences. The journal aims to make significant contributions to applied research and knowledge globally through the publication of original high-quality research papers and review articles on recent advances and frontier achievements in Biology, Mathematics, Chemistry, Physics, and Computer Science, as well as their related and subfields.

Scope of Research

The journal encompasses both fundamental and applied investigations across a wide range of interdisciplinary topics. Articles of an interdisciplinary nature are particularly welcome. Any paper reporting scientifically accurate and valuable research that adheres to accepted ethical and scientific publishing standards will be considered for publication.

Publication Ethics

Pure Sciences International Journal of Kerbala is committed to upholding the highest standards of publication ethics. We adhere to the principles and policies outlined by the Committee on Publication Ethics (COPE).

Duties of Editors

- Editors have full authority to reject or accept manuscripts.
- Editors maintain the confidentiality of submitted manuscripts under review until they are published.
- Editors preserve the anonymity of reviewers.
- Editors disclose and try to avoid any conflict of interest.
- Editors comment on ethical questions and possible misconduct raised by submissions.

Duties of Reviewers

- Reviewers assist the editorial board in making editorial decisions.
- Reviews should be conducted objectively, and observations should be formulated clearly with supporting arguments.
- Reviewers should not consider manuscripts in which they have conflicts of interest.
- Reviewers should treat the manuscript as a confidential document.

Duties of Authors

- The submitted manuscript should not be submitted to more than one journal for simultaneous consideration.
- The submitted work should be original and should not have been published elsewhere.
- Authors should adhere to discipline-specific rules for acquiring, selecting, and processing data.
- Authors should properly cite all content referenced from other materials.

Research Involving Humans, Animals, and Plants

- Research involving humans must be conducted in accordance with the Declaration of Helsinki.
- Research involving animals must adhere to international, national, and institutional guidelines for the humane treatment of animals.
- Studies on plants must be carried out within the guidelines provided by the authors› institution and national or international regulations.

Consent for Publication

- Written informed consent must be obtained from individuals who are featured in the manuscript.
- The consent form must state that the details/images will be freely available on the internet.

Fundamental Errors in Published Works

- Authors are obligated to promptly notify the journal editor of any significant errors or inaccuracies in the published work.

Plagiarism

- Plagiarism in any form constitutes a serious violation of publication ethics and is not acceptable.
- All submitted manuscripts are checked for plagiarism using professional plagiarism-checking software.

Complaints/Appeals

- All complaints, concerns, or appeals regarding authorship issues or the peer-review process should be addressed to the Editor-in-Chief.

Conflicts of Interest/Competing Interests

- Authors must disclose any conflicts of interest they may have with the publication of the manuscript.

Confidentiality

- A submitted manuscript is a confidential material.
- The journal will not disclose submitted manuscripts to anyone except individuals who partake in the processing and preparation of the manuscript for publication.

Misconduct

- Misconduct constitutes a violation of this editorial policy, journal policies, publication ethics, or any applicable guidelines/policies specified by COPE, WAME, and ICMJE.

Correction and Retraction of Articles

- Corrections may be made to a published article with the authorization of the editor of the journal.
- When necessary, the retraction of articles will be done according to COPE retraction guidelines.

Acknowledgment

- Individuals who participated in the development of a manuscript but do not qualify as an author should be acknowledged.
- Organizations that provided support in terms of funding and/or other resources should also be acknowledged.

Editorial board

Pure Sciences International Journal of kerbala

Year:2026 Volume : 3 Issue : 9 ISSN: 6188-2789 Print 3005 -2394 Online

2026,Volume 3 , Issue 9 , PSIJK (11-16)

Pure Sciences International Journal of Kerbala

Synthesis and Antimicrobial Activity of New imine Derivatives Containing Drug Molecule

Diaa Hussein Faraj Mansour [a]* , Abbas F-Noori [a]

a Educational Directorate of Karbala, Kerbala, Iraq

P A P E R I N F O

Received: 07.07.2025
Accepted: 21.07.2025
Published: 31.03.2026

***Keywords*:**
Mesalazine, Klebsiella pneumoniae, Pseudomonas aeruginosa, Schiff base.

A B S T R A C T

The research involved the synthesis four of new Schiff base derivatives (SC_1, SC_3, SC_4, SC_6) through the condensation reaction of Three amines (drugs) with four aldehydes, all conducted under mild conditions. To validate their chemical structures, the produced compounds were analyzed utilizing spectroscopic methods such as FT-IR, 1H-NMR, and 13C-NMR. The antibacterial activity of Schiff base derivatives was tested against *(Pseudomonas aeruginosa, Escherichia coli, Klebsiella pneumoniae, Proteus spp., and Staphylococcus aureus)* using the agar well diffusion technique.

The findings revealed that SC1 was the most powerful and broad-spectrum antibacterial activity of all of the chemicals tested, with inhibition zone widths ranging from 18 to 30 mm, while SC3 showed moderate activity against most tested strains, with the highest activity against *E. coli* (21 mm) and *S. aureus* (25 mm). The structure-activity relationship (SAR) research revealed that electron-donating and electron-withdrawing substituents on the aromatic ring affected biological activity. These findings indicate that Schiff bases may be viable candidates for the creation of novel antibacterial medicines.

DOI: 10.53851/psijk.v3.i9. 11-16

1. INTRODUCTION

Schiff bases are a kind of imine chemical generated by the condensation of primary amines with carbonyl compounds like aldehydes or ketones. The imine (-C=N-) linkage determines the biological and chemical properties of these molecules (Raczuk E. et al., 2022) .Schiff bases have been widely researched for their antibacterial, antifungal, anticancer, and antioxidant effects, due to their ease of synthesis, structural diversity, and ability to interact with metal ions (Ceramella J. et al., 2022) (Hassan A. M. et al., 2022) (Soroceanu A. & Bargan A., 2022).

The proliferation of multidrug-resistant (MDR) bacterial species constitutes a substantial threat to public health, prompting the quest for novel antimicrobial drugs with new modes of action (Salam M. A. et al., 2023) . Schiff bases, generated from aromatic amines and aldehydes, have demonstrated potential antibacterial action, which is frequently attributed to their capacity to interfere with bacterial enzymes or membrane function (Khan R. et al., 2024).

Studies show that adding electron-donating or electron-withdrawing groups to the aromatic ring of Schiff base derivatives can considerably impact their biological activity (Rana M. S. et al., 2024) .Furthermore, the presence of heteroatoms such as nitrogen, sulfur, and oxygen in the molecular framework improves the ability of these compounds to interact with biological targets (Waziri I. et al., 2024) (Yasmeen Z. et al., 2025) (Yasmeen Z. et al., 2025) (Uddin E. et al., 2025). In this respect, the current study seeks to create a variety of new Schiff base derivatives by condensing different substituted aromatic amines with aldehydes under moderate circumstances. The produced compounds are characterized spectroscopically and tested for antibacterial activity against chosen Gram-positive and Gram-negative bacterial strains. This study also

*Corresponding Author Institutional Email:
deyaa1974hussein@gmail.com (Diaa Hussein Faraj Mansour)

looks at the link between the chemical structure and antibacterial activity of the produced compounds.

2. MATERIALS AND METHODS

Analytical-grade chemical compounds from Sigma Aldrich, Fluka, CDH, and Thomas Backer are utilized. We bought sulfadiazine and mesalzine from the Leyan Company in China. A Bruker Multinuclear spectrometer was used to determine the 1H NMR (400 MHz) and 13C NMR (100 MHz) FTIR spectra, while the Gallenkamp MFB-600-Melting point Stuart equipment was used to perform the melting point.

Synthesis of 2-hydroxy-5-((pyridin-2-ylmethylene)amino)benzoic acid[SC1]

In 40 ml of ethanol (1g, 9.33mmole) of pyridine2-carbaldehyde) and (1.45g, 9.33 mmole) of mesalazine prodrug was dissolved and transferred to (100 ml) round bottom flask. The mixture was refluxed for 3 hrs. until no spot of mesalazine shown on TLC plat. Then the formed precipitate was filtered and recrystallized from hot ethanol to afforded 1.9 g, 83% yield of [SC1] as light brown powder, m.p 179 C. FTIR νmax, cm-1: 2520-3000 (COOH and OH), 1651 (CO, acid), 1593 (C=N, imine), 1487 and 1446 (aromatic rings); 1H NMR (500 MHz, DMSO), ppm: 11.00 (s, 1H, COOH), 9.67 (s, 1H, Ar-OH), 7.88 (1 H, CH=N), 7.34 -6.36 (Ar-H). 13C NMR (125 MHz), ppm: 171.05 (1C, COOH), 133.02-101.45 (13C, Ar-C).

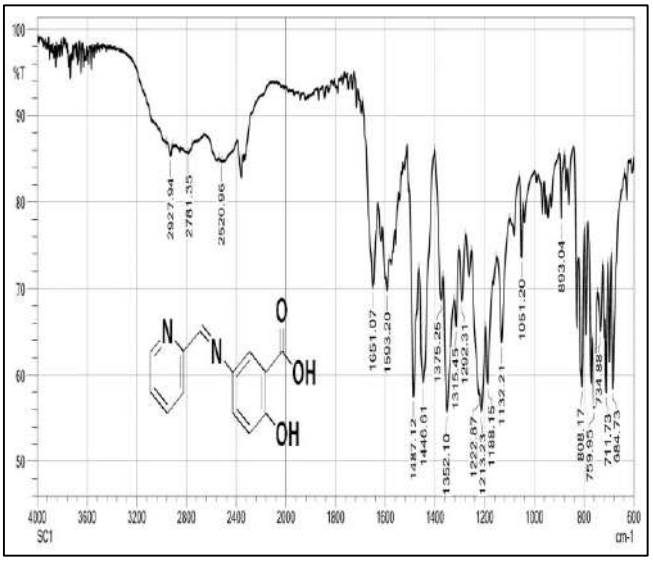

Figure 1. IR spectrum of compound SC1

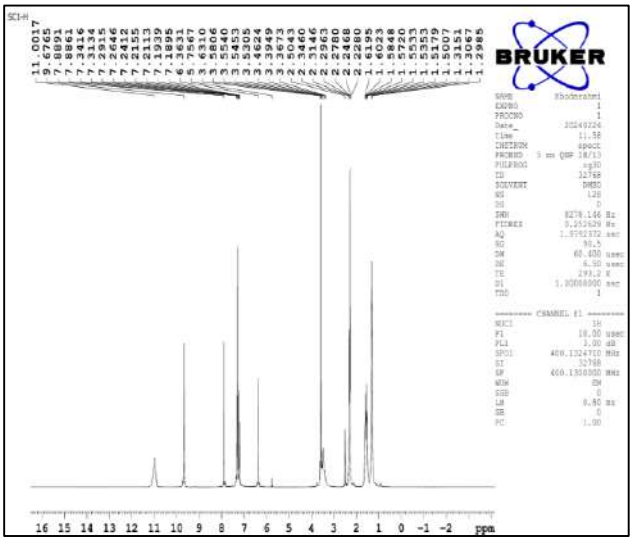

Figure 2. 1H-MNR spectrum of compound SC1

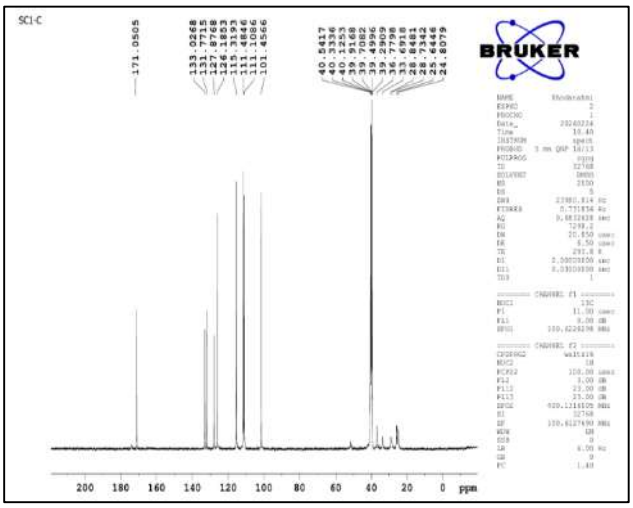

Figure 3. 13C-MNR spectrum of compound SC1

Synthesis of 5-((2,5-dimethoxybenzylidene)amino)-2-hydroxybenzoic acid [Sc3]

In 40 ml of ethanol (1g, 6 mmole) of 2,5-dimethoxybenzaldehyde and (0.92g, 6 mmole) of mesalazine prodrug was dissolved and transferred to (100 ml) round bottom flask. The mixture was refluxed for 3 hrs. until no spot of mesalazine shown on TLC plat. Then, the formed precipitate was filtered and recrystallized from hot ethanol to afforded 1.4 g, 77% yield of [SC3] as beige color powder, m.p 158 C. FTIR νmax, cm-1: 2520-3000 (COOH and OH), 2977 (O-CH_3), 1645 (CO, acid), 1612 (C=N, imine), 1557-1446 (aromatic rings);

1H NMR (500 MHz, DMSO), ppm: 11.15 (s, 1H, COOH), 8.68 (s, 1H, Ar-OH), 8.30 (1 H, CH=N), 7.99 -6.34 (Ar-H). 13C NMR (125 MHz), ppm: 171.41 (1C, COOH), 155.78 (1C, C=N), 140.52-111.88 (12C, Ar-C), 53.48 (2C, O-CH_3).

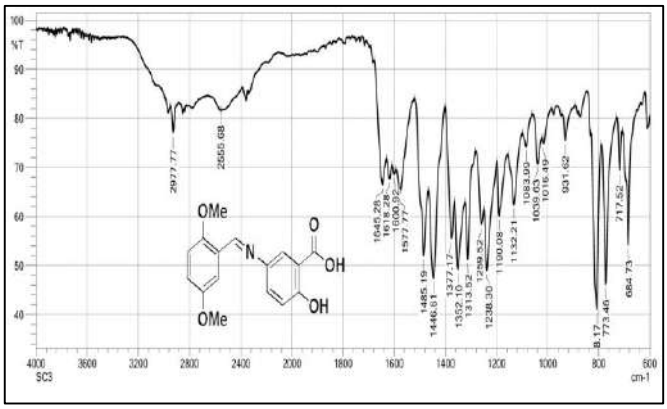

Figure 4. IR spectrum of compound SC3

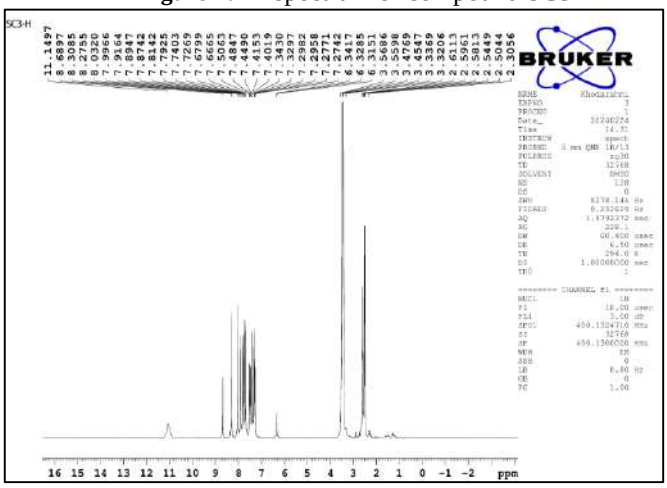

Figure 5. 1H-NMR spectrum of compound SC3

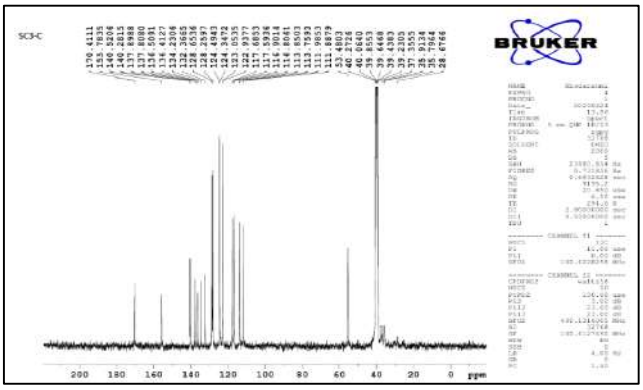

Figure 6. 13C-NMR spectrum of compound SC3

Synthesis of 4-((3-hydroxybenzylidene)amino)-1,5-dimethyl-2-phenyl-1,2-dihydro-3H-pyrazol-3-one [Sc4] In 40 ml of ethanol (1g, 8.2 mmole) 3-hydroxybenzaldehyde and (1.66 g, 8.2 mmole) of 4-Aminoantipyrine was dissolved and transferred to (100 ml) round bottom flask. The mixture was refluxed for 3 hrs. until no spot for reactants was shown on TLC plat. Then, the formed precipitate was filtered and recrystallized from hot ethanol to afforded 2 g, 80% yield of [SC4] as brown powder, m.p 181 ^{O}C. FTIR νmax, cm-1: 3138 (OH), 2926 (CH_3), 1614 (CO, pyrazole), 1591 (C=N, imine), 1555-1448 (aromatic rings); 1H NMR (500 MHz, DMSO), ppm: 9.99 (s, 1H, OH), 8.70 (1 H, CH=N), 7.92 -6.34 (Ar-H). 13C NMR (125 MHz), ppm: 155.82 (1C, C=O), 140.58 (1C. C=N), 137.97-111.97 (14C, Ar-C), 37.44 and 35.94 (2C, -CH_3).

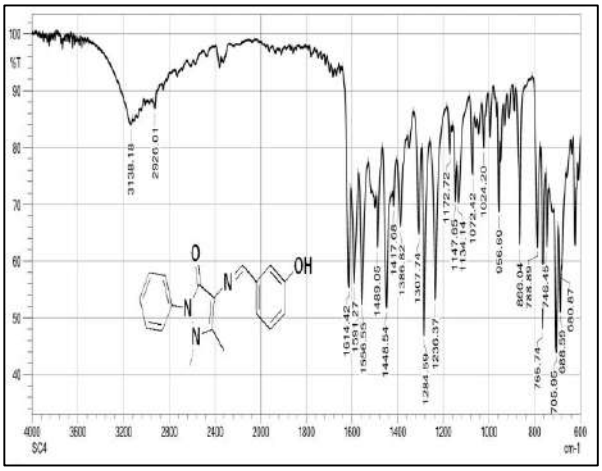

Figure 7. 1IR spectrum of compound SC4

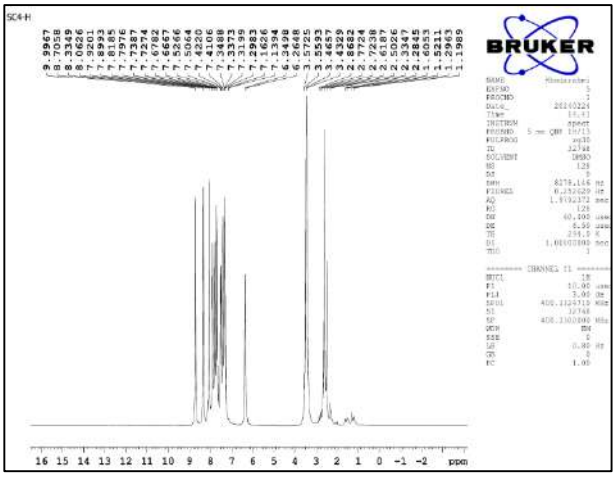

Figure 8. 1H-MNR spectrum of compound SC4

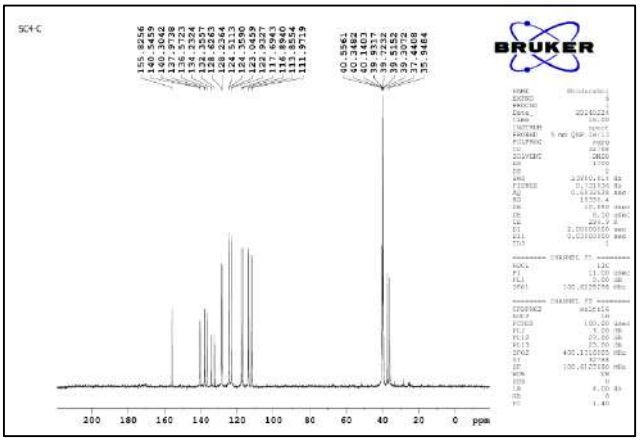

Figure 9. 13C-MNR spectrum of compound SC4
Synthesis of 4-((4-hydroxybenzylidene)amino)-N-(pyrimidin-2-yl)benzenesulfonamide [Sc6]

In 40 ml of ethanol (1g, 8.2 mmole) 3-hydroxybenzaldehyde and (2.05 g, 8.2 mmole) of sulfadiazine was dissolved and transferred to (100 ml) round bottom flask. The mixture was refluxed for 3 hrs. until no spot for reactants was shown on TLC plat. Then the formed precipitate was filtered and recrystallized from hot ethanol to afforded 2 g, 69% yield of [SC6] as off-white powder, m.p 213 C. FTIR νmax, cm-1: 3352 (N-H), 3257 (OH), 1614 (CO, pryrazole), 1557 (C=N, imine), 1489-1406 (aromatic rings); 1H NMR (500 MHz, DMSO), ppm: ~10.99 (s, 1H, N-H), ~9.50(1 H, O-H), ~8.50 (s, 1H, HC=N), 7.45 -7.04 (Ar-H). 13C NMR (125 MHz), ppm: 169.62 (1C, pyrimidine ring), ~158.82 (1C. C=N), 138.44-111.02 (9 C, Ar-C), 37.44 and 35.94 (2C, -CH_3).

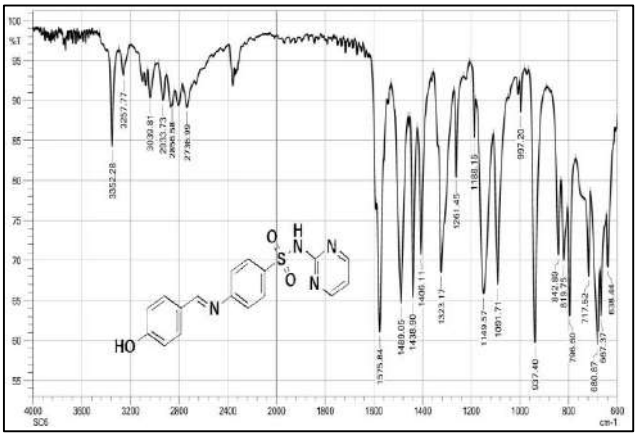

Figure.10. IR spectrum of compound SC6

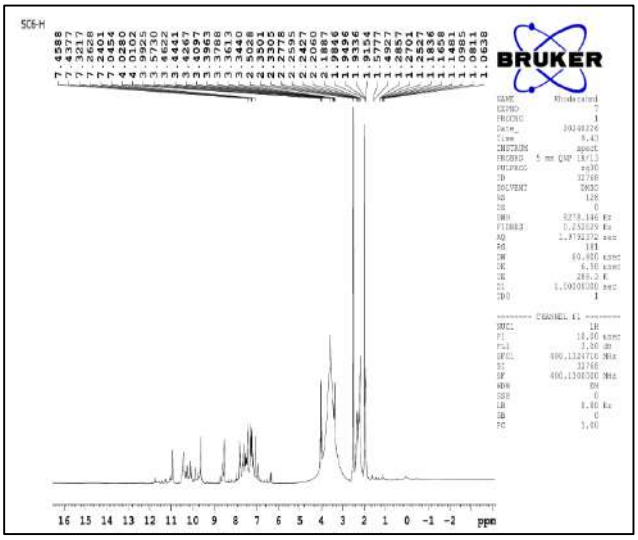

Figure 11. 1H-NMR spectrum of compound SC6

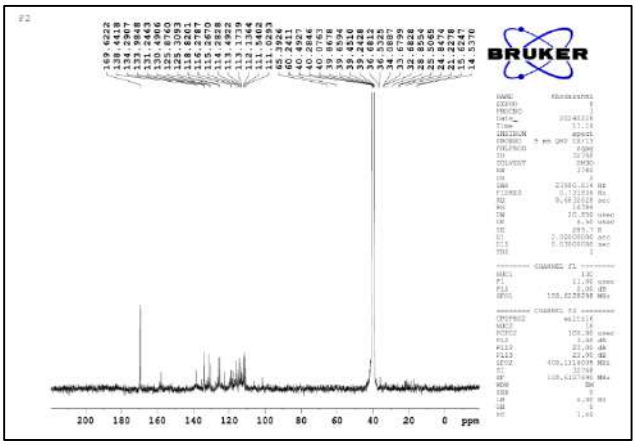

Figure 12. 13C-NMR spectrum of compound SC6

1- 3. RESULTS AND DISCUSSION

3.1. Chemistry

The new compounds (SC_1, SC_3, SC_4, SC_6) were synthesized through a direct condensation reaction between various aromatic amino drugs and an aromatic aldehyde, as illustrated in Scheme 1.

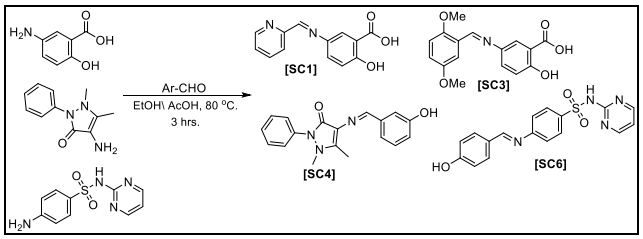

Scheme 1. Synthesis of compounds (SC_1, SC_3, SC_4, SC_6).

Several spectroscopic methods were used to confirm the structures of the prepared compounds. Successful synthesis was demonstrated by the FT-IR spectra's broad bands

representing aldehydes carbonyls and amino groups disappearing, as well as the emergence of new bands for the imine (C=N) stretching vibrations at 1595, 1618, 1614, and 1575 cm^{-1}. The formation of the imine bonds and the elimination of the aldehyde proton signal were confirmed by the ^1H NMR spectra, which displayed distinctive singlets for the imine protons at 7.88, 8.66, 8.70, and 8.50 ppm.

3.2. Anti-Bacterial Activity

Five clinically relevant bacterial strains (*Pseudomonas aeruginosa, Escherichia coli, Klebsiella pneumoniae, Proteus spp., and Staphylococcus aureus*) were used to test the antimicrobial properties of the synthesized compounds SC1, SC3, SC4, and SC6. The antibacterial efficacy was measured using amoxicillin as the reference standard.

TABLE 1. The diameter of inhibition zone of compounds (SC_1, SC_3, SC_4, SC_6) against *P. aeruginosa, E. Coli, K. pneumonia, Proteus* and *S. aureus*

Sample code	***P. aeruginosa***	***E. Coli***	***K. pneumoniae***	***Proteus***	***S. aureus***
SC1	30	18	26	18	30
SC3	25	21	18	11	25
SC4	11	19	12	18	11
SC6	12	8	4	0	15
Amoxicillin	30	24	19	18	32

SC1 was the most powerful and broad-spectrum antibacterial activity of all of the chemicals tested, with inhibition zone widths ranging from 18 to 30 mm. It had notably robust action against *P. aeruginosa and S. aureus* (30 mm each), equivalent to that of amoxicillin (30 mm and 32 mm, respectively), as well as considerable suppression against *K. pneumoniae* (26 mm). This shows that SC1 may have a structural or functional characteristic that helps it engage with both Gram-positive and Gram-negative bacterial cell targets.

SC3 showed moderate activity against most tested strains, with the highest activity against *E. coli* (21 mm) and *S. aureus* (25 mm). SC3 was significantly less effective than SC1, although it still demonstrated a wide spectrum of action, indicating that certain structural variations may impact its potency or bacterial target selectivity.

In contrast, SC4 and SC6 had relatively low antibacterial activity, notably SC6, which was ineffective against *Proteus* (0 mm) and had negligible inhibitory zones against other strains. SC4 has considerable effectiveness against *E. coli* (19 mm) and *Proteus* (18 mm), but low efficacy against *P. aeruginosa* and *S. aureus* (11 mm). These data suggest that SC4 and SC6 may lack crucial pharmacophoric characteristics required for efficient bacterial suppression or they have low cell wall penetration. When all compounds are compared to normal amoxicillin, SC1 emerges as the most promising contender, with equivalent or slightly lower activity in most circumstances. The decreased activity of SC4 and SC6 suggests either suboptimal chemical properties or a low affinity for the bacterial targets tested.

Overall, the findings suggest that structural alterations to Schiff base derivatives have a major impact on their antibacterial properties. Further structure-activity relationship (SAR) studies, as well as mechanistic research, are needed to maximize the potency and selectivity of these compounds, particularly SC1 and SC3, as potential antimicrobial agents against resistant bacteria, including ESBL-producing strains.

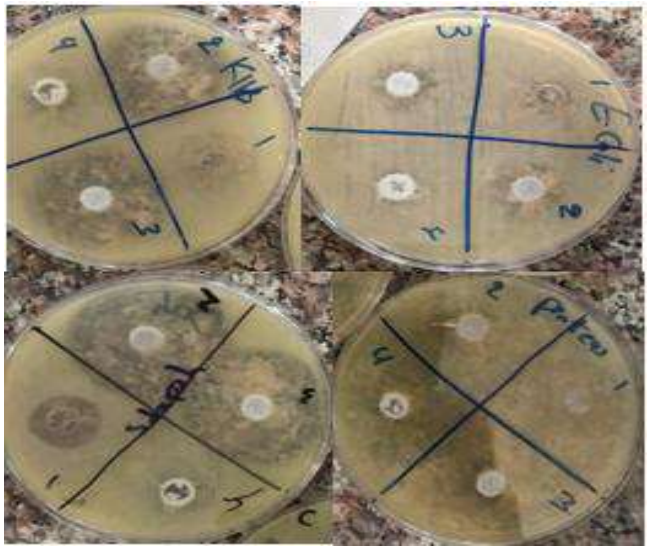

Figure 13. Antibacterial activity of (SC_1, SC_3, SC_4, SC_6): (1= SC1), (2= SC3), (3= SC4), (4= SC6).

4. CONCLUSION

In this study, a series of drug-derived Schiff base compounds (SC1, SC3, SC4, and SC6) were successfully synthesized and tested for antimicrobial activity against a panel of clinically significant bacterial strains such as *Pseudomonas aeruginosa, Escherichia coli, Klebsiella pneumoniae, Proteus spp., and Staphylococcus aureus*. SC1 had the most effective and broad-spectrum antibacterial action of the investigated compounds, with inhibitory zones equivalent to the conventional antibiotic amoxicillin, notably against P. aeruginosa and S. aureus.

The findings identify Schiff base derivatives, particularly SC1 and SC3, as attractive candidates for future development as antibacterial drugs. These findings further confirm the significance of structural change in increasing biological activity, implying that additional optimization and structure-activity relationship (SAR) research might provide even more effective analogues.

REFERENCES

Ceramella, J., Iacopetta, D., Catalano, A., Cirillo, F., Lappano, R., & Sinicropi, M. S. (2022). A Review on the Antimicrobial Activity of Schiff Bases: Data Collection and Recent Studies. Antibiotics (Basel, Switzerland), 11(2), 191. https://doi.org/10.3390/antibiotics11020191.

Hassan, A. M., Said, A. O., Heakal, B. H., Younis, A., Aboulthana, W. M., & Mady, M. F. (2022). Green Synthesis, Characterization, Antimicrobial and Anticancer Screening of New Metal Complexes Incorporating Schiff Base. ACS omega, 7(36), 32418–32431. https://doi.org/10.1021/acsomega.2c03911.

Khan, R., Rashid, S., Khan, S. et al. Synthesis and evaluation of vanillin Schiff bases as potential antimicrobial agents against ESBL-producing bacteria: towards novel interventions in antimicrobial stewardship. Sci Rep 14, 28007 (2024). https://doi.org/10.1038/s41598-024-78302-9.

Raczuk, E., Dmochowska, B., Samaszko-Fiertek, J., & Madaj, J. (2022). Different Schiff Bases-Structure, Importance and Classification. Molecules (Basel, Switzerland), 27(3), 787. https://doi.org/10.3390/molecules27030787.

Rana, M. S., Rayhan, N. M. A., Emon, M. S. H., Islam, M. T., Rathry, K., Hasan, M. M., Islam Mansur, M. M., Srijon, B. C., Islam, M. S., Ray, A., Rakib, M. A., Islam, A., Kudrat-E-Zahan, M., Hossen, M. F., & Asraf, M. A. (2024). Antioxidant activity of Schiff base ligands using the DPPH scavenging assay: an updated review. RSC advances, 14(45), 33094–33123. https://doi.org/10.1039/d4ra04375h.

Salam, M. A., Al-Amin, M. Y., Salam, M. T., Pawar, J. S., Akhter, N., Rabaan, A. A., & Alqumber, M. A. A. (2023). Antimicrobial Resistance: A Growing Serious Threat for Global Public Health. Healthcare (Basel, Switzerland), 11(13), 1946. https://doi.org/10.3390/healthcare11131946.

Soroceanu, A., & Bargan, A. (2022). Advanced and Biomedical Applications of Schiff-Base Ligands and Their Metal Complexes: A Review. Crystals, 12(10), 1436. https://doi.org/10.3390/cryst12101436.

Uddin, E., Sardar, M.N., Reza, M.S. et al. Emerging pharmaceutically active drugs: synthesis and pharmacology of Schiff base ligands with their metal complexes. Discov. Chem. 2, 153 (2025). https://doi.org/10.1007/s44371-025-00228-6.

Waziri, I., Kelani, M. T., Oyedeji-Amusa, M. O., Oyebamiji, A. K., Coetzee, L. C., & Muller, A. J. (2024). Comparative investigation of derivatives of (E)-N-((E)-3-phenylallylidene)aniline: Synthesis, structural characterization, biological evaluation, density functional theory analysis, and in silico molecular docking. Heliyon, 10(4), e26632. https://doi.org/10.1016/j.heliyon.2024.e26632.

Yasmeen, Z., Khan, M. A., Masood, A., Akram, T., Breena, Bhat, M. A., … Ullah, F. (2025). Exploring Schiff base bromhexine derivatives: study on synthesis, characterization, biological assays, molecular docking. Future Medicinal Chemistry, 1–12. https://doi.org/10.1080/17568919.2025.2527619.

Pure Sciences International Journal of kerbala

Year:2026 Volume : 3 Issue : 9 ISSN: 6188-2789 Print 3005 -2394 Online

2026,Volume 3 , Issue 9 , PSIJK (18-24)

Pure Sciences International Journal of Kerbala

Measuring and Evaluation of Power Density Emitted by Communication Towers with Location and Time for Selected Areas in Karbala, Iraq

Rusul Amer Mahdi [a*] , Fadel Abdul Zahra Murad [a]

[a] *Department of Physics, College of Education for Women, University of Kufa , Najaf, Iraq*

P A P E R I N F O

Received: 16.07.2025
Accepted: 13.08.2025
Published: 31.03.2026

***Keywords*:**
Communication towers, HF 59B analyzer, magnetic field, non-ionizing electromagnetic radiation, power density.

A B S T R A C T

This study aims to measure and evaluate the energy density of electromagnetic radiation emitted by cell phone towers in three locations in Karbala, Iraq. The first location is the area between the Holy Shrine of Imam Hussain and Abbas that represents religion area, while the second area is Al-Hussein District Street which represents a commercial location. The third place is Al-Ghadeer District (a residential area). Field measurements were performed by using an HF 59B Analyzer. This device is distinguished by its accuracy in measuring the energy density levels of electromagnetic radiation in the bands used in modern communication systems. The results showed that the highest radiation power density was recorded at 6:00 PM between the two Holy Shrine, with the average radiation intensity in some evening periods exceeding 2,000 μW/m². This is attributed to increased human activity during the evening hours and increased use of mobile phones during that time. In the Al-Ghadeer District, peak radiation was observed at 1:00 PM.

DOI: 10.53851/psijk.v3.i9. 18-24

1. INTRODUCTION

With the rapid growth of the telecommunications sector, the proliferation of telecom towers has increased significantly. Since mobile phones have become an integral part of people's daily lives due to the development of telecommunications, the widespread use of these phones has led to a massive increase in the number of mobile phone towers installed in communities. This expansion has led to increased exposure to microwave electromagnetic waves, especially those used in the 900 and 1800 MHz frequencies, which has contributed to the rise in electromagnetic pollution. Such towers comprise antennas and electronic equipment that transmit cell phone signals using radio frequency waves (Jafaar & Nema, 2019) (Yahya, 2019) (Zamanian & Hardiman, 2005). These towers are supplied with antennas and other apparatuses essential for getting and transmitting signals (Gupta, 2015).

There is increased stress, fatigue, irritability, poor sleep quality, headaches, and a host of other difficulties due to increased used of mobile phones (Miller et al., 2019) (Ying et al., 2013). The brain absorbs radio frequency (RF) or electromagnetic field (EMF) emitted by such phones through the skull (Wiart et al., 2008). This absorbed electromagnetic radiation causes health problems. These problems have sparked the interest of researchers and scientists to study the effect of radiation levels on the human body (Foster et al., 1997).

The Federal Communications Commission (FCC) has set standards and controls to ensure that radio frequency levels, including Global System for Mobile Communications (GSM) frequencies, remain within safe limits that do not cause harmful effects. Mobile phone systems are divided into three main generations: the first generation operates in the frequency range of 450-900 MHz, the second generation (GSM) relies on digital technology in the range of 900, 1800, and 1900 MHz, while the third generation operates in the 2000 MHz range (Cansiz et al., 2016).

Although humans and animals are constantly exposed to electromagnetic radiation, analyzing its internal effects is a significant challenge due to its absorption within tissues. These effects vary depending on the radiation source, as they depend on the frequency, modulation methods, specific absorption rate (SAR) specifications, and duration of exposure. Variations in SAR values lead to tissue heating, causing different changes depending on the level of absorption. Exposure

*Corresponding Author Institutional Email:
rusula.alhamadani@student.uokufa.edu.iq, (Rusul Amer Mahdi)

to low levels of electromagnetic radiation may also lead to electromagnetic hypersensitivity in humans (Traini et al., 2023) . Reported symptoms from electromagnetic radiation exposure include headaches, body aches, lethargy, tinnitus, nausea, burning sensations, irregular heartbeat, and anxiety (Kızıloğlu et al., n.d.).

Workers interact with wireless communication devices, exposing them to varying degrees of electromagnetic radiation depending on the device specifications and frequency of operation. The effect of radiation varies according to the absorption rate of each individual, so the distribution of electric and magnetic fields is analyzed to determine potential risks. Despite theoretical and experimental research, studies on radiation exposure from communication devices remain limited. According to the 2020 International Commission on Non-Ionizing Radiation Protection (ICNIRP) report (Kavet & Tell, 2023), guidelines have been developed to limit exposure, but no explicit minimum value has been established, as this depends on biological and environmental factors. Exposed groups are classified into professionals and the general public, and this research focuses on the effects on the general public.

Read (Read, 1980) explained that when a wave is emitted from its source, it emits a certain energy. As it propagates, this energy is distributed spherically and equally in all directions around the source. The further away we are from the source, the less energy the wave has. This means that as the distance from the source increases, the energy density decreases, and there is an inverse proportion between the energy density and the square of the distance. Despite the differences in the frequencies of electromagnetic waves, the waves retain the same basic shape and characteristics (Juutilainen et al., 2009) . Electromagnetic waves are used in communication processes between two points separated by a large distance, without the need for transmission media or wire lines to transmit data between the transmitter and receiver. These systems are known as wireless communication systems, which rely primarily on antennas to convert electrical signals into electromagnetic waves capable of traveling long distances. These systems have witnessed significant development due to technological advances in antenna design, given their pivotal role in improving the efficiency and success of wireless performance (Rappaport et al., 2013) (Murch & Letaief, 2002).

In study in Sri Lanka, where residential areas have witnessed an increase in the installation of mobile base stations, concerns have been raised about radio frequency radiation and its health impacts. The results showed that current exposure levels are below the permissible limits, although they are relatively high in the cities of Ratnapura and Gampaha. The highest exposure was in Ratnapura due to the 2 GHz range, but it was still at one-tenth of the permissible limit (Karunarathna et al., 2018).

In France, in 2020, Regrain, Caudeville (Regrain et al., 2020) presented a mapping design to assess population exposure to radio frequency sources. Maps were developed that integrate geodatabases of individual exposure to electromagnetic frequencies (RF-EMF) within the frequency range (100 kHz - 300 GHz). A statistical tool was also designed to assess population exposure, integrating geodatabases and alternative models to describe temporal and spatial exposure to outdoor, indoor, and mobile phone sources. They concluded that built-up areas experience higher absorption rates than unbuilt areas. When the results were compared with the recommendations of the ICNIRP, the measured values were found to be significantly lower than the permissible values.

In 2020, a study was conducted in Mosul, Iraq, where the power density levels of mobile phone towers for the downlink of GSM 900 and GSM 1800 bands were measured for both Asiacell and Korek, operating in Mosul. The measurements were compared with local and international standards. An SRM-3006 device was used to measure the power density of electromagnetic radiation emitted by the towers. The results showed that the highest total density measured was 0.17914139 W/m^2, which was within local limits as well as within the FCC and ICNIRP limits, but exceeded the permissible limits in Russia (Al-Tamer & Al-Ahmady, 2020) .

Another study investigated the effect of electromagnetic energy density emitted by mobile phone towers in Al-Kifl District, Babil Governorate, Iraq. An EMF Strength Meter was used to measure radiation within frequencies (900–1800 MHz) at 30 points covering the study area. The results showed that the highest readings were recorded in the center of Al-Kifl District, an area characterized by its high population density and the presence of a large number of towers. Despite the high readings in some areas, they remained within the limits permitted by CMC, ICNIRP, and FCC (Huwair, 2024).

This study is a necessary study in the city of Karbala, Iraq as it fills a research gap in this field. Studies on similar topics, such as electromagnetic radiation in Karbala, are lacking. This thesis provides a comprehensive understanding of the effects of electromagnetic radiation on the residents of the holy city of Karbala. Furthermore, this thesis will provide important information to government agencies and companies involved in developing and improving the communications infrastructure, contributing to improved public health and reducing potential negative impacts on the population.

2. DEVICE USED IN THE RESEARCH: HF 59B ANALYSER

The HF 59B Analyser is a device designed to measure the energy density of high-frequency (HF) electromagnetic radiation. It is a handheld device with high accuracy operating from 700 MHz to 3.3 GHz, particularly in the critical lower and upper frequency ranges. It is equipped with a compensated antenna for frequencies from 700 MHz to 2.7 or 3.3 GHz to improve measurement accuracy. It is manufactured in Germany by Gigahertz Solutions. This device is used to measure the electromagnetic energy density emitted by cell phone towers. It is equipped with a non-folding antenna, which enables it to receive frequencies. Figure 1 shows a picture of this device. The units used to measure radiation intensity per unit area ($\mu W/m^2$) were used.

Figure 1. HF 59B Analyzer

3. DETERMINE PEAK TIME

The power density emitted by mobile phone towers varies from hour to hour throughout the day, and also from day to day throughout the week. On weekends, for example, radiation intensity levels are different from other days of the week, depending on the number of mobile phone users. To determine the peak time during a single day, three points were selected to represent three locations in the city of Karbala (one point representing a religious area, one point representing a commercial area, and one point representing a residential area). The first point was selected to represent a religious area located in the center of Karbala, in the area between the two holy shrines (the shrines of Imam Hussein and Al-Abbas. This area is considered the primary destination for visitors to the city of Karbala, and is characterized by thousands of people visiting the holy shrines daily. On important religious occasions, such as the Arbaeen and Sha'ban pilgrimages, the number of visitors reaches millions in a matter of days. On Thursdays and Fridays of each week, the number of visitors reaches hundreds of thousands. Based on the above, a study point was selected in the area between the two holy shrines. The study was conducted on Thursdays, where the population density is in the hundreds of thousands. The second point was selected in the Al-Hussein District Street, which represents a major commercial area and a second destination for visitors to Karbala, home to malls, restaurants, and shopping areas. The third point was selected in the Al-Ghadeer District, a large and densely populated District. The coordinates of the points were determined using GPS technology, as shown in Figures 2, 3, and 4. Multiple readings were taken at these points throughout the day, at a rate of three readings per hour, starting at 7:00 a.m. and ending at 12:00 midnight.

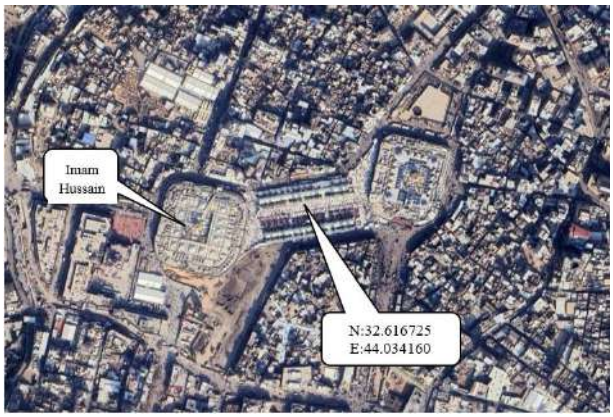

Figure 2. An aerial photo showing the study area between the two shrines in Karbala

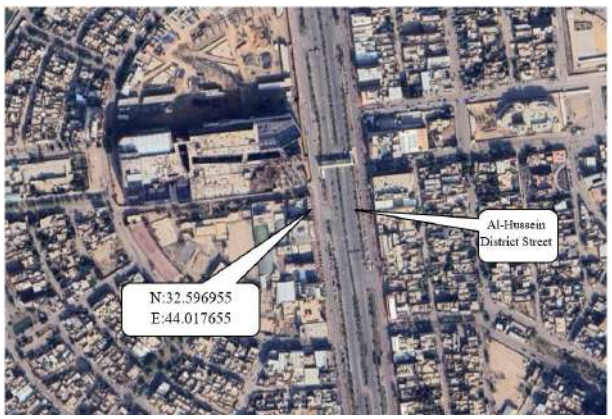

Figure 3. An aerial photo showing the study area in Al-Hussein District Street

Figure 4. An aerial photo showing the study area in Al-Ghadeer District.

3.1. Determining Peak Times in the Area Between the Two Holy Shrines

The area shown in Figure 2 was selected, and its GPS coordinates are shown in Table 1. This table shows the readings of electromagnetic energy intensity levels in the study area (the area between the two Holy Shrines in the centre of Karbala) during time periods starting from 7:00 AM to 12:00 AM. Thursday was chosen for the study, as visits to the holy shrines are at their peak on this day of the week, meaning very high population density. Note that the table above shows electromagnetic energy intensity measurements (μW/m²) in four different directions (I_1, I_2, I_3, I_4).

We note from the table that there is a very sharp increase in energy levels starting at 7:00 a.m. and continuing until 7:00 p.m., the peak time. Energy intensity levels remain high thereafter until midnight. The results of electromagnetic energy intensity measurements in this area show a clear pattern linked to the activity of visitors and the intensive use of mobile phones. It is noted that values were low in the early morning hours (although high compared to the rest of Karbala), with the lowest reading recorded at 7:00 a.m., averaging 170 microwatts/m². Then, as the day progressed, we observed that values began to gradually rise until they reached an average peak at 12:00 p.m. (266 microwatts/m²) (around the time of the noon prayers). We then observed a temporary decrease in the afternoon due to the high air temperature (approximately 43°C). After 3:00 PM, we notice a sharp increase in the average electromagnetic energy intensity, coinciding with the increasing number of visitors to the area, reaching its highest levels at 7:00 PM (close to the time of the Maghrib prayer), at an average of 2,040 microwatts/m². This is due to the increased number of users, as thousands of people gather in one area. This in turn prompts base stations to pump higher power to provide wider coverage and better connection quality. A slight decrease was observed after that, reaching 1,777 microwatts/m² at 8:00 PM (Figure 5). This indicates the presence of strong sources of electromagnetic radiation in that area, such as towers. At least three mobile phone towers were observed in the area between the Two Holy Shrines, and these towers were at low altitudes.

TABLE 1. Energy density readings in the area between the two Holy Shrines in the center of Karbala city.

GPS					**N:32.616725 E:44.034160**
Time	**I_1, μw/m²**	**I_2, μw/m²**	**I_3, μw/m²**	**I_4, μw/m²**	**$I_{av.}$, μw/m²**
7:00 am	165	174	186	154	170
8:00 am	184	169	181	164	175
9:00 am	220	194	191	225	226
10:00 am	265	205	190	215	233
11:00 am	265	271	199	201	246
12:00 am	236	246	256	215	266
1:00 pm	215	236	199	232	221
2:00 pm	201	245	236	198	220
3:00 pm	321	354	421	298	349
4:00 pm	521	621	456	512	592
5:00 pm	1201	1001	998	856	1014
6:00 pm	1610	1645	1821	2645	1930
7:00 pm	1921	1954	1832	2452	2040
8:00 pm	2545	1452	1356	1221	1777
9:00 pm	2565	1642	1564	1452	1806
10:00 pm	1712	516	1532	2071	1714
11:00 pm	1545	1215	2812	1121	1673
12:00 pm	1152	1456	2724	1624	1739

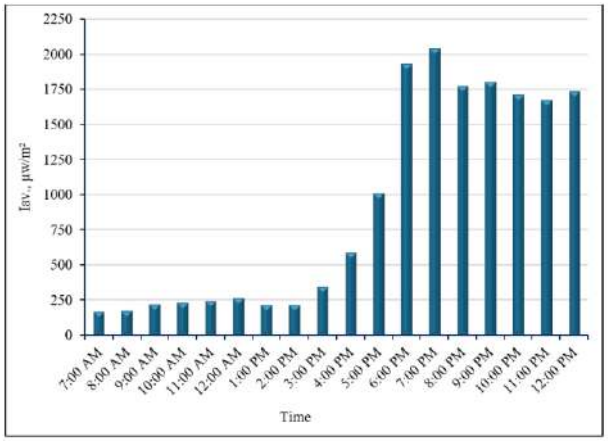

Figure 5. A diagram of the relationship between time and energy density in the area between the two holy shrines / Karbala

3.2. Determining Peak Times in the Al-Hussein District Street

We note that the values in Table 2 and Figure 6 start in the morning at relatively low levels (less than 30 μW/m²), with a morning average of approximately 20-30 μW/m². The values then gradually increase during the day, with rates increasing significantly and reaching 34.7

µW/m² at 3:00 p.m., reflecting increased activity during the daytime. The highest average electromagnetic radiation values are then seen in the evening and night, with rates ranging from 38.8 µW/m² to 57.1 µW/m², with a peak at 11:00 p.m. This indicates the presence of strong radiation sources or increased electromagnetic activity during these hours. We also note a clear variation in values between different points, indicating an uneven distribution of radiation sources or local effects such as buildings. It can be concluded that radiation is low in the early morning, begins to rise as the day progresses, and peaks in the evening hours (6:00–8:00 p.m.). Average values (I_{AV}) range from approximately 19.8 µW/m² in the morning to 56.8 µW/m² at midnight.

TABLE 2. Energy density readings in the Al-Hussein district

GPS				**N:32.596955 E:44.017655**	
Time	**I_1, µw/m²**	**I_2, µw/m²**	**I_3, µw/m²**	**I_4, µw/m²**	**$I_{av.}$, µw/m²**
7:00 am	22.3	29.2	13.4	14.3	19.8
8:00 am	15.6	24.3	28.1	15.2	20.8
9:00 am	27.3	25.3	14.4	17.5	21.1
10:00 am	19.2	27.5	25.1	18.4	22.6
11:00 am	36.2	22.4	14.6	45.3	29.6
12:00 am	45.2	25.1	18.3	25.4	28.5
1:00 pm	25.6	36.4	45.2	35.1	35.6
2:00 pm	51.2	36.2	18.4	28.6	33.6
3:00 pm	18.5	27.6	35.4	57.2	34.7
4:00 pm	45.6	28.7	35.6	45.3	38.8
5:00 pm	72.3	35.4	25.4	36.2	42.3
6:00 pm	35.2	85.3	37.6	52.6	52.7
7:00 pm	96.1	35.4	62.6	29.3	55.9
8:00 pm	76.9	56.3	42.4	45.2	55.2
9:00 pm	45.2	44.3	78.2	51.4	54.8
10:00 pm	70.2	52.4	37.2	55.3	53.8
11:00 pm	76.3	51.4	45.6	54.9	57.1
12:00 pm	76.4	49.5	52.6	48.5	56.8

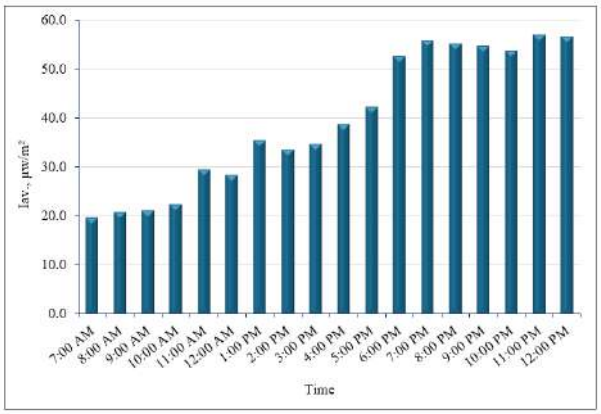

Figure 6. Time-energy density relationship diagram in the Al-Hussein commercial district

3.3. Determining Peak Times in the Al-Ghadeer District

Measurements were taken every hour from 7 a.m. to 12 midnight (Table 3 and Figure 7). Four electromagnetic radiation intensity values were recorded (I_1, I_2, I_3, I_4), with an average of (I_{avg}). We note from the average electromagnetic radiation intensity that the lowest value is approximately 36.5 µW/m² (7 a.m.), while the highest value is 69.9 µW/m² (1 p.m.). After that, a relative decrease is observed during the afternoon (2 p.m.). It is also noted that most values range between 55 and 70 µW/m² during most of the day and evening hours. In the evening, it is noted that the values maintain an average level of 60-68 µW/m². At 8:00 p.m., we notice a clear increase, reaching a value of (96.4 µw/m²) is the highest I4 value in the table, with the average continuing to rise (68.1 µw/m²).

TABLE 3. Energy density readings in the Al-Ghadeer district

GPS				**N:32.608023 E:43.994475**	
Time	**I_1, µw/m²**	**I_2, µw/m²**	**I_3, µw/m²**	**I_4, µw/m²**	**$I_{av.}$, µw/m²**
7:00 am	36.2	45.6	29.6	34.6	36.5
8:00 am	45.3	39.2	45.6	48.1	44.6
9:00 am	56.3	62.3	48.4	45.2	53.1
10:00 am	81.6	77.3	49.4	45.3	63.4
11:00 am	91.1	82.4	45.6	38.3	64.4
12:00 am	82.3	40.3	72.3	51.2	61.5
1:00 pm	90.3	76.3	56.4	56.5	69.9
2:00 pm	91.4	68.3	34.5	25.6	55.0
3:00 pm	82.3	45.6	45.6	56.4	57.5
4:00 pm	49.3	56.3	80.2	58.3	61.0
5:00 pm	60.3	84.6	54.6	48.6	62.0
6:00 pm	61	76.5	50.1	79.3	66.7
7:00 pm	77.1	53.2	79.4	54.2	66.0
8:00 pm	68.4	40.3	67.2	96.4	68.1
9:00 pm	91.2	68.3	60.5	45.9	66.5
10:00 pm	86.5	47.3	97.2	32.1	65.8
11:00 pm	50.6	87.2	45.3	88.4	67.9
12:00 pm	76.4	81.7	49.5	56.2	66.0

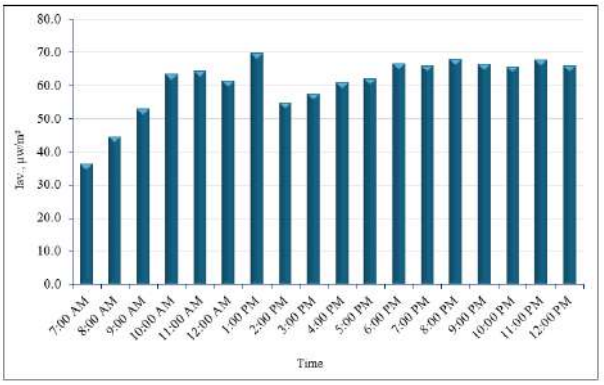

Figure 7. The relationship between time and energy density in the Al-Ghadeer district

3.4. Comparison of peak times

Figure 8 show a comparison between the peak measurement areas for the average intensity of electromagnetic energy density ($I_{avg.}$, μW/m²) in three different areas of Karbala city, representing diverse urban and functional patterns: religious (the area between the two Holy Shrines), residential (Al-Ghadeer District), and commercial (Al-Hussein District Street). This comparison helps clarify the extent to which the type of human activity and the intensity of technological uses in each area affect energy density levels.

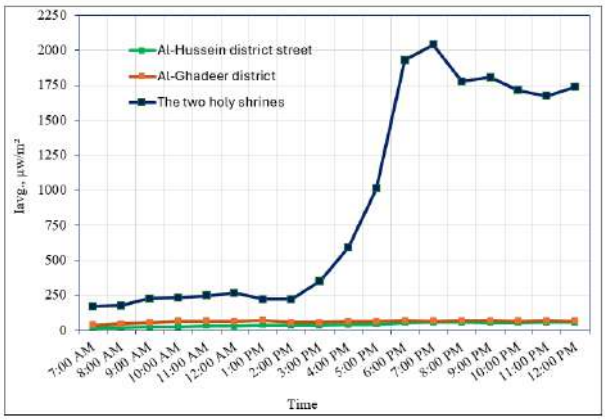

Figure 8. Comparison between peak measurement areas over a full day

4. CONCLUSIONS

Based of the result of this study, the following can be concluded:

- The measurement results showed a clear variation in electromagnetic radiation intensity levels between the studied areas. The area between the Two Holy Mosques recorded the highest electromagnetic energy intensity values, with averages reaching more than 2,000 μW/m² in some time periods. This is attributed to the high density of telecommunications towers and increased human activity in this area, in addition to the presence of multiple radiation sources within a narrow geographical area.
- To demonstrate the effect of time on radiation energy density, three points were selected within different areas of Karbala city center, including the area between the two holy shrines, Al-Ghadeer District, and Al-Hussein District Street. At each point, coordinates were established, and measurements were conducted throughout the day, starting from 7:00 a.m. until 12:00 a.m. The location between the two holy shrines, considered an important religious area, recorded high levels of more than 2,000 μW/m² at 6:00 p.m., reflecting peak usage in this densely populated area during the evening hours. On the other hand, areas such as Al-Hussein District Sreet and Al-Ghadeer District recorded relatively low radiation levels, ranging between 20 and 70 μW/m², reflecting the scarcity of radiation sources and the low number of towers in these areas, which have relatively lower population densities compared to the city center.
- When readings were taken at different times of the day, a relationship was observed between the timing of the measurement and the recorded radiation energy intensity levels, with radiation intensity gradually increasing as the day progresses, reaching its peak in the evening hours (particularly after 5 pm and until 9 pm). This is attributed to the increased heavy use of mobile phone networks during these times of the day as a result of intense population activity.
- Although some relatively high readings were recorded in some locations, all measurements remain within the permissible limits recommended by the WHO and the ICNIRP, indicating that there are no immediate risks to public health at these levels.
- The results of field measurements in different areas of Karbala showed a clear variation in the radiation levels recorded from one area to another, depending on the nature of each area in terms of population density, commercial activity, and the number of communication towers available. These results underscore the importance of continuing to monitor radiation levels regularly, especially in densely populated areas, and of working to distribute telecommunications towers in a thoughtful manner that balances service quality with maintaining public safety.

Acknowledgments

The support of University of Kufa in Iraq is gratefully acknowledged.

REFERENCES

Al-Tamer, M. Y., & Al-Ahmady, K. K. (2020). Measurement of levels of electromagnetic energy density emitted by mobile phone towers in the city of Mosul, Iraq.

Cansiz, M., et al. (2016). Mobile measurement of radiofrequency electromagnetic field exposure level and statistical analysis. Measurement, 86, 159–164.

Foster, K. R., Erdreich, L. S., & Moulder, J. E. (1997). Weak electromagnetic fields and cancer in the context of risk assessment. Proceedings of the IEEE, 85(5), 733–746.

Gupta, S. (2015). Telecommunications at the crossroads in India. IIMB Management Review, 27(3), 196–208.

Huwair, R. S. (2024). Study and determination of power density levels of radiation emitted by telecommunications towers in Babil Governorate – Al-Kifl District (Master's thesis, University of Kufa).

Jafaar, A. N., & Nema, B. M. (2019). Geolocation android mobile phones using GSM/UMTS. Baghdad Science Journal, 16(1 Supplement).

Juutilainen, J., et al. (2009). Exposure to high frequency electromagnetic fields, biological effects and health consequences (100 kHz–300 GHz). In P. Vecchia et al. (Eds.), Review of experimental studies of RF biological effects (pp. 94–319).

Karunarathna, M. A. A., Fernando, C. A. N., & Samarasekara, P. (2018). Experimental observations & comparison on RF emissions due to mobile base station antennas in Sri Lanka. International Journal of Advanced Research in Science, Engineering and Technology, 5(4), 5526–5533.

Kavet, R., & Tell, R. A. (2023). Aligning exposure limits for contact currents with exposure limits for electric fields. Health Physics, 124(5), 351–371.

Kızıloğlu, İ., et al. (n.d.). Effects of electromagnetic field (1.8/0.9 GHz) exposure on spleen in rats. Medical Records, 5(Supplement 1), 177–181.

Miller, A. B., et al. (2019). Risks to health and well-being from radio-frequency radiation emitted by cell phones and other wireless devices. Frontiers in Public Health, 7, 223.

Murch, R. D., & Letaief, K. B. (2002). Antenna systems for broadband wireless access. IEEE Communications Magazine, 40(4), 76–83.

Rappaport, T. S., et al. (2013). Millimeter wave mobile communications for 5G cellular: It will work! IEEE Access, 1, 335–349.

Read, F. H. (1980). Electromagnetic radiation. Chichester.

Regrain, C., et al. (2020). Design of an integrated platform for mapping residential exposure to RF-EMF sources. International Journal of Environmental Research and Public Health, 17(15), 5339.

Traini, E., et al. (2023). Time course of health complaints attributed to RF-EMF exposure and predictors of electromagnetic hypersensitivity over 10 years in a prospective cohort of Dutch adults. Science of the Total Environment, 856, 159240.

Wiart, J., et al. (2008). Analysis of RF exposure in the head tissues of children and adults. Physics in Medicine & Biology, 53(13), 3681.

Yahya, S. I. (2019). The use of camouflaged cell phone towers for a quality urban environment. UKH Journal of Science and Engineering, 3(1), 29–34.

Ying, D., Love, D. J., & Hochwald, B. M. (2013). Beamformer optimization with a constraint on user electromagnetic radiation exposure. IEEE.

Zamanian, A., & Hardiman, C. (2005). Electromagnetic radiation and human health: A review of sources and effects. High Frequency Electronics, 4(3), 16–26

Pure Sciences International Journal of kerbala

Year:2026 Volume : 3 Issue : 9 ISSN: 6188-2789 Print 3005 -2394 Online

2026,Volume 3 , Issue 9 , PSIJK (26-33)

Pure Sciences International Journal of Kerbala

A Flexible Extended Exponential Distribution With Its Statistical Features, Inference, and Real Application

Ali Abd Ali Mohammed Najm [a], Nadia Hashim Al-Noor [a*]

[a] *Department of Mathematics, College of Science, Mustansiriyah University, Baghdad, Iraq*

P A P E R I N F O

Received: 07.07.2025
Accepted: 21.07.2025
Published: 31.03.2026

Keywords:
traditional exponential, unit half logistic geometric, generator family, statistical features, simulation

A b s t r a c t

This paper introduces a new version of the exponential distribution, offering a more flexible model for real-life data, namely unit half logistic geometric exponential (UHLGeE). The essential statistical functions and features of the two-parameter proposed distribution are discussed. Different techniques, maximum likelihood, ordinary least squares, weighted least squares, and Cramer-Von-Mises minimum distance, are employed to estimate the two unknown parameters. Consequently, extensive simulation experiments are conducted to evaluate the performance of all estimation methods. Lastly, the efficacy and adaptability of the new distribution are illustrated through an analysis of a real data set. Based on the outcomes of the empirical and real applications, it is recommended to adopt and employ UHLGeE in additional applications due to its features and adaptability.

DOI: 10.53851/psijk.v3.i9. 26-33

1. INTRODUCTION

Lifetime distributions are an effective tool for determining the lifespan of devices, systems, and time-to-event data in general. These distributions are commonly employed in various fields, including biology, insurance, engineering, and reliability. With a large range of continuous univariate models, the literature on lifespan distributions is extensive and rapidly expanding. Many modifications to widely used distributions have been introduced over time to handle the complicated nature of real-life data. This includes incorporating one or more extra parameters into the traditional (existing/baseline) distribution. These parameters were valuable for evaluating tail features and enhancing the goodness-of-fit of the resulting distribution. The traditional one-scale exponential (E) distribution is among the most common distributions in various applications. It has a constant hazard function. But, different systems in real life rarely have a stable hazard/risk rate across time (see Singh et al., 2013). Consequently, it appears plausible to assume the hazard as a function of time, which resulted in the creation of an alternative modified/extended model for lifetime data analysis. Numerous distributions have been introduced as extensions of the E distribution. Notable examples of these extensions can be found in the literature, for example, generalized E (Marshall & Olkin, 1997 and Gupta & Kundu, 1999), exponentiated E (Gupta & Kundu, 2001), beta E (Nadarajah & Kotz, 2006), Kumaraswamy E as a special case form the Kumaraswamy Weibull (Cordeiro et al., 2010), extension E (Nadarajah & Haghighi, 2011), gamma-exponentiated E (Ristić & Balakrishnan, 2012), Kumaraswamy generalized exponentiated E (Mohammed, 2014), transmuted generalised E (Khan et al., 2017), exponentiated Weibull-E (Elgarhy et al., 2017), Marshall-Olkin length-biased E (ul Haq et al., 2019), new extension of extended E (Alghamedi et al., 2020), modified extended E (Mahmoud et al., 2022), truncated inverse Rayleigh odd Weibull E (Al-Noor & Sultan, 2024), and unit extended E (Ragab et al., 2024), among others. This paper aims to introduce a new flexible extended version of the E distribution by adding an extra parameter to its traditional version. The rest of the paper is organized as follows: Section 2 contains the statistical methodology for constructing the new distribution. Section 3 discusses the distribution's essential statistical

*Corresponding Author Institutional Email: (Nadia Hashim Al-Noor)
nadialnoor@uomustansiriyah.edu.iq

features. Section 4 presents four estimation procedures to estimate the unknown parameters. Section 5 provides the empirical and real-life applications. Section 6 provides some concluding remarks.

2. CONSTRUCTING THE NEW DISTRIBUTION

This section explores the new distribution, providing its essential statistical functions: the cumulative distribution function (CDF), probability density function (PDF), reliability function (RF), and hazard function (HF). In this context, the focus is on adding a shape parameter to the traditional version of the E distribution by employing the unit half logistic geometric generator (UHLGe-G) family recently introduced by Najm & Al-Noor (2025), which is characterized by the following CDF and PDF,

$$F(x;\theta,\delta)=\frac{2G(x;\delta)}{\theta+(2-\theta)G(x;\delta)}\;;\;\theta>0 \qquad (1)$$

$$f(x;\theta,\delta)=\frac{2\theta g(x;\delta)}{(\theta+(2-\theta)G(x;\delta))^2}\;;\;\theta>0 \qquad (2)$$

where θ is the shape parameter, $G(x;\delta)$ and $g(x;\delta)$ are the input baseline CDF and PDF with a parameter vector δ.

Using the CDF and PDF of the traditional E distribution with scale parameter β as the inputs instead of $G(x;\delta)$ and $g(x;\delta)$ in (1) and (2), the two-parameter new distribution, namely unit half logistic geometric exponential (UHLGeE), can be constructed with the following CDF and PDF for $x\geq 0$ and $\theta,\beta>0$,

$$F(x;\theta,\beta)=\frac{2\left(1-e^{-\beta x}\right)}{\theta+(2-\theta)(1-e^{-\beta x})} \qquad (3)$$

$$f(x;\theta,\beta)=\frac{2\theta\beta e^{-\beta x}}{\left(\theta+(2-\theta)(1-e^{-\beta x})\right)^2} \qquad (4)$$

For more specialized cases, the CDF in (3) can be reformed according to the value of the shape parameter θ as follows

$$F(x;\theta,\beta)=\begin{cases}\frac{1-e^{-\beta x}}{1-\frac{2-\theta}{2}e^{-\beta x}} & ;\theta\in(0,2)\\ \frac{2\left(1-e^{-\beta x}\right)}{\theta\left(1-\left(\frac{\theta-2}{\theta}\right)\left(1-e^{-\beta x}\right)\right)} & ;\theta>2\\ 1-e^{-\beta x} & ;\theta=2\end{cases} \qquad (5)$$

The corresponding PDF will be

$$f(x;\theta,\beta)=\begin{cases}\frac{\theta\beta e^{-\beta x}}{2\left(1-\frac{2-\theta}{2}e^{-\beta x}\right)^2} & ;\theta\in(0,2)\\ \frac{2\beta e^{-\beta x}}{\theta\left(1-\left(\frac{\theta-2}{\theta}\right)(1-e^{-\beta x})\right)^2} & ;\theta>2\\ \beta e^{-\beta x} & ;\theta=2\end{cases} \qquad (6)$$

Equations (5) and (6) emphasize that the proposed UHLGeE distribution with $\theta=2$ is reduced to the baseline traditional E distribution, and thus it can also be described as a generalized E distribution.

The RF and HF can be attained as

$$R(x;\theta,\beta)=1-F(x;\theta,\beta)=\frac{\theta e^{-\beta x}}{\theta+(2-\theta)\left(1-e^{-\beta x}\right)} \qquad (7)$$

$$h(x;\theta,\beta)=\frac{f(x;\theta,\beta)}{R(x;\theta,\beta)}=\frac{2\beta}{\theta+(2-\theta)\left(1-e^{-\beta x}\right)} \qquad (8)$$

Figures 1 and 2 illustrate the versatility of the PDF and HF, demonstrating their potential to take different shapes. These graphical representations highlight the proposed distribution's adaptability and ability to capture various data patterns with increasing and decreasing HF.

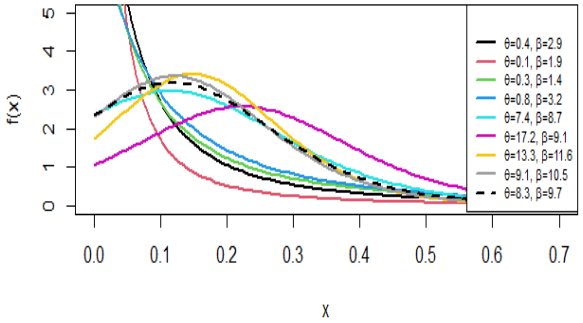

Figure 1. Plot of PDF with different default parameter values

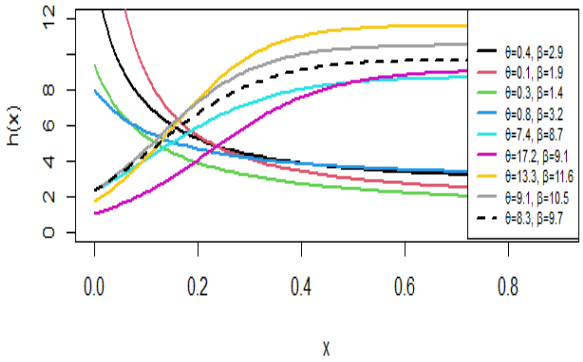

Figure 2. Plot of HF with different default parameter values

3. STATISTICAL FEATURES

This section investigates essential statistical features of the proposed distribution, including linear expansions of the PDF and CDF, moments, quantile measures, order statistics, and entropy. These features provide vital insights into the distribution's behavior and structure.

3.1. Linear expansions

Calling $F(x;\theta,\beta)$ from (5) and $f(x;\theta,\beta)$ from (6) with employing the following expansion series that valid for $|z|<1$ and $a>0, (1-z)^{-a}=\sum_{i=0}^{\infty}\binom{i+a-1}{i}z^i$ and $(1-z)^a=\sum_{i=0}^{\infty}(-1)^i\binom{a}{i}z^i$, the linear expansions of the CDF and PDF formulae will be

$$F^e(x;\theta,\beta)=\begin{cases}\sum_{i,j=0}^{\infty}c_{i,j}\,(1-e^{-\beta x})^{j+1}; \theta\in(0,2)\\ \frac{2}{\theta}\sum_{i=0}^{\infty}u_i\,(1-e^{-\beta x})^{i+1}\,; \theta>2\end{cases} \quad (9)$$

and

$$f^e(x;\theta,\beta)=\begin{cases}\frac{\theta}{2}\beta e^{-\beta x}\sum_{i,j=0}^{\infty}c_{i,j}\,(i+1)\\ \qquad (1-e^{-\beta x})^{j}\,; \theta\in(0,2)\\ \frac{2}{\theta}\beta e^{-\beta x}\sum_{i=0}^{\infty}u_i(i+1)\\ \qquad (1-e^{-\beta x})^{i}\;; \theta>2\end{cases} \quad (10)$$

where $c_{i,j}=c_{i,j}(\theta)=(-1)^j\left(\frac{2-\theta}{2}\right)^i\binom{i}{j}$, $\binom{i}{j}=\frac{i!}{j!(i-j)!}$, and $u_i=u_i(\theta)=\left(\frac{\theta-2}{\theta}\right)^i$.

It should be noted that, when $\theta=2$, the CDF expansion formula and its associated PDF are respectively related to the expansion CDF and PDF of the baseline E distribution.

3.2. Quantile Measurements

The quantile function $Q(q)$of the proposed distribution can be obtained easily by solving (3) for $Q(q)$ in terms of q, i.e., $F(Q(q);\theta,\beta)=q$, as

$$Q(q)=x_q=\frac{-1}{\beta}\ln\left(\frac{2(1-q)}{2-(2-\theta)q}\right); q\in(0,1),\theta>0 \quad (11)$$

By replacing q with u, where u denotes a value of standard Uniform distribution, simulate a random variable related to the UHLGeE is

$$Q(u)=x_q=\frac{-1}{\beta}\ln\left(\frac{2(1-u)}{2-(2-\theta)u}\right); u\in(0,1),\theta>0 \quad (12)$$

With specific values of q, see Al-Noor & Hadi (2021) related quantile measures can be attained, including the median by setting $q=1/2$, skewness $\left(S(X)=\frac{Q(3/4)-2Q(2/4)+Q(1/4)}{Q(3/4)-Q(1/4)}\right)$, and kurtosis $\left(K(X)=\frac{Q(7/8)-Q(5/8)-Q(3/8)+Q(1/8)}{Q(6/)-Q(2/8)}\right)$.

3.3. Order Statistics (O.S.)

Consider $X_{1:n}\le\ldots\le X_{n:n}$ denote the O.S. related to a random sample of size n related to UHLGeE. The PDF of the i$^{\text{th}}$ O.S. can be expressed for $i=1,2,\ldots,n$ as

$$f_{i:n}(x;\theta,\beta)=\frac{n!2^i\theta^{n-i+1}\beta\left(1-e^{-\beta x}\right)^{i-1}e^{-\beta x(n-i+1)}}{(i-1)!(n-i)!\left(\theta+(2-\theta)\left(1-e^{-\beta x}\right)\right)^{n+1}} \quad (13)$$

The PDFs of the smallest and largest O.S. can be attained simply from (13) with $(i=1)$ and $(i=n)$ respectively, as

$$f_{1:n}(x;\theta,\beta)=\frac{2n\theta^n\beta e^{-n\beta x}}{\left(\theta+(2-\theta)(1-e^{-\beta x})\right)^{n+1}} \quad (14)$$

$$f_{n:n}(x;\theta,\beta)=\frac{2^n n\theta\beta e^{-\beta x}\left(1-e^{-\beta x}\right)^{n-1}}{\left(\theta+(2-\theta)(1-e^{-\beta x})\right)^{n+1}} \quad (15)$$

3.4. Moments and Moments Generating Function

Using the definition of the r^{th} moment about the origin, $\mu_r=E(X^r)=\int_0^{\infty}x^r f(x;\theta,\beta)\,dx$ with the expansion PDF given in (10), the outcomes are easily attained as

$$\mu_r=E(X^r)=\begin{cases}\frac{\theta}{2}\sum_{i,j=0}^{\infty}c_{i,j}\,(i+1)\,\mu_{r,j}^{(PW)}\;; \theta\in(0,2)\\ \frac{2}{\theta}\sum_{i=0}^{\infty}u_i\,(i+1)\,\mu_{r,i}^{(PW)}\quad ; \theta>2\end{cases} \quad (16)$$

where the probability weighted moments

$$\mu_{r,j}^{(PW)}=\sum_{k=0}^{\infty}(-1)^k\binom{j}{k}\frac{1}{k+1}\int_0^{\infty}x^r\,\beta(k+1)e^{-\beta(k+1)x}dx$$

and

$$\mu_{r,i}^{(PW)}=\sum_{j=0}^{\infty}(-1)^j\binom{i}{j}\frac{1}{j+1}\int_0^{\infty}x^r\,\beta(j+1)e^{-\beta(j+1)x}dx.$$

Since the two integrals represent the r^{th} moments about the origin of the traditional E distribution respectively with parameters $(\beta(k+1))$ and $(\beta(j+1))$, then

$$\mu_{r,j}^{(PW)}=\sum_{k=0}^{\infty}(-1)^k\binom{j}{k}\frac{r!}{\beta^r(k+1)^{r+1}} \quad (17)$$

and

$$\mu_{r,i}^{(PW)}=\sum_{j=0}^{\infty}(-1)^j\binom{i}{j}\frac{r!}{\beta^r(j+1)^{r+1}} \quad (18)$$

Substituting (17) and (18) in (16), the r^{th} moment of UHLGeE is

$$\mu_r = \begin{cases} \frac{\theta}{2} \sum_{i,j,k=0}^{\infty} c_{i,j} (-1)^k \binom{j}{k} \frac{r!\ (i+1)}{\beta^r (k+1)^{r+1}}; \theta \in (0,2) \\ \frac{2}{\theta} \sum_{i,j=0}^{\infty} u_i (-1)^j \binom{i}{j} \frac{r!\ (i+1)}{\beta^r (j+1)^{r+1}} \quad ; \theta > 2 \end{cases} \tag{19}$$

The moments generating function of the UHLGeE can be attained by applying its definition with the Maclaurin series by $M_X(t) = E(e^{tX}) = \sum_{r=0}^{\infty} \frac{t^r}{r!}\ \mu_r$, and μ_r given in (2.21), as

$$M_X(t) = \begin{cases} \frac{\theta}{2} \sum_{i,j,k,r=0}^{\infty} c_{i,j} \binom{j}{k} \frac{(-1)^k\, t^r\, (i+1)}{\beta^r (k+1)^{r+1}}; \theta \in (0,2) \\ \frac{2}{\theta} \sum_{i,j,r=0}^{\infty} u_i \binom{i}{j} \frac{(-1)^j\, t^r (i+1)}{\beta^r (j+1)^{r+1}} \quad ; \theta > 2 \end{cases} \tag{20}$$

Further, the characteristic function can also be attained by the mentioned series as $\emptyset_X(t) = E(e^{itX}) = \sum_{r=0}^{\infty} \frac{(it)^r}{r!} \mu_r$.

3.5. Entropies

According to information theory, a random variable's entropy measures the typical degree of information or ambiguity surrounding its various states or outcomes. Rényi and Shannon, two major types of entropy, are discussed due to their important applications. For more details about these entropies, including their formulas, see Reyad et al., 2018 and Al-Noor & Sultan, 2024.

The Rényi entropy can be specified based on the PDF in (4) by

$I_R(\Upsilon) = \frac{1}{1-\Upsilon} \ln\left(\int_{\forall x} f^{\Upsilon}(x;\theta,\beta)\, dx\right); \Upsilon > 0, \Upsilon \neq 1.$

Then, using the generalized binomial formula, $f^{\Upsilon}(x;\theta,\beta)$ can be expressed as a series expansion, which is then applied to get the formula of $I_R(\Upsilon)$ as

$$I_R(\Upsilon) = \begin{cases} \frac{1}{1-\Upsilon}\left[\Upsilon \ln\left(\frac{\theta}{2}\right) + \ln(A_1)\right]; \theta \in (0,2) \\ \frac{1}{1-\Upsilon}\left[\Upsilon \ln\left(\frac{2}{\theta}\right) + \ln(A_2)\right]; \theta > 2 \end{cases} \tag{21}$$

where

$A_1 = \sum_{i,j,k=0}^{\infty} c_{i,j}(\theta,\Upsilon)\,(-1)^k \binom{j}{k} \frac{\beta^{\Upsilon-1}}{\gamma+k}$;

$A_2 = \sum_{i,j=0}^{\infty} u_i(\theta,\Upsilon)\,(-1)^j \binom{i}{j} \frac{\beta^{\Upsilon-1}}{\gamma+j}$;

$c_{i,j}(\theta,\Upsilon) = (-1)^j \left(\frac{2-\theta}{2}\right)^i \binom{i}{j} \binom{2\Upsilon+i-1}{i} = c_{i,j} \binom{2\Upsilon+i-1}{i}$;

and $u_i(\theta,\Upsilon) = \left(\frac{\theta-2}{\theta}\right)^i \binom{2\Upsilon+i-1}{i} = u_i \binom{2\Upsilon+i-1}{i}$.

The Shannon entropy can be obtained by applying $\Upsilon \longrightarrow 1$ to $I_R(\Upsilon)$ in (21) or is specified by $\eta(X) = E\big(-\ln\big(f(x;\theta,\delta)\big)\big)$. Recall (4), then

$$\eta(X) = \begin{cases} \ln\left(\frac{2}{\theta}\right) - E\big(\ln\big(\beta e^{-\beta X}\big)\big) + 2E_1 \ ; \theta \in (0,2) \\ \ln\left(\frac{\theta}{2}\right) - E\big(\ln\big(\beta e^{-\beta X}\big)\big) + 2E_2 \ ; \theta > 2 \end{cases} \tag{22}$$

where $E\big(\ln\big(\beta e^{-\beta X}\big)\big) = \ln(\beta) - \beta E(X)$, and the other required mathematical expectations can be obtained with $\ln(1-z) = -\sum_{i=1}^{\infty} \frac{1}{i} z^i; |z| < 1$, along with the expansion exponential series, and $(1-z)^{\alpha}$ as

$E_1 = E\left(\ln\left(1 - \frac{2-\theta}{2} e^{-\beta X}\right)\right)$

$= -\sum_{i=1}^{\infty} \sum_{j=0}^{\infty} \frac{1}{i} c_{i,j}\ E\left(\left(1 - e^{-\beta X}\right)^j\right)$

$= \sum_{i=1}^{\infty} \sum_{j,k,r=0}^{\infty} c_{i,j} \frac{(-1)^{k+r+1}}{r!\, i} \binom{j}{k} (k\beta)^r E(X^r)$

and

$E_2 = E\left(\ln\left(1 - \frac{\theta-2}{\theta}\left(1 - e^{-\beta X}\right)\right)\right)$

$= -\sum_{i=1}^{\infty} \frac{1}{i} u_i\, E\left(\left(1 - e^{-\beta X}\right)^i\right)$

$= \sum_{i=1}^{\infty} \sum_{j,r=0}^{\infty} u_i \frac{(-1)^{j+r+1}}{r!\, i} \binom{i}{j} (j\beta)^r E(X^r)$

where $c_{i,j}$ and u_i as defined previously, and $E(X)$ can be attained from $E(X^r)$ given in (19) with $r = 1$.

4. INFERENCE WITH DIFFERENT METHODS

For this purpose, consider $x_1, x_2, \ldots, x_n$ a random sample of size n from the UHLGeE represents the data, and their ascending ordering values are denoted by $x_{(1)}, x_{(2)}, \ldots, x_{(n)}$. Four methods: maximum likelihood (ML), ordinary least squares (OLS), weighted least squares (WLS), and Cramer Von-Mises (CVM) minimum distance are considered. For more details on the considered methods, see Hassan et al., 2023.

The ML methodology is the most often used parameter estimation method due to its desirable features such as consistency, asymptotic efficiency, and invariance (Dey et al., 2019). The ML estimates of a vector of parameters $\varphi = \theta, \beta$ are attained through $\hat{\varphi}^{\mathrm{ML}} = \operatorname{argmax} \mathrm{L}(\varphi)$ or, equivalently $\hat{\varphi}^{\mathrm{ML}} = \operatorname{argmax} \ell(\varphi)$ where $\mathrm{L}(\varphi) = \prod_{i=1}^{n} f(x_i;\varphi)$ and $\ell(\varphi) = \ln\big(\mathrm{L}(\varphi)\big)$ are the likelihood and natural logarithm likelihood functions. Now, recall the PDF in (4), then

$$\ell(\theta,\beta) = n\ln(2) + n\ln(\theta) + n\ln(\beta) - \beta\sum_{i=1}^{n} x_i - 2\sum_{i=1}^{n} \ln\big(\theta + (2-\theta)(1 - e^{-\beta x_i})\big)$$

The ML estimates of the parameters can be obtained by solving simultaneously the two non-linear equations $\partial\ell(\theta,\beta)/\partial\theta = 0$ and $\partial\ell(\theta,\beta)/\partial\beta = 0$, where

$$\frac{\partial \ell(\theta,\beta)}{\partial \theta} = \frac{n}{\theta} - 2\sum_{i=1}^{n} \frac{e^{-\beta x_i}}{\theta + (2-\theta)(1 - e^{-\beta x_i})} \tag{23}$$

and

$$\frac{\partial \ell(\theta,\beta)}{\partial \beta} = \frac{n}{\beta} - \sum_{i=1}^{n} x_i - 2(2-\theta) \sum_{i=1}^{n} \frac{x_i\, e^{-\beta x_i}}{\theta + (2-\theta)(1-e^{-\beta x_i})} \quad (24)$$

On the other side, the OLS estimates of φ are attained through $\hat{\varphi}^{\mathrm{OLS}} = \operatorname{argmin} \mathrm{OL}S(\varphi)$ where $\mathrm{OL}S(\varphi) = \sum_{i=1}^{n}\left(F(x_{(i)};\varphi) - \frac{i}{n+1}\right)^2$ and $F(x_{(i)};\varphi)$ is the CDF of the considered distribution with ascending ordering observations. Now, recall the CDF given in (3), then

$$\mathrm{OLS}(\theta,\beta) = \sum_{i=1}^{n}\left(\frac{2(1-e^{-\beta x_{(i)}})}{\theta+(2-\theta)(1-e^{-\beta x_{(i)}})} - \frac{i}{n+1}\right)^2 \quad (25)$$

Similarly, the WLS estimates of φ are attained through $\hat{\varphi}^{\mathrm{WLS}} = \operatorname{argmin} \mathrm{WL}S(\varphi)$ where $\mathrm{WL}S(\varphi) = \sum_{i=1}^{n} w_i\left(F(x_{(i)};\varphi) - \frac{i}{n+1}\right)^2$ and $w_i = \frac{(n+1)^2(n+2)}{i(n-i+1)}$. Based on the CDF given in (3), then

$$\mathrm{WLS}(\theta,\beta) = \sum_{i=1}^{n} w_i\left(\frac{2(1-e^{-\beta x_{(i)}})}{\theta+(2-\theta)(1-e^{-\beta x_{(i)}})} - \frac{i}{n+1}\right)^2 \quad (26)$$

Finally, the CVM estimates of φ are attained through $\hat{\varphi}^{\mathrm{CVM}} = \operatorname{argmin} \mathrm{CVM}(\varphi)$ where $\mathrm{CVM}(\varphi) = \frac{1}{12n} + \sum_{i=1}^{n}\left(F(x_{(i)};\varphi) - \frac{2i-1}{2n}\right)^2$. Based on the CDF given in (3), then

$$\mathrm{CVM}(\theta,\beta) = \frac{1}{12n} + \sum_{i=1}^{n}\left(\frac{2(1-e^{-\beta x_{(i)}})}{\theta+(2-\theta)(1-e^{-\beta x_{(i)}})} - \frac{2i-1}{2n}\right)^2 \quad (27)$$

Based on (25), (26), and (27), the OLS, WLS, and CVM estimates can be obtained by solving simultaneously the two non-linear equations attained from taking the partial derivatives of $\mathrm{OLS}(\theta,\beta)$, $\mathrm{WLS}(\theta,\beta)$, and $\mathrm{CVM}(\theta,\beta)$ concerning the unknown parameters (θ,β) and equating them to zero.

5. EMPIRICAL AND REAL APPLICATIONS

To evaluate the model's behavior concerning parameter estimations over different default values and sample sizes, simulation experiments are conducted. Furthermore, the utility of the proposed distributions with various statistical measures is evaluated through a real dataset. All graphical and numerical illustrations are obtained using the R programming language.

5.1. Empirical Application

The performances of the discussed estimation methods are investigated empirically via simulation. Based on different default parameter sets and sample sizes, simulation studies experimentally evaluate the behavior of the ML, OLS, WLS, and CVM estimates for parameters. The default parameter values are set as: set I $(\theta = 0.4, \beta = 2.9)$, set II $(\theta = 17.2, \beta = 9.1)$, and set III $(\theta = 13.3, \beta = 11.6)$. The sample sizes are chosen as: $n = 25, 50, 100,$ and 200. The simulated formula in (12) is used to generate a random sample of size n that follows UHLGeE. This step is repeated 1000 times to yield 1000 independent samples of varying sizes. After obtaining the ML, OLS, WLS, and CVM estimates, calculate the mean squared error (MSE) (Al-Noor & Abd Al-Ameer, 2013) for each parameter, as follows

$$MSE(\hat{\varphi}) = \frac{1}{1000}\sum_{i=1}^{1000}(\hat{\varphi}_{\mathrm{i}} - \varphi)^2;\ \varphi = \theta, \beta \quad (28)$$

Tables 1 – 3 present the empirical results of the simulation studies of the considered set. Further, Table 4 presents the number of times that a specified method app ears as the best method.

TABLE 1. Values of MSE of different estimates for Set I

φ	n	ML	OLS	WLS	CVM	Best
θ	25	0.025163	0.040717	0.033419	0.055569	ML
	50	0.012423	0.019829	0.017620	0.023257	ML
	100	0.007168	0.011044	0.008964	0.012039	ML
	200	0.004523	0.007122	0.005720	0.007371	ML
β	25	0.106065	0.150210	0.128624	0.187161	ML
	50	0.064048	0.104979	0.089875	0.115435	ML
	100	0.039350	0.063872	0.050265	0.067242	ML
	200	0.025820	0.043173	0.033616	0.043773	ML

TABLE 2. Values of MSE of different estimates for Set II

φ	n	ML	OLS	WLS	CVM	Best
θ	25	0.891148	1.014250	1.048576	1.491813	ML
	50	0.407929	0.415534	0.406135	0.497186	WLS
	100	0.241490	0.247699	0.242495	0.269948	ML
	200	0.148502	0.155783	0.150715	0.161957	ML
β	25	0.074956	0.079702	0.075895	0.086233	ML
	50	0.047855	0.053458	0.050117	0.055340	ML
	100	0.034801	0.038384	0.036215	0.039055	ML
	200	0.024134	0.027136	0.025184	0.027198	ML

TABLE 3. Values of MSE of different estimates for Set III

φ	n	ML	OLS	WLS	CVM	Best
θ	25	0.714291	0.667275	0.642940	0.951644	WLS
	50	0.309732	0.355257	0.330148	0.419651	ML
	100	0.175848	0.178639	0.171925	0.195199	WLS
	200	0.105318	0.111173	0.106752	0.114202	ML
β	25	0.103398	0.111535	0.107009	0.122748	ML
	50	0.066509	0.074938	0.069464	0.077397	ML
	100	0.045873	0.051771	0.047708	0.053029	ML
	200	0.030769	0.035552	0.032405	0.035389	ML

TABLE 4. Number of times that the specified estimates is the best

Set	ML	OLS	WLS	CVM
I	8	0	0	0
II	7	0	1	0
III	6	0	2	0

From the empirical results in Tables 1–3, the most important outcomes can be stated as:

1. The ML method is the best for estimating parameter θ for all sample sizes in set I as well as in other subsequent sets, except II with $n = 50$, and III with $n = 25, 100$, where the WLS method is the best.
2. The ML method outperformed other methods in estimating parameter β across all sets and sample sizes.
3. Overall, for both parameters, the ML method was most often reported as the best. Noting that neither OLS nor CVM recorded any appearances. See Table (4).
4. The MSE values decrease with increasing sample size, demonstrating the estimators' consistency.

5.2. Real Application

The dataset used to examine the applicability of the proposed distribution reflects the birth rate with abnormalities in Iraqi governorates in 2020, as reported in Iraq's Ministry of Health Annual Report. The values of the considered data are: "2.9, 2.0, 3.8, 2.1, 1.8, 1.6, 10.9, 4.0, 5.8, 3.9, 2.5, 3.6, 2.0, 0.2, 3.2, 1.1, 3.2, 1.2". The basic descriptive statistics for this medical dataset are given in Table 5. The common statistical information criteria (IC) are employed for the evaluation process, as tools for model selection, Akaike: $A = 2(m - \hat{\ell})$; Consistent Akaike: $CA = 2\left(\frac{nm}{n-m-1} - \hat{\ell}\right)$; Bayesian: $B = m\ln(n) - 2\hat{\ell}$; and Hannan and Quinn: $HQ = 2(m\ln(\ln(n)) - \hat{\ell})$ where n: sample size, m: number of estimated parameters, and $\hat{\ell}$: estimated ℓ evaluated at ML estimates, as their performances are quite satisfactory for all competitive distributions. The p-values of the KS (Kolmogorov-Smirnov) goodness-of-fit statistic are also considered during the evaluation procedure. The model with a smaller value of the IC and a higher p-value is preferred (Alizadeh et al., 2018). To broaden the investigation process, the traditional E along with its common extended versions, beta E (BE), Kumaraswamy E (KE), exponentiated generalized E (EGE), Weibull E (WE), and Gompertz E (GoE), are also included. For more details about the families to which the competing distributions belong, see Eugene et al. (2002), Cordeiro & De Castro (2011), Cordeiro et al. (2013), Bourguignon et al. (2014), and Alizadeh et al. (2017). The numerical results are displayed in Tables 6 and 7.

TABLE 5. Basic descriptive statistics for Data

St.	Mean	Sk	Ku	Q1	Med.	Q3
Val.	3.1	2.27	6.96	1.75	2.7	3.825

TABLE 6. ML estimate's values for Data

Dist.	$\hat{\delta}$	$\hat{\theta}$	$\hat{\beta}$
UHLGeE		11.94395	0.72182
BE	1.08121	2.23714	0.48139
KE	1.56019	2.07478	0.36064
EGE	2.25284	1.14394	0.44959
WE	1.30352	1.46570	0.37939
GoE	0.32812	0.74871	0.32290
E			0.32258

TABLE 7. Values of fitting Data

Dist.	A	CA	B	HQ	KS p-value
UHLGeE	76.4194	77.2194	78.2001	76.6649	0.8160
BE	78.1144	79.8287	80.7855	78.4827	0.7855
KE	78.0645	79.7788	80.7356	78.4328	0.7776
EGE	78.1156	79.8299	80.7868	78.4840	0.7866
WE	78.7679	80.4822	81.4390	79.1362	0.6363
GoE	81.2902	83.0045	83.9613	81.6585	0.5328
E	78.7304	78.9804	79.6208	78.8532	0.2376

The numerical outcomes indicate that: The descriptive statistics show that the data set is right-skewed and leptokurtic, The proposed UHLGeE has the lowest values of all IC and the largest p-values compared to other competitive distributions, making it the most appropriate distribution to represent the considered medical data. Further, the p-values for all distributions are significant, higher than 0.05. Thus, all distributions are fit for modeling data, but the proposed one is the best. Moreover, the best fitting of UHLGeE is shown by the plots of the estimated PDFs and CDFs in Figures 3 and 4.

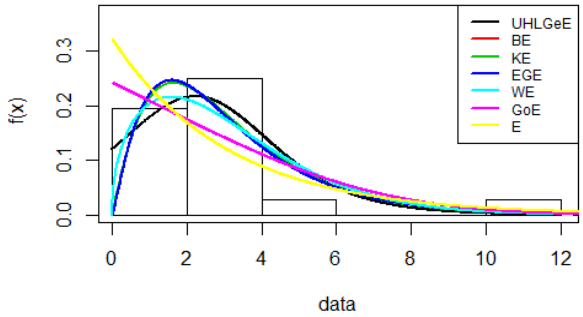

Figure 3. Estimated PDF of UHLGeE and competitive distributions

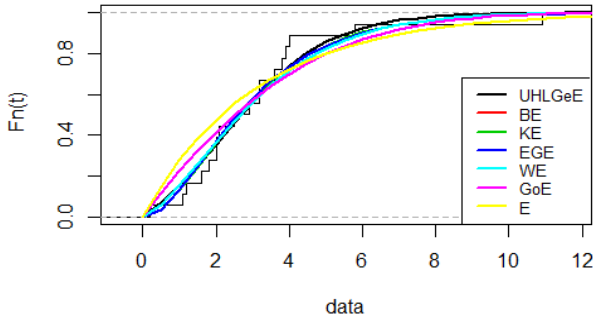

Figure 4. Empirical CDF of UHLGeE and competitive distributions

6. CONCLUSIONS

Over the years, there has been renewed interest in constructing new univariate continuous distributions. In this paper, the unit half logistic geometric exponential (UHLGeE) distribution is proposed as a new flexible extension of the traditional exponential (E) distribution. The proposed distribution includes incorporating one extra parameter into the existing traditional E distribution. The traditional version can be obtained as a special case of the proposed distribution. Thus, the proposed distribution can be characterized as a generalized exponential distribution. The UHLGeE's density and hazard functions can have a variety of shapes, indicating its applicability to analyzing varied real-life data. Further, the closed expression of the quantile function is what makes the proposed distribution remarkable. Inverse transform sampling can therefore be used to provide the distribution values, and skewness and kurtosis measurements are simple to compute. Through a wide range of simulation experiments, the accuracy and stability of the two parameters are emphasized by employing four estimation techniques, and then providing optimism regarding the distribution's flexibility in real-life applications. The proposed distribution has the lowest values of all information criteria and the largest p-values compared to other competitive distributions, making it the most appropriate distribution to represent the considered real-life data. For future studies, it is recommended to adopt and employ UHLGeE in additional applications due to its features and adaptability, and consider rank set sampling or Bayesian methods besides the four methods considered here to estimate the unknown parameters and reliability measures.

REFERENCES

Alghamedi, A., Dey, S., Kumar, D., & Dobbah, S. A. (2020). A new extension of extended exponential distribution with applications. *Annals of Data Science*, *7*(1), 139-162.

Alizadeh, M., Cordeiro, G. M., Pinho, L. G. B., & Ghosh, I. (2017). The Gompertz-G family of distributions. *Journal of Statistical Theory and Practice*, *11*(1), 179-207.

Alizadeh, M., Rasekhi, M., Yousof, H. M., & Hamedani, G. G. (2018). The transmuted Weibull-G family of distributions. *Hacettepe Journal of Mathematics and Statistics*, *47*(6), 1671-1689.

Al-Noor, N. H., & Abd Al-Ameer, H. A. (2013). Comparison of Classical and Bayesian Estimations for Shape Parameter in Burr Type XII Distribution under the Jeffrey's and modified Jeffrey's Priors. *Al-Mustansiriyah Journal of Science*, *24*(5), 199-208.

Al-Noor, N. H., & Hadi, H. H. (2021). properties and applications of truncated exponential Marshall Olkin Weibull distribution. In *Journal of Physics: Conference Series* (Vol. 1879, No. 3, p. 032024). IOP Publishing.

Al-Noor, N. H., & Sultan, A. J. (2024). Inference of truncated inverse Rayleigh Odd Weibull exponential distribution with simulation and application to COVID-19 data. In *AIP Conference Proceedings* (Vol. 3036, No. 1, p. 040008). AIP Publishing.

Bourguignon, M., Silva, R. B., & Cordeiro, G. M. (2014). The Weibull-G family of probability distributions. *Journal of Data Science*, *12*(1), 53-68.

Cordeiro, G. M., & De Castro, M. (2011). A new family of generalized distributions. *Journal of Statistical Computation and Simulation*, *81*(7), 883-898.

Cordeiro, G. M., Ortega, E. M., & da Cunha, D. C. (2013). The exponentiated generalized class of distributions. *Journal of Data Science*, *11*(1), 1-27.

Cordeiro, G. M., Ortega, E. M., & Nadarajah, S. (2010). The Kumaraswamy Weibull distribution with application to failure data. *Journal of the Franklin Institute*, *347*(8), 1399-1429.

Dey, S., Nassar, M., Kumar, D., Alzaatreh, A., & Tahir, M. H. (2019). A new lifetime distribution with decreasing and upside-down bathtub-shaped hazard rate function. *Statistica*, *79*(4), 399-426.

Elgarhy, M., Shakil, M., & Golam Kibria, B. M. (2017). Exponentiated Weibull-exponential distribution with applications. *Applications and Applied Mathematics: An International Journal (AAM)*, *12*(2), 710-725.

Eugene, N., Lee, C., & Famoye, F. (2002). Beta-normal distribution and its applications. *Communications in Statistics-Theory and Methods*, *31*(4), 497-512.

Gupta, R. D., & Kundu, D. (1999). Theory & methods: Generalized exponential distributions. *Australian & New Zealand Journal of Statistics*, *41*(2), 173–188.

Gupta, R. D., & Kundu, D. (2001). Generalized exponential distribution: different method of estimations. *Journal of Statistical Computation and Simulation*, *69*(4), 315-337.

Hassan, E. A., Elgarhy, M., Eldessouky, E. A., Hassan, O. H. M., Amin, E. A., & Almetwally, E. M. (2023). Different estimation methods for new probability distribution approach based on environmental and medical data. *Axioms*, *12*(2), 220.

Khan, M. S., King, R., & Hudson, I. L. (2017). Transmuted generalized exponential distribution: A generalization of the exponential distribution with applications to survival data. *Communications*

in Statistics-Simulation and Computation, *46*(6), 4377-4398.

Mahmoud, M. A., Ramadan, D. A., & Mansour, M. M. (2022). Estimation of lifetime parameters of the modified extended exponential distribution with application to a mechanical model. *Communications in Statistics-Simulation and Computation*, *51*(12), 7005-7018.

Marshall, A. W., & Olkin, I. (1997). A new method for adding a parameter to a family of distributions with application to the exponential and Weibull families. *Biometrika*, *84*(3), 641-652.

Mohammed, B. E. (2014). Statistical properties of Kumaraswamy-generalized exponentiated exponential distribution. *International Journal of Computer Applications*, *94*(4), 1-8.

Nadarajah, S., & Haghighi, F. (2011). An extension of the exponential distribution. *Statistics*, *45*(6), 543-558.

Nadarajah, S., & Kotz, S. (2006). The beta exponential distribution. *Reliability Engineering and System Safety*, *91*(6), 689-697.

Najm, A. A. A. M., & Al-Noor, N. H. (2025). A new extended Gompertz distribution with increasing and bathtub shape hazard function: Theory and applications. In *AIP Conference Proceedings* (Vol. 3282, No. 1, p. 040015). AIP Publishing.

Ragab, I. E., Alsadat, N., Balogun, O. S., & Elgarhy, M. (2024). Unit extended exponential distribution with applications. *Journal of Radiation Research and Applied Sciences*, *17*(4), 101118.

Reyad, H., Jamal, F., Othman, S., & Hamedani, G. G. (2018). The transmuted Gompertz-G family of distributions: properties and applications. *Tbilisi Mathematical Journal*, *11*(3), 47-67.

Ristić, M. M., & Balakrishnan, N. (2012). The gamma-exponentiated exponential distribution. *Journal of Statistical Computation and Simulation*, *82*(8), 1191-1206.

Singh, S. K., Singh, U., & Kumar, M. (2013). Estimation of Parameters of Generalized Inverted Exponential Distribution for Progressive Type-II Censored Sample with Binomial Removals. *Journal of Probability and Statistics*, *2013*(1), 183652.

ul Haq, M. A., Usman, R. M., Hashmi, S., & Al-Omeri, A. I. (2019). The Marshall-Olkin length-biased exponential distribution and its applications. *Journal of King Saud University-Science*, *31*(2), 246-251.

Pure Sciences International Journal of kerbala

Year:2026 Volume : 3 Issue : 9 ISSN: 6188-2789 Print 3005 -2394 Online

2026,Volume 3 , Issue 9 , PSIJK (35-41)

Pure Sciences International Journal of Kerbala

Synthesis And Characterization Of Manganese Dioxide Nanoparticles Prepared By Chemical Preciptation Method

Sarah F.AL Mayali [a*], Aula M. Al Hindawi [a] , Ibtihal Alshamarti [b]

[a] *Department of Chemistry, College of Education for Pure Sciences, University of Kerbala, kerbala, Iraq*
[b]*Department of Basic Science, College of Dentistry, University of Kufa Najaf, Iraq*

P A P E R I N F O

Received: 25.05.2025
Accepted: 12.10.2025
Published: 31.03.2026

Keywords:
nanoparticles, chemical precipitation , MnO2

A B S T R A C T

In this research, manganese dioxide nanoparticles (MnO_2 NPs) were prepared using a simple chemical precipitation method, using sodium thiosulfate ($Na_2S_2O_3$) as an effective reducing agent to control the size and shape of the nanoparticle crystals. This method represents a promising approach for preparing nanomaterials due to the possibility of tuning their structural properties under mild conditions, opening the way for innovative medical applications. The prepared particles were characterized using advanced analytical techniques, including Ultraviolet-visible (UV-Vis) spectroscopy to study the optical properties, Fourier-transform infrared (FTIR) spectroscopy to determine the chemical bonds, X-ray diffraction (XRD) to analyze the crystal phase and calculate the crystal size. The results showed that the particles belong to the α-MnO_2 phase and crystallized in the tetragonal crystal system, Transmission electron microscopy (TEM) and scanning electron microscopy (FESEM) to study the shape and size, with images showing that the particles exhibit a somewhat spherical structure, with slightly heterogeneous proportions, Energy-dispersive X-ray (EDX) analysis to determine the elemental composition.The results showed that the prepared particles are characterized by their small size, relatively regular shape, and large surface area, characteristics that contribute to improving their effectiveness in biological applications. Manganese dioxide nanoparticles show promising potential in the medical field, especially in nanomaterial-based therapeutic and diagnostic applications.

DOI: 10.53851/psijk.v3.i9. 35-41

NOMENCLATURE

MnO2	Mnganese dioxide	FTIR	Fourier Transform Infrared spectroscopy
NPs	Nanoparticles	XRD	X-ray Diffraction
$N_2S_2O_3$	Sodium thiosulfate	TEM	Transmission Electron Microscopy
UV-Vis	Ultraviolet-Visible spectroscopy	FESEM	Field Emission Scanning Electron Microscopy
EDX	Energy Dispersive X-ray spectroscopy	GSH	Glutathione
eV	Electron Volt	%	Percent transmittance
cm^{-1}	Wavenumber	Sol-gel	Solution-Gelation

1. INTRODUCTION

Nanomaterials science has witnessed many developments in recent years due to their unique properties that cannot be found in their bulk counterparts. Small particle size within the scale (1-100 nanometers) leads to changes in physical and chemical properties such as high surface area, optical properties, catalytic efficiency, and electrical conductivity make the resulting nanomaterials unique and ideal for numerous applications, such as energy, the environment,

*Corresponding Author Institutional Email:
sarah.fadhel@uokerbala.edu.iq (Sarah F.AL Mayali)

electronics, and medicine (Hajinasiri & Esmaeili, 2022). Among these materials, manganese dioxide (MnO_2) is a substance with multiple crystalline forms, and it also has the ability to react strongly as an oxidizing agent, It also has the advantage of chemical stability and wide applications. The properties of its molecules are significantly improved when prepared using nano-methods(Hoseinpour et al., 2018). These properties include high catalytic properties(Sobańska et al., 2021), ease of surface modification(Shi et al., 2018), antibacterial properties(Ikram et al., 2024) , high surface area(Wang et al., 2017), high environmental compatibility, and other properties, which makes it more effective in practical applications such as medicine(Yang et al., 2017). MnO_2 NPs are an ideal candidate in medical applications that combine diagnosis and therapy (neurotherapeutics) (Sisakhtnezhad et al., 2023). MnO_2 exploits the properties of the tumor environment, such as high glutathione (GSH) (Yang et al., 2021), and low oxygen levels (hypoxia), to perform several functions, such as generating oxygen within the tumor(Chen et al., 2023) , and improving the effectiveness of chemotherapy and radiotherapy (Song et al., 2016) It also activates the response to treatment by stimulating oxidative stress within cancer cells(Yang et al., 2021) (Bonet-Aleta et al., 2022). MnO_2 also has the ability to modify its surface to work on the synthesis of anti-cancer drugs(Liu et al., 2024) , or to coat it with molecules directed towards specific receptors present on the surface of cancer cells, which makes it a directed and effective drug carrier (Xie et al., 2024). Several methods have been developed to prepare MnO_2 NPs, including chemical methods such as co-precipitation (Kapil et al., 2024) (Kahattha & Santhaveesuk, 2019) , sol-gel (Tang et al., 2014) , hydrothermal synthesis (Islam et al., 2024), and chemical reduction (Yadav et al., 2023). Physical methods include, laser evaporation(Corrales et al., 2022) , plasma irradiation(Kim et al., 2016) , mechanical grinding(Ochirkhuyag et al., 2020) and high-energy ball milling(Song et al., 2024). In addition to the previous methods, environmentally friendly methods have been developed that use plant extracts as reducing agents (Ghorbani et al., 2023) or use microorganisms to stimulate sedimentation (Ogunyemi et al., 2020) . In this research, we adopted the chemical precipitation method using sodium thiosulfate ($Na_2S_2O_3$) as a reducing agent. It is a method characterized by its simplicity, low cost, and ease of control over reaction conditions. In addition to the fact that the reducing agent ($Na_2S_2O_3$) is a relatively non-toxic compound (Schulz et al., 2010) (Neuwelt et al., 2006) its use allows the formation of nanoparticles with good dispersion without the need for harsh conditions of temperature or pressure .

MATERIALS AND METHOD

1.Materials

Sodium thiosulfate were brought from Alpha Chemika. Manganese sulphate ($MnSO_4.H_2O$, 99%) and sodium hydroxide were purchased from QualiKems Fine Chem and CDH, respectively. Deionized water was utilized as reactor medium.

1.1 .preparation of the reducing Agent:

Weigh 0.09 g from Sodium thiosulfate ($Na_2S_2O_3.5H_2O$) and add 25 mL of deionized water in a 50 ml beaker Stir the solution at room temperature with a magnetic stirrer for 5-10 minutes look at Figure1.

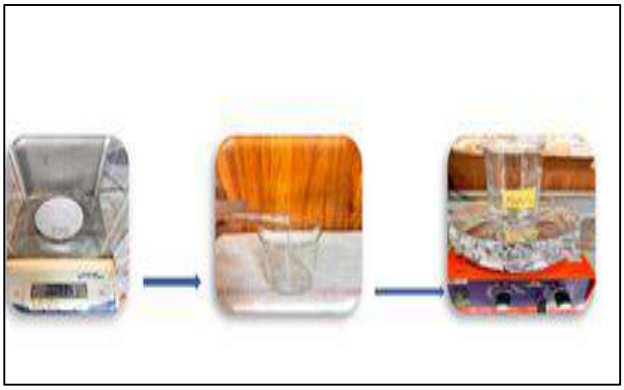

Figure 1: shows the preparation of sodium thiosulfate solution.

1.2. preparation MnO_2 NPs

Weigh 0.1267 g of manganese sulfate ($MnSO_4.H_2O$) and add 75 ml of deionized water in a 200 ml beaker Stir the solution at room temperature with a magnetic stirrer for 10-15 minutes.Gradually add drops of 0.1 M sodium hydroxide solution until the pH becomes 11 (checked with litmus paper), We notice that the solution turns light brown. Then, sodium thiosulfate solution is added as a reducing agent gradually and the temperature is raised to 70°C with magnetic stirring for two hours, the color of the solution gradually changes from light brown to dark brown, indicating the formation of nano manganese dioxide particles. Then we separate the precipitate from the solution using centrifugation (2500 rpm) and then wash the precipitate several times to get rid of impurities. The precipitate is dried at 100°C for 30-60 minutes in a selector drying oven then grind well. , the dried sample is then burned in a laboratory furnace (MAFEL) for 2-3 hours at 400°C to remove organic matter. A very dark brown precipitate is then obtained, which represents nanoscale manganese dioxide particles (MnO_2 NPs). the formation steps of MnO_2 nanoparticles was summariz in Figure 2.

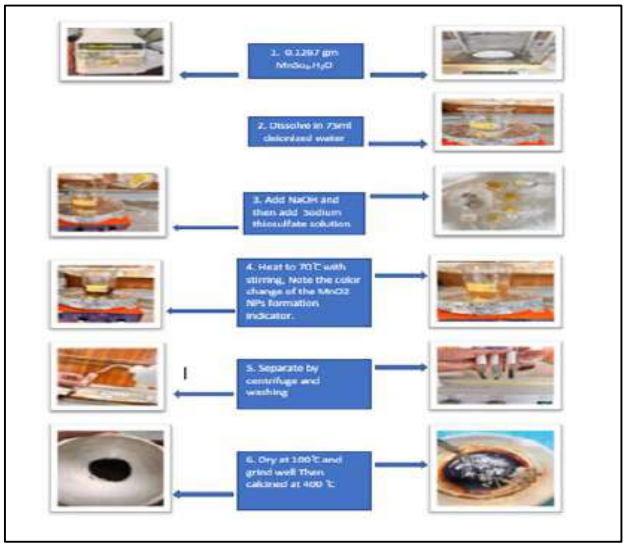

Figure.2 schematic showing the formation process of MnO2 nanoparticle using sodium thiosulfate solution .

CHARACTERIZATION

We studied the optical properties of the prepared manganese dioxide (MnO2) nanoparticles, using UV-visible spectroscopy, The morphology and particle size of the prepared particles were examined using field emission scanning electron microscope (FESEM) and transmission electron microscope (TEM), Elemental analysis was performed using energy dispersive X-ray spectroscopy (EDX) and X-ray diffraction (XRD) was used to determine the crystal structure of the prepared MnO2 particles, Fourier transform infrared spectroscopy (FTIR) was used to identify the functional groups on the surfaces of the nanoparticles.

RESULTS AND DISCUSSION

The color change from light brown to dark brown after heating for (1-2) hours is an indicator and evidence of the formation of chemically manufactured MnO2 particles look (Figure 3) In addition to providing further evidence confirming the formation of MnO2 nanoparticles by studying the optical properties of the particles.

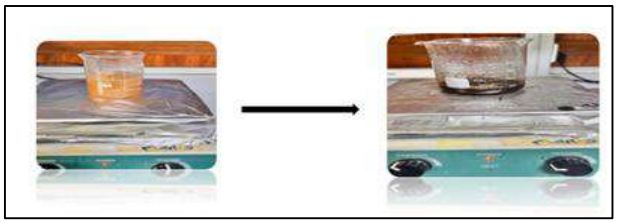

Figure 3. Images shows the color change to brown indicating the formation of MnO2 nanoparticles.

Optical Properties

We studied the optical properties of manganese dioxide nanoparticles formed by reacting manganese sulfate solution MnSO4.H2O with basic medium (NaOH 0.1 M) and adding sodium thiosulfate solution as a chemical reducing agent and ideal reaction conditions of 70°C, pH 11 and reaction time of 2 hours. To know the optical properties of the prepared MnO2 sample, we used the UV-Vis spectroscopy technique. Figure 4(a) shows the spectra of manganese oxide nanoparticles, where an absorption peak appeared at a wavelength of , which is smaller than the spectrum of bulk manganese dioxide, which usually appears at a wavelength of (380 nm). This shift towards lower wavelengths is due to the phenomenon of quantum confinement, where the smaller the size of the produced material and the greater its surface area, the shorter wavelengths appear(Anguraj et al., 2023). The energy band gap of manganese oxide nanoparticles can be estimated from the absorption spectrum using the Tauc plot, according to the following equation:

$$(\alpha h\nu)^n = C(h\nu - E_{(g)})^n$$

Where:

n	0.5 (for direct electron transition allowed)
h	is Planck's constant (6.626×10^{-34} J⁴ s or 4.135×10^{-15} eV⁴)
ν	is the photon frequency,
C	is a constant that depends on the material properties
α	is the absorption coefficient (cm^{-1}),
$E_{(g)}$	is the energy gap.

By plotting the relationship between $(\alpha h\nu)^2$ and photon energy (hν), the energy gap value can be estimated from the intersection of the linear portion of the curve with the horizontal axis. The Tauck curve (Figure 4(b)) showed that the energy gap of the prepared nanoparticles is approximately 4.4 eV, which is higher than the energy gap of the bulk material (MnO_2), which is estimated at approximately 1.6 eV. This difference is due to quantum effects resulting from the small nanoscale size. Reducing the particle dimensions leads to an increase in the energy gap (quantum confinement effect) and a shift in optical absorption toward shorter wavelengths (blue shift). These results support that the prepared particles fall within the true nanoscale and possess distinct electronic and optical properties that differ from their bulk counterparts(Anguraj et al., 2023).

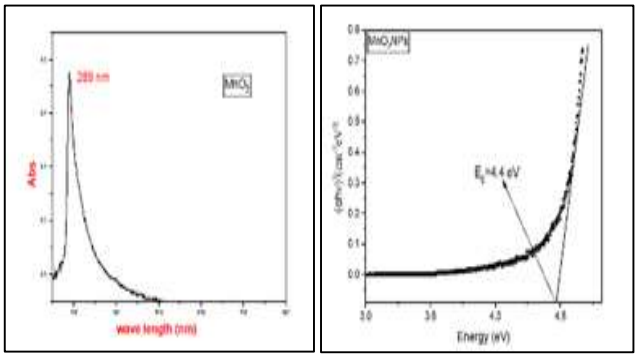

Figure 4 .(a). UV-Vis spectrum of MnO2 nanoparticle, (b) Energy band gap of MnO2 nanoparticleSynthesized by chemical method.

FTIR spectroscopy is a technique used to identify and determine the type of organic and inorganic compounds by knowing the functional groups present in the

$$n\lambda = 2d \sin \Theta \qquad 2$$

n rank of deviation
ʎ which is equal to 0.154 nm(the wavelength of X-ray (Cu Kα))
Θ is angle of diffraction
d layer thickness

where it is found to be equal 2.48 nm.
Where the results of the Scherrer equation:

$$D = K\lambda / \beta \cos \Theta \qquad 3$$

D crystallite size (in radians)
β is the complete width at half maximum
K Constant scherrer = 0.9
λ which is equal to 0.154 nm(the wavelength of X-ray (Cu Kα))
θ is angle of diffraction (in radians)

compound to be analyzed. It is also used to detect the purity of samples, as any impurities present in the sample are identified, which gives it great importance in the quality of scientific research.In addition to its speed and the lack of need for complex sample preparation, it is also non-destructive to the compound after analysis.Figure 5 shows the FTIR spectrum of the prepared sample (MnO2NPs) showing the appearance of two medium intensity peaks at (615 cm-1) and (489 cm-1) due to O-Mn-O stretching vibrations, which clearly indicates the formation of MnO2 nanoparticles. The broad low peak that appeared at (3415 cm-1) is due to the -OH stretching vibrations and H-O-H bending of water molecules, most likely due to the sample being exposed to moisture during transport for analysis, The simple peak that appeared at (1634cm-1) reflects the bending vibrations of water molecules, while the peak at(1118cm-1) indicates the extensions of the S-O or S=O bond resulting from Na2S2O3 residues on the surface of the nanocomposite as a result of its use as a reducing agent (Jaganyi et al., 2013) (Sivakumar & Prabu, 2021).

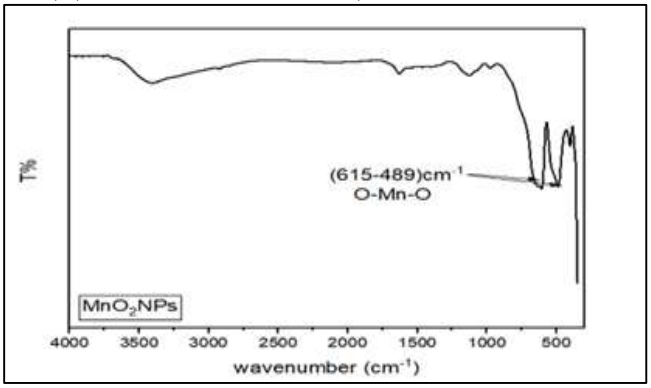

Figure 5. FTIR spectrum plot between wavenumber (cm-1) and transmittance (%) of MnO2 nanoparticle.

Structural Properties

XRD it is a technique that uses X-ray diffraction to study the crystalline structure of solid materials and to determine the size of nanomaterials. The interpreted results confirmed that the prepared material is α MnO2 and has a tetrahedral crystal structure. According to the apparent peaks (18.25) (29.01) (32.68) (36.23) (60.11) , the diffraction angles are consistent , With crystal faces (101) (310) (102) (110) (521) respectively look at Figure (6), according to the card of MnO2(JCPDS card No. 44-0141), These results are very similar to previous results of (Abdullah et al., 2021), The crystal structure was confirmed by the Bragg equation :

$$(\alpha h\nu)^n = C(h\nu - E_{(g)})^n \qquad 1$$

Where:
The crystallite size was found about 9.118 nm.
Field Emission Scanning Electron Microscopy (FESEM) analysis: This technique is used to provide high-resolution images of the surfaces of nanomaterials

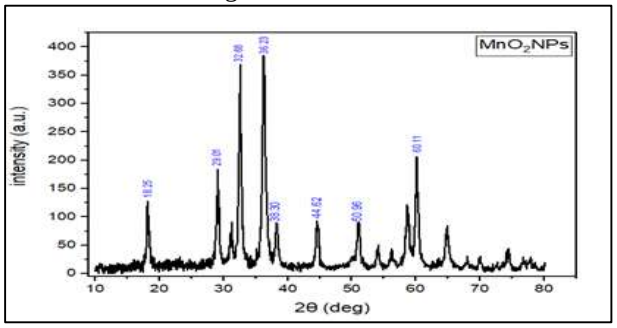

Figure 6: XRD pattern of α-MnO2 nanoparticles

for study and determination of surface composition with high accuracy. The morphology of the MnO2 NPs sample shows that the particles are irregularly spherical in shape due to their small external dimensions and high surface area, with a diameter of approximately 40 nm look to Figure 7(a), The particles are irregularly distributed with clear clumps of dark and light colours as a result of exposure to moisture during storage(Vetrikarasan et al., 2023) (Sivakumar & Prabu, 2021).Elemental analysis confirms that the (EDX) of the sample is composed of 71% manganese and 29% oxygen note Figure 7(b). The presence of gold in the analysis result is due to the sample being coated with gold to increase conductivity, as the sample is a semiconducto(Ghandali et al., 2024).

Transmission Electron Microscopy (TEM) This technique is one of the most accurate techniques, as it uses a beam of electrons that passes through the sample and is not limited to just its surface. This technique is used to study the crystal structure accurately, image the particles from the inside, and determine the shape and size of the particles of the sample, The results, as shown in Figure 7(C), showed that the particles had a somewhat spherical shape with simple clusters. Using the Image J analysis program, it appeared that the nano-size was approximately (Ghorbani et al., 2023).

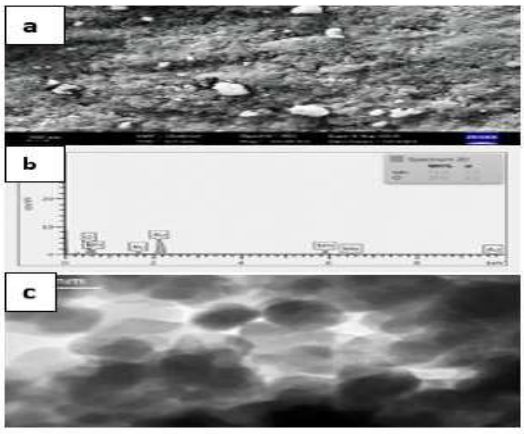

Figure 7 : FESEM aimages of MnO2 nanoparticle synthesized in the presence of Na2S2O3 (a) , EDX chart for MnO2 (b) ,and TEM image (c) .

CONCLUSION

In this study, nanosized manganese dioxide (MnO_2) was prepared by a simple chemical method using sodium thiosulfate ($Na_2S_2O_3$) as a reducing agent. This agent proved effective in controlling the size and structure of the crystalline particles. X-ray diffraction (XRD) analysis results showed that the prepared material crystallizes in the well-known α-MnO_2 crystal phase and belongs to the tetragonal crystal system, indicating the regularity of the material's structural conformation. The size of the nanocrystals was calculated using the Scherrer equation, with an average size of approximately 9.118 nm, confirming the nanoscale nature of the produced particles.Various characterization techniques (UV-Vis, FTIR, XRD, SEM, TEM, and EDX) also revealed that the prepared particles exhibit small sizes and favorable surface structures. Transmission electron microscope (TEM) and scanning electron microscope (FESEM) images revealed that the particles were relatively spherical in shape, with some slight variation in the degree of homogeneity, possibly due to slight differences in crystal growth rates during the reaction. This spherical formation contributes to an increased relative surface area, an important factor in biological applications.Based on the acquired structural and morphological properties, including a stable crystalline phase, regular nanoscale size, and favorable surface area, the prepared nano-MnO_2 exhibits promising potential for multiple future medical applications, especially in areas requiring high reactivity and improved surface properties.

REFERENCES

Abdullah, T., et al. (2021). Preparation and characterization of MnO_2-based nanoparticles at different annealing temperatures and their application in dye removal from water. *International Journal of Environmental Science and Technology, 18*, 1499–1512.

Anguraj, G., et al. (2023). MnO_2 doped with Ag nanoparticles and their applications in antimicrobial and photocatalytic reactions. *Catalysts*, *13*(2), 397.

Bonet-Aleta, J., Calzada-Funes, J., & Hueso, J. L. (2022). Manganese oxide nano-platforms in cancer therapy: Recent advances on the development of synergistic strategies targeting the tumor microenvironment. *Applied Materials Today, 29*, 101628.

Chen, Z., et al. (2023). Hypoxia-ameliorated photothermal manganese dioxide nanoplatform for reversing doxorubicin resistance. *Frontiers in Pharmacology, 14*, 1133011.

Corrales, J., et al. (2022). Manganese dioxide nanoparticles prepared by laser ablation as materials with interesting electronic, electrochemical, and disinfecting properties. *Nanomaterials, 12*(22), 4061.

Ghandali, M. V., Safarzadeh, S., Ghasemi-Fasaei, R., & Zeinali, S. (2024). Heavy metals immobilization and bioavailability in multi-

metal contaminated soil under ryegrass cultivation as affected by ZnO and MnO_2 nanoparticle-modified biochar. *Scientific Reports, 14*(1), 10684.

Ghorbani, S., Mirzaei, Y., Bordbar, M., & Gholami, A. (2023). Green synthesis of MnO_2 nanoparticles using cumin extract composited with *Hypericum* plant: Investigation of antibacterial and anticancer properties. *Journal of Nanostructures, 13*(1), 151–158.

Hajinasiri, R., & Esmaeili, J. M. (2022). Synthesis of ZnO nanoparticles via flaxseed aqueous extract.

Hoseinpour, V., Souri, M., & Ghaemi, N. (2018). Green synthesis, characterisation, and photocatalytic activity of manganese dioxide nanoparticles. *Micro & Nano Letters, 13*(11), 1560–1563.

Ikram, M., Moeen, S., Shahzadi, A., Al-Anazy, M. M., & Jeridi, M. (2024). Carbohydrate polymers based MnO_2 nanostructures for catalytic and antibacterial activity; kinetic modeling and molecular docking analysis. *Materials Science in Semiconductor Processing, 181*, 108633.

Islam, M. R., Bhuiyan, M. A., Ahmed, M. H., & Rahaman, M. (2024). Hydrothermal synthesis of NiO nanoparticles decorated hierarchical MnO_2 nanowire for supercapacitor electrode. *Heliyon, 10*(4).

Jaganyi, D., Altaf, M., & Wekesa, I. (2013). Synthesis and characterization of whisker-shaped MnO_2 nanostructure at room temperature. *Applied Nanoscience, 3*, 329–333.

Kahattha, C., & Santhaveesuk, S. (2019). Influence of calcination temperature on physical and electrochemical properties of MnO_2 nanoparticles synthesized by co-precipitation method. *Ferroelectrics, 552*(1), 121–131.

Kapil, I., Yadav, C., Yadav, P., & Bhaduri, A. (2024). Synthesis and characterization of mixed phase manganese oxide nanoparticles prepared by simple co-precipitation method. *Journal of Physics: Conference Series, 2844*(1), 012010.

Kim, H., Watthanaphanit, A., & Saito, N. (2016). Synthesis of colloidal MnO_2 with a sheet-like structure by one-pot plasma discharge. *RSC Advances, 6*(4), 2826–2834.

Kumar, H., Manisha, S. P., & Sangwan, P. (2013). Synthesis and characterization of MnO_2 nanoparticles using co-precipitation technique. *International Journal of Chemical and Chemical Engineering, 3*(3), 155–160.

Liu, J., et al. (2024). Hollow manganese dioxide nanoparticles for drug delivery and imaging. *ACS Applied Nano Materials, 7*(11), 13557–13567.

Neuwelt, E. A., et al. (2006). Toxicity profile of delayed high dose sodium thiosulfate in children treated with carboplatin. *Pediatric Blood & Cancer, 47*(2), 174–182.

Ochirkhuyag, A., Sápi, A., Szamosvölgyi, Á., Kozma, G., Kukovecz, Á., & Kónya, Z. (2020). One-pot mechanochemical ball milling synthesis of MnO_x nanostructures. *Physical Chemistry Chemical Physics, 22*(25), 13999–14012.

Ogunyemi, S. O., et al. (2020). The bio-synthesis of metal oxide nanoparticles and their antibacterial activity. *Frontiers in Microbiology, 11*, 588326.

Schulz, L. T., et al. (2010). Stability of sodium nitroprusside and sodium thiosulfate intravenous admixture. *Hospital Pharmacy, 45*(10), 779–784.

Shi, Y., Guenneau, F., Wang, X., Hélary, C., & Coradin, T. (2018). MnO_2-gated nanoplatforms with targeted controlled drug release. *Nanotheranostics, 2*(4), 403.

Sisakhtnezhad, S., Rahimi, M., & Mohammadi, S. (2023). Biomedical applications of MnO_2 nanomaterials as nanozyme-based theranostics. *Biomedicine & Pharmacotherapy, 163*, 114833.

Sivakumar, S., & Prabu, L. N. (2021). Synthesis and characterization of α-MnO_2 nanoparticles for supercapacitor application. *Materials Today: Proceedings, 47*, 52–55.

Sobańska, Z., Roszak, J., Kowalczyk, K., & Stępnik, M. (2021). Applications and biological activity of manganese oxide nanoparticles. *Nanomaterials, 11*(5), 1084.

Song, M., Liu, T., Shi, C., Zhang, X., & Chen, X. (2016). Bioconjugated manganese dioxide nanoparticles enhance chemotherapy response. *ACS Nano, 10*(1), 633–647.

Song, S., Yang, Y., Pan, X., Chai, X., & Wang, M. (2024). Ball milling of pyrolytic residue with MnO_2 and reuse as PMS activator. *Process Safety and Environmental Protection, 192*, 600–612.

Tang, W., Shan, X., Li, S., Liu, H., Wu, X., & Chen, Y. (2014). Sol–gel synthesis of ultrafine MnO_2 nanowires and nanorods. *Materials Letters, 132*, 317–321.

Vetrikarasan, B. T., et al. (2023). Co-precipitation synthesis of λ-MnO_2 for supercapacitor applications. *Journal of Energy Storage, 72*, 108403.

Wang, X., Huo, S., Wang, R., Wang, H., Brett, D. J., & Ji, S. (2017). Synthesis of mesoporous MnO_2 via aqueous interfacial reaction. *Journal of Colloid and Interface Science, 503*, 76–85.

Xie, L., Jiang, S., Zhang, C., Liu, M., & Qu, Y. (2024). Dual-drug loaded manganese dioxide nanoparticles for chemo-immunotherapy. *Materials & Design, 247*, 113406.

Yadav, P., Bhaduri, A., & Thakur, A. (2023). Manganese oxide nanoparticles: Structure, synthesis and applications. *ChemBioEng Reviews, 10*(4), 510–528.

Yang, G., et al. (2017). Hollow MnO_2 as tumor-microenvironment-responsive biodegradable nano-platform. *Nature Communications, 8*(1), 902.

Yang, G., Ji, J., & Liu, Z. (2021a). Multifunctional MnO_2 nanoparticles for tumor microenvironment modulation. *Wiley Interdisciplinary Reviews: Nanomedicine and Nanobiotechnology, 13*(6), e1720.

Yang, Y., et al. (2021b). MnO_2 nanoflowers induce immunogenic cell death. *Advanced Science, 8*(4), 2002667.

Pure Sciences International Journal of kerbala

Year:2026 Volume : 3 Issue : 9 ISSN: 6188-2789 Print 3005 -2394 Online

2026,Volume 3 , Issue 9 , PSIJK (43-50)

Pure Sciences International Journal of Kerbala

Type 2 Diabetes with Insulin Resistance Markers Fatty Liver Disease: A Biochemical Approach

Moamel abduljabbar m.hussein [a*], Rehab Jasim Mohammed [a], Mahmoud Azeez Mohammed [b]

a Department of Chemistry, College of Education for Pure Sciences, University of Kerbala
b Department of Gastroenterology and hepatology,Faculty of Medicine, University of Kufa

P A P E R I N F O

Received: 20.10.2025
Accepted: 16.11.2025
Published: 31.03.2026

***Keywords*:**
Keywords: Type 2 Diabetes, Fatty Liver Disease, Insulin Resistance, C-peptide, HbA1c, Liver Enzymes

A b s t r a c t

This study examined the correlation between type 2 diabetes mellitus (T2DM), insulin resistance, and fatty liver disease (FLD) using biochemical assessment of 50 diabetic patients diagnosed with FLD in comparison to 40 healthy persons. The findings indicated a substantial elevation in HOMA-IR among the patients (16.25±12.75) relative to the control group (1.74±0.96; p<0.001), signifying an increase of nearly ninefold. The C-peptide level was significantly enhanced in the patients (3.88±2.70) compared to the control group (2.64±1.02; p<0.001), and insulin levels were nearly 3.5 times more (31.61±21.53 vs. 8.70±5.16; p=0.007).
Concerning hepatic functioning, patients exhibited markedly elevated levels of AST (37.00±19.34 vs. 22.53±5.11; p<0.001) and ALT (41.84±22.48 vs. 24.63±7.29; p<0.001), signifying hepatocellular injury, although ALP levels did not demonstrate a significant difference (110.70±45.97 vs. 104.20±22.08; p=0.414). A modest yet statistically significant reduction in albumin levels was noted (4.27±0.58 vs. 4.41±0.30; p=0.001).
The HbA1c level in patients was considerably elevated at 8.24±1.28 compared to the control group at 4.93±0.47 (p<0.001), reflecting inadequate blood sugar regulation and a level about 67% greater in the diabetes-FLD cohort. Clinically, 78% of individuals had non-alcoholic fatty liver disease (NAFLD), whereas 22% presented with alcoholic fatty liver disease, underscoring the prevalence of NAFLD among diabetes patients.

DOI: 10.53851/psijk.v3.i9. 43-50

1. INTRODUCTION

Insulin resistance (IR) is defined by a diminished responsiveness of insulin-sensitive organs and tissues to insulin stimulation. Insulin resistance (IR) is characterized by diminished insulin sensitivity resulting from a suboptimal response to insulin signals regulating blood glucose levels. This abnormal physiological response elevates plasma insulin levels, resulting in hyperinsulinemia (Kashyap & Defronzo, 2007; Li et al., 2022; Szablewski, 2024). The liver plays a vital role in the balance of glucose and fat metabolism in the body. Insulin resistance (IR) is considered a major causative factor for metabolic disorders in the liver, such as metabolic dysfunction-associated steatotic liver disease (MASLD), which is one of the most common chronic liver disorders and a precursor to a wide range of liver diseases, ranging from fatty liver, liver fibrosis, and cirrhosis, ultimately leading to hepatocellular carcinoma (Bo et al., 2024).

Type 2 diabetes is a metabolic disorder clinically defined by both acute and chronic hyperglycemia. This disorder is frequently related with liver problems. The spectrum of hepatic disorders extends from mild hepatitis to Metabolic associated fatty liver disease (MAFLD). Metabolic associated fatty liver disease (MAFLD) encompasses non-alcoholic fatty liver (fatty liver) characterized by the absence of inflammation (normal transaminases), metabolic dysfunction-associated steatohepatitis (MASH) without fibrosis, MASH with fibrosis that may ultimately advance to cirrhosis, hepatocellular carcinoma, and liver failure resulting in mortality(Niranjan, Phillips, & Giannoukakis, 2023). As type 2 diabetes advances to a

*Corresponding Author Institutional Email:
moamel.a@s.uokerbala.edu.iq (*Moamel abduljabbar m.hussein*)

chronic phase, it can inflict considerable harm on several organ systems, including the eyes, blood vessels, kidneys, and cardiovascular system, and is frequently linked with illnesses such as dyslipidemia and hypertension(Ranade et al., 2024). The global burden of diabetes is considerable, and its growing prevalence poses significant pressure on healthcare systems, exacerbating preexisting societal challenges such as food insecurity and poverty (Ogunjobi et al., 2025)

The development of IR is influenced by several factors, such as age, genetic predisposition, obesity, oxidative stress, among others. Irregularities in the insulin-signaling pathway—encompassing defects in insulin receptors, internal environmental disruptions, and metabolic changes in muscles, liver, and intracellular organelles—are central to the pathogenesis of IR (Mir et al., 2025; Sinaiko & Caprio, 2012).

In addition to that T2DM and fatty liver disease (FLD) are common and interrelated conditions that influence one another through shared mechanisms. A link between T2DM and FLD has been hypothesized. Lipid accumulation in the liver has been proposed as a contributing factor in the development of T2DM . Therefore, the early detection and intervention of FLD are essential to prevent disease progression toward fibrosis, cirrhosis, and hepatocellular carcinoma(Tanase et al., 2020).

Fatty liver disease (FLD) is highly prevalent among individuals with excessive alcohol intake as well as those with obesity, particularly in the context of insulin resistance (Habibullah et al., 2024; Mitra, De, & Chowdhury, 2020).

Non-alcoholic fatty liver disease (NAFLD) and alcoholic fatty liver disease (AFLD) are the two predominant metabolic liver disorders globally. Metabolic liver illnesses profoundly impact human health and quality of life, resulting in substantial public health challenges and considerable medical burdens. Fat buildup, insulin resistance, oxidative stress, inflammation, and dietary practices are intricately associated with non-alcoholic fatty liver disease and alcoholic fatty liver disease.(Zhang et al., 2021).

(MAFLD) and (AFLD) are linked to extrahepatic risk factors and consequences, including metabolic syndrome, characterized by obesity, hypertension, type 2 diabetes, and chronic kidney disease. Alcoholic fatty liver disease is linked to hypertension and cardiovascular illnesses, as well as harm to other organs. This narrative review examines the associations, causal variables, and diagnostic biological determinants linking (MAFLD) and (AFLD) to elevated mortality rates (Johnston, Patel, & Byrne, 2020):

1. 1. Patients and Methods

Fifty samples were collected from the Najaf Diabetes and Endocrinology Center and the Specialized Hospital for Digestive and Liver Diseases. The samples comprised male patients aged 30 to 60 years. They received a diagnosis of type 2 diabetes and fatty liver disease upon confirmation of an 8-12 hour fasting period before to the test. The Research Ethics Committee of the College of Education, University of Karbala, in conjunction with the Diabetes and Endocrinology Center and the Gastroenterology and Liver Diseases Hospital in Najaf Al-Ashraf, sanctioned the study protocol. The investigation occurred from November 2024 to May 2025 .

The blood samples underwent centrifugation for 5 minutes at 5000 rpm to separate the serum. Biochemical analyses were conducted with a COBAS analyzer that employs electrochemiluminescence immunoassay (ECLIA) technology to quantify serum insulin and C-peptide levels. The results were juxtaposed with those derived from 40 healthy subjects in the control group. Individuals with any type of viral hepatitis and those who had recently had gastrointestinal surgery were excluded. The statistical analysis was conducted using (SPSS), and (t-test) was used to compare the groups and find (Means ± SD) and (p- value < 0.05). in addition origin Lab program it used in this study and .

1. 2. Results

Table (1.1) delineates the demographic features of the study participants, consisting of 50 patients and 40 control people. The age distribution of the patient group revealed a greater prevalence in older age groups, with the most significant proportion (n=29) in the 51-60 years group, while compared to control (n=8). In contrast, the 30-40 years cohort exhibited a significantly greater number of control subjects (n=18) compared to patients (n=8). in the 41-50 years It was observed that the numbers of control individuals (n=14) compared to patients (n=13) were very similar.

All 60 patients were identified with a hepatic disease, mainly fatty liver, with 32 categorized as Grade 1 and 18 as Grade 2. Among the patients identified with fatty liver disease, 11 were classified with Alcoholic Fatty Liver and 39 with Non-alcoholic Fatty Liver.

This signifies that the predominant etiology of fatty liver in the patient cohort (39 out of 50, 78%) was non-alcoholic, whereas a lesser fraction (11 out of 50, 22%) was ascribed to alcoholic fatty liver.

The smoking status revealed a disparity, with 11 patients identifying as smokers, whilst the control group had no smokers. All 40 control subjects identified as non-

smokers, whereas 39 patients also claimed being non-smokers. Within the patient cohort, the duration of diabetes exhibited variability: 24 patients had diabetes for over 4 years, 14 patients for 3 to 4 years, and 12 patients for 1 to 2 years. The control group exhibited no documented history of diabetes.

A familial history was more common in the patient group, with 28 patients indicating a positive family history compared to 12 control subjects. In contrast, 28 control volunteers indicated no family history, but 22 cases did.

Table (1.1): Distribution of the Samples According to demographic information

Variable	**Groups**	**Patient N=50**	**Control N=40**
Age. Groups	30-40 Years	8	18
	41-50 Years	13	14
	51-60 Years	29	8
hepatic condition			
	GRADE 1	32	0
	GRADE 2	18	0
Type of FL	alcoholic fatty liver	11	0
	non-alcoholic fatty liver	39	0
smoking	YES	11	0
	NO	39	40
Duration of diabetes	1-2 Years	12	0
	3-4 Years	14	0
	More than 4 Years	24	0
History of family	Yes	28	12
	No	22	28

Table (1.2) Mean levels of serum HOMA IR, C-PEPTIDE and INSULIN between patients with fatty liver disease (FLD), and healthy control

Biomarkers	**Patient Mean±SD N=50**	**Control Mean±SD N=40**	**P value**
HOMA IR	16.25±12.75	1.74±0.96	**<0.001[S]**
C-PEPTIDE	3.88±2.70	2.64±1.02	**<0.001[S]**
INSULIN	31.61±21.53	8.70±5.16	**0.007[S]**
T -test was *: significant at p ≤ 0.05 SD: standard deviation; S: significant; NS= Non-significant.			

Table (1.2) displays the average blood concentrations of Homeostatic Model Assessment for Insulin Resistance (HOMA-IR), C-Peptide, and Insulin in patients with fatty liver disease (FLD) (N=50) in contrast to healthy control subjects (N=40). Statistical significance was evaluated by an independent samples t-test, with a p-value of < 0.05 .being significant

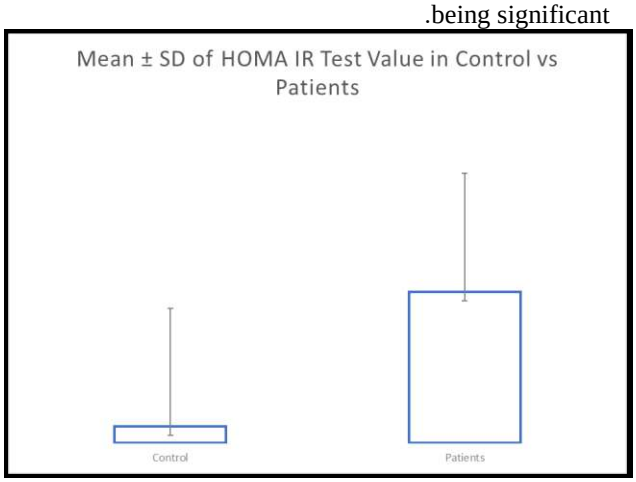

Figure 1. Patients with fatty liver disease (FLD) showed a significantly elevated average serum HOMA-IR level (16.25±12.75) compared to the healthy control group (1.74±0.96). This difference was highly statistically significant (p<0.001), indicating a profound level of insulin resistance in patients with fatty liver disease.

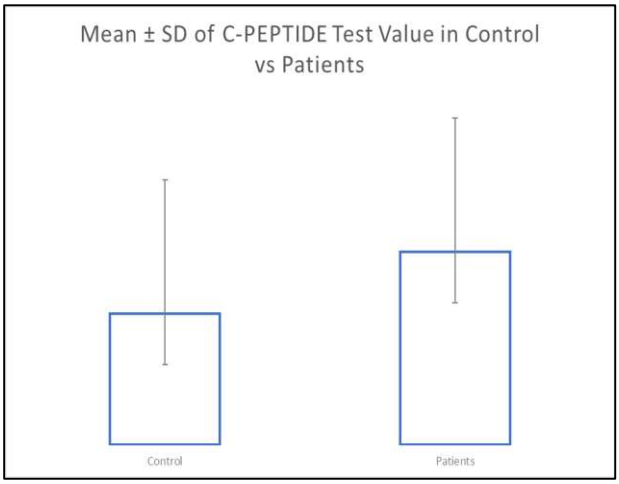

Figure 2. The average levels of C-PEPTIDE in the blood were high compared to the control group achieved a statistical significance of (P<0.001).

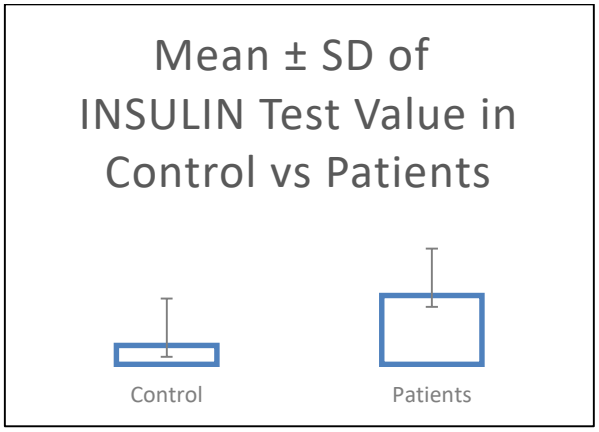

.

Figure 3. Patients with FLD exhibited a markedly elevated mean blood insulin level in comparison to control controls. The observed difference was statistically significant (p=0.007).

Table (1.3) *Mean levels of serum ALBUMIN & Liver enzymes (AST, ALT and ALP) between patients with fatty liver disease (FLD), and healthy control*

Biomarkers	Patient Mean±SD N=50	Control Mean±SD N=40	P value
ALBUMIN	4.27±0.58	4.41±0.30	0.001[S]
AST	37.00±19.34	22.53±5.11	**<0.001[S]**
ALT	41.84±22.48	24.63±7.29	**<0.001[S]**
ALP	110.70±45.97	104.20±22.08	0.414[NS]
T -test was *: significant at p ≤ 0.05 SD: standard deviation; S: significant; NS= Non-significant.			

Table (1.3) displays the average serum concentrations of Albumin and liver enzymes, namely Aspartate Aminotransferase (AST), Alanine Aminotransferase (ALT), and Alkaline Phosphatase (ALP), contrasting patients with fatty liver disease (FLD) (N=50) with healthy control participants (N=40). An independent samples t-test was employed to assess statistical significance, with p≤0.05 being significant.

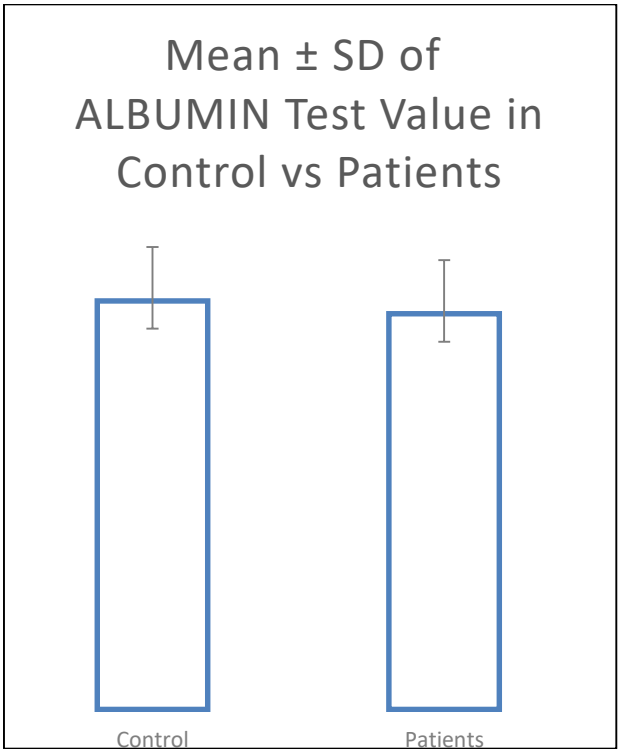

Figure 4. The average serum albumin level in FLD patients (4.27±0.58) was slightly lower than the albumin level in the control group (4.41±0.30). Despite this numerical difference, the result was statistically significant (p=0.001).

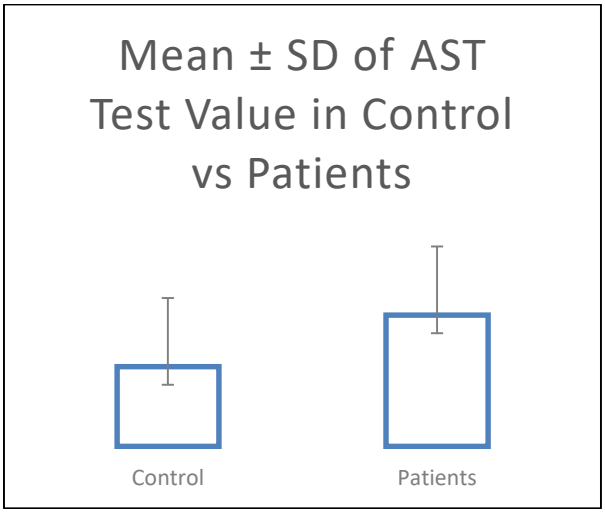

Figure 5. Patients with fatty liver disease (FLD) showed a significantly higher average serum AST enzyme level (37.00±19.34) compared to the healthy control group (22.53±5.11). The difference was statistically significant (p<0.001).

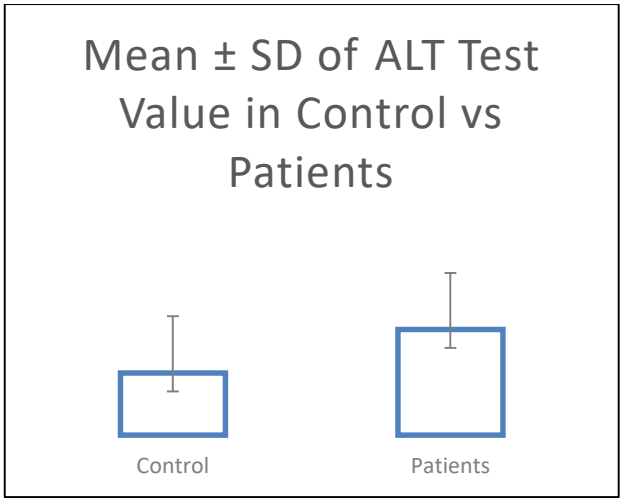

Figure 6. The ALT levels in the serum of the group of patients with fatty liver showed elevated levels compared to the control group, with a statistically significant (p <0.001).

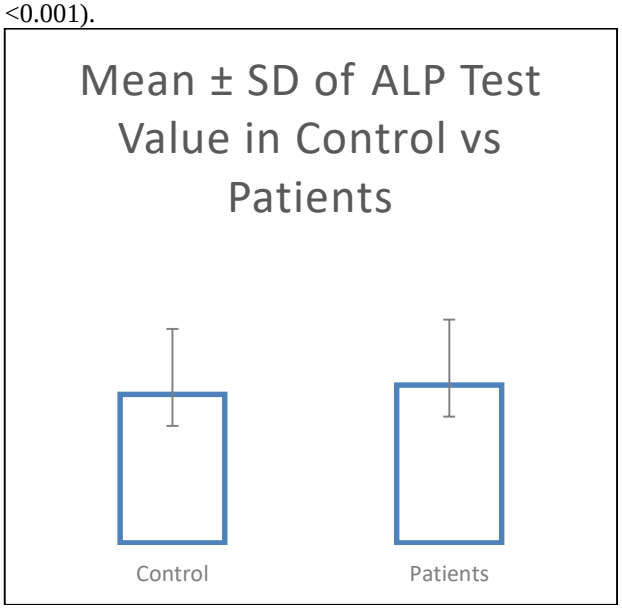

Figure 7. The mean ALP level in the serum of patients with fatty liver disease (110.70±45.97) was statistically higher than the level in the control group (104.20±22.08). However, this gap was not statistically significant (p=0.414, referred to as NS), indicating that ALP levels were similar between the two groups,

The results indicate clear differences in liver function markers between FLD patients and healthy controls

Table (1.4) *Mean levels of HbA1c Profile between patients with fatty liver disease (FLD), and healthy control*

Biomarkers	**Patient Mean±SD N=50**	**Control Mean±SD N=40**	**P value**
HbA1c	8.24±1.28	4.93±0.47	**<0.001[S]**
T -test was *: significant at p ≤ 0.05 SD: standard deviation; S: significant; NS= Non-significant.			

Table (3.5) shows that FLD patients have significantly higher HbA1c levels compared to the control group, with a p-value of <0.001, which is a clear statistical significance.

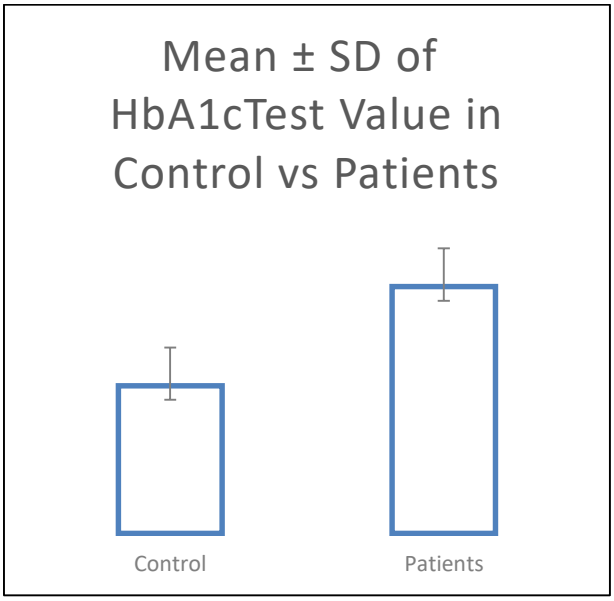

Figure 7. The HbA1c levels in the serum of the group of patients with fatty liver showed elevated levels compared to the control group, with a statistically significant (p <0.001).

1. 3. Discussion:

The results can be explained of the shared mechanisms of both diseases consequently amplify the analytical measurements, which is attributed to the role of insulin resistance and the impaired function of beta cells in responding to insulin, as well as the increased concentrations of insulin in the blood. This, in turn, affects the process of lipolysis, leading to an increased accumulation of fat in liver cells after storage, which explains the significant increase (Qasem, Al-Shami, & Al-Olofi, 2025) .

This elevation reflects the stress the liver is subjected to due to insulin resistance and the high secretion of insulin from beta cells in response to elevated blood sugar levels. C-peptide, which is secreted in equal amounts with insulin from beta cells, along with the accumulation of fat in patients and insulin resistance, supports this high blood level(Fawzi, Abd El Aziz, Mohamed, Kamal, & El Shenawy, 2025) (LIU, WANG, LIU, & WEI, 2025).

The results consistently indicate a substantial disruption in glucose homeostasis and insulin sensitivity measures in patients with fatty liver disease relative to healthy controls. Insulin levels in the blood rise in response to high sugar levels due to insulin resistance. Consequently, the pancreas reacts by secreting more insulin to lower blood sugar levels and restore glucose balance. This increase leads to the production of more fats in the liver, resulting in the accumulation of more fats within liver cells in patients with fatty liver disease, which exacerbates the condition(Bae et al., 2025; Guerra & Gastaldelli, 2020).

The significantly raised HOMA-IR in the FLD group signifies substantial insulin resistance, a characteristic of metabolic dysfunction frequently linked to fatty liver disease. These findings corroborate the notion that insulin resistance is pivotal in the development and advancement of fatty liver disease(Sung & Kim, 2011).

Significant changes occur in the reduction of albumin protein levels in fatty liver disease, but in advanced cases of liver damage and albumin leakage into the blood due to liver cell damage. However, in our study, there were few cases of fibrosis, so this did not cause a significant statistical change. But the role of albumin remains important and crucial in this disease(Takahashi et al., 2023).

Indicating an increase in AST levels in the FLD group, This increase is due to liver fibrosis and inflammation associated with fatty liver, resulting from oxidative stress, fat accumulation within liver cells, and mitochondrial damage in the liver .An elevated AST is considered a clear clinical biomarker indicating fatty liver disease. (Paulino, Cuthrell, & Tzenios, 2024; Sharma & Arora, 2020; Wang et al., 2024).

The accumulation of fat leads to inflammation and oxidative stress, resulting in damage to the cell membrane and the leakage of the AST enzyme from the cytoplasm into the blood. This enzyme is considered a reliable marker and indicator of the onset of liver injury, as well as the appearance of fibrosis and liver failure (Paulino et al., 2024; Sharma & Arora, 2020; Wang et al., 2024; Zhyzhneuskaya et al., 2025).

As it is abundantly expressed in the liver and bones. Often, when it rises due to liver conditions, it is the result of bile duct obstruction or a severe inflammatory process. Therefore, an elevated alkaline phosphatase level may indicate the severity of liver disease, such as the progression of fatty liver disease (FLD) to non-alcoholic steatohepatitis (NASH), and even cirrhosis and fibrosis. Given this possibility, alkaline phosphatase can be a useful marker for monitoring the progression of fatty liver disease (FLD) in patients with type 2 diabetes(Aransiola & Balogun, 2024).

HbA1c levels, as a primary indicator for glucose control, are usually associated with improved management of type 2 diabetes and reduced risk of complications. It reflects the glycemic state over a period of 2-3 months, resulting from the breakdown of red blood cells by the spleen, which is then released into the bloodstream(Chen, Yin, & Dou, 2023).

A study conducted in 2024 on the role of diabetes in the development of fatty liver showed that there is a strong positive correlation between its increase and the worsening of fatty liver and the increase in liver fibrosis. And a study in 2025 found that HbA1c is one of the three strongest biomarkers used in the study, which helps in the early detection of fatty liver. We should not forget that the increase in HbA1c is due to chronic high blood sugar, which is stored in the liver, increasing inflammation and oxidative stress, and activating hepatic stellate cells that lead to liver deterioration and fibrosis(Han et al., 2024; Yanmei Liu et al., 2025).

1. 4. Practical implications

This study's conclusions possess numerous significant clinical and practical implications. Pragmatic ramifications. The consistent use of HOMA-IR and C-peptide evaluations is recommended as initial screening tools for type 2 diabetes patients to identify individuals at increased risk of developing fatty liver disease before the onset of significant complications. Moreover, the integration of these indicators with regular monitoring of HbA1c levels and liver enzymes (AST, ALT) can produce a comprehensive biochemical profile for the early detection and intervention of diseases.

Moreover, the results support the development of a clinical care protocol for those demonstrating elevated HbA1c (>7.5%) or increased HOMA-IR readings. This treatment may include lifestyle modifications (dietary changes and increased physical activity), biannual liver function assessments, and the timely administration of

insulin-sensitizing drugs (such as metformin or pioglitazone) under medical supervision.

Thirdly, the results of this study may serve as a foundation for health education initiatives designed to enhance awareness among diabetic patients about the critical relationship between poor blood sugar control and the development of fatty liver, emphasizing the importance of rigorous blood sugar regulation and weight management to reduce the risk of fibrosis and hepatocellular carcinoma.

From a public health perspective, integrating HOMA-IR and HbA1c into the routine clinical evaluation of diabetes patients in specialized facilities can improve early detection rates, reduce healthcare costs associated with advanced liver diseases, and ultimately promote better long-term outcomes.

1. 5. Conclusion

The current investigation establishes that individuals with type 2 diabetes and fatty liver disease demonstrate significant insulin resistance, shown by a HOMA-IR increase of nearly ninefold compared to healthy subjects. Increased C-peptide and insulin levels signify compensatory hyperinsulinemia, although markedly elevated AST and ALT levels (up to 70% higher than controls) suggest persistent liver damage. The substantial elevation in HbA1c (8.24 vs. 4.93; $p<0.001$) underscores chronic hyperglycemia as a critical contributor to the advancement of fatty liver disease.

The results underscore the significance of early biochemical monitoring (HOMA-IR, insulin, C-peptide, HbA1c, liver enzymes) in diabetic patients. to identify high-risk individuals and avert progression to fibrosis, cirrhosis. Rigorous regulation of blood glucose levels, lifestyle alterations, and specific pharmacological interventions are crucial in mitigating the combined challenges of type 2 diabetes and fatty liver disease.

REFERENCES

Aransiola, C., & Balogun, W. (2024). NON-ALCOHOLIC FATTY LIVER DISEASE AND RELATIONSHIP WITH ADIPOSITY IN NIGERIAN PATIENTS WITH TYPE 2 DIABETES MELLITUS: THE IBADAN EXPERIENCE. *Annals of Ibadan Postgraduate Medicine*, *22*(2), 74.

Bae, J. H., Lee, M. J., Kim, S. H., Kim, J. Y., Khang, A. R., Kang, Y. H., & Yi, D. (2025). Fatty liver index and risk of type 2 diabetes of adults with normoglycemia: Insights into insulin sensitivity and beta-cell function. *PloS one*, *20*(6), e0327058.

Bo, T., Gao, L., Yao, Z., Shao, S., Wang, X., Proud, C. G., & Zhao, J. (2024). Hepatic selective insulin resistance at the intersection of insulin signaling and metabolic dysfunction-associated steatotic liver disease. *Cell Metabolism*, *36*(5), 947-968.

Chen, J., Yin, D., & Dou, K. (2023). Intensified glycemic control by HbA1c for patients with coronary heart disease and Type 2 diabetes: a review of findings and conclusions. *Cardiovascular Diabetology*, *22*(1), 146.

Fawzi, M. M., Abd El Aziz, G. R., Mohamed, R. A. E. D., Kamal, M. M., & El Shenawy, A. (2025). The level of serum C-peptide signals fibrosis in obese patients with NAFLD. *The Egyptian Journal of Internal Medicine*, *37*(1), 108.

Guerra, S., & Gastaldelli, A. (2020). The role of the liver in the modulation of glucose and insulin in non alcoholic fatty liver disease and type 2 diabetes. *Current opinion in pharmacology*, *55*, 165-174.

Habibullah, M., Jemmieh, K., Ouda, A., Haider, M. Z., Malki, M. I., & Elzouki, A.-N. (2024). Metabolic-associated fatty liver disease: A selective review of pathogenesis, diagnostic approaches, and therapeutic strategies. *Frontiers in medicine*, *11*, 1291501.

Han, X., Zhang, X., Liu, Z., Fan, H., Guo, C., Wang, H., . . . Zhang, T. (2024). Prevalence of nonalcoholic fatty liver disease and liver cirrhosis in Chinese adults with type 2 diabetes mellitus. *Journal of Diabetes*, *16*(5), e13564.

Johnston, M. P., Patel, J., & Byrne, C. D. (2020). Causes of mortality in non-alcoholic fatty liver disease (NAFLD) and alcohol related fatty liver disease (AFLD). *Current Pharmaceutical Design*, *26*(10), 1079-1092.

Kashyap, S. R., & Defronzo, R. A. (2007). The insulin resistance syndrome: physiological considerations. *Diabetes and Vascular Disease Research*, *4*(1), 13-19.

Li, M., Chi, X., Wang, Y., Setrerrahmane, S., Xie, W., & Xu, H. (2022). Trends in insulin resistance: insights into mechanisms and therapeutic strategy. *Signal transduction and targeted therapy*, *7*(1), 216.

Liu, Y., Shi, R., Cao, H., Zhang, J., Li, S., Kang, X., . . . Feng, L. (2025). AIP, fatty liver, and HbA1c as modifiers of the C-index and diabetes risk relationship. *Lipids in health and disease*, *24*(1), 129.

LIU, Y., WANG, X., LIU, Y., & WEI, L. (2025). Correlation of Fasting C-peptide to Diabetes Duration Ration and Type 2 Diabetes Mellitus Combined with Metabolism-related Fatty Liver Disease. *Chinese General Practice*, *28*(23), 2852.

Mir, M. M., Jeelani, M., Alharthi, M. H., Rizvi, S. F., Sohail, S. K., Wani, J. I., . . . Alshahrani, A. M. (2025). Unraveling the Mystery of Insulin Resistance: From Principle Mechanistic Insights and Consequences to Therapeutic Interventions. *International journal of molecular sciences*, *26*(6), 2770.

Mitra, S., De, A., & Chowdhury, A. (2020). Epidemiology of non-alcoholic and alcoholic fatty liver diseases. *Translational gastroenterology and hepatology*, *5*, 16.

Niranjan, S., Phillips, B. E., & Giannoukakis, N. (2023). Uncoupling hepatic insulin resistance–hepatic inflammation to improve insulin sensitivity and to prevent impaired metabolism-associated fatty liver disease in type 2 diabetes. *Frontiers in Endocrinology*, *14*, 1193373.

Ogunjobi, T., Adeyanju, S., Akinwande, K., Obasi, D., Aigbagenode, A., Musa, A., & Abdul, S. (2025). Improving the prevention and treatment of Lean Type 2

Diabetes in Sub-Saharan Africa: A review. *European Journal of Sustainable Development Research, 9*(2).

Paulino, P., Cuthrell, K. M., & Tzenios, N. (2024). Non Alcoholic Fatty Liver Disease; Disease Burden, Management, and Future Perspectives. *International Research Journal of Gastroenterology and Hepatology, 7*(1), 1-13.

Qasem, L., Al-Shami, A., & Al-Olofi, A. (2025). Evaluation of anthropometric parameters, Liver Enzymes, Albumin, and Lipid Profile Levels in Patients with Type Two Diabetes Mellitus, in Amran City, Yemen..

Ranade, S. D., Alegaon, S. G., Khatib, N. A., Gharge, S., Kavalapure, R. S., & Kumar, B. P. (2024). Reversal of insulin resistance to combat type 2 Diabetes mellitus by newer thiazolidinedione's in fructose induced insulin resistant rats. *European Journal of Medicinal Chemistry, 280*, 116939.

Sharma, P., & Arora, A. (2020). Clinical presentation of alcoholic liver disease and non-alcoholic fatty liver disease: spectrum and diagnosis. *Translational gastroenterology and hepatology, 5*, 19.

Sinaiko, A. R., & Caprio, S. (2012). Insulin resistance. *The Journal of pediatrics, 161*(1), 11.

Sung, K.-C., & Kim, S. H. (2011). Interrelationship between fatty liver and insulin resistance in the development of type 2 diabetes. *The Journal of Clinical Endocrinology & Metabolism, 96*(4), 1093-1097.

Szablewski, L. (2024). Changes in cells associated with insulin resistance. *International journal of molecular sciences, 25*(4), 2397.

Takahashi, H., Kawanaka, M., Fujii, H., Iwaki, M., Hayashi, H., Toyoda, H., . . . Munekage, K. (2023). Association of serum albumin levels and long-term prognosis in patients with biopsy-confirmed nonalcoholic fatty liver disease. *Nutrients, 15*(9), 2014.

Tanase, D. M., Gosav, E. M., Costea, C. F., Ciocoiu, M., Lacatusu, C. M., Maranduca, M. A., . . . Floria, M. (2020). The intricate relationship between type 2 diabetes mellitus (T2DM), insulin resistance (IR), and nonalcoholic fatty liver disease (NAFLD). *Journal of diabetes research, 2020*(1), 3920196.

Wang, S., Lin, X., Zhu, C., Dong, Y., Guo, Y., Xie, Z., . . . Chen, M. (2024). Association between nonalcoholic fatty liver disease and increased glucose-to-albumin ratio in adults without diabetes. *Frontiers in Endocrinology, 14*, 1287916.

Zhang, P., Wang, W., Mao, M., Gao, R., Shi, W., Li, D., . . . Meng, X. (2021). Similarities and differences: a comparative review of the molecular mechanisms and effectors of NAFLD and AFLD. *Frontiers in Physiology, 12*, 710285.

Zhyzhneuskaya, S., Al-Mrabeh, A., Peters, C., Barnes, A., Hollingsworth, K., Welsh, P., . . . Taylor, R. (2025). Clinical utility of liver function tests for resolution of metabolic dysfunction-associated steatotic liver disease after weight loss in the Diabetes Remission Clinical Trial. *Diabetic Medicine, 42*(3), e15462.

Pure Sciences International Journal of kerbala

Year:2026 Volume : 3 Issue : 9 ISSN: 6188-2789 Print 3005 -2394 Online

2026,Volume 3 , Issue 9 , PSIJK (52-61)

Pure Sciences International Journal of Kerbala

Minimize Total Completion Time, Total Number of Tardy Jobs, and the Range of Lateness for Single Machine Scheduling problems

Nagham M. Neamah [a]*, Tahani Jabbar Khraibet [b]

a Mathematics Department, College of Science for Women, University of Baghdad, Baghdad, Iraq
b Thi-Qar Directorates of Education, Ministry of Education, Iraq

P A P E R I N F O

Received: 21.10.2025
Accepted: 09.12.2025
Published: 31.03.2026

***Keywords*:**
Completion Time, Number of Tardy Jobs, Range of Lateness Time, Single Machine, Scheduling, Dominance Rules.

A b s t r a c t

Machine scheduling challenges are growing more intricate and dynamic. The scale and complexity of these problems demand the creation of approaches and solutions that can deliver satisfactory outcomes within an acceptable timeframe. In response, this paper introduces a novel mathematical framework tailored to multi-objective functions, focusing on single-machine scheduling issues by minimizing the discounted total completion time ($\sum C_j$), the total number of tardy jobs ($\sum U_j$), and the range of lateness time (R_L) denoted $1//(\sum C_j , \sum U_j , R_L)$ or CUR-TC. Also, minimizing the sum of total completion time ($\sum C_j$), the total number of tardy jobs ($\sum U_j$), and the range of lateness time (R_L) denoted $1//(\sum C_j + \sum U_j + R_L)$ or CUR-TO. In this paper, we prove the existence of an efficient sequence for problem $1//(\sum C_j , \sum U_j , R_L)$, where jobs are sorted in ascending order based on their processing times. Certain specific cases are highlighted to provide efficient and, in some instances, optimal solutions to the problem under consideration. The dominance rule can be used to solve problems to improve them and find efficient solutions. Accordingly, we proposed two heuristic methods for solving search problems. These are two fast methods for finding (near-optimal) solutions to optimization problems with the least possible number of tables, in comparison to the complete enumeration method and the branch and bound method. The first method is based on dominance rules, while the second method is based on MST and SPT rules.

DOI: 10.53851/psijk.v3.i9. 52-61

1. INTRODUCTION

Scheduling is a popular topic in operations (OR) and production management. A variety of research industries, including manufacturing facilities, are affected by the machine scheduling problem (MSP), It which is addressed through scheduling theory. involves determining how resources will be used over time to accomplish a set of tasks and is defined as the challenge of scheduling n jobs, each requiring one or more operations, on one or more machines within specific time frame to minimize a particular objective function (Nagham M. Neamah and Bayda A. Kalaf, 2024a). The structural nature of task ordering, especially as the number of tasks and their constraints increase, is the root cause of the complexity of scheduling problems. Since 1954, scheduling issues have gotten a lot of attention in the literature. Initially, the researchers focused on only one objective function. In practice, the decision-maker must choose only one of several objectives. Multi-criteria scheduling problems are now receiving more attention in studies (Nagham M. Neamah and Bayda A. Kalaf, 2023). Generally speaking, scheduling entails allocating machines to tasks so that all of the tasks may be finished within the given limitations (Nagham M. Neamah and Bayda A. Kalaf, 2024b). The challenge is to determine which sequence these jobs should be processed on each machine in order to reduce the specified goal function (Nagham M. Neamah & Bayda A. Kalaf, 2024). The best and most efficient way to minimize a multi-objective function is to use a table, which is a multi-objective function solver (Hoogeveen, 1996). Instead of producing a single optimal solution,

*Corresponding Author Institutional Email: naghamm_math@csw.uobaghdad.edu.(Nagham M. Neamah)

these objective functions produce multiple solutions (Khraibet & Ghafil, 2021). Each objective function has multiple optimal solutions, making it impossible to choose one solution over another. According to Hoogeveen (1996), a table, which is the solution to the MSP, is the most efficient method for minimizing a multiple objective function. These objective functions produce multiple optimal solutions rather than just one. Each objective function has more than one optimal solution, and therefore it is impossible to choose one that is better than two.] Non-dominated solutions are the best options in this case (Khraibet et al., 2025). Multi-objective scheduling challenges on a single machine are highly fascinating because they mimic real-world situations in which decision makers must balance multiple performance criteria to achieve the best results (Neufeld et al., 2023). It also adds several objectives to the classic issues, objectives that are often incompatible. This is an important area of research because it enhances operational efficiency and meets the needs of multiple stakeholders (Ezugwu, 2024). In most scheduling theory research, it is assumed that processing orders takes the same amount of time throughout the planning horizon. The difficulty of dealing with many objectives makes it difficult to apply classic optimization methods to multi-objective single-machine scheduling problems. However, they can be excellent tools for tackling well-defined scheduling problems. The branch and bound (BAB) algorithm was introduced by Tapan Sen et al. (1988) (Tapan S., Farhad M. E., 1988)to solve the $1//\sum C_j + R_L$ problem. By considering a linear combination of the two objectives, they were able to solve the problem with $n \leq 15$. The algorithm developed by Liao and Huang (1991) (Liao & Huang, 1991)is designed to minimize the range of delay (R_L) on a single device. Addressing the complexity of multi-objective scheduling problems often requires employing advanced multi-objective optimization methods, metaheuristic In this study, we algorithms, or hybrid strategies [6]. focused on the theoretical element by obtaining the best solution in a direct way without the need for precise methodologies by proving several special cases.

The rest of this article is organized as follows: In Sections 2 and 4, we propose two mathematical models that aim to address the three conflicting criteria in the single-device scheduling problem. Sections 3 and 5 present specific cases that demonstrate the identification of effective (optimal) solutions for the given problem. The dominance rule is described in Section 6. Section 7 presents and discusses the main outcomes from the preceding section. Conclusions are given in Section 8.

Prior to presenting the mathematical model, the following notations were used in the creation of the multi-objective model for MSP:

- $\varsigma = (\varsigma(1), \varsigma(2), \dots, \varsigma(m))$
- Av: Average.
- ANS: Average number of efficient solutions.
- AT/S: Average of CPU-Time per second
- CUR−TC: Mathematical Formulation of Problem $1//(\sum C_j, \sum U_j, R_L)$,
- CUR−TO: Mathematical Formulation of Problem $1//\sum C_j + \sum U_j + R_L$,
- $C_{\varsigma(j)}$: Duration necessary to finish job j within sequence ς.[Time required to complete task (job) j in sequence ς]
- $\sum C_{\varsigma(j)}$: Total completion time within sequence ς
- $d_{\varsigma(j)}$: Due date of job j within sequence ς
- EFS: Efficient solution
- $E_{\varsigma(j)}$: Earliness of job j within sequence ς
- $E_{max(\varsigma)}$: Maximum earliness inside sequence ς
- F_{CUR-TC}: Objective Function of $1//(\sum C_j, \sum U_j, R_L)$,
- F_{CUR-TO}: Objective Function of $1//\sum C_j + \sum U_j + R_L$,
- $L_{\varsigma(j)}$: The lateness of job j within sequence ς
- $L_{max(\varsigma)}$: Maximum lateness within sequence ς
- $L_{min(\varsigma)}$: Minimum lateness within sequence ς
- $M = \{1,2, \dots, m\}$: A collection of tasks requiring scheduling.
- OPS: Optimal solution
- $p_{\varsigma(j)}$: Processing time of job j within sequence ς
- R: $0 < Real < 1$
- $R_{L(\varsigma)}$: The Range of Lateness within sequence ς
- $U_{\varsigma(j)}$: Number of tardy jobs within sequence ς
- $\sum U_{\varsigma(j)}$: Total number of tardy times within the sequence ς
- TCMSP: Tri-Criteria Machine Scheduling Problem
- TOMSP: Tri-Objective Machine Scheduling Problem

Definition (1): When a schedule ς is unable to meet $f_{\varsigma'(j)} \leq f_{\varsigma(j)}, j = 1, \dots, k$, with at least one of the aforementioned holdings as a rigorous inequality, then

that schedule is considered efficient. This is also known as ϙ′ dominating ϙ.

Definition (2): Let $(h_{i(0)}: i = 1,2,3)$ be a solution for the tri-criteria problem $1//(h_1, h_2, h_3)$, then the Euclidean distance (d) for this solution is: $d = \sqrt{\sum h_{i(0)}^2} = \sqrt{h_{1(0)}^2 + h_{2(0)}^2 + h_{3(0)}^2}$ (1)

Note (1): A useful measure for determining the most efficient solution from a Pareto-optimal set is the distance d.

Proposition (1): Let $(h_{1(0)}, h_{2(0)}, h_{3(0)})$ be a solution for the tri-criteria problem $1//(h_1, h_2, h_3)$, and $h_{i(0)} \neq 0, i = 1,2,3$, then always: $h_{i(0)} \leq d, i = 1,2,3$.

Proof: Let's assume that $h_{i(0)} > d$, from (1):

$h_{i(0)} > \sqrt{h_{1(0)}^2 + h_{2(0)}^2 + h_{3(0)}^2}$

$h_{1(0)}^2 > h_{1(0)}^2 + h_{2(0)}^2 + h_{3(0)}^2$

This is a contradiction since the above inequality is not true even $h_{i(0)} = 0, i = 1,2,3$.

2. Problem Description

After reviewing the terminology of the mathematical model, we move on to constructing the mathematical model of the research topic: Let $M = \{1,2, \dots, m\}$ be a set of jobs that want to be scheduled on a tri-criteria machine scheduling problem (TCMSP) with $p_j \leq d_j$, and the tri-criteria machine scheduling problem (TCMSP) for each NP-hard problem. The MSP can only process one job at a time using the three fields' classification. Using the table $ϙ = (ϙ(1), ϙ(2), \dots, ϙ(m))$, the discussed TCMSP is denoted by $1//(\sum C_j, \sum U_j, R_L)$, and CUR−TC. which can be formulated as follows:

$$F_{CUR-TC} = Min \begin{cases} \sum C_{ϙ(j)} \\ \sum U_{ϙ(j)} \\ R_{L(ϙ)} \end{cases} \quad (2)$$

Subject to

$$\left.\begin{array}{l} C_0 = 0 \\ C_{ϙ(j)} = C_{ϙ(j-1)} + p_{ϙ(j)} \\ C_{ϙ(j)} > 0 \end{array}\right\} \quad (3)$$

$$\left.\begin{array}{l} L_{ϙ(j)} = C_{ϙ(j)} - d_{ϙ(j)} \\ L_{max(ϙ)} = \max\limits_{1 \leq j \leq m} \{L_{ϙ(j)}\} \\ L_{min(ϙ)} = \min\limits_{1 \leq j \leq m} \{L_{ϙ(j)}\} \end{array}\right\} \quad (4)$$

$$\left.\begin{array}{l} U_{ϙ(j)} = 0 \quad \text{if} \quad L_{ϙ(j)} \leq 0 \\ U_{ϙ(j)} = 1 \quad \text{if} \quad L_{ϙ(j)} > 0 \end{array}\right\} \quad (5)$$

$$\left.\begin{array}{l} E_{ϙ(j)} \geq d_{ϙ(j)} - C_j \\ E_{max(ϙ)} = \max\limits_{1 \leq j \leq m} \{E_{ϙ(j)}\} \\ E_{ϙ(j)} \geq 0 \end{array}\right\} \quad (6)$$

$$\left.\begin{array}{l} R_{L(ϙ)} = L_{max(ϙ)} + E_{max(ϙ)} \\ E_{max(ϙ)} = -L_{min(ϙ)} \\ R_{L(ϙ)} \geq 0 \end{array}\right\} \quad (7)$$

In this paper, we will try to find an efficient solution to CUR−TO, given the difficulty of solving this problem.

Proposition (2): There is an efficient sequence for problem $1//(\sum C_j, \sum U_j, R_L)$, which obeys the shortest processing time (SPT) rule.

Proof: (i) Firstly, assume that $p_i \neq p_j$ for all i, j .The unique sequence SPT_1, and consequently (SPT_2), delivers the absolute minimum value of $\sum C_j$. Thus, there is no alternative sequence $\delta \neq \text{SPT}_2$ such that.

$$\left.\begin{array}{l} \sum C_{j(\delta)} \leq \sum C_{j(\text{SPT}_2)}, \\ \sum U_{j(\delta)} \leq \sum U_{j(\text{SPT}_2)}, \\ and\ R_{L(\delta)} \leq R_{L(\text{SPT}_2)} \end{array}\right\} \quad (8)$$

At least one strict inequality must be present.

(ii) If multiple SPT_1 sequences exist for certain jobs with identical processing times, the SPT_2 sequence should adhere to the SPT_1 rule while prioritizing jobs with the same processing time in EDD order (noting that EDD and MOOR sequences are equivalent). For a subset of jobs categorized as early or relatively early, this EDD = MOOR sequence effectively minimizes $L_{max}, \sum U_j$.

The due date is the same for all jobs that take the same amount of time to process. If there are periods when things are slow, then SPT_2 is not unusual. Demonstrate that any SPT_2 sequencing constitutes an efficient sequencing that does not adhere to the SPT_1 rule, which states that an SPT_1 cannot dominate an SPT_2 sequencing, as indicated in (8). If δ is an SPT sequence, it cannot be SPT_2 sequencing since it cannot dominate SPT_2

$$\left.\begin{array}{l} \sum C_{j(\delta)} = \sum C_{j(\text{SPT}_2)}, \\ \sum U_{j(\text{SPT}_2)} \leq \sum U_{j(\delta)}, \\ \text{and } R_{L(\text{SPT}_2)} \leq R_{L(\delta)} \end{array}\right\} \quad (9)$$

Due to the implementation of the EDD rule, all of the SPT_2 sequences function effectively.

3. SPECIAL CASES FOR PROBLEM CUR−TC

Case (3.1): For problem CUR−TC, if the processing times for all jobs are uniform and the due dates are similarly uniform $(p_j = p \text{ and } d_j = d, \forall_j)$, Consequently, a singular optimal solution exists with n! sequences under a constant objective function.

Proof: As known:

$C_{ϙ(j)} = \sum_{k=1}^{j} p_k = jp$, then $\sum_{j=1}^{m} C_{ϙ(j)} = p\frac{m(m+1)}{2}$, and $L_{ϙ(j)} = C_{ϙ(j)} - d_{ϙ(j)} = jp - d$

$L_{max(ϙ)} = \max\limits_{1<j\leq m} \{L_{ϙ(j)}\} = mp - d$ and $L_{min(ϙ)} = \min\limits_{1<j\leq m} \{L_{ϙ(j)}\} = p - d$

$\therefore R_{L(ϙ)} = L_{max(ϙ)} - L_{min(ϙ)} = mp - d - (p - d) = mp - p = (m-1)p$ (10)

$E_{\varsigma(j)} = max\{d_{\varsigma(j)} - C_{\varsigma(j)}, 0\} = max\{d - jp, 0\}$
$E_{\varsigma(j)} = max\{d - p, d - 2p, \dots, d - jp, \dots, d - mp, 0\}$ (11)
$T_{\varsigma(j)} = max\{C_{\varsigma(j)} - d_{\varsigma(j)}, 0\} = max\{jp - d, 0\}$
$T_{\varsigma(j)} = max\{p - d, 2p - d, \dots, jp - d, \dots, mp - d, 0\}$ (12)

1) If all jobs are early, this means $d > C_{\varsigma(j)} = jp$ & $L_{\varsigma(j)} \leq 0$, then $U_{\varsigma(j)} = 0$ and the maximum difference in relation (11) is $d - p$, then:

a) If $L_{\varsigma(j)} = 0, \forall j$, hence $L_{max(\varsigma)} = L_{min(\varsigma)} = 0$. Then
$\left(\sum C_{\varsigma(j)}, \sum U_{\varsigma(j)}, R_L\right) = \left(p\frac{m(m+1)}{2}, 0, 0\right)$ (13)

b) If $L_{max(\varsigma)} = 0$ and $L_{min(\varsigma)} < 0$, $E_{max(\varsigma)} = -L_{min(\varsigma)} = d - p$, then
$\left(\sum C_{\varsigma(j)}, \sum U_{\varsigma(j)}, R_L\right) = \left(p\frac{m(m+1)}{2}, 0, d - p\right)$. (14)

c) If $L_{max(\varsigma)} = C_{max(\varsigma)} - d < 0$ and $L_{min(\varsigma)} = p_{\varsigma(1)} - d < 0$, then:

$R_{L(\varsigma)} = C_{max(\varsigma)} - p_{\varsigma(1)}$, and
$\left(\sum C_{\varsigma(j)}, \sum U_{\varsigma(j)}, R_L\right) = \left(p\frac{m(m+1)}{2}, 0, C_{max(\varsigma)} - p_{\varsigma(1)}\right) = \left(p\frac{m(m+1)}{2}, 0, C_{max(\varsigma)} - p_{\varsigma(1)}\right)$ (15)

From (13), (14), and (15), we obtain that there exists a unique efficient solution with n! sequences with a constant objective function

2) If all jobs are late (except the 1st job, this means $d = p$), $U_{\varsigma(j)} = 1, and\ E_{\varsigma(j)} = 0, \forall_j$, then:
$E_{max(\varsigma)} = 0$ (16)
$L_{max(\varsigma)} = \max\limits_{1\leq j\leq m}\{L_{\varsigma(j)}\} = mp - d = mp - p = (m - 1)p$ and $L_{min(\varsigma)} = p - d = 0$
$R_{L(\varsigma)} = L_{max(\varsigma)} - L_{min(\varsigma)} = (m - 1)p - 0 = (m - 1)p$ (17)

From relations (15) and (16), we obtain:
$\left(\sum C_{\varsigma(j)}, \sum U_{\varsigma(j)}, R_L\right) = \left(p\frac{m(m+1)}{2}, m - 1, (m - 1)p\right)$.

3) If $p_{\varsigma(1)} = C_{\varsigma(1)} < d < C_{\varsigma(j>1)}$:
$L_{max(\varsigma)} = \max\limits_{1<j\leq m}\{L_{\varsigma(j)}\} = \max\limits_{1<j\leq m}\{C_{\varsigma(j)} - d, 0\}$.
$L_{max(\varsigma)} = C_{max(\varsigma)} - d$ (18)
Then:
$T_{max} = C_{max(\varsigma)} - d$ (19)
$L_{min(\varsigma)} = \min\limits_{1\leq j\leq m}\{L_j\} = -E_{max(\varsigma)} = -(d - p)$ (20)

From relations (18) and (20), $R_{L(\varsigma)} = T_{max} - (-E_{max(\varsigma)}) = T_{max} + E_{max(\varsigma)} = C_{max(\varsigma)} - d + (d - p) = mp - p = (m - 1)p$.

From relations (18), (19), and (20), the CUR-TCMSP is converted to $\left(\sum C_{\varsigma(j)}, \sum U_{\varsigma(j)}, R_L\right) = \left(p\frac{m(m+1)}{2}, k, (m - 1)p\right)$, where k represents the number of delayed jobs (k is constant).

Case (3.2): When the due date for all tasks is uniform (denoted by $d_j = d$, for each j), applying the rule $\varsigma = SPT$ provides an efficient solution to the CUR-TC problem.

Proof: Let's have the sequence ς = SPT, $L_{max(\varsigma)} = C_{max(\varsigma)} - d$ and $L_{min(\varsigma)} = C_{min(\varsigma)} - d = p_{\varsigma(1)} - d$.
$R_{L(\varsigma)} = L_{max(\varsigma)} - L_{min(\varsigma)} = \max\limits_{1\leq j\leq m}\{L_{\varsigma(j)}\} - \min\limits_{1\leq j\leq m}\{L_{\varsigma(j)}\} = \max\limits_{1\leq j\leq m}\{C_{\varsigma(j)} - d\} - \min\limits_{1\leq j\leq m}\{C_{\varsigma(j)} - d\} = \max\limits_{1\leq j\leq m}\{C_{\varsigma(j)}\} - d - \left\{\min\limits_{1\leq j\leq m}\{C_{\varsigma(j)}\} - d\right\} = \max\limits_{1\leq j\leq m}\{C_{\varsigma(j)}\} - d - \min\limits_{1\leq j\leq m}\{C_{\varsigma(j)}\} + d = \max\limits_{1\leq j\leq m}\{C_{\varsigma(j)}\} - \min\limits_{1\leq j\leq m}\{C_{\varsigma(j)}\} = \max\limits_{1\leq j\leq m}\{C_{\varsigma(j)}\} - p_{\varsigma(1)} = C_{max(\varsigma)} - p_{\varsigma(1)} = \sum_{j=2}^{m} p_{\varsigma(j)}$.

1) If $d \geq C_{\varsigma(j)}$:

$T_{max(\varsigma)} = 0$ (Since all jobs are early), $U_{\varsigma(j)} = 0$ then $1//\left(\sum C_{\varsigma(j)}, \sum U_{\varsigma(j)}, R_{L(\varsigma)}\right)$ reduce to $1//\left(\sum C_{\varsigma(j)}, R_{L(\varsigma)}\right) = \left(\sum C_{\varsigma(j)}, C_{max(\varsigma)} - p_{\varsigma(1)}\right) = \left(\sum C_{\varsigma(j)}, \sum_{j=2}^{m} p_{\varsigma(j)}\right)$. In this case, the SPT rule gives an efficient solution to CUR-TCMSP.

2) If $d < C_{\varsigma(j)}, \forall j$:

$L_{max(\varsigma)} = \max\limits_{1\leq j\leq m}\{L_{\varsigma(j)}\} = \max\limits_{1\leq j\leq m}\{C_{\varsigma(j)} - d, 0\} = C_{max(\varsigma)} - d = T_{max(\varsigma)}$, $L_{min} = min\{L_{\varsigma(j)}\} = -E_{max(\varsigma)} = 0$ ($E_{max(\varsigma)} = 0$ Since all jobs are late), $R_{L(\varsigma)} = C_{max(\varsigma)} - d$, and $\sum_{j=1}^{m} U_{\varsigma(j)} = m$. Then $1//\left(\sum C_{\varsigma(j)}, \sum U_{\varsigma(j)}, R_{L(\varsigma)}\right) = 1//\left(\sum C_{\varsigma(j)}, m, C_{max(\varsigma)} - d\right)$. In this case, the SPT rule gives an efficient solution to CUR−TCMSP.

Case (3.3): For problem CUR−TC,

1) For ς = SPT, if all jobs are neither early and not late $\left(C_{\varsigma(j)} = d_{\varsigma(j)}, \forall j\right)$, then we obtain an efficient solution.
2) For ς = EDD, if all jobs are early $\left(C_{\varsigma(j)} < d_{\varsigma(j)}, \forall j\right)$, then we obtain an efficient solution.
3) For ς = MST, if all jobs are late $\left(C_{\varsigma(j)} \geq d_{\varsigma(j)}, \forall j\right)$, then we obtain an efficient solution.

Proof: 1. Since $\left(C_{\varsigma(j)} = d_{\varsigma(j)}, \forall j\right)$, then $T_{max(\varsigma)} = E_{max(\varsigma)} = 0$. Hence, $1//\left(\sum C_{\varsigma(j)}, \sum U_{\varsigma(j)}, R_{L(\varsigma)}\right)$ reduces to $1//\left(\sum C_{\varsigma(j)}\right)$; this problem has an optimal solution and an efficient solution for CUR−TC when using $\varsigma = SPT$. $1//\left(\sum C_{\varsigma(j)}, \sum U_{\varsigma(j)}, R_{L(\varsigma)}\right) = 1//\left(\sum C_{\varsigma(j)}\right)$.

2. Since all jobs are early for ς = MST, thus: $T_{max(\varsigma)} = \sum U_{\varsigma(j)} = 0$, then $L_{max(\varsigma)} \leq 0$ and $L_{min(\varsigma)} \leq 0$

Notice that $L_{max(\varsigma)}$ is the minimum L_{max} and $L_{min(\varsigma)}$ is the minimum L_{min} for all feasible sequences, then $R_{L(\varsigma)} = L_{max(\varsigma)} - L_{min(\varsigma)}$ is the minimum R_L for all feasible sequences. Since $C_{\varsigma(j)} \leq d_{\varsigma(j)}, \forall j$, with minimum $R_{L(\varsigma)}$ and $T_{max(\varsigma)} = \sum U_{\varsigma(j)} = 0$, then ς gives an efficient solution for CUR-TCMSP.

$1//\left(\sum C_{\varsigma(j)}, \sum U_{\varsigma(j)}, R_{L(\varsigma)}\right) = 1//\left(\sum C_{\varsigma(j)}, 0, R_{L(\varsigma)}\right) = 1//\left(\sum C_{\varsigma(j)}, L_{max(\varsigma)} - L_{min(\varsigma)}\right)$

3. Since $\left(C_{\varsigma(j)} \geq d_{\varsigma(j)}, \forall j\right)$, thus: $E_{max(\varsigma)} = 0$, then $1//\left(\sum C_{\varsigma(j)}, \sum U_{\varsigma(j)}, R_{L(\varsigma)}\right) = 1//\left(\sum C_{\varsigma(j)}, m, R_{L(\varsigma)}\right) = 1//\left(\sum C_{\varsigma(j)}, m, L_{max(\varsigma)}\right)$, then ς gives an efficient solution for CUR−TC.

Case (3.4): For problem CUR−TC: If $p = p_j, \forall_j$, then the CUR-TC can be solved by using the EDD rule.

Proof: Let's have the sequence $\varsigma = EDD$.

As known $L_{\varsigma(j)} = C_{\varsigma(j)} - d_{\varsigma(j)}$, and since $p = p_j, \forall_j$ then $C_j = jp, \sum_{j=1}^{m} C_j = \sum_{j=1}^{m} jp = p\frac{m(m+1)}{2}$ (21)

So, $L_{\varsigma(j)} = jp - d_{\varsigma(j)} = \{p - d_{\varsigma(1)}, 2p - d_{\varsigma(2)}, \dots, np - d_{\varsigma(m)}\}$

$R_{L(\varsigma)} = L_{max(\varsigma)} - L_{min(\varsigma)} = \max_{1\leq j\leq m}\{L_{\varsigma(j)}\} - \min_{1\leq j\leq m}\{L_{\varsigma(j)}\} = \max_{1\leq j\leq m}\{jp - d_{\varsigma(j)}\} - \min_{1\leq j\leq m}\{jp - d_{\varsigma(j)}\} = mp - d_{max(\varsigma)} - (p - d_{min(\varsigma)})$

$R_{L(\varsigma)} = (m-1)p - (d_{max(\varsigma)} - d_{min(\varsigma)})$ (22)

1) If $d_{max(\varsigma)} < C_m = C_{max(\varsigma)} = mp$, then $L_{max(\varsigma)} = mp - d_{max(\varsigma)} > 0 \therefore T_{L_{max(\varsigma)}} = L_{max(\varsigma)} = mp - d_{max(\varsigma)} = R_{L(\varsigma)}$, & $\sum_{j=1}^{m} U_{\varsigma(j)} = m$ (23)

2) If $C_m \leq d_{min(\varsigma)}$, then all jobs are early $\therefore T_{L_{max(\varsigma)}} = 0$ & $\sum_{j=1}^{m} U_{\varsigma(j)} = 0$ (24)

3) $C_{\varsigma(j)} = jp = d_{\varsigma(j)}$, this means $T_{max(\varsigma)} = 0$& $E_{max(\varsigma)} = 0$, then $\sigma = EDD$, and $L_{max(\varsigma)} = L_{min(\varsigma)} = 0$, then $R_{L(\varsigma)} = 0$ & $\sum_{j=1}^{m} U_{\varsigma(j)} = 0$.

From relations (21), (22), (23), and (24), If all functions are constants, then any sequence has a job order with $d_{min(\varsigma)}$ and $d_{max(\varsigma)}$ at the first and last positions, respectively, provides the same unique efficient solution , and there are $(n-2)!$ sequences. This relation depends on the variable. $d_{\varsigma(j)}$, then $R_{L(\varsigma)}$, $U_{\varsigma(j)}$ depend on $d_{\varsigma(j)}$ only, then the EDD rule gives an optimal solution for CUR−TC.

Case (3.5): For problem CUR−TC, if the rules for MOOR, EDD, and SPT are the same, we have an effective solution.

1) If ς = SPT = EDD = MST = MOOR at the same time, then there is an efficient solution.

2) If ς = SPT = EDD = MOOR and $p_j$and d_j are different, then there is only one efficient solution.

Proof:

1) It is well known that the SPT rule minimizes $\sum C_{\varsigma(j)}$, the EDD rule minimises $T_{max(\varsigma)}$, and the MOOR rule minimizes $\sum U_{\varsigma(j)}$. The ideal solution for $\sum C_{\varsigma(j)}$, $T_{max(\varsigma)}$, and $\sum U_{\varsigma(j)}$ will be provided by a schedule ς s.t ς = SPT = EDD = MOOR simultaneously.

2) Similar to (1), if we have ς = SPT = EDD = MOOR and all $p_j$and d_j are distinct from one another, then ς will be unique and there won't be any τ s.t. $\sum C_{\tau(j)} \leq \sum C_{\varsigma(j)}$, $\sum U_{\tau(j)} \leq \sum U_{\varsigma(j)}$, and $R_{L(\tau)} \leq R_{L(\varsigma)}$, where at least one of the inequalities is stringent. Then, regardless of whether σ minimises R_L or not, it provides a special, effective solution for CUR-TC in two scenarios.

4. Mathematical Formulation of Subproblem for CUR−TOMSP

In this section, we will discuss the sub-problem of CUR−TC; we will try to find the optimal solution using the table $\varsigma = (\varsigma(1), \varsigma(2), \dots, \varsigma(m))$. This is a tri-objective problem (TOMSP), which is defined as $1//\left(\sum C_{\varsigma(j)} + \sum U_{\varsigma(j)} + R_{L(\varsigma)}\right)$, and is denoted by CUR−TO. It can be formulated as follows:

$F_{CUR-TO} = Min\left(\sum C_{\varsigma(j)} + \sum U_{\varsigma(j)} + R_{L(\varsigma)}\right)$ (25)

Subject to (3) − (7)

Proposition (3): For problem CUR−TO, and schedule ς. If $m \to \infty$, then $1//\sum C_{\varsigma(j)} + \sum U_{\varsigma(j)} + R_{L(\varsigma)} \to \infty$.

Proof: Since the range of lateness ($R_{L(\varsigma)}$) is equal to the difference between the maximum lateness time ($L_{max(\varsigma)} = \max_{1\leq j\leq m}(L_{\varsigma(j)})$), the minimum lateness time ($L_{min(\varsigma)} = \min_{1\leq j\leq m}\{L_{\varsigma(j)}\}$)

if $m \to \infty$, $\max_{1\leq j\leq m}\{L_{\varsigma(j)}\} \to \infty$, since $\max_{1\leq j\leq m}\{L_{\varsigma(j)}\} \to L_m$ and since $C_{\varsigma(j)} = C_{max} \gg d_m$, then

$\therefore L_m \to \infty$, since $R_{L(\varsigma)} = \max_{1\leq j\leq m}\{L_{\varsigma(j)}\} - \min_{1\leq j\leq m}\{L_{\varsigma(j)}\}$, that implies $\lim_{m\to\infty} R_{L(\varsigma)} = L_m - L_{min(\varsigma)} \approx L_m$ as $m \to \infty$.

$\therefore R_{L(\varsigma)} \to \infty$

CUR−TOMSP, if $m \to \infty$, then $\sum C_{\varsigma(j)} + \sum U_{\varsigma(j)} + R_{L(\varsigma)}$.

The Proposition below describes the relationship between CUR−TC and CUR−TO and shows that any optimal solution to problem CUR−TO is an efficient solution to problem CUR−TC.

Proposition (4): Let ς represent the schedule that provides one of the efficient solutions for CUR-TC, if and only if ς represents the optimal solution for CUR-TO.

Proof: Let $\mathcal{Q} = \{\mu_1, \mu_2, \dots, \mu_r\}$ represent the set of all efficient schedules yielding efficient outcomes$\left((g,h,w) = (g_i, h_i, w_i)\right) \forall, i = 1,2,\dots,r$, in the framework of CUR-TC. Let us consider that the optimal solution $(g_k + h_k + w_k)$ for CUR-TOMSP does not belong to the set of efficient solutions for CUR-TC. Under this assumption, the schedule ς, which yields $(g_k + h_k + w_k)$ such that $\varsigma \notin \mathcal{Q}$, leads to the conclusion that $g_i + h_i + w_i < g_k + h_k + w_k, \forall\, i = 1,2,\dots,r$. This implies that $g_k + h_k + w_k$ cannot be an optimal solution for CUR-TO, which creates a logical contradiction.

Now reconsider ϱ as a schedule providing the optimal solution $g_k + h_k + w_k$ for CUR-TOMSP. Suppose ϱ does not deliver an efficient solution for CUR-TC; this condition implies that $\varrho \notin S$ meaning there exists an efficient solution $g_i + h_i + w_i < g_k + h_k + w_k$. Consequently, $(g_i + h_i + w_i)$ would serve as the optimal solution for CUR-TO and achieve a value smaller than $g_k + h_k + w_k$. This reasoning again leads to a contradiction since $g_k + h_k + w_k$ cannot simultaneously be a valid optimal solution for CUR-TO under these circumstances. Hence, the initial assumption must be incorrect.

5. The key special cases of the CUR-TO

Case (5.1): For problem CUR−TO, if the processing times of all jobs are identical and the due date is also identical ($p_j = p$ and $d_j = d, \forall_j$), then there exists a unique optimal solution with n! sequences with a constant objective function

Proof: From case (3.1) for problem CUR−TO, we prove that:

1)If all jobs are early, this means $d > C_{\varrho(j)} = jp$, then $\left(\sum C_{\varrho(j)}, \sum U_{\varrho(j)}, R_L\right) = \left(p\frac{m(m+1)}{2}, 0, (m-1)p\right)$

So, for CUR−TO, we obtain: $\left(\sum C_{\varrho(j)} + \sum U_{\varrho(j)} + R_L\right) = \left(p\frac{m(m+1)}{2} + 0 + (m-1)p\right) = p\frac{m^2+3m-2}{2}$

2) If all jobs are late (except the 1st job), then $\left(\sum C_{\varrho(j)}, \sum U_{\varrho(j)}, R_L\right) = \left(p\frac{m(m+1)}{2}, m-1, (m-1)p\right)$

So, for CUR−TO, we obtain: $\left(\sum C_{\varrho(j)} + \sum U_{\varrho(j)} + R_L\right) = \left(p\frac{m(m+1)}{2} + m - 1 + (m-1)p\right) = p\frac{m^2+3m-2}{2} + m - 1$.

3) If $p_{\varrho(1)} = C_{\varrho(1)} < d < C_{\varrho(j>1)}$, then we prove $\left(\sum C_{\varrho(j)}, \sum U_{\varrho(j)}, R_L\right) = \left(p\frac{m(m+1)}{2}, k, (m-1)p\right)$, where k represents the number of delayed jobs (k is constant).

So, for CUR−TO, we obtain: $\left(\sum C_{\varrho(j)} + \sum U_{\varrho(j)} + R_L\right) = p\frac{m(m+1)}{2} + k + (m-1)pp\frac{m^2+3m-2}{2} + k$

Case (5.2): When the due date for all tasks is uniform (denoted by $d_j = d$, for each j), applying the rule $\varrho = SPT$ provides an efficient solution to the CUR−TO problem.

Proof: From case (3.2) of CUR−TC:

1. If $d \geq C_{\varrho(j)}$; we prove that: $1//\left(\sum C_{\varrho(j)}, \sum U_{\varrho(j)}, R_{L(\varrho)}\right)$ reduce to $1//\left(\sum C_{\varrho(j)}, R_{L(\varrho)}\right) = \left(\sum C_{\varrho(j)}, C_{max(\varrho)} - p_{\varrho(1)}\right) = \left(\sum C_{\varrho(j)}, \sum_{j=2}^{m} p_{\varrho(j)}\right)$.

So, for CUR-TO, we obtain: $\left(\sum C_{\varrho(j)} + \sum U_{\varrho(j)} + R_{L(\varrho)}\right) = \left(\sum C_{\varrho(j)} + R_{L(\varrho)}\right) = \left(\sum C_{\varrho(j)} + C_{max(\varrho)} - p_{\varrho(1)}\right) = \left(\sum C_{\varrho(j)} + \sum_{j=2}^{m} p_{\varrho(j)}\right)$

2. If $d < C_{\varrho(j)}, \forall j$; we prove that: $1//\left(\sum C_{\varrho(j)}, \sum U_{\varrho(j)}, R_{L(\varrho)}\right) = 1//\left(\sum C_{\varrho(j)}, m, C_{max(\varrho)} - d\right)$.

So, for CUR−TO we obtain: $1//\left(\sum C_{\varrho(j)} + \sum U_{\varrho(j)} + R_{L(\varrho)}\right) = 1//\left(\sum C_{\varrho(j)} + m + C_{max(\varrho)} - d\right)$.

Case (5.3): For problem CUR,

1) For ϱ = SPT, if all jobs are neither early and not late $\left(C_{\varrho(j)} = d_{\varrho(j)}, \forall j\right)$, then we obtain an optimal solution.
2) For ϱ = MST, if all jobs are early $\left(C_{\varrho(j)} \leq d_{\varrho(j)}, \forall j\right)$, then we obtain an optimal solution.
3) For ϱ = EDD, if all jobs are late $\left(C_{\varrho(j)} \geq d_{\varrho(j)}, \forall j\right)$, then we obtain an optimal solution.

Proof: From case (3.3) of CUR−TC:

1) If $\left(C_{\varrho(j)} = d_{\varrho(j)}, \forall j\right)$; we prove that: $1//\left(\sum C_{\varrho(j)}, \sum U_{\varrho(j)}, R_{L(\varrho)}\right) = 1//\left(\sum C_{\varrho(j)}\right)$

So, for TOMSP−CUR, we obtain: $1//\sum C_{\varrho(j)} + \sum U_{\varrho(j)} + R_{L(\varrho)} = 1//\sum C_{\varrho(j)}$

2) If $C_{\varrho(j)} \leq d_{\varrho(j)}, \forall j$; we prove that:$1//\left(\sum C_{\varrho(j)}, \sum U_{\varrho(j)}, R_{L(\varrho)}\right) = 1//\left(\sum C_{\varrho(j)}, 0, R_{L(\varrho)}\right)$

So, for CUR−TO, we obtain: $\sum C_{\varrho(j)} + \sum U_{\varrho(j)} + R_{L(\varrho)} = \sum C_{\varrho(j)} + 0 + R_{L(\varrho)}$

3. If $\left(C_{\varrho(j)} \geq d_{\varrho(j)}, \forall j\right)$; we prove that: $1//\left(\sum C_{\varrho(j)}, \sum U_{\varrho(j)}, R_{L(\varrho)}\right) = 1//\left(\sum C_{\varrho(j)}, m, R_{L(\varrho)}\right) = 1//\left(\sum C_{\varrho(j)}, m, L_{max(\varrho)}\right)$

So, for CUR−TO, we obtain: $\sum C_{\varrho(j)} + \sum U_{\varrho(j)} + R_{L(\varrho)} = \sum C_{\varrho(j)} + m + R_{L(\varrho)} = \sum C_{\varrho(j)} + m + L_{max(\varrho)}$.

Case (5.4): For problem CUR−TO−TOMSP if $p = p_j, \forall_j$, then the problem CUR can be solved by the EDD rule.

Proof: (See case (3.4) of CUR−TC). [Refer to case (3.4) of CUR−TC]

1) If $d_{max(\varrho)} < C_m = C_{max(\varrho)} = mp$, we prove $1//\left(\sum C_{\varrho(j)}, \sum U_{\varrho(j)}, R_{L(\varrho)}\right) = 1//\left(\sum C_{\varrho(j)}, m, mp - d_{max(\varrho)}\right)$. So, we obtain: $1//\sum C_{\varrho(j)} + \sum U_{\varrho(j)} + R_{L(\varrho)} = 1//\, p\frac{m(m+1)}{2} + m + mp - d_{max(\varrho)}$.

2) If $C_m \leq d_{min(\varrho)}$, we prove $1//\left(\sum C_{\varrho(j)}, \sum U_{\varrho(j)}, R_{L(\varrho)}\right) = 1//\left(\sum C_{\varrho(j)}, R_{L(\varrho)}\right)$. So, we obtain: $1//\sum C_{\varrho(j)} + \sum U_{\varrho(j)} + R_{L(\varrho)} = 1//\sum C_{\varrho(j)} + R_{L(\varrho)} = p\frac{m(m+1)}{2} + mp - p$.

3) If $C_{\varrho(j)} = jp = d_{\varrho(j)}$, we prove $1//\left(\sum C_{\varrho(j)}, \sum U_{\varrho(j)}, R_{L(\varrho)}\right) = 1//\left(\sum C_{\varrho(j)}\right)$. So, we obtain: $1//\sum C_{\varrho(j)} + \sum U_{\varrho(j)} + R_{L(\varrho)} = 1//\sum C_{\varrho(j)} = p\frac{m(m+1)}{2}$.

Case (5.5): For problem CUR−TO, if SPT, EDD, and MOOR rules are identical, then we obtain an efficient solution.

1) If ϱ = SPT = EDD = MST = MOOR at the same time, then ∃ an efficient solution.
2) If p_j and d_j are all different and ϱ = SPT = EDD = MOOR, then ∃ a unique efficient solution.

Proof: (see case (3.5) of CUR−TC).

	Job_1	Job_2	Job_3	Job_4
p_j	3	11	12	6
d_j	16	14	29	25
$S_j = d_j - p_j$	13	3	17	19

6.Heuristic Methods for CUR−TTCMSP and CUR−TOMSP

When solving a scheduling problem, implicit counting techniques (BAB and CEM) are typically used to determine optimal solutions. Precise techniques cannot address large problems and require a very long time to find the best answer. When it comes to an NP-hard problem, the computational requirements are enormous for a large-scale problem. To avoid these drawbacks, we can resort to heuristics. Heuristic methods (HMs) are search processes that identify (near-optimal) solutions to optimization problems in a short period of time. It can also be defined as, A heuristic approach is a methodology that aims to identify a decent solution (i.e., one that is near ideal) at a reasonable computing cost. It cannot ensure optimality or feasibility, or even assess how close a potential solution is to optimal in many circumstances. First method: DR−CUR, based on DRs, is .proposed to solve the CUR−TC and CUR−TO DR−CUR is based on identifying the type of sequence with minimal p_j and s_j, which is compatible with DRs, and calculating the objective function. The DR−CUR - based method is summarized in the following steps:

Algorithm (1): DR− CUR Heuristic Method for CUR− TCMSP(CUR− TOMSP)

Step 1: Input: $m, p_j \; and \; d_j, j = 1,2, \dots, m.$

Step 2: To determine the dominant relationships (DRs) and the corresponding adjacency matrix$A$; $M = \{1,2, \dots, m\}$; compute $s_j = d_j - p_j, \forall j \in N, \mu = \varphi$, if $p_i \le p_j$ and $s_i \le s_j$, an efficient solution exists where job i precedes job j.

Step 3: Identify a sequence α_1 that maintains a non-increasing order of p_j without conflicting with the DR (matrix A); if multiple job orders α_1 exist based on d_j, then $\mu = \mu \cup \{\alpha_1\}$.

Step 4: Determine a sequenceα_2 that follows a non-increasing order of (arranged in non-increasing order of) s_j and does not conflict with the DR (that aligns with the DR) (matrix A); if multiple jobs disrupt links, arbitrarily arrange them (In cases where multiple jobs create link disruptions, assign an arbitrary order) α_2 based on p_j, then $\mu = \mu \cup \{\alpha_2\}$.

Step 5: Extract the dominant sequence μ' from μ.

Step 6: Calculate (Compute) $F_{CUR-TC}(\mu')$, and identify(obtain) $F_{CUR-To(i)} = F_{CUR-To}(\mu'(i)), f = min(F_{CUR-To(i)}, k = i)$.

Step 7: Output: Effective solution set μ', with the optimal solution being along f with the sequence set $\mu'(k)$.

Step 8: End.

Example (1): For the CUR−TC−TCMSP, and CUR−TO−TOMSP, assume we possess the following data for = 4:

Using the following rule [If $p_i \le p_j$ and $s_i \le s_j$, then task i is executed before task j.], we obtain the DRs shown in Figure 1.

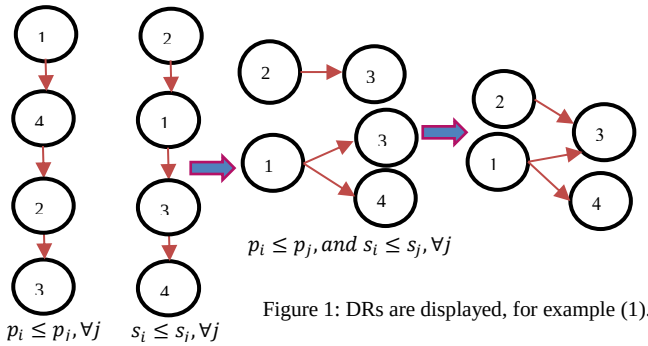

Figure 1: DRs are displayed, for example (1).

$1 \to 3, 1 \to 4$, and $2 \to 3$ are the three visible sequences. Some (or all) of the five possible sequences are controlled by the DRs described earlier in Table 1. Here is the adjacency matrix A:

$$A = \begin{bmatrix} 0 & a_{12} & 1 & 1 \\ a_{21} & 0 & 1 & a_{24} \\ 0 & 0 & 0 & a_{34} \\ 0 & a_{42} & a_{43} & 0 \end{bmatrix},$$

such that, if $i \to j$ then $a_{ij} = 1$, and $j \to i$ then $a_{ji} = 1$. The lists of possible effective sequences in example (1) subject to DR are shown in Table (1), and Table (1) shows the lists of effective sequences in example (1) subject to DR.

Table (1): lists the possible efficient sequences in Example (1) subject to DR.

Sequence	$\sum C_j$	$\sum U_j$	R_L	CUR−TC	d	CUR−TO
3,2,4,1	64	2	22	(64,2,22)	67.7052	88
2,1,4,3	77	1	8	(77,1,8)	77.4209	86
3,4,2,1	69	1	16	(69,1,16)	70.8378	86
1,2,3,4	75	1	20	(75,1,20)	77.6273	96
2,1,3,4	83	1	10	(83,1,10)	83.6062	94

Table (2): lists the efficient sequences in Example (1) subject to DR.

Sequence	$\sum C_j$	$\sum U_j$	R_L	CUR−TC	d	CUR−TO
3,2,4,1, (SPT)	64	2	22	(64,2,22)	67.7052	88
3,4,2,1	69	1	16	(69,1,16)	70.8378	86
2,1,3,4, (MST)	83	1	10	(83,1,10)	83.6062	94

Second method: The MS−CUR method is based on the following steps: First, we use the MST rule to determine the objective function. Second, we put the first job in order in the MST rule, then we arrange the remaining jobs according to the SPT rule, then we calculate the objective function. Subsequently, the second job is prioritized for scheduling by adhering to the Minimum Slack Time (MST) rule. Following this, the remaining jobs are sequentially arranged based on the Shortest Processing Time (SPT) rule. After the scheduling is established, the objective function is evaluated to assess performance outcomes. We continue in this manner until we reach a set of efficient solutions.

Algorithm (2): MS− CUR Heuristic Method for CUR− TCMSP(CUR− TOMSP)

Step 1: Input: $m, p_j \; and \; d_j, j = 1,2, \dots, m.$

Step 2: For each job j, calculate its slack time: $s_j = d_j - p_j \; , \forall \; j$, apply the MST rule (Sort the jobs in non-decreasing order of slack times).

Step 3: Create candidate sequences

For each position $k = 1,2, \dots, n$

- Choose the first job = the k^{th} job in MST order.
- Take the remaining jobs, and sort them by the SPT (non-descending order of processing time) rule.
- Construct the filter sequence = [first job, remaining jobs].

Step 4: calculate the objective function F_{CUR-TC} , and F_{CUR-TO} for each sequence.

Step 5: Evaluate the candidate sequence

Step 6: Final output after checking all n possible first jobs: output the set of efficient solutions (optimal solution).

Step 8: End**.**

Example (2): For the CUR−TC−TCMSP, and CUR−TO−TOMSP, assume we possess the following data for = 4:

	Job_1	Job_2	Job_3	Job_4
p_j	10	3	10	6
d_j	20	20	25	22
$S_{j=}d_j - p_j$	10	17	15	16

Applying the MS−CUR method results in the following:

Step (1): The MST sequence (1,3,4,2) is the first candidate sequence with objective function $\left(\sum C_j \, , \sum U_j \, , R_L\right) = (85,19,2)$.

Step (2): Place the first job in order in the MST rule, then arrange the remaining jobs according to the SPT rule; we get the second filter sequence (1,2,4,3) with objective function $\left(\sum C_j \, , \sum U_j \, , R_L\right) = (71,14,1)$.

Step (3): Place the second job in order in the MST rule, then arrange the remaining jobs according to the SPT rule; we get the third filter sequence (3,2,4,1) with objective function $\left(\sum C_j \, , \sum U_j \, , R_L\right) = (71,24,1)$.

Step (4): Place the third job in order in the MST rule, then arrange the remaining jobs according to the SPT rule; we get the fourth filter sequence (4,2,1,3) with objective function $\left(\sum C_j \, , \sum U_j \, , R_L\right) = (63,20,1)$.

Step (5): Place the fourth job in order in the MST rule, then arrange the remaining jobs according to the SPT rule; we get the fifth filter sequence (2,4,1,3) with objective function $\left(\sum C_j \, , \sum U_j \, , R_L\right) = (60,21,1)$.

Step (5): Filter the solution set to get a set of efficient solutions to the problems.

Table (9) shows the lists of effective sequences in example (8).

Table (3): lists the efficient sequences in Example (2).

Sequence	$(\sum C_j \, , \sum U_j \, , R_L)$	d	$\sum C_j + \sum U_j + R_L$
(1,2,4,3)	(71,14,1)	72.3740	86
(4,2,1,3)	(63,20,1)	66.1059	84
(2,4,1,3)	(60,21,1)	63.5767	82

7. RESULTS AND DISCUSSION

In this section, the findings we have reached in the previous sections are formulated as follows:

An efficient sequence that satisfies the SPT rule exists for problem $1//\left(\sum C_j \, , \sum U_j \, , R_L\right)$.

- The OPS for problem $1//\sum C_j + \sum U_j + R_L$ if and only if it is one of the EFS to problem $1//\left(\sum C_j \, , \sum U_j \, , R_L\right)$.
- If the processing time for all jobs is uniform and the due dates are also the same, there exists a unique efficient solution characterized by n! sequences that maintain a constant objective function.
- If the due date of all jobs is identical, then the ϱ = SPT rule implies an EFS(OPS) solution for the problems CUR−TC (CUR−TO).
- If the processing time of all jobs is identical, then the ϱ = EDD rule implies an EFS(OPS) solution for the problems CUR−TC(CUR−TO).
- If the rules for SPT, EDD, and MOOR are identical, we can derive the EFS(OPS) solution to the CUR TC (CUR TO) problems.

In conclusion, this study presents two heuristics designed to address research problems, specifically targeting the rapid identification of (near-optimal) solutions to optimization challenges within a constrained time frame. We have reached the following conclusions through mathematical experiments: We observe that the MS− CUR heuristic method gives better results than the DR− CUR heuristic method for the CUR− TCMSP ; see

table (4) for different n. Table (5) shows that although the results of the two proposed approaches are identical, MS− CUR performs better at CPU time for n different durations. Furthermore, both approaches were able to solve all problems when $n \leq 1000$, but failed when $n > 1000$.

Note: In each example, the values of p_j and d_j are produced randomly based on the uniform distribution s.t. $p_j \in [1,10]$ and $d_j \in [1,70]$, according to the condition $p_j \leq d_j$, when $j = 1{:}n$.

$\sum U_j + R_L$. Also, the submitted work demonstrates that the OPS for problem (CUR−TO) is if and only if one of the EFS for the problem (CUR−TC). Finally, we propose two heuristics for solving search problems, which are fast ways to find (near-optimal) answers to optimization problems.

Table 4: compares the results of using MS-CUR and DR-CUR to find the optimal solution for different values of *n*.

m	MS− CUR			DR− CUR		
	Av (F_{CUR-TC})	AT/S	ANS	Av (F_{CUR-TC})	AT/S	ANS
4	(55.5, 2.9,14.2)	R	3.0	(58.9, 3.1,14.9)	R	2.0
5	(73.6, 5.0,20.1)	R	4.4	(76.6, 4.7,21.2)	R	2.8
6	(85.4, 5.6,20.7)	R	4.8	(92.3, 6.5,23.1)	R	2.2
7	(144.7, 5.3,32.9)	R	6.0	(154.5, 5.8,32.6)	R	3.0
8	(174.5, 6.2,41.5)	R	6.4	(189.9, 6.6,41.0)	R	3.4
9	(203.8, 7.5,43.8)	R	7.0	(223.9, 9.1,38.8)	R	3.4
10	(256.9, 8.3,46.0)	R	5.6	(280.3, 8.4,44.1)	R	3.0
40	(3071.3, 33.0,183.7)	R	12.4	(3568.4, 34.3,167.5)	R	4.4
70	(10183.6, 44.4,362.9)	R	12.4	(11429.6, 46.5,342.0)	R	3.8
100	(20553.4, 74.4,520.0)	R	14.2	(21929.4, 66.7,494.4)	R	3.6
400	(327276.8, 162.0,2173.3)	1.9	14.0	(365665.4,143.1,2128.5)	2.4	2.8
700	(1021727.1, 413.5,3851.6)	5.0	13.8	(1105138.4,414.4,3788.8)	13.2	2.2
1000	(2040377.5, 225.2,5479.1)	13.4	13.0	(2136874.9,228.6,5401.4)	34.0	2.0

Table 5: Comparison between MS− CUR, DR− CUR for the CUR−TO problem, for different n.

m	MS− CUR			DR− CUR		
	Av (F_{CUR-TO})	AT/S	ANS	Av (F_{CUR-TO})	AT/S	ANS
4	72.6	R	3.0	72.6	R	2.0
5	98.7	R	4.4	98.7	R	2.8
6	111.7	R	4.8	111.7	R	2.2
7	182.9	R	6.0	182.9	R	3.0
8	222.2	R	6.4	222.2	R	3.4
9	255.1	R	7.0	255.1	R	3.4
10	311.4	R	5.6	311.4	R	3.0
40	3288	R	12.4	3288	R	4.4
70	10590.9	R	12.4	10590.9	R	3.8
100	21147.8	R	14.2	21147.8	R	3.6
400	329612.1	1.9	14.0	329612.1	2.4	2.8
700	1025992.2	5.0	13.8	1025992.2	13.2	2.2
1000	2046081.8	13.4	13.0	2046081.8	34.0	2.0

8. CONCLUSIONS

In this work, it has been proven that the specified rules provide efficient (optimal) solutions to the difficulties (CUR−TC and CUR−TO), and they are solved directly without the need for mathematical programming techniques, BAB, or CEM methodology, after a mathematical model is constructed to deal with the research problems $1//(\sum C_j, \sum U_j, R_L)$, $1//\sum C_j +$

ACKNOWLEDGMENTS

The author would like to thank the reviewers of this work for their helpful comments and suggestions that contributed to the improvement of the work.

REFERENCES

Ezugwu, A. E. S. (2024). Metaheuristic Optimization for Sustainable Unrelated Parallel Machine Scheduling: A Concise Overview With a Proof-of-Concept Study. *IEEE Access*, *12*(January), 3386–3416. https://doi.org/10.1109/ACCESS.2023.3347047

Hoogeveen, J. A. (1996). Single-Machine Scheduling to Minimize a Function of Two or Three Maximum Cost Criteria. *Journal of Algorithms*, *21*(2), 415–433. https://doi.org/10.1006/jagm.1996.0051

Khraibet, T. J., & Ghafil, W. K. (2021). Using hybrid GA-PSO algorithm to solve problem in machine scheduling. *Journal of Discrete Mathematical Sciences and Cryptography*, *24*(7), 2027–2035. https://doi.org/10.1080/09720529.2021.1958998

Khraibet, T. J., Kalaf, B. A., & Mansoor, W. (2025). A new metaheuristic algorithm for solving multi-objective single-machine scheduling problems. *Journal of Intelligent Systems*, *34*(1). https://doi.org/10.1515/jisys-2024-0373

Liao, C. J., & Huang, R. H. (1991). An algorithm for minimizing the range of lateness on a single machine. *Journal of the Operational Research Society*, *42*(2), 183–186. https://doi.org/10.1057/jors.1991.32

Nagham M. Neamah and Bayda A. Kalaf. (2023). Solving the multi-criteria: total completion time, total late work, and maximum earliness problem. *Periodicals of Engineering and Natural Sciences*, *11*(3), 46–57. https://doi.org/10.21533/pen.v11i3.3559.g1288

Nagham M. Neamah and Bayda A. Kalaf. (2024a). A Hybrid Approach for Efficiently Solving Multi-Criteria Scheduling Problems on a Single Machine. *Iraqi Journal of Science*, *65*(12), 7117–7129. https://doi.org/10.24996/ijs.2024.65.12.26

Nagham M. Neamah and Bayda A. Kalaf. (2024b). Solving the Multi-Criteria Problem: Total Completion Time, Total Late Work, Total Earliness Time, Maximum Earliness, and Maximum Tardiness. *Iraqi Journal of Science*, *65*(5), 2724–2735. https://doi.org/10.21533/pen.v11i3.3559.g1288

Nagham M. Neamah, & Bayda A. Kalaf. (2024). Solving tri-criteria: total completion time, total late work, and maximum earliness by using exact, and heuristic methods on single machine scheduling problem. *Iraqi Journal for Computer Science and Mathematics*, *5*(3), 14–25. https://doi.org/10.52866/ijcsm.2024.05.03.002

Neufeld, J. S., Schulz, S., & Buscher, U. (2023). A systematic review of multi-objective hybrid flow shop scheduling. *European Journal of Operational Research*, *309*(1), 1–23. https://doi.org/10.1016/j.ejor.2022.08.009

Tapan S., Farhad M. E., P. D. (1988). A Branch-and-Bound Approach to the Bicriterion Scheduling Problem Involving Total Flowtime and Range of Lateness. *Management Science*, *34*(2), 254–260.

Pure Sciences International Journal of kerbala

Year:2026 Volume : 3 Issue : 9 ISSN: 6188-2789 Print 3005 -2394 Online

2026,Volume 3 , Issue 9 , PSIJK (63-68)

Pure Sciences International Journal of Kerbala

Enhancing Cancer Diagnosis through Machine Learning and Swarm Intelligence Techniques

Maha Sabri Altememe [a*]

a College of Computer Science and Information Technology, University of Kerbala, Iraq

P A P E R I N F O

Received: 12.09.2025
Accepted: 15.12.2025
Published: 31.03.2026

***Keywords*:**
classification, breast cancer, medical images, ABC algorithm

A b s t r a c t

Machine learning has achieved wide success in detecting and identifying cancer diseases, especially those based on medical images. To increase the performance of models, machine learning techniques are combined with other techniques in the processing stage. In this research, the ABC algorithm was used in the feature identification process to help the algorithm choose the optimal solution more accurately.The medical images used are CT images of breast cancer collected in the form of a standard dataset of 570 known as WDBC dataset. The proposed model achieved classification accuracy 94.74%.

DOI: 10.53851/psijk.v3.i9.63-68

1. INTRODUCTION

Today, artificial intelligence has become widely important in many applications through the use of its multiple branches. Among these branches are machine learning techniques that are used to classify data and achieve high performance in implementation. The implementation of machine learning techniques requires the use of data for the purpose of training the model and then predicting the results and making decisions on new data (Zhang et al., 2020). However, the effectiveness of the models depends on a number of determinants, including the percentage of data, its quality, the type of algorithm that was applied and its suitability for this data, in addition to the method of extracting features from this data. Therefore, to increase the efficiency of the model, algorithms are used that help extract important features. One of these algorithms is the artificial bee colony algorithm, which works to select the ideal features and can be applied to medical images, especially in medical image data for cancer. It is considered one of the major determinants due to the differences in cancer diseases, so it needs high-quality techniques to infer features(Tharwat et al., 2017). In this research, a model is designed that combines machine learning techniques and ABC algorithm to select optimal features. Contributions to this study: Artificial Bee Colony algorithm-based feature selection for breast cancer detection. In order to improve patient care and diagnosis accuracy in the field of oncology, the project intends to create an efficient .

1. 1. Artificial Bee Colony algorithm

Karaboga presented the Artificial Bee Colony (ABC) algorithm in 2005 (Karaboga, 2005) as a swarm-based technique to solve numerical problems (Rao et al., 2020) This algorithm's concept is derived from the clever ways that colonies of honey bees hunt for food. The work crew is divided into three primary groups. The first group is known as the scout bees, and their primary duty is to randomly hunt for food. The job of the second team, known as the worker bees, is to look for food sources around the ones that have already been found. The job of the third team, known as the observer bees, is to keep an eye on the worker bees and assess the food's worth and quality in order to choose the best (Tharwat et al., 2017). In the ABC theory, the search process extracts the features present in the data in general, which represents finding specific solutions to the problem, and then the optimization stage is chosen by finding the best types of features, and this process is repeated repeatedly until the best features are obtained that help us in the classification stages. To clarify the work of the algorithm that is used to find the optimal solution, as mentioned previously, it consists of three groups: worker bees, spectator bees, and scout bees. The following code illustrates the steps of the ABC algorithm. Pseudo-code of the ABC algorithm (Rao et al., 2020) (Shahini Shamsabadi & B. S., 2009).

1. 2. Machin learning algorithms

Machine learning algorithms are mathematical techniques that help understand patterns, make decisions based on data, and predict results without the need for continuous programming. In the field of artificial intelligence, there are a number of learnable algorithms, including machine learning and deep learning. In these techniques, the model can be trained on a portion of the data and is called the learning phase. Based on this phase, the results are extracted and decisions are made based on the experience gained by the model without human intervention using these algorithms. Machine learning algorithms are divided into two groups, the first is called supervised and the other is unsupervised. To implement these algorithms, a large amount of data is needed (Shahini Shamsabadi & B. S., 2009) (Vetteth & K. W., 2003).

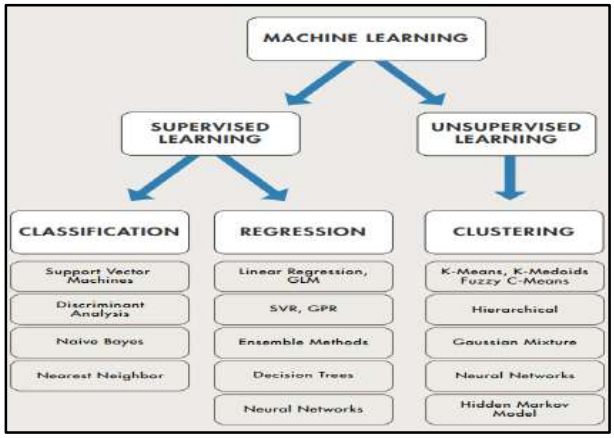

Figure 1. Types Of Machin Learning(Lent & M. L., 2006).

1.2.1 Logistic Regression

A statistical technique called logistic regression is employed to examine the correlation between a set of independent variables and a binary dependent variable.

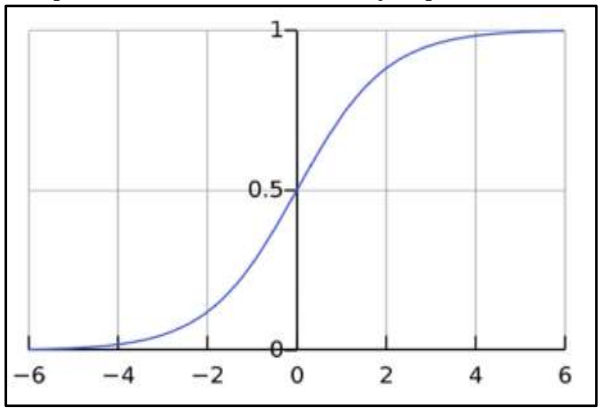

Figure 2. displays the regression function(Karaboga & Ozturk, 2011).

The goal of using logistic regression is to ascertain the odds, or adjusted odds, of a specific event taking place in relation to the independent variables. In order to transform the regression results into a range between 0 and 1, which can be used to produce probability estimates, the logistic function utilized in logistic regression is crucial. A useful tool for data analysis and forecasting decisions is logistic regression. It can be useful in determining the variables that affect an event's likelihood of occurring and in calculating the event's probability based on the available independent variables (Fallah-Mehdipour et al., 2018).

1.2.2 Decision Tree

A decision tree is a binary tree where each node is assigned a letter and each edge represents a possible value for the letter. A path label is produced that leads to each leaf of the tree, and the result is either 0 or 1. The number of nodes in the decision tree determines its size.

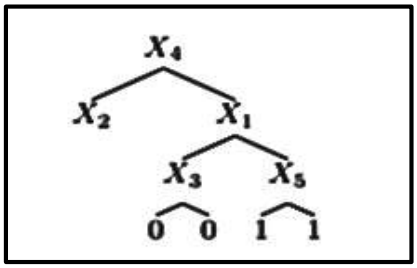

Figure 3: shows an example of a decision tree (Karaboga & Ozturk, 2011).

1.2.3 Random Forest

As the name implies, it is an improvement on decision trees known as the random forest and is made up of numerous independent decision trees that collaborate to produce predictions that are more reliable and accurate. The highest voting result is derived from this group's prediction outcomes, which is better than the outcome of employing the best model alone. In Figure 4 the algorithm is shown (Huang & M. M., 2007).

Figure 4. Random Forest (Harini & Uma Maheswari, 2023).

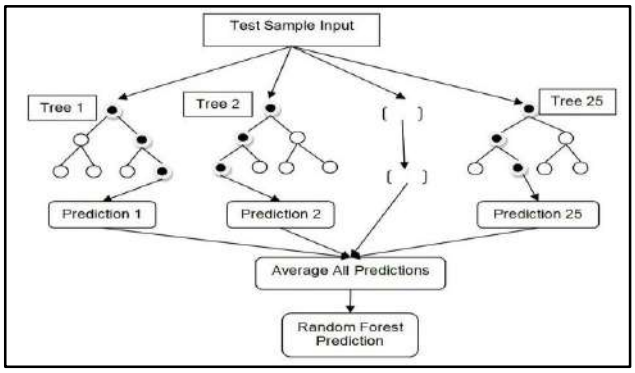

2. RELATED WORKS

Over the past ten years, artificial intelligence has become widely used for the identification of different tumors. Consequently, it is vital to look for extremely effective

techniques. I'll go over a few of the accomplishments from the previous years, which include the following:

In (Tharwat et al., 2017) this work presents a hybrid technique that selects features using ABC algorithm and classifies them using SVM. The contributions of this work are through the importance of removing irrelevant data features that affect classification performance by applying the SVM algorithm. The established method is typically employed in the diagnosis of diabetes and liver illnesses, which are prevalent and lower quality of life. The UCI database's hepatitis, liver disease, and diabetes datasets were utilized to diagnose these conditions; the suggested method achieved classification accuracy of 94.92%, 74.81%, and 79.29%, in that order.

In (Walus & T. D., 2004) This paper proposes a Deep CNN system, which outperforms the Vision Transformer model and other transfer learning models in terms of accuracy. In this work, the model demonstrated high performance in breast cancer detection and classification by combining the advantages of MobileNet and Xception models. The proposed model has a remarkable accuracy of 87.82% according to our test results.

In (Khurasia, 2006) this paper, used on Self-Care Activities Dataset based on ICF-CY (SCADI) with disabilities containing 206 features was used. Therefore, the ABC algorithm was applied to select the features for classification purpose. Only 7 features were selected by the algorithm and an accuracy rate of 88.5714% and a scale value of 0.871 were obtained, while the percentage was lower, 84.2857%, was obtained by applying Gain Ratio and Chi-Square.

3.ROPOSED METHODOLOGY

In this research, the ABC algorithm was applied to features selection and then we applied three different classification models for breast cancer diagnosis, including Random Forest (RF), Decision Tree (DT) and Logistic Regression (LR). These process stages were applied to breast cancer data by using cross-sectional images and Figure 6 shows the model's working stages.

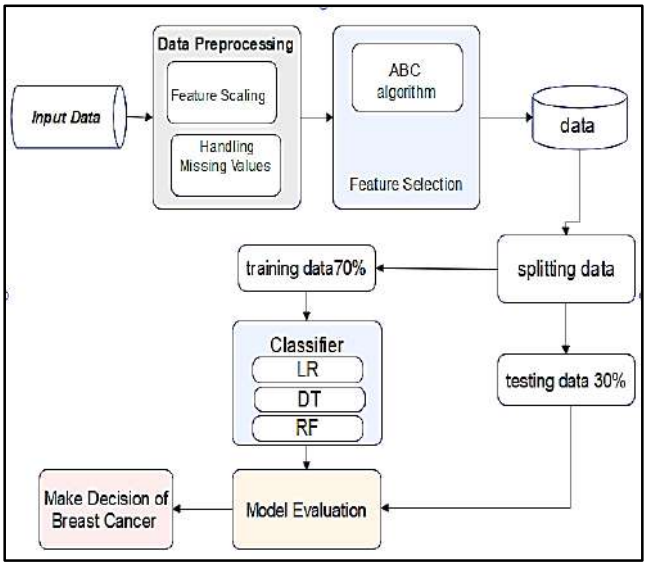

Figure 5. Proposed Methodology Diagram

3.1. Database

The Breast Cancer Wisconsin (Diagnostic) Data Set is a popular dataset for big data and machine learning applications. When dealing with issues related to the categorization of diagnosis for breast cancer, it is really helpful. It possesses traits that can be used to identify malignant or benign masses. These properties are calculated using digital photographs. There are 570 cancer-related photos in the dataset. In table 1. Explain the characteristics of dataset and Figure 6 shows a sample of the data.

Table 1. Properties of the Dataset

Inf	No.
Total number of situations	570
Attributes in data	30
Classification	2(Malignat,Benign)

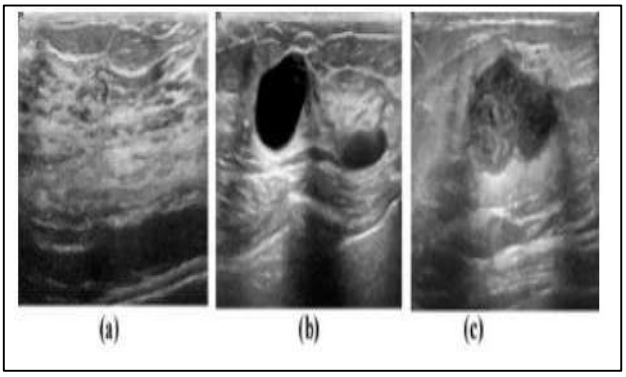

Figure 6.Sample Test

3.2 Data preprocessing

Dataset analysis is the process of looking through, cleaning, transforming, and modeling data to make sense of it, uncover useful information, and help make decisions. The purpose of the data cleaning process is to remove any anomalies, including missing or distorted information, from the data that require attention.

3.3 Feature Selection

This process, which is the feature selection process, is used to obtain the most relevant features in the dataset, which helps improve the performance of machine learning algorithms. The bee algorithm was applied because it is useful and achieves good results with high-dimensional data because it can identify complex relationships between features and is also flexible with different machine learning algorithms. The program looks for the best answer using a colony of bees. Every bee has a fitness value, which indicates the extent to which the features it represents improve the machine learning model's accuracy. Higher fitness bees are more proximate to the ideal outcome. The figure 7 shows the results of feature selection and the figure 8 shows the cross-sectional image after feature selection. According to the data used, a number of features were relied upon, including the following in table 2. In figure 7 shows Illustrative images after extracting features.

Table 2. Properties of the features for Dataset

No	Features	Description
1.	Radius:	Mean of distances from center to points on the perimeter.
2.	Texture:	Standard deviation of gray-scale values.
3.	Perimeter:	Perimeter of the cell nucleus.
4.	Area:	Area of the cell nucleus.
5.	Smoothness:	Variation in radius lengths.
6.	Compactness:	Perimeter^2/Area - 1.0.
7.	Concavity:	Severity of concave portions of the contour.
8.	Concave Points:	Number of concave portions of the contour.
9.	Symmetry:	Symmetry of cell nuclei.

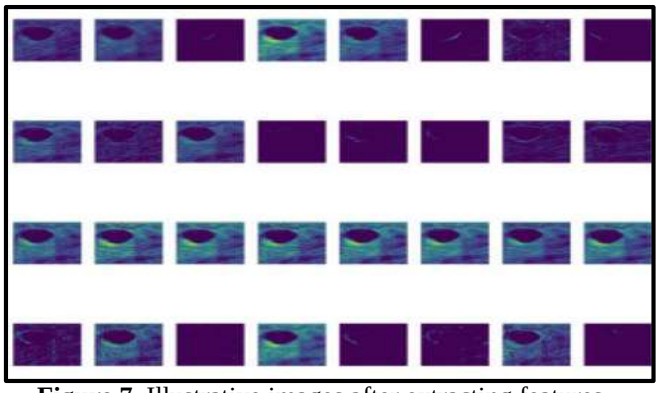

Figure 7. Illustrative images after extracting features

3.4 Implementation Machin learning

The algorithmic performance in terms of accuracy, precision, recall, and F1 score is displayed in the table. Among the algorithms tested, the RF Classifier yielded the lowest accuracy rate. The decision tree approach also produced the best accuracy rate. Additionally, the recall, precision, and F1 scores for each approach are included in this table. When it came to all confusion matrices and other scores, the decision tree strategy performed admirably overall. In table 3 shows the outcomes for all algorithms.

TABLE 3. Outcomes For Implementation

ML Algorithms	**Dataset**	**Processing**	Result of Model
			Accuracy
LR	Collection Dataset	Training	94.95%
		Testing	92.98%
RF	Collection Dataset	Training	1.00%
		Testing	94.74%
DT	Collection Dataset	Training	52.98%
		Testing	61.40%

- Logistic Regression: For both the training and test datasets, the accuracy score is calculated. This shows how effectively the model predicts the categories of the training set of data. With a score of around 94.95%, the model has classified 94.95% of the training dataset's cases correctly. This gauges how well the model adapts to fresh, untested data. A score of roughly 92.98% indicates that roughly 92.98% of the test dataset's cases were properly classified by the model.
- Decision Tree: This algorithm was This algorithm was used to process the ready-to-classify data, which was obtained from images of infected people. We obtained somewhat acceptable results, as the accuracy rate during training reached up to 52% and 61% testing data.
- Random Forest: While implementing the algorithm on the same data that was mentioned previously, it achieved good results, as the accuracy of 1% was achieved during the training phase, while the accuracy rate during the testing phase was 94%. With these results, the RF algorithm achieved the highest results that can be relied upon in discovering and classifying data.

1. CONCLUSION

Breast cancer has become common recently and it causes death for women, so it has become necessary to detect this disease early with wide importance. This helps to reduce the mortality rate because early detection helps in speeding up the treatment of this disease. Early breast cancer tumor detection has grown more precise and effective in recent times thanks to the development of sophisticated machine-learning classifiers. In order to diagnose breast cancer, this work combines feature selection and classifiers. To test the classification accuracy of three different methods, we ran them on the WDBC dataset. With an average accuracy of 94.00%, our study's results demonstrate that the RF model was the most successful. The topic of machine learning for breast cancer diagnosis has a number of opportunities for future research and development. To increase the precision and dependability of breast cancer detection, integrating several machine-learning algorithms is one possible field of study. To help find the most pertinent features for breast cancer diagnosis, more research into feature selection techniques may be conducted. This could ultimately result in more precise and effective diagnoses.

References

Altememe, M. S., & El Abbadi, N. K. (2022). Gesture interpreting of alphabet Arabic sign language based on machine learning algorithms. Iraqi International Conference on Communication & Information Technologies (IICCIT-2022), University of Basrah.

Altememe, M. S., & El Abbadi, N. K. (2023). A hybrid model between one-dimensional convolutional neural network and machine learning algorithms for Arabic sign language word recognition. 4th International Scientific Conference of AlKafeel University (ISCKU 2022).

Fallah-Mehdipour, E., Bozorg-Haddad, O., & Mariño, M. (2018). Prediction and simulation of monthly groundwater levels by genetic programming. Journal of Hydro-environment Research, 7, 253–260. https://doi.org/10.1016/j.jher.2013.03.005

Harini, K., & Uma Maheswari, S. (2023). A novel static and dynamic hand gesture recognition using self-organizing map with deep convolutional neural network. Journal for Control, Measurement, Electronics, Computing and Communications, 64(4).

Huang, J., & others. (2007). Design of sequential circuits by quantum-dot cellular automata. Microelectronics Journal, 38, 525–537.

Islam, M. R., Rahman, M. M., Ali, M. S., Nafi, A. A. N., Alam, M. S., Godder, T. K., Miah, M. S., & Islam, M. K. (2024). Enhancing breast cancer segmentation and classification using ensemble deep convolutional neural network and U-net. Machine Learning with Applications. https://doi.org/10.1016/j.mlwa.2024.100555

Karaboga, D., & Ozturk, C. (2011). A novel clustering approach: Artificial bee colony (ABC) algorithm. Applied Soft Computing, 11(1), 652–657.

Keleş, M. K., & Kılıç, Ü. (2018). Artificial bee colony algorithm for feature selection on SCADI dataset. 3rd International Conference on Computer Science and Engineering (UBMK), Sarajevo. https://doi.org/10.1109/UBMK.2018.8566287

Khurasia, P. G. (2006). Quantum cellular automata.

Kim, K., & others. (2006). Quantum-dot cellular automata design guideline. IEICE Transactions on Fundamentals, 6, 1607–1614.

Lent, C. S., & others. (2006). Bennett clocking of quantum-dot cellular automata. Nanotechnology, 17, 4240–4251.

Liu, J., et al. (2019). River level estimation using camera images and machine learning. Water Resources Research, 55(5), 4321–4335.

Mustafa, W. A., & Abdul Kader, M. M. (2017). A review of histogram equalization techniques in image enhancement application. 1st International Conference on Green and Sustainable Computing (ICoGeS). https://doi.org/10.1088/1742-6596/1019/1/012026

Niemir, M. (2004). Designing digital systems in quantum cellular automata (Master's thesis). University of Notre Dame.

Rao, S. S., et al. (2020). Machine learning approaches for water level prediction in rivers: A review. IEEE Journal of Selected Topics in Applied Earth Observations and

Remote Sensing, 13, 5325–5344.
Sara, H., & others. (2012). New robust QCA D flip-flop and memory structures. Microelectronics Journal, 43, 929–940.
Shahini Shamsabadi, A., & others. (2009). Applying inherent capabilities of quantum-dot cellular automata to design: D flip-flop case study. Journal of Systems Architecture, 55, 180–187.
Tharwat, A., Gaber, T., Ibrahim, A., & Hassanien, A. E. (2017). Linear discriminant analysis: A detailed tutorial. AI Communications, 30, 169–190.
Tougaw, P. D., & Lent, C. S. (1994). Logical devices implemented using quantum cellular automata. Journal of Applied Physics, 75, 1818–1824.
Uzer, M. S., & Yilmaz, N. (2013). Feature selection method based on artificial bee colony algorithm and support vector machines for medical datasets classification. The Scientific World Journal. https://doi.org/10.1155/2013/419187
Vankamamidi, V., & others. (2008). Two-dimensional schemes for clocking/timing of QCA circuits. IEEE Transactions on Computer-Aided Design of Integrated Circuits and Systems, 27, 34–44.
Vetteth, A., & others. (2003). RAM design using quantum-dot cellular automata. Nanotechnology Conference and Trade Show, 2, 160–163.
Walus, K., & others. (2004). QCA designer: A rapid design and simulation tool for quantum-dot cellular automata. IEEE Transactions on Nanotechnology, 3, 26–31.
Zhang, R., et al. (2004). A method of majority logic reduction for quantum cellular automata. IEEE Transactions on Nanotechnology, 3(4), 443–450.
Zhang, Y., et al. (2020). River level estimation from river-camera images using deep learning. IEEE Transactions on Geoscience and Remote Sensing, 58(5), 3421–3432.

Pure Sciences International Journal of kerbala

Year:2026 Volume : 3 Issue : 9 ISSN: 6188-2789 Print 3005 -2394 Online

2026,Volume 3 , Issue 9 , PSIJK (70-86)

Pure Sciences International Journal of Kerbala

A Review :Drug–Gene Interactions in Precision Cancer Therapy: Emerging Roles of Immunotherapy, Suicide Genes, and Molecular Editing Tools

Bassma Maytham Oleiwia [a*] , Maha Jassim Manshad [a] , Saly Naser Abbas [b], Nada Habeeb Obaid [a]

a Department of Chemistry, College of Education for Pure Sciences, University of Kerbala, Iraq
b Department of Biology, College of Education for Pure Sciences, University of Kerbala, Iraq

P A P E R I N F O

Received: 12 .10.2025
Accepted: 18.12.2025
Published: 31.03.2026

***Keywords*:**
gene therapy, , cancer gene therapy , biomedicine

A b s t r a c t

Cancer remains one of the major threats to human fitness, and although there are many treatments available to address this problem, conventional treatments including radiotherapy and chemotherapy have significant adverse effects and are by no means ideal. Gene therapy is a newly developed treatment modality that provides superior targeting with fewer adverse effects than conventional treatments. To change the expression of gene products, foreign genetic material is injected into the host tissue during gene therapy. Gene therapy provides the opportunity to influence the course of many diseases. Therefore, reliable and safe gene products and vector application coupled with advanced biotechnology will be crucial in the treatment of various diseases in the future. Gene therapy is a treatment strategy of opportunity that has been extensively studied recently. The therapeutic genes are implanted at the specified site. Cell or tissue specific to the majority of tumors these compounds have the ability to either induce cell death or inhibit the rate of cell proliferation. Of most types of cancer. Many viral and non-viral genes and vectors are being used in investigations because this treatment uses unique approaches that involve either silencing inactivated or unwanted genes or activating recovery genes. Activation of tumor suppressor genes is a crucial mechanism that helps control the growth of tumors and suppress them, and controls the function of oncogenes and inhibits their activation. Our explanation in this article covers gene therapy, methods of treating most tumors using genes, the use of approved genetic drugs to treat most malignant tumors, and the future of gene therapy for cancer. . Gene therapy no longer meets the criteria to completely replace conventional treatments. But with a deeper understanding of the process behind cancer treatment, one can choose the optimal course of action and target for future gene therapy, either alone or in combination with other therapies.

DOI: 10.53851/psijk.v3.i9. 70-86

1. INTRODUCTION

Globally, cancer remains one of the most serious public health challenges and continues to be a leading cause of mortality in the twenty-first century, despite recent advances in prevention and treatment. The American Cancer Society (ACS) estimated that approximately 600,000 cancer-related deaths would occur in the United States in 2022 (Siegel et al., 2022). In addition, approximately 58 million Americans today have a history of cancer and this is expected to reach a higher

*Corresponding Author Institutional Email:
maha.j@uokerbala.edu.iq (Maha Jassim Manshad)

number of over 22.1 million by 2030, which is mainly attributed to population increase and the aging process. (Miller et al., 2019). The use of conventional cancer treatment methods which involve chemotherapy, radiotherapy and surgery is associated with less than ideal results due to high mortality rates, high side effects on the body and long term problems like tumor metastasis and recurrence. These restrictions emphasize that there is a dire necessity of new and more specific therapeutic interventions..

Gene therapy has become one of the most promising advanced therapeutic methods over the last 30 years and is currently viewed as a significant supplementary method to the traditional cancer therapies. Gene therapy; a type of therapeutic intervention used in contrast to conventional therapy, includes the therapeutic transfer of exogenous or intact genes into host cells to selectively kill precancerous or malignant cells, sparing normal tissues. (Pan, Liu, & Shi, 2018). Interaction of two or more genetic mutations in a cell results in complex gene-gene interactions, which usually cause unanticipated phenotypic effects.. A negative or synthetic genetic interaction results where two mutations applied alone are non-lethal, but by combining with each other, the resulting mutation is lethal, and is used in the treatment of cancer to selectively kill tumor cells. On the contrary, positive genetic interactions are where mutations that happen simultaneously lead to a smaller phenotype than expected which is an indication of functional compensation between genes. The knowledge of such interactions is crucial to discovering the most important molecular targets and unmeasured hidden genetic processes of human diseases.

Gene therapy has shown therapeutic promise in a very wide range of diseases, such as viral disease, inherited diseases, and cancer. Many gene delivery mechanisms have been formulated such as non-viral and viral vectors. (Griesenbach, 2007; Carlin, 2011). Currently, gene therapy mainly is under investigation on the diseases that cannot be treated easily by conventional methods. This is possible by successful gene molecule delivery to the nucleus of host cells, which leads to its therapeutic expression in the form of somatic cell production of a given therapeutic protein that is able to correct or regulate genetic abnormalities. Consequently, the creation of effective communication among target cells and delivery systems is a vital factor towards effective gene transfer. (Gonçalves et al., 2017).

One of the biggest advances in the clinical translation of gene therapy was when the European Medicines Agency granted approval to the first gene therapy drug, Alipogene Tiparvovec (Glybera), in Western medicine. (Kaufman, Kohlhapp, & Zloza, 2015). The cornerstone findings to this historical breakthrough include the explanation of the DNA-double helix structure that formed the basis of the establishment of contemporary genetic-based treatment. Within the past 10 years, the latest molecular technologies have permitted the accurate editing of DNA and mRNA alteration by means of post-transcriptional effects.

Gene therapy works by administering certain genetic content that controls the expression of a gene or altering the biological characteristics in target tissues. Genetic therapy is a potent alternative to peptide-based therapies in the event of low bioavailability, instability, toxicity and high cost of production. (Bulaklak & Gersbach, 2020). This mode of therapy acts based on a few mechanisms, that is, replacing the bad genes, silencing of bad genes or transfection of therapeutic genes. With the help of specialized vectors, either viral or non-viral, genetic material, DNA or RNA, is delivered to target cells to produce the desired therapeutic effect.

Gene therapy is a relatively new treatment method due to its rapid acceptance as a feasible approach to treat various medical and health conditions, such as rheumatoid arthritis, since the early 1990s, diseases of cardiovascular, infectious, and various malignancies (Wirth, Parker, & Ylä-Herttuala, 2013; Ma et al., 2020; Sudhakar & Richardson, 2019; Deng et al., 2020; Neves et al., 2020; Sims et al., 2020). The genes that play a role in the initiation and progression of cancer are currently the subject of extensive research in both experimental and clinical studies, and the domain of cancer gene therapy is experiencing rapid growth. (Ma, Cui-Cui, et al., 2020).

Recent developments in gene therapy products emphasize the importance of safe delivery and long-lasting genetic stability by utilizing innovative systems like lipid nanoparticles, polymer-based carriers, CRISPR-Cas delivery platforms, and self-amplifying RNA vectors.These systems improve transfection efficiency, minimize toxicity, and enhance the intracellular stability of therapeutic genes, especially in treatments based on drug-gene interactions.

Together, These advancements pave the way for gene therapy as a highly promising approach for the future treatment of cancer and a wide range of other human diseases.

2.GENE THERAPY

The technology encompasses the incorporation of Putting outside DNA into cells, be it inside a living body or not Outside the body, used to help treat or find health issues Whatever the goal in lab work might be clinical gene therapy, the primary challenge persists in attaining effective cellular uptake of the therapeutic gene Yet ensuring controlled gene activity remains key for one or the other Spells that come and go. Or stick around longer than expected. (Iglesias-Lopez et al.,

2019 Inside cells, genetic fixes come through strands like DNA or RNA. These pieces step in where broken genes cause illness. Messenger RNA delivers instructions anew. Tiny siRNA blocks trouble messages quietly. Antisense bits redirect faulty signals one by one. Each molecule plays its part without fanfare.

Picking a nucleic acid depends on what job it needs to do inside the body. For swapping out broken genes, scientists lean toward DNA since it can carry working copies right into cells. When quick but brief protein creation is needed, messenger RNA steps in, turning on proteins without changing inherited code. On another path, siRNA along with antisense strands dial down gene activity, putting harmful signals like MYC on pause. To check if that quieting effect took hold, researchers turn to qRT-PCR, tracking how much message molecule vanishes after treatment - this number often tells the story. Such precision makes these molecules key players when studying tumor targets or how medicines shape genetic behavior. (Iglesias-Lopez et al., 2019) . Starting off differently - gene therapy medicines fall under a special group called advanced therapies, according to the European Medicines Agency. These treatments face strict review because of how complex they are biologically. That detail comes from Liang and Wang's work back in 2020Neuhaus, Schaudien, & Dehmel, 2023). These technologically sophisticated agents may carry therapeutic, preventive, or diagnostic genes and are widely employed in tissue regeneration, correction of metabolic deficiencies, restoration of physiological functions, and the inhibition of undesirable gene expression (Cesur-Ergün & Demir-Dora, 2023; Cesur, 2019; D'Aria et al., 2020). Gene therapy can be executed through several principal molecular strategies (Neuhaus, Schaudien, & Dehmel, 2023):

1. Replacement of mutated genes with functional counterparts,
2. Gene Action of aberrant, suppression
3. Inhibition of undesirable gene expression,
4. Compensation for missing genes, and
5. Targeted delivery of therapeutic genes to specific tissues.

Gene suppression and inactivation techniques—especially those utilizing antisense oligonucleotides and nuclear RNA-mediated silencing—have proven effective in blocking oncogene activity and curbing the growth of cancer cells. In suicide gene therapy, a specific gene is delivered into tumor cells to enable the conversion of a harmless prodrug into a toxic agent directly within the cancerous tissue. This approach, termed gene-directed enzyme prodrug therapy, improves the precision of treatment and reduces harmful side effects on healthy tissuesFully working versions of broken genes get delivered into cancer cells, different from other methods. Vectors carry these replacements carefully inside. Normal cell behavior starts returning once the fix takes hold. This approach fixes errors at their source instead of just managing symptoms.

Flying genes from one place to another needs special shuttles - these helpers go by the name of gene delivery systems, using either viruses or non-virus options. Even though virus-based and synthetic methods get the job done, more scientists now lean toward the man-made kind. Safety steps up a level without viral parts onboard. The body's alarm system tends to stay quiet when artificial carriers arrive. Factories also find it easier to crank out copies of these lab-built tools compared to growing actual viruses. (D'Aria et al., 2020). Gene transfer strategies are additionally categorized based on the type of target cells, which can be somatic or germ cells, as well as the method of delivery, which may be ex vivo or in vivo. (Chen et al., 2022). Gene therapy is fundamentally focused on modifying gene expression and the biological behavior of living cells for therapeutic aims. (Dora, 2021). Gene therapy has the potential to address both somatic and germ cells, the current clinical focus is solely on somatic cell therapy of gene, which is non-heritable and therefore regarded as ethically and legally acceptable (Goswami et al., 2019).

Traditional gene therapy approaches involve the genetic modification of autologous or allogeneic T cells, transplantation of hematopoietic stem cells (HPSCs), and the engineering of chimeric antigen receptor T cells (CAR-T) through ex vivo transduction, in addition to direct in vivo gene delivery into patient tissues. Still, once tools like zinc-finger nucleases showed up - along with TALENs and CRISPR - fixing broken genes got a whole lot more accurate. What shifted the game was aiming straight at broken DNA pieces. No more hoping - now fixes land exactly on target. With every leap forward, changes turned crisper, simpler, trustworthy. Where clumsy tries once failed, accuracy finally took hold (Motta et al., 2019).Fair accuracy marks where ZFNs land in DNA, although setting them up means long hours plus steep expenses. Hardly a quick fix, their complexity bogs progress in extra steps. Hitting targets more reliably, TALENs open wider paths forward but remain slow to assemble and costly just the same. Then comes CRISPR-Cas - precision climbs, design simplifies, cost drops, speed rises. Exact changes matter when fixing DNA in cancer care - CRISPR delivers just that, hitting only what needs correction. Watch a cell shift after silencing one stubborn gene; responses reveal how medicines might work better when guided precisely. (Motta et al., 2019).System of gene therapy comprises setup includes three main parts:

1. Active copy of a gene, designed to produce the protein needed
2. A small circular piece of DNA that includes a region controlling whether genes are turned on or off.
3. A tool moves the treatment package into the body's cells (Mali, 2013). One method carries ge netic material where it needs to go inside living tissu e (Mali, 2013).

A component of the gene therapy system consists of three main parts. One part delivers the genetic material, while another targets specific cells. The third element ensures stability once inside the body

A working copy of a gene, designed to produce the needed protein, A small DNA circle carrying a control segment for turning genes on or off, A tool moves the treatment package into the body's cells (Mali, 2013). One method carries genetic material where it needs to go inside living tissue (Mali, 2013). This approach shuttles a designed sequence across cell boundaries (Mali, 2013). The process involves guiding engineered DNA into target areas of an organism (Mali, 2013). Moving helpful genes relies on such transport setups (Mali, 2013). Modern gene therapy rests on these linked systems, built molecule by molecule. Their combined actions explain how treatments now reach cancer care with greater accuracy. Step by step, they shape the way therapies match individual patients. From one cell to another, function follows form in tailored medical approaches

2.1. Advantages of gene therapy

Advantages of gene therapy in cancer treatment involve various methods such as using plasmid Deoxyribonucleic acid with curative nucleotides, modulating gene expression, and utilizing RNA intrusion (Liu et al., 2019) Gene therapy offers benefits like high efficacy, specificity, low off-target toxicity, and multiplexed delivery of genes targeting cancer tumor genesis, recurrence, and drug resistance (Ni et al., 2022)The effectiveness of gene therapy in cancer treatment has been greatly enhanced by genomics editing techniques. Gene therapy has become a common practice in medicine. Its key features include gene addition, gene excision, and transgenes is. Unlike viral vectors, gene therapy is limited to facilitating the addition of genes. For instance, Cell therapy for adoption employs The process of gene delivery is employed to modify T cells, resulting in a targeted antitumor response. This approach aims to enhance the body's antitumor immune response through artificial means, leading to a sustained and potent antitumor effect. A remarkable advancement in the field of adoptive cell therapy, chimeric antigen receptor T-cell therapy has been devised to effectively combat a wide range of malignant hematological tumors and solid tumors. (D'Aloia et al., 2018). Suicide gene therapy, on the other hand, involves By introducing a suicide gene into targeted tissues, like tumors, it is possible to trigger cell death through the production of Distinct enzymes, toxins, or pro-apoptotic proteins. within cancer cells. (Zhao et al., 2021). This therapy can also increase the sensitivity of cancer cells to chemotherapy (Li et al., 2020) by utilizing a specific tumor promoter to regulate gene expression in cancer cells (Qiu et al., 2021).

However, despite the significant advantages of CRISPR/Cas9-based gene editing, major challenges remain, including unintended off-target DNA cleavage and substantial barriers to efficient delivery in solid tumors, which limit its full clinical translation (Guo et al., 2023).

2.2.Gene delivery technologies.

Ensuring the safe and effective delivery of genetic products has proven to be quite a challenge ever since the emergence of recombinant DNA methods. Gene delivery depends on vectors to transport the gene into specific tissues, ensuring proper delivery of a suitably sized genetic construct to achieve accurate expression. Different methods including viral vectors, non-viral vectors, and bacterial systems are employed for gene transfer. Recent reviews have shown that both viral and non-viral vectors remain central to gene therapy development, each with distinct advantages and trade-offs (Butt et al., 2022; Taghdiri et al., 2024).

.2.2.1Systems Utilizing Viral Gene Therapy

Viral vectors have emerged as a highly promising tool in the field of gene therapy technology. due to their significant potential and efficient gene transfer capabilities. They can be administered locally and/or systemically, The delivery of genes into human cells in a pathogenic manner is regarded as a valuable technique by scientists, as it allows for the substitution of accessories of the viral genome with the desired the rapeutic gene, resulting in increased efficiency(Raty et al., 2008)Despite the need to address various shortcomings before clinical use, viral gene therapy has progressed through recent trials and approvals for treating head and neck carcinoma, skin cancer, and Deficiency of lipoprotein lipase. Ongoing clinical development includes combinations of viral gene therapy such as AAV, lentivirus, and retrovirus. While viruses are the primary vectors under investigation, research has expanded to explore non-viral alternatives due to ongoing safety concerns(Liu & Kirn, 2008) (Kaufman et al., 2010) (Scott, 2015) (Shaw & Suzuki, 2019)

2.2.Systems Utilizing Non-Viral Gene Therapy

Non-viral vectors, such as liposomes or polymers, utilize a positive charge from cationic liposomes or polymers to bind to DNA, which carries negative charges on the phosphate group. Another method for creating DNA nanoparticles is through calcium phosphate coprecipitation (Hosseinkhani & Tabata, 2006) While co-precipitation of plasmid DNA with calcium phosphate is used for cell transfection, the efficiency is lacking. There is a necessity to enhance the materials used. Polycation technology relies on the interaction of cells through a simple and constant electrostatic force (Hosseinkhani et al., 2004) (Abedini et al., 2011) (Hosseinkhani et al., 2015) (Abdullah et al., 2010)(Abedini et al., 2010) (Shi et al., 2020)

2.2.3. Risks affiliated with viral vectors

The primary worries linked with viral vectors include the potential for ignition, insertional mutations, and off-target effects (Chattopadhyay & Sen, 2017) (Stolberg, 1999)The case of Jesse Gel singer's death in 1999 serves as a notable example of infection caused by an adenovirus overdose. Insertional mutagenesis poses a significant obstacle that needs to be addressed when employing gene therapies. Occasionally, vectors may align with undesired sections of the genome. To mitigate this issue, it is advisable to utilize a non-integrating vector (Alnasser, 2021)

3.Effectively Employing Gene Therapy Strategies In The Field Of Cancer Treatment

Cancer is a complex and diverse disease characterized by the uncontrolled growth and invasion of cells in the body. The appropriate treatment for cancer depends on various factors such as the specific type of cancer, its stage of progression, and the individual patient. There are several treatment options available, including chemotherapy, surgery, radiotherapy, hormonal therapy, and photodynamic therapy .Other treatment options to consider include High temperature, Immune therapy, stem cell planting, Directed treatment, and gene therapy. Gene therapy, in particular, stands out from conventional treatments as it has the potential to be applied with minimal side effectsA range of strategies for gene therapy in cancer comprise suicide gene therapy, tumour suppressor gene activation, and immunotherapy., and gene suppression. Furthermore, gene therapy can also be used to activate oncogenes and for antiangiogenic purposes. (Rajakumar et al., 2022)

3.1. Immunotherapy

To date, the primary focus of cancer gene therapy research has been on immunotherapy. This approach utilizes the patient's own immune system to identify and attack cancer cells (Riley et al., 2019)Cancer cells possess immunogenic properties and contain intracellular cancer antigens, making T-cell-mediated cellular immunity more crucial than B-cell-mediated hum oral immunity. However, a regular immune response is insufficient to completely eliminate cancer cells. The ability of cancer cells to evade the immune system is dependent on factors such as the secretion of immunosuppressive substances, antigen expression, and down-regulation. In gene immunotherapy, various immune molecules are employed to stimulate a potent antitumor immune response (Feins et al., 2019) For example, genes encoding various cytokines are introduced into cancer cells either ex vivo or in vivo. as a result, Cancer cells produce proteins from the transfected genes in the tumor microenvironment. These Alarm clocks of the immune system alter the tumor microenvironment, ultimately boosting the immune response to fight against cancer. (Alnasser, 2021)

3.2.Suicide gene therapy

Utilizing gene therapy is a revolutionary way to address genetic and acquired diseases that do not respond well to conventional treatments (Duarte et al., 2012)Suicide gene therapy involves introducing a specific gene, referred to as a "suicide" gene, into tumors to trigger the conversion of a prodrug into a potent and lethal substance(Ketola et al., 2004)

3.2.1Suicide gene therapy systems

Suicide gene therapy represents a targeted therapeutic strategy in which a specific gene is introduced into cancer cells to convert a non-toxic prodrug into a cytotoxic compound, thereby selectively inducing tumor cell death. The delivery of genes into human cells using One reason viral vectors stand out? They move genes effectively, work reliably inside cells, leave lasting effectsFaster than most, adenoviruses appear frequently - retroviruses tag along - not far behind, herpes simplex tags in - each slips through cell walls easily, pulled toward tumors as if guided. Though imperfect by design, their structure keeps them lingering near cancerous zones on intent. When precision counts, their ability to infect turns useful without trying. Finding their way inside cells comes naturally to these, which is why researchers keep coming back. Not merely active but driven, they track cancer spots much like a beacon guiding without pause.

A piece of the herpes virus works when combined with a specific drug, according to research. Since it targets only some cancer cells, the added gene produces an

enzyme activating ganciclovir. This initial step creates ganciclovir monophosphate thanks to a viral protein at work. Within the cell, regular enzymes keep altering it until reaching ganciclovir triphosphate. Resembling one piece used in DNA construction, this transformed compound gets woven into growing DNA chains. When the mimic joins replication, DNA creation stops. Because of this, rapidly dividing cancer cells break down on their own (Shi et al., 2016).

Outside virus-based tricks, some try shaking genes together with chalky stuff, linking them to rubbery bits, or tucking them inside oily shells - often quieter on the body's alarm system, gentler too. Still, getting every gene inside a cell remains a puzzle. For sharper results, teams reshape polymer skins, craft miniature carriers one piece at a time, adjust how fat pockets form - each change nudging genes toward smoother entry, tougher survival, quicker escape after arrival. With these shifts, synthetic helpers now move DNA with strength close to natural invaders, widening paths to fight tumors minus viral baggage. When heat from radiofrequency is applied, cancer cells respond differently to gene therapy with HSV-TK and GCV. Because of the warmth, drug entry improves as the cell surface changes shape. With temperature on its side, genetic treatment finds an easier path inside. Mice and rat studies recorded clear drops in tumor size under these conditions. Working side by side, rather than solo, the two approaches press further into abnormal tissue. Heat shapes how well treatment travels through tissue. Evidence shows gains come from motion, not molecules. Tests on living creatures show tighter control when fever leads the way. What matters most is order - warmth opens paths before medicine follows. Results hold promise, arriving quickly where they’re needed (Li et al., 2020).

3.2.2.Mesenchyme stem cells (MSCs) designed as vectors

Mesenchymal stem cells (MSCs) have emerged as promising tools in anti-tumor gene therapy because of their unique biological advantages, including tumor-homing ability and immune privilege, which enable them to migrate selectively toward tumor microenvironments (Shah, 2012; Ding et al., 2021). These characteristics make MSCs attractive candidates for delivering therapeutic genes particularly suicide genes directly to solid tumors while minimizing damage to surrounding healthy tissues. One approach tested a lot uses the CYP2B6TM-RED gene setup to turn cyclophosphamide into an active drug. This gene, when placed in stem cells near tumors, changes the medicine right where it's needed. Inside the tumor, those altered cells make powerful cancer-killing substances. Mice getting these modified stem cells directly into their tumors showed full shrinkage in one third of cases. Six months passed without signs of return in those successful instances. The results point toward real impact against cancer growth. A sharper immune reaction also appeared alongside the shrinking masses. Earlier experiments back up what was seen again recently. Findings from 2014 and another set in 2020 support the pattern.

Not built by accident, MSCs are adjusted using various ways to reach their target. While viruses show up a lot due to how well they enter cells, they bring dangers such as tumors and immune trouble - slowing down real-world treatment use. For this reason, research has shifted slowly toward non-virus methods, considered kinder to biology and more flexible when tuning MSC behavior (Amara et al., 2016).MSCs can be harvested from accessible tissues such as bone marrow and adipose tissue, making them practical for clinical translation. When engineered, MSCs produce tumoricidal byproducts that selectively kill cancer cells within the tumor microenvironment (Amara et al., 2014). Furthermore, the clinical evaluation of gene therapy vectors, such as Ad5-yCD/mutTK (SR39)-ADP combined with gemcitabine, demonstrated acceptable safety and tolerability in pancreatic cancer patients, reinforcing the feasibility of MSC-based gene delivery in cancer treatment (Engeland, 2022).Despite these promising outcomes, careful consideration must be given to the potential effects of activated prodrug metabolites on surrounding non-malignant tissues to ensure therapeutic precision and safety.

3. 3.Gene activation for tumor suppression.

A lone flaw in a gene copy rarely shuts down tumor suppressors - these keepers of order demand both versions harmed to lose function. Running strong, they halt unchecked expansion, sometimes halting cell progress or launching self-destruct sequences. Take Rb: it jumps in during G1, hitting pause. Damage found? Then p53 takes charge, enforcing strict rules. Certain ones, like CDK inhibitors, dampen growth cues at critical gates. Different types, including BRCA1 and BRCA2, help fix broken DNA strands accurately. Their combined work keeps mutations in check, reducing chances of cancer forming (Tamura et al., 2020).

Among these, the p53 gene is the most important and extensively studied tumor suppressor. It functions as a genomic gatekeeper by detecting DNA damage and activating DNA repair pathways or inducing apoptosis when damage is irreparable (Ibnat et al., 2019). Experimental studies have demonstrated that p53 gene transfection results in significant tumor growth inhibition and regression in animal models, confirming its therapeutic potential (Zhang et al., 2018).Now scientists are tuning how p53 shows up in cells, thanks to sharp new tools like CRISPR/Cas9 and TALENs.

Instead of a blunt approach, these methods fix broken p53 bits right where they need it - inside cancerous tissue - with far less drift elsewhere. What helps? Better carriers, both virus-based and synthetic, that steer the healthy version of p53 straight to tumors without scattering. Precision grows when delivery learns where to go.People in cancer tests did better when researchers slipped synthetic p53 into chemotherapy using viruses. Higher survival rates popped up - beyond what scientists had predicted. The real surprise? Results stayed strong month after month. Gains crept ahead, steady in every group studied. Even when past therapies did not work, doctors saw shifts in tough patient cases (Ma, Ma, & Xing, 2017). Pooled findings across research point to p53 playing a key role in fighting cervical cancer. Because it guides cell division and triggers cell death, unchecked tumor expansion is less likely. That kind of regulation proves vital in halting irregular tissue development (Valente, Queiroz, & Sousa, 2018). For these reasons, methods using gene therapy to adjust p53 levels remain among the more effective paths being explored in oncology (Siddiqui et al., 2020). Popping into the system early, adenoviruses arrive fast - retroviruses tag along not long afterward. Soon after comes herpes simplex, sliding into cells the way rain slips down glass. As if pulled by whispers, they drift toward tumors without rush. Designed with quirks on purpose, they linger near cancer spots more than anyone thought. What makes them spread so easily becomes crucial when precision counts, operating on their own. Deep within cells they always land, pulled in as naturally as air into breathing. This force keeps researchers coming back, drawn by what it reveals. Not merely traveling, they seek out cancer spots much like sunlight reaches clearings. When paired with a certain medication, part of the herpes virus becomes active, studies show (Wang et al., 2020).

3.4Antiangiogenic gene manipulation for therapy

How tumors grow ties closely to blood vessel creation, which feeds them oxygen and needed resources. That link makes blocking new vessels a key angle in fighting cancer. Not every method tries to ramp up VEGF or angiopoietin. Some turn instead to reinforcing the body’s own stop signs - substances like endostatin, angiostatin, interleukin-12, or the p53 protein. Delivering these precisely where required? Still a puzzle, mostly because today's delivery tools miss the mark too often. A newer tactic slips in a split virus built to haul both human endostatin and angiostatin at once, tripping up rogue blood vessel formation more completely. In tests on liver cancer setups, this setup slowed tumors sharply while stretching out life spans in lab mice (Fallah et al., 2019).

Monoclonal Antibodies Targeting VEGF

Two decades back, a handful of lab-made antibodies targeting blood vessel growth got the green light from U.S. regulators to stop VEGF signals - bevacizumab leads that group. Even though they work, their impact fades fast inside the body, plus the price tag keeps many from using them regularly or broadly over time.

Lentiviral Anti-VEGF Antibody Gene Expression Systems

Now, with a gene-based anti-VEGF monoclonal antibody delivery system, the problem has been resolved to some extent. It has become possible to produce antibody continuously following a single administration.The results indicated that using such a lentivirally mediated gene expression system, functional bevacizumab could be produced in modified HEK293T cells, with stable and persistent inhibition of VEGF effects (Zhou et al., 2019).This makes effects that were not previously possible a reality. This development represents in essence one step forward for long-term antiangiogenic therapy with less frequent administration and lower cost.

Exosome-Mediated miRNA Delivery in Angiogenesis Suppression

Recent studies have shown that miR-155 can influence the production process of blood vessels in stomach cancer through its control over FOXO3a. Once gene expression is reduced to a critical level, tumour growth tends to lessen instead of rising fast--this relationship holds true even on closer examination. Those minuscule balls of fat and protein--exosomes, which were originally thought to be refuse from cells--are in fact packed with treasure. Like a shuttle service, they carry molecules and traffic through bodily fluids with remarkable precision. Such molecular delivery within these spaces is essential for the tenuous interaction between miR-155 and the protein FOXO3a that regulates new blood vessel growth in gastric cancers(cell line: Bao et al., 2014). As one day they may shuttle approaches that starve blood supply lines for tumors so effectively to their destinations.

Combined Drug and Gene Therapy Approaches

Once treatments stop building nuclei for fresh aphid infestations, a new phenomenon arises in tumors. This new phenomenon, however, may not be as tough to deal with as people think. As course, it depends where the drug goes after it gets inside. Mixing genetic switches with drugs in a PEI ploy has so far had quite good suppressive effect on tumor growth--early signs seem to suggest this (Prados et al., 2012).

4. Enhancing The Therapeutic Impact By Integrating Gene Therapy With Complementary Cancer Therapies

4.1.Maximizing Treatment Efficacy through the Integration of Gene Therapy and Chemotherapy

many people still end up facing even with big progress in cancer treating, spread of the illness, often beyond cure. For these individuals, body-wide chemo stays the go-to option. Some mixtures of drugs work better than others depending on tumor type - yet using multiple chemicals at once, though it may help live longer, tends to bring strong harm along with it. Because of this, scientists now push harder to make poison-based therapies strike smarter without wrecking healthy tissues.

Sending genes into cells is becoming a useful way to boost cancer drug effectiveness, especially against stubborn or spreading tumors. Alongside standard chemo, genetic treatments have worked well in increasing how strongly medicines stop cancer growth - seen clearly in lung, bladder, pancreas, colon, and breast types. Finding an inhibitor of programmed death cells or RNA cutters that can take away maligenant genes, with therapy combined such killers still more many types of cancer cells will die. (Lin et al., 2023)Chemotherapy is a combined action strategy using conventional drugs that can be participated with gene therapy. Advanced drug delivery technology enables the agent to target and greatly elevate its effect throughout the body. Clinical trials have tried several gene-based agents given alongside chemotherapeutic drugs (Xu et al., 2018). For example, TRAIL (tumor necrosis factor-related apoptosis-inducing ligand) is a member of the TNF family. TRAIL plays a unique role in programming cells for destruction. It effectively promotes cancer cells to kill themselves by connecting with death receptor DR5 and death receptor DR4; both are overexpressed in many malignant tumors. Also, TRAIL encoding gene therapy exerts a bystander effect with significant antitumor activity in vivo (Amreddy et al., 2018).Yet the triumph has been hampered by the impossibility of cancerous tissues to combat death receptors.In the face of this enemy, scientists took on a new line of defense: HuR. With its strong links to tumour genesis, cancer progress and spread, HuR was deemed a promosingtreatment target (Qin et al., 2020).Targeting HuR could increase the sensitivity of a tumor sample to genes that induce apoptosis, so increasing the combined effect of gene therapy and chemotherapy.

4.2.Gene Therapy Combined with Phototherapy: A Powerful Treatment Approach.

The latest medical methods to fight illness Light is also now turning on gene remedies. ”Not only does this construct ship habile genes, it brings them active wherever that may be required. At the right moment triggery medical repairs pour into body continually with illumination help. Instead of expansive results, through a thin line of light control The two separate ideas of once stand now more closely linked than before. The one side provides them with genetic apparatus and the other side uses the rays to get on line again. Because two methods thereby combine each other's capacities, the weakened effect and raised stability Treatment then gets the upper hand without spreading, precise effective for target areas. Merging these two modalities into a synergistic platform facilitates targeting gene activation at specific sites of disease. The result has both greatest efficacy and minimal effect on surrounding healthy tissues.The concept of combining gene therapy with phototherapy has shown great promise for treating a variety of medical conditions, including cancer, genetic diseases and infections. In the field of gene therapy for caner, an artificial gene can be introduced into tumor cells so that it only attacks them, and a new approach also uses phototherapy in order to turn on genes One way to express this is to make highly focused local destruction for malignant cells while sparing normal ones.Two major types of phototherapy are generally recognized.Photothermal therapy (PTT, which in fact does not use light at all) Photodynamic therapy (PDT) are both effective in the treatment of specific cancers, albeit at a high cost (Stahel & Zangemeister-Wittke, 2003).In photothermal therapy, light-induced heat generated by near-infrared radiation is used to destroy cancer cells, while at the same time minimizing any damage to nearby healthy tissue (Kim et al., 2016). Compared to conventional modes of treatment, PTT has a number of attractive advantages: minimal invasiveness, deep tissue penetration and a low procedural trauma (Kim et al., 2020).On the other hand, Photodynamic therapy (PDT) is a new type of cancer treatment, that uses visible light to activate a photosensitizer (PS)--a light-sensitive molecule that turns into reactive oxygen species (ROS) following its activation -- ultimately resulting in cancer cell death (Cai et al., 2020). PDT is especially successful in treating surface tumors like esophageal cancer, bladder cancer and melanoma. The many advantages it possesses--such as low invasiveness, targeted cytotoxicity and minimal side effects--contribute greatly to its clinical success. (Chen, Luo & Zhang, 2019; Revia & Zhang, 2016).

4.3.Combined approach of gene therapy and magneto thermal therapy

This method that relies on a particular magnetic field makes the little particles inside of tumors begin to heat up. Only sick cells get burned--the rest are okay, even if they do have a fever. Energy from outside causes these small materials to sway back and forth, making everything nice and warm where it should be. The temperature rise pushes damaged cells to self-destruct, without bursting the buds too tightly. This treatment is precise: the effect follows where the particles are put. Only those places where particles have gone get warm. Nearby healthy tissue feels next to nothing at all; shift a tumor cell, and the results show up in the 1960s research of Tay et al. As for where the magnetic nanoparticles goes to in the body? Frequently, magnetic particle imaging needs to take over this chore, as Yang et al. proved in 2022. The heat inside a tumor caused by a magnetic field has worked well - little side effects, deep infiltration - and is now on trial patients with the number NCT02033447. To succeed, we must maintain our success in keeping the heat between 43 and 46 degrees Celsius. This is achieved if we can place enough particles where they are needed precisely where we want them. (Gavilán et al., 2021).

Thirty years ago, researchers started looking at the possibility of using heat from magnets to treat hard balls in the body. Now, tests focus on small iron-made particles to stop lumps in the head or pelvic region. Inside just such approaches, little particles actually get deposited right into the troubled tissue and then exposed to a slight wave field at roughly 100,000 cycles per second. Moreover, although such particles have already been approved for the sake of scanning, and to cure low blood counts others for heating alone must be made with more rigorous physical qualities. They need an adjusted magnetism, stable external layer, and predictable agglomeration so as efficiently turn the field into heat will deliver heating with precision. Big strides have been made in recent times in creating the next-generation magnetic nanoparticles for treating hormone-related cancers. And this transformation is removing obstacles to combining magnetic heating with chemo, radiation, immune treatment, light-driven methods of treatment, or gene therapy -opening up multi-faceted methods for dealing with tumours. Work still proceeds on how heat spreads in the centre of a tumour and keeping the target temperature exact during treatment, gradually improving both reliability and effect without making more noise (Stahel & Zangemeister-Wittke, 2003).

5.Current Molecular Methodologies Used In The Field Of Cancer Gene Therapy

Scientists have also developed a new way of moving around genes that means very different medicine is likely as well. This has may well support existing therapies while opening up entirely fresh ones for action. keep coming out, Out of this shift - perhaps net delimited by the double entitled stripped or semi-narrative blog post which rules left by science but otherwise ignored and unread over time - has emerged a number of novel cancer strategies. With genetic material shifting its goal: analytics have gone haywire and TALENs take the foreground, iRNA appears in conjunction with CRISPR-like DNA repeats. Up near ZFNs attend local settings looking for damage while recycled DNA units, self-destructing genes, and repeat patterns similar to CRISPR move into labs on bite wheels more and more frequently.

5.1.Antisense technology is a captivating and auspicious way to treat cancer

One of the most promising strategies for treating cancer is antisense technology. Inthis approach, particular sequences of antisense oligonucleotides (ASOs) are used to bind specifically to corresponding target mRNA, thereby inhibiting gene translation. Furthermore, thisinteraction's high specificity arises from Watson–Crick base pairing, which allows ASOs to be powerful tools for target validation, gene regulation, andspecific therapeutic interventions in cancerand genetic diseasesthe specificity of this interaction is receptor-legated by Watson–Crick base pairing, making antisense oligonucleotides powerful tools for target validation, gene regulation, and selective therapeutic intervention.

Prime targets for antisense-based therapy might be ones that havetheir expression governed by certain slew genes, which are implicated inthe comport of cancer cells. Only one antisense compound has been accorded topical registration to date, but clinical trials are now in progress. These are looking at antisense-based treatments for cytomegalovirus-inducedretinitis, as well as experimental therapies targeting the people key oncogene mRNAs Bcl-2,protein kinase C-α (PKC-α),c-raf, was (Dias and Stein, 2002:550).Antisense oligonucleotides by binding to their respective mRNAtargets can trigger distinct molecular mechanisms of action (Le et al., 2019; Lundin, Gissberg, & Smith, 2015).

These mechanisms can be broadly classified into two major categories:

1. mechanisms that promote RNA degradation, and
2. mechanisms that inhibit RNA function by steric blockade without inducing RNA degradation.

Regardless of the specific pathway involved, the therapeutic application of antisense oligonucleotides demonstrates significant potential for effective and selective cancer treatment (Bennett et al., 2017; Karim et al., 2018).

5.2.RNA molecules with interfering properties

The advent of RNAi can be dated to 1998 with its first observation in Caenorhabditis elegans (C. elegans) (Fire et al, 1998), Before long, RNAi has emerged as an efficient gene silencing technology with important implications for treating cancer.This is called RNA interference. It is a post-transcriptional gene regulation mechanism mediated by double-stranded RNA (dsRNA). dsRNA only binds complementary copies of malicious HIV virus RNA sequence while leaving your own cellular machinery undisturbed. In three major groups of small regulatory RNAs have been found in animal,you will normally find: small interfering RNAs (siRNAs), microRNAs (miRNAs), and piwi-interacting RNAs (piRNAs) (Schuster, Miesen, & van Rij, 2019; Sun et al., 2023).

SiRNA-based RNA interference holds great promise as a potential therapy for cancer. Yet currently the use of this method in a clinical setting is hampered by key complications such as metabolism instability, limited targeting specificity towards tumours and problems with getting into cells. A potential way around this is to structurally change the siRNA using synthetic nucleic acid bases so that it is more stable in vivo. In this study, we produced and tested functionally modified siRNAs containing different numbers of the hydrophobic F base. We systematically studied the interactions between F-base modified siRNA (F-siRNA) and plasma protein human serum albumin. The F bases significantly improved the tumor-targeting capability of those siRNAs, their lifetime in the body and also their ability to penetrate tissues. Mechanically, the F bases serve to stabilize siRNA–albumin complexes so that this combination can preferentially achieve selective translocation to and retention in tumors through the enhanced permeability and retention (EPR) effect. Meanwhile, the F bases increase siRNA binding to transport proteins in cell membranes and so promote broad uptake by cells. The data underscore that F-base modified siRNAs dramatically improve the stability, conveyance efficiency and selective tumor accumulation of siRNAs deposited in new liposomes like those investigated here as potential cancers treatments. (Feng et al., 2023)

A tumor-targeting fluorescence probe for the near-infrared region was developed in order to narrow down targets even further.The probe f-CRI is designed to detect RNA, and is targeted to tumors through a cyclic RGD peptide, a furan furan group for modifying mtRNA (mitochondrial ribosnucleic acid), and was covalently linked with monoxide-sensitive IR780 receptors. When f-CRI is irradiated by an 808 nm laser, photoactivation occurs and it is covalently bonded to mitochondrial RNA (mtRNA) with a prolonged residence time in the targeted tumor. This covalent modification destroys mitochondrial function and induces significant regression of tumor.

The f-CRI Strategy's new

What really sets the f-CRI system apart is its ability to direct, RNA-level targeting of mitochondria--it's a great improvement over traditional photothermal therapy (PTT) or photodynamic therapy (PDT). With traditional PTT and PDT, at the cellular level, all they really do are induce thermal damage or cause damage with reactive oxygen species (ROS) generation. In contrast, direct covalent modification of mtRNA by the f-CRI probe disrupts tumor metabolism at its genetic and mitochondrial nucleus. Such a mechanism greatly increases the precision of therapy done by these molecular agents as well as improves the spatial control they offer. And best of all? There's far less harm to surrounding healthy tissue that results from off-target effects-- making f-CRI a next-generation monogenic photogene therapy.

6.CONCLUSION AND FUTURE PERSPECTIVE

Cancer is among the most complex and insoluble problems now because of its genetic differences, diverse direction of development resistance to normal treatment methods Despite the existence of many different routes to therapy, there is an increasing optimism that advanced molecular techniques in particular gene therapy will help turn cancer into history over coming decades. At present, most gene-based clinical experiments are in a relatively early stage. Although gene therapy cannot meet the current criteria to replace traditional treatments such as chemotherapy and radiotherapy, it shows wonderful potential replaced by another powerful way togo. Petrinjisonista itself has amazing prospects for an adjunct treatment. Enhancing the selection means that genes used to kill diseased cells were able to hit the mark directly. The enemy will soon be taught by this method and his voice shall never bother us again. It's complementary with modern therapies but impinges very little on them. With precision increased,the trouble to the body decreases. The therapy still remains effective after a consecutive

knock-out instead of pacing second round over wilderness.

In recent years, treatments targeting cancer-related genes have come closer to being used across humanity. That is in part due to both new drug approvals and a growing number of studies watching their effectiveness in people. Sometimes much easier to deal with than many side effects of chemotherapy, these therapies aim for a specific molecule instead -- particularly when used with another type of treatment,

Tomorrow's cancer treatments could well be induced by mixing some immune-based strategy with self-destruct gene switches. Genes that once had the senior lot of responsibility as targets for old-school treatments are being slid into oblivion by precise edits cut straight into DNA. Frequently, these tools are also used secondarily; for example CRISPR/Cas9, instead of just for editing at the outset.Trouble spots in people's genes are the target of this new approach. Faulty system code is tweaked like fixing typos in programs. Databases on the Internet help monitor what works—such as TSGene, found in Nucleic Acids Research, which contains valuable tips on genes that safeguard against cells' turning into cancers. Papers portend still deeper changes ahead. For example, articles in the popular press carry titles like "The Coming Epoch of Tumor Suppressor Genes," a look at where things may be headed down to the finer levels inside cells. The work that was once scattered all over now congregates behind these fine-grained fixes within cells. Control over wayward behavior by cells is becoming more and more precise with each passing year.

However, change is always happening. In particular, minuscule molecules are now steering the way scientists study cancer. It is not one process but the precision steps which join laboratory advances in sequence in real time. The old-school treatments remain indispensable as new tools also come into their own. Instead of genes being edited to kill tumors today, they could play a more repetitive role tomorrow. The immune system now teams with DNA corrections more often than before. Change progresses slowly rather than abruptly, in small but continued steps. What was once unheard-of may indeed become everyday care in a short time. Hope grows silently, without sound, through personalized paths to wellness.

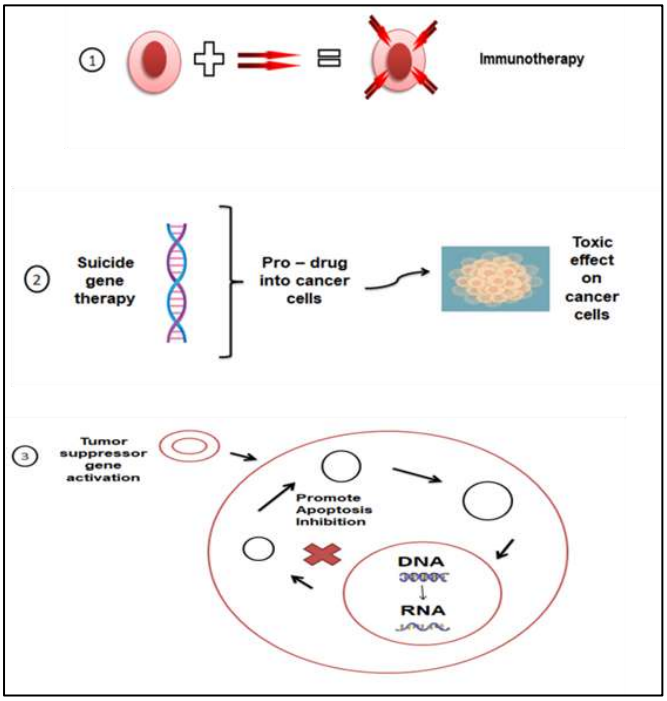

Figure 1: The summarized gene therapy strategies for cancer treatment are outlined

1. Immunotherapy: Designed to stimulate or enhance the reaction of T cells against tumor antigens, cancer immunotherapies play a crucial role .

2.Suicide gene therapy: This strategy employs prodrugs that undergo activation, resulting in cytotoxic effects specifically within cancer cells .

3.Activation of tumor suppression genes: By introducing tumor suppressor genes into cancer cells, either cell cycle inhibition or apoptosis can be induced.

Funding

This study received no specific financial support from any funding
institute in the public, commercial, or not-for-profit sectors.

Data availability statement

The generated datasets in this study are accessible from the corresponding author on reasonable appeal.

Ethics approval

Not applicable.

Consent to participate

Not applicable.

TABLE 1. Active clinical trials using viral vectors to treat cancer (Zhao et al., 2017) (Cañadas et al., 2018) (Deblois et al., 2020) (Konkalmatt et al., 2013) (Li, C., & Samulski, R. J. (2020). Wang, D., Tai, P. W. L., & Gao, G. (2024)

Virus	Cancer	Serotype	Vector Generation/Purpose
Adenovirus	Prostate cancer	Ad5-yCD/ mutTKSR39rep-hIL-12	Oncolytic
	Pancreatic cancer	LOAd703 Ad5F35	Oncolytic
Retrovirus	Colon carcinoma cell lines.	RRX-001	Lowers DNMT expression levels to induce a state of viral mimicry.
	Mice were injected with an ovarian cancer cell line and a colorectal cancer cell line, allowing for the study of these specific types of cancer in a controlled environment.	MC180295 CDK9	Triggers viral-like response Enhances cell sensitivity to α-PD-1 checkpoint inhibitor.
Adeno-associated virus	Plectin-positive tumor cells	AAV-PTP /AAV2	AAV-PTP preferentially targets human PDAC cells over non-PDAC cells in vitro.
	β1-integrin positive tumor cells	AAV-I-587 / AAV2	

TABLE 2. Non-viral delivery systems utilized for cancer gene therapy research in early stages (Shi et al., 2020) (Zhao et al., 2020) (Liu et al., 2018) (Wonder et al., 2018) (Zhao et al., 2019) (Chattopadhyay & Sen, 2014)

Distribution system	Cancer subtype	Active compound	Animal testing	Safety framework.	assessment Key findings
Nanoparticles composed of polymer hybrids.	Non-small cell lung cancer, abbreviated as NSCLC.	Small interfering RNA targeting PLK1.	Male nude mice were used to establish the subcutaneous A549 tumor model.	Efficient gene delivery platform.	Exceptional tumor growth inhibition was observed with the PHD/PLL/siRNA NP.
Fatty membrane	lung carcinoma	CYP1A1-specific siRNA.	Nude BALB/c xenograft models.	The absence of any discernible toxicity	was observed, and the down-regulation of CYP1A1 expression
Nanoparticles with polymer-inorganic hybrid composition	Breast cancer	Plasmid in the NIR-II spectrum	Breast cancer model 4T1 implanted subcutaneously.	The low in vivo cytotoxicity of the tri-modal therapy is confirmed by the H&E staining analysis of major organs and the absence of noticeable body weight loss.	The therapeutic potential of trimodal gene/PT/chemotherapy treatment for malignant breast cancer was exemplified by the remarkable effect observed in NPs during in vitro and in vivo studies.
The self-organization of DOTAP and MPEG-PLA (DMA) showcases an intriguing mechanism.	colon cancer and rectal cancer (CRC)	"pIL15" is used to denote the plasmid that carries the IL-15 gene.	Exploring Subcutaneous and Peritoneal Models for Research Purposes	Vital organs showed normal histological morphology with no signs of toxicity following exposure to DMA-pIL15. sections	The activation of the host immune system plays a crucial role in inhibiting angiogenesis, promoting apoptosis, and reducing proliferation.
DNA nanoparticles encapsulated in cationic liposomes with peptide tags	Stomach cancer,	pGFP is short for "plasmid Green Fluorescent Protein." It refers to a specific plasmid that contains the gene encoding the Green Fluorescent Protein (GFP).	Injection of MKN-45P cells into the peritoneal cavity of athymic nude mice was performed.	Slight aggregation in normal tissue samples.	Augmented tumor accumulation, prioritized penetration of smaller tumor nodules, a target of utmost clinical relevance known to be a driving force behind the recurrence of peritoneal cancer.
By incorporating Oleylamine (OA) modification and disulfide groups, the PEI compound undergoes a significant alteration.	hepatic cancer	Specific gene silencing of Survivin.	Uncovered mice hosting HepG2 xenografts.	The absence of toxicity towards normal tissues ensures their well-being.	Enhanced tumor localization, Marked inhibition of tumor development.

REFERENCES

Abdullah, S., Wendy-Yeo, W. Y., Hosseinkhani, H., Hosseinkhani, M., Masrawa, E., Ramasamy, R., … & Domb, A. J. (2010). Gene transfer into the lung by nanoparticle dextran-spermine/plasmid DNA complexes. *BioMed Research International*, 2010(1), 284840.

Abedini, F., Hosseinkhani, H., Ismail, M., Chen, Y. R., Omar, A., Chong, P., & Domb, A. (2011). In vitro intracellular trafficking of biodegradable nanoparticles dextran-spermine in cancer cell lines. *International Journal of Nanotechnology*, 8(8–9), 712–723.

Abedini, F., Ismail, M., Hosseinkhani, H., Azmi, T., Omar, A. R., Chong, P. P., … & Domb, A. J. (2010). Toxicity evaluation of dextran-spermine polycation as a tool for gene therapy in vitro. *Journal of Cell and Animal Biology*, 4(12), 170–176.

Al-Dosari, M. S., & Gao, X. (2009). Nonviral gene delivery: Principle, limitations, and recent progress. *The AAPS Journal*, 11, 671–681.

Alnasser, S. M. (2021). Review on mechanistic strategy of gene therapy in the treatment of disease. *Gene*, 769, 145246.

Amara, I., Pramil, E., Senamaud-Beaufort, C., Devillers, A., Macedo, R., Lescaille, G., … & de Waziers, I. (2016). Engineered mesenchymal stem cells as vectors in a suicide gene therapy against preclinical murine models for solid tumors. *Journal of Controlled Release*, 239, 82–91.

Amara, I., Touati, W., Beaune, P., & de Waziers, I. (2014). Mesenchymal stem cells as cellular vehicles for prodrug gene therapy against tumors. *Biochimie*, 105, 4–11.

Amreddy, N., Babu, A., Panneerselvam, J., Srivastava, A., Muralidharan, R., Chen, A., … & Ramesh, R. (2018). Chemo-biologic combinatorial drug delivery using folate receptor-targeted dendrimer nanoparticles for lung cancer treatment. *Nanomedicine: Nanotechnology, Biology and Medicine*, 14(2), 373–384.

Bao, X., Wang, W., Wang, C., Wang, Y., Zhou, J., Ding, Y., … & Jin, Y. (2014). A chitosan-graft-PEI-candesartan conjugate for targeted co-delivery of drug and gene in anti-angiogenesis cancer therapy. *Biomaterials*, 35(29), 8450–8466.

Bennett, C. F., Baker, B. F., Pham, N., Swayze, E., & Geary, R. S. (2017). Pharmacology of antisense drugs. *Annual Review of Pharmacology and Toxicology*, 57(1), 81–105.

Bulaklak, K., & Gersbach, C. A. (2020). The once and future gene therapy. *Nature Communications*, 11(1), 1–4.

Butt, M. H., Zaman, M., Ahmad, A., Khan, R., Mallhi, T. H., Hasan, M. M., ... & Cavalu, S. (2022). Appraisal for the potential of viral and nonviral vectors in gene therapy: A review. *Genes*, *13*(8), 1370.

Cai, Y., Ni, D., Cheng, W., Ji, C., Wang, Y., Müllen, K., … & Yin, M. (2020). Enzyme-triggered disassembly of perylene monoimide-based nanoclusters for activatable and deep photodynamic therapy. *Angewandte Chemie*, 132(33), 14118–14122.

Cañadas, I., Thummalapalli, R., Kim, J. W., Kitajima, S., Jenkins, R. W., Christensen, C. L., … & Barbie, D. A. (2018). Tumor innate immunity primed by specific interferon-stimulated endogenous retroviruses. *Nature Medicine*, 24(8), 1143–1150.

Carlin, J. L. (2011). Mutations are the raw materials of evolution. *Nature Education Knowledge*, 3(10), 10.

Cesur, B. (2019). *Meme kanseri gen tedavisi tıbbi ürünleri için nanotaşıyıcı sistemlerin geliştirilmesi*.

Cesur, B. Ü. Ş. R. A., & Demir-Dora, D. (2019). Non-biological complex drugs.

Cesur-Ergün, B., & Demir-Dora, D. (2023). Gene therapy in cancer. *The Journal of Gene Medicine*, 25(11), e3550.

Chattopadhyay, S., & Sen, G. C. (2014). Tyrosine phosphorylation in Toll-like receptor signaling. *Cytokine & Growth Factor Reviews*, 25(5), 533–541.

Chattopadhyay, S., & Sen, G. C. (2017). RIG-I-like receptor-induced IRF3 mediated pathway of apoptosis (RIPA): A new antiviral pathway. *Protein & Cell*, 8, 165–168.

Chen, J., Nie, W., Hu, Y., Shen, Y., Lin, Y., Wang, B., … & Gao, X. (2022). A folic acid-modified non-viral vector combines gene therapy with chemotherapy to reverse cancer chemotherapy resistance. *Applied Materials Today*, 26, 101277.

Chen, W. H., Luo, G. F., & Zhang, X. Z. (2019). Recent advances in subcellular targeted cancer therapy based on functional materials. *Advanced Materials*, 31(3), 1802725.

D'Aloia, M. M., Zizzari, I. G., Sacchetti, B., Pierelli, L., & Alimandi, M. (2018). CAR-T cells: The long and winding road to solid tumors. *Cell Death & Disease*, 9(3), 282.

D'Aria, F., D'Amore, V. M., Di Leva, F. S., Amato, J., Caterino, M., Russomanno, P., … & Giancola, C. (2020). Targeting the KRAS oncogene: Synthesis, physicochemical and biological evaluation of novel G-quadruplex DNA binders. *European Journal of Pharmaceutical Sciences*, 149, 105337.

Deblois, G., Tonekaboni, S. A. M., Grillo, G., Martinez, C., Kao, Y. I., Tai, F., … & Lupien, M. (2020). Epigenetic switch–induced viral mimicry evasion in chemotherapy-resistant breast cancer. *Cancer Discovery*, 10(9), 1312–1329.

Deng, J., Guo, M., Li, G., & Xiao, J. (2020). Gene therapy for cardiovascular diseases in China: Basic research. *Gene Therapy*, 27(7), 360–369.

Dias, N., & Stein, C. A. (2002). Antisense oligonucleotides: Basic concepts and mechanisms. *Molecular Cancer Therapeutics*, 1(5), 347–355.

Ding, Y., Wang, C., Sun, Z., Wu, Y., You, W., Mao, Z., & Wang, W. (2021). Mesenchymal stem cells engineered by nonviral vectors: A powerful tool in cancer gene therapy. *Pharmaceutics*, 13(6), 913.

Dora, D. D. (2021). Gen tedavisinde kullanılan viral olmayan taşıyıcı sistemler. *Turkiye Klinikleri Medical Genetics-Special Topics*, 6(1), 20–26.

Duarte, S., Carle, G., Faneca, H., de Lima, M. C. P., & Pierrefite-Carle, V. (2012). Suicide gene therapy in cancer: Where do we stand now? *Cancer Letters*, 324(2), 160–170.

Dunbar, C. E., High, K. A., Joung, J. K., Kohn, D. B., Ozawa, K., & Sadelain, M. (2018). Gene therapy comes of age. *Science*, 359(6372), eaan4672.

Engeland, K. (2022). Cell cycle regulation: p53-p21-RB signaling. *Cell Death & Differentiation*, 29(5), 946–960.

Fallah, A., Heidari, H. R., Bradaran, B., Sisakht, M. M., Zeinali, S., & Molavi, O. (2019). A gene-based anti-angiogenesis therapy as a novel strategy for cancer treatment. *Life Sciences*, 239, 117018.

Feins, S., Kong, W., Williams, E. F., Milone, M. C., & Fraietta, J. A. (2019). An introduction to chimeric antigen receptor (CAR) T-cell immunotherapy for human cancer. *American Journal of Hematology*, 94(S1), S3–S9.

Feng, Y., Fang, J., Zhao, Y., Ye, S., Wang, A., Zhang, Y., … & Shi, H. (2023). NIR light-mediated mitochondrial RNA modification for cancer RNA interference therapeutics. *Angewandte Chemie*, 135(19), e202218969.

Fire, A., Xu, S., Montgomery, M. K., Kostas, S. A., Driver, S. E., & Mello, C. C. (1998). Potent and specific genetic interference by double-stranded RNA in *Caenorhabditis elegans*. *Nature*, 391(6669), 806–811.

Gavilán, H., Avugadda, S. K., Fernández-Cabada, T., Soni, N., Cassani, M., Mai, B. T., … & Pellegrino, T. (2021). Magnetic nanoparticles and clusters for magnetic hyperthermia: Optimizing their heat performance and developing combinatorial therapies to tackle cancer. *Chemical Society Reviews*, 50(20), 11614–11667.

Girod, A., Ried, M., Wobus, C., Lahm, H., Leike, K., Kleinschmidt, J., … & Hallek, M. (1999). Genetic capsid modifications allow efficient re-targeting of adeno-associated virus type 2. *Nature Medicine*, 5(9), 1052–1056.

Gonçalves, G. A. R., & Paiva, R. D. M. A. (2017). Gene therapy: Advances, challenges and perspectives. *Einstein (São Paulo)*, 15, 369–375.

Goswami, R., Subramanian, G., Silayeva, L., Newkirk, I., Doctor, D., Chawla, K., … & Betapudi, V. (2019). Gene therapy leaves a vicious cycle. *Frontiers in Oncology*, 9, 297.

Griesenbach, U. (2007). Progress and prospects: Gene therapy clinical trials (part 2). *Gene Therapy*, 14(22), 1555–1563.

Guo, C., Ma, X., Gao, F., & Guo, Y. (2023). Off-target effects in CRISPR/Cas9 gene editing. *Frontiers in bioengineering and biotechnology*, *11*, 1143157.

Hosseinkhani, H., & Tabata, Y. (2006). Self assembly of DNA nanoparticles with polycations for the delivery of genetic materials into cells. *Journal of Nanoscience and Nanotechnology*, 6(8), 2320–2328.

Hosseinkhani, H., Abedini, F., Ou, K. L., & Domb, A. J. (2015). Polymers in gene therapy technology. *Polymers for Advanced Technologies*, 26(2), 198–211.

Hosseinkhani, H., Azzam, T., Tabata, Y., & Domb, A. J. (2004). Dextran–spermine polycation: An efficient nonviral vector for in vitro and in vivo gene transfection. *Gene Therapy*, 11(2), 194–203.

Huang, J., Xiao, Z., Chen, G., Li, T., Peng, Y., & Shuai, X. (2022). A pH-sensitive nanomedicine incorporating catalase gene and photosensitizer augments photodynamic therapy and activates antitumor immunity. *Nano Today*, 43, 101390.

Ibnat, N., Kamaruzman, N. I., Ashaie, M., & Chowdhury, E. H. (2019). Transfection with p21 and p53 tumor suppressor plasmids suppressed breast tumor growth in syngeneic mouse model. *Gene*, 701, 32–40.

Ichikawa, M., Matsunaga, W., Ishikawa, T., & Gotoh, A. (2019). Lentiviral vector-mediated gene transfer combined with cisplatin enhances tumor suppression in human bladder cancer cell lines. *Personalized Medicine Universe*, 8, 15–19.

Iglesias-López, C., Agustí, A., Obach, M., & Vallano, A. (2019). Regulatory framework for advanced therapy medicinal products in Europe and United States. *Frontiers in Pharmacology*, 10, 471441.

Karim, M. E., Tha, K. K., Othman, I., Borhan Uddin, M., & Chowdhury, E. H. (2018). Therapeutic potency of nanoformulations of siRNAs and shRNAs in animal models of cancers. *Pharmaceutics*, 10(2), 65.

Kaufman, H. L., Kim, D. W., DeRaffele, G., Mitcham, J., Coffin, R. S., & Kim-Schulze, S. (2010). Local and distant immunity induced by intralesional vaccination with an oncolytic herpes virus encoding GM-CSF in patients with stage IIIc and IV melanoma. *Annals of Surgical Oncology*, 17, 718–730.

Kaufman, H. L., Kohlhapp, F. J., & Zloza, A. (2015). Oncolytic viruses: A new class of immunotherapy drugs. *Nature Reviews Drug Discovery*, 14(9), 642–662.

Ketola, A., Määttä, A. M., Pasanen, T., Tulimäki, K., & Wahlfors, J. (2004). Osteosarcoma and chondrosarcoma as targets for virus vectors and herpes simplex virus thymidine kinase/ganciclovir gene therapy. *International Journal of Molecular Medicine*, 13(5), 705–710.

Kim, J., Kim, J., Jeong, C., & Kim, W. J. (2016). Synergistic nanomedicine by combined gene and photothermal therapy. *Advanced Drug Delivery Reviews*, 98, 99–112.

Kim, N. Y., Blake, S., De, D., Ouyang, J., Shi, J., & Kong, N. (2020). Two-dimensional nanosheet-based photonic nanomedicine for combined gene and photothermal therapy. *Frontiers in Pharmacology*, 10, 1573.

Konkalmatt, P. R., Deng, D., Thomas, S., Wu, M. T., Logsdon, C. D., French, B. A., & Kelly, K. A. (2013). Plectin-1 targeted AAV vector for the molecular imaging of pancreatic cancer. *Frontiers in Oncology*, 3, 84.

Kosaka, H., Ichikawa, T., Kurozumi, K., Kambara, H., Inoue, S., Maruo, T., … & Hamada, H. (2012). Therapeutic effect of suicide gene-transferred mesenchymal stem

cells in a rat model of glioma. *Cancer Gene Therapy*, 19(8), 572–578.

Kumar, C. S., & Mohammad, F. (2011). Magnetic nanomaterials for hyperthermia-based therapy and controlled drug delivery. *Advanced Drug Delivery Reviews*, 63(9), 789–808.

Le, B. T., Raguraman, P., Kosbar, T. R., Fletcher, S., Wilton, S. D., & Veedu, R. N. (2019). Antisense oligonucleotides targeting angiogenic factors as potential cancer therapeutics. *Molecular Therapy – Nucleic Acids*, 14, 142–157.

Lee, J. C., Shin, D. W., Park, H., Kim, J., Youn, Y., Kim, J. H., … & Hwang, J. H. (2020). Tolerability and safety of EUS-injected adenovirus-mediated double-suicide gene therapy with chemotherapy in locally advanced pancreatic cancer: A phase 1 trial. *Gastrointestinal Endoscopy*, 92(5), 1044–1052.

Li, C., & Samulski, R. J. (2020). Engineering adeno-associated virus vectors for gene therapy. *Nature Reviews Genetics*, *21*(4), 255-272.

Li, Y., Liu, L., Ji, W., Peng, H., Zhao, R., & Zhang, X. (2020). Strategies and materials of "SMART" non-viral vectors: Overcoming the barriers for brain gene therapy. *Nano Today*, 35, 101006.

Li, Y., Zhao, S., Zhang, F., Jin, G., Zhou, Y., Li, P., … & Yang, X. (2020). Molecular imaging-monitored radiofrequency hyperthermia-enhanced intratumoral herpes simplex virus-thymidine kinase gene therapy for rat orthotopic ovarian cancer. *International Journal of Hyperthermia*, 37(1), 101–109.

Liang, H., & Wang, M. (2020). MET oncogene in non-small cell lung cancer: Mechanism of MET dysregulation and agents targeting the HGF/c-Met axis. *OncoTargets and Therapy*, 13, 2491–2510.

Lin, J., Wang, X., Ni, D., Chen, Y., Chen, C., & Liu, Y. (2023). Combinational gene therapy toward cancer with nanoplatform: Strategies and principles. *ACS Materials Au*, 3(6), 584–599.

Liu, T. C., & Kirn, D. (2008). Gene therapy progress and prospects: Cancer—oncolytic viruses. *Gene Therapy*, 15(12), 877–884.

Liu, X., Li, Y., Sun, X., Muftuoglu, Y., Wang, B., Yu, T., … & Wei, Y. (2018). Powerful anti-colon cancer effect of modified nanoparticle-mediated IL-15 immunogene therapy through activation of the host immune system. *Theranostics*, 8(13), 3490–3502.

Liu, Y., Bhattarai, P., Dai, Z., & Chen, X. (2019). Photothermal therapy and photoacoustic imaging via nanotheranostics in fighting cancer. *Chemical Society Reviews*, 48(7), 2053–2108.

Lundin, K. E., Gissberg, O., & Smith, C. E. (2015). Oligonucleotide therapies: The past and the present. *Human Gene Therapy*, 26(8), 475–485.

Ma, C. C., Wang, Z. L., Xu, T., He, Z. Y., & Wei, Y. Q. (2020). The approved gene therapy drugs worldwide: From 1998 to 2019. *Biotechnology Advances*, 40, 107502.

Ma, W. S., Ma, J. G., & Xing, L. N. (2017). Efficacy and safety of recombinant human adenovirus p53 combined with chemoradiotherapy in recurrent nasopharyngeal carcinoma. *Anti-Cancer Drugs*, 28(2), 230–236.

Mali, S. (2013). Delivery systems for gene therapy. *Indian Journal of Human Genetics*, 19(1), 3–8.

Miller, K. D., Nogueira, L., Mariotto, A. B., Rowland, J. H., Yabroff, K. R., Alfano, C. M., … & Siegel, R. L. (2019). Cancer treatment and survivorship statistics, 2019. *CA: A Cancer Journal for Clinicians*, 69(5), 363–385.

Motta, I., Ghiaccio, V., Cosentino, A., & Breda, L. (2019). Curing hemoglobinopathies: Challenges and advances of conventional and new gene therapy approaches. *Mediterranean Journal of Hematology and Infectious Diseases*, 11(1).

Neuhaus, V., Schaudien, D., & Dehmel, S. (2023). Advanced therapy medicinal products. In *Drug Discovery and Evaluation: Safety and Pharmacokinetic Assays* (pp. 1–25). Springer.

Neves, A. R., Sousa, A., Faria, R., Albuquerque, T., Queiroz, J. A., & Costa, D. (2020). Cancer gene therapy mediated by RALA/plasmid DNA vectors: Nitrogen to phosphate groups ratio (N/P) as a tool for tunable transfection efficiency and apoptosis. *Colloids and Surfaces B: Biointerfaces*, 185, 110610.

Ni, D., Lin, J., Zhang, N., Li, S., Xue, Y., Wang, Z., … & Liu, Y. (2022). Combinational application of metal–organic frameworks-based nanozyme and nucleic acid delivery in cancer therapy. *Wiley Interdisciplinary Reviews: Nanomedicine and Nanobiotechnology*, 14(3), e1773.

Pan, L., Liu, J., & Shi, J. (2018). Cancer cell nucleus-targeting nanocomposites for advanced tumor therapeutics. *Chemical Society Reviews*, 47(18), 6930–6946.

Prados, J., Alvarez, P. J., Melguizo, C., Rodriguez-Serrano, F., Carrillo, E., Boulaiz, H., … & Aranega, A. (2012). How is gene transfection able to improve current chemotherapy? The role of combined therapy in cancer treatment. *Current Medicinal Chemistry*, 19(12), 1870–1888.

Qin, L., Jiang, S., He, H., Ling, G., & Zhang, P. (2020). Functional black phosphorus nanosheets for cancer therapy. *Journal of Controlled Release*, 318, 50–66.

Qiu, N., Wang, G., Wang, J., Zhou, Q., Guo, M., Wang, Y., … & Shen, Y. (2021). Tumor-associated macrophage and tumor-cell dually transfecting polyplexes for efficient interleukin-12 cancer gene therapy. *Advanced Materials*, 33(2), 2006189.

Rajakumar, T., Horos, R., Jehn, J., Schenz, J., Muley, T., Pelea, O., … & Steinkraus, B. R. (2022). A blood-based miRNA signature with prognostic value for overall survival in advanced stage non-small cell lung cancer treated with immunotherapy. *NPJ Precision Oncology*, 6(1), 19.

Raty, J. K., Pikkarainen, J. T., Wirth, T., & Ylä-Herttuala, S. (2008). Gene therapy: The first approved gene-based medicines, molecular mechanisms and clinical indications. *Current Molecular Pharmacology*, 1(1), 13–23.

Revia, R. A., & Zhang, M. (2016). Magnetite nanoparticles for cancer diagnosis, treatment, and treatment

monitoring: Recent advances. *Materials Today*, 19(3), 157–168.

Riley, R. S., June, C. H., Langer, R., & Mitchell, M. J. (2019). Delivery technologies for cancer immunotherapy. *Nature Reviews Drug Discovery*, 18(3), 175–196.

Schuster, S., Miesen, P., & van Rij, R. P. (2019). Antiviral RNAi in insects and mammals: Parallels and differences. *Viruses*, 11(5), 448.

Scott, L. J. (2015). Alipogene tiparvovec: A review of its use in adults with familial lipoprotein lipase deficiency. *Drugs*, 75, 175–182.

Shah, K. (2012). Mesenchymal stem cells engineered for cancer therapy. *Advanced Drug Delivery Reviews*, 64(8), 739–748.

Shaw, A. R., & Suzuki, M. (2019). Immunology of adenoviral vectors in cancer therapy. *Molecular Therapy – Methods & Clinical Development*, 15, 418–429.

Shi, M., Zhang, J., Huang, Z., Chen, Y., Pan, S., Hu, H., … & Zhao, X. (2020). Stimuli-responsive release and efficient siRNA delivery in non-small cell lung cancer by a poly(L-histidine)-based multifunctional nanoplatform. *Journal of Materials Chemistry B*, 8(8), 1616–1628.

Shi, Y., Wang, J., Bai, Z., Li, Y., Qiu, L., Zhai, B., … & Yang, X. (2016). Radiofrequency hyperthermia-enhanced herpes simplex virus-thymidine kinase/ganciclovir direct intratumoral gene therapy of esophageal squamous cancers. *American Journal of Cancer Research*, 6(9), 2054–2066.

Siddiqui, S., Libertini, S. J., Lucas, C. A., Lombard, A. P., Baek, H. B., Nakagawa, R. M., … & Mudryj, M. (2020). The p14ARF tumor suppressor restrains androgen receptor activity and prevents apoptosis in prostate cancer cells. *Cancer Letters*, 483, 12–21.

Siegel, R. L., Miller, K. D., Fuchs, H. E., & Jemal, A. (2022). Cancer statistics, 2022. *CA: A Cancer Journal for Clinicians*, 72(1), 7–33.

Sims, J. J., Greig, J. A., Michalson, K. T., Lian, S., Martino, R. A., Meggersee, R., … & Wilson, J. M. (2021). Intranasal gene therapy to prevent infection by SARS-CoV-2 variants. *PLoS Pathogens*, 17(7), e1009544.

Singh, A., et al. (2012). Gene therapy for oral cancer—Journey to a new horizon. *Oral & Maxillofacial Pathology Journal*, 3(1).

Stahel, R. A., & Zangemeister-Wittke, U. (2003). Antisense oligonucleotides for cancer therapy—An overview. *Lung Cancer*, 41, 81–88.

Stolberg, S. G. (1999). The biotech death of Jesse Gelsinger. *The New York Times Magazine*, 28, 136–140.

Sudhakar, V., & Richardson, R. M. (2019). Gene therapy for neurodegenerative diseases. *Neurotherapeutics*, 16(1), 166–175.

Sun, Y., Yu, D., Geng, X., Ding, D., Yang, Y., Liu, Z., … & Tan, W. (2023). Artificial base-directed in vivo assembly of an albumin–siRNA complex for tumor-targeting delivery. *ACS Applied Materials & Interfaces*, 15(7), 8872–8883.

Taghdiri, M., & Mussolino, C. (2024). Viral and non-viral systems to deliver gene therapeutics to clinical targets. *International Journal of Molecular Sciences*, *25*(13), 7333.

Tamura, R. E., Lana, M. G., Costanzi-Strauss, E., & Strauss, B. E. (2020). Combination of cabazitaxel and p53 gene therapy abolishes prostate carcinoma tumor growth. *Gene Therapy*, 27(1), 15–26.

Tay, Z. W., Chandrasekharan, P., Chiu-Lam, A., Hensley, D. W., Dhavalikar, R., Zhou, X. Y., … & Conolly, S. M. (2018). Magnetic particle imaging-guided heating in vivo using gradient fields for arbitrary localization of magnetic hyperthermia therapy. *ACS Nano*, 12(4), 3699–3713.

Valente, J. F., Queiroz, J. A., & Sousa, F. (2018). p53 as the focus of gene therapy: Past, present and future. *Current Drug Targets*, 19(15), 1801–1817.

Walther, W., & Stein, U. (2000). Viral vectors for gene transfer: A review of their use in the treatment of human diseases. *Drugs*, 60(2), 249–271.

Wang, J. H., Gessler, D. J., Zhan, W., Gallagher, T. L., & Gao, G. (2024). Adeno-associated virus as a delivery vector for gene therapy of human diseases. *Signal Transduction and Targeted Therapy*, *9*(1), 78.

Wang, Z., Li, M., Ji, Y., Yang, M., Yang, W., Wang, J., & Li, W. (2020). Development of a novel bivalent baculovirus vectors for complement resistance and sustained transgene expression and its application in anti-angiogenesis gene therapy. *Biomedicine & Pharmacotherapy*, 123, 109765.

Wirth, T., Parker, N., & Ylä-Herttuala, S. (2013). History of gene therapy. *Gene*, 525(2), 162–169.

Wonder, E., Simón-Gracia, L., Scodeller, P., Majzoub, R. N., Kotamraju, V. R., Ewert, K. K., … & Safinya, C. R. (2018). Competition of charge-mediated and specific binding by peptide-tagged cationic liposome–DNA nanoparticles in vitro and in vivo. *Biomaterials*, 166, 52–63.

Xu, F., Zhong, H., Chang, Y., Li, D., Jin, H., Zhang, M., … & Huang, Y. (2018). Targeting death receptors for drug-resistant cancer therapy: Codelivery of pTRAIL and monensin using dual-targeting and stimuli-responsive self-assembling nanocomposites. *Biomaterials*, 158, 56–73.

Yang, X., Shao, G., Zhang, Y., Wang, W., Qi, Y., Han, S., & Li, H. (2022). Applications of magnetic particle imaging in biomedicine: advancements and prospects. *Frontiers in physiology*, *13*, 898426.

Ylä-Herttuala, S. (2012). Endgame: Glybera finally recommended for approval as the first gene therapy drug in the European Union. *Molecular Therapy*, 20(10), 1831–1832.

Zhang, W. W., Li, L., Li, D., Liu, J., Li, X., Li, W., … & Lam, D. M. K. (2018). The first approved gene therapy product for cancer Ad-p53 (Gendicine): 12 years in the clinic. *Human Gene Therapy*, 29(2), 160–179.

Zhao, H., Ning, S., Nolley, R., Scicinski, J., Oronsky, B., Knox, S. J., & Peehl, D. M. (2017). The immunomodulatory anticancer agent, RRx-001, induces an interferon response through epigenetic

induction of viral mimicry. *Clinical Epigenetics*, 9, 1–11.

Zhao, N., Fan, W., Zhao, X., Liu, Y., Hu, Y., Duan, F., & Xu, F. J. (2020). Polycation–carbon nanohybrids with superior rough hollow morphology for the NIR-II responsive multimodal therapy. *ACS Applied Materials & Interfaces*, 12(10), 11341–11352.

Zhao, N., Yan, L., Xue, J., Zhang, K., & Xu, F. J. (2021). Degradable one-dimensional dextran-iron oxide nanohybrids for MRI-guided synergistic gene/photothermal/magnetolytic therapy. *Nano Today*, 38, 101118.

Zhao, Y., Lee, R. J., Liu, L., Dong, S., Zhang, J., Zhang, Y., … & Teng, L. (2019). Multifunctional drug carrier based on PEI derivatives loaded with small interfering RNA for therapy of liver cancer. *International Journal of Pharmaceutics*, 564, 214–224.

Zhou, Z., Zhang, H., Deng, T., Ning, T., Liu, R., Liu, D., … & Ba, Y. (2019**:** Exosomes carrying microRNA-155 target FOXO3 of endothelial cells and promote angiogenesis in gastric cancer. *Molecular Therapy – Oncolytics*, 15, 223–233.

Pure Sciences International Journal of kerbala

Year:2026 Volume : 3 Issue : 9 ISSN: 6188-2789 Print 3005 -2394 Online

2026,Volume 3 , Issue 9 , PSIJK (88-91)

Pure Sciences International Journal of Kerbala

First Report of Alternaria alternata Causing Leaf Spot on Orange (*Citrus sinensis* (L.) Osbeck) in Karbala Province, Iraq

Zainab L. Hameed [a*]

a Field Crop Department, Agriculture College, University of Kerbala, Karbala, Iraq

P A P E R I N F O

Received: 25.11.2025
Accepted: 12.03.2026
Published: 31.03.2026

***Keywords*:**
Citrus sinensis; citrus leaf spot; Alternaria alternata; ITS-rDNA; fungal foliar disease

A b s t r a c t

During a field survey conducted in 2022 in citrus groves in Alhusaynia territory, Karbala Province, Iraq, leaf spot symptoms were observed on orange foliage. A fungal pathogen was regularly isolated from diseased leaves and identified as Alternaria alternata based on colony and conidial morphology and internal transcribed spacer (ITS-rDNA; PX763615.1) sequence analysis. Pathogenicity was evaluated using a detached-leaf assay, and typical symptoms were reproduced on inoculated leaves, followed by re-isolation of the same fungus. This investigation is the first documented occurrence of A. alternata associated with leaf spot on orange in Karbala Province, Iraq

DOI: 10.53851/psijk.v3.i9. 88-91

1. INTRODUCTION

Sweet orange (Citrus sinensis (L.) Osbeck; family Rutaceae) is an evergreen fruit tree and one of the most widely grown citrus crops (Xu et al.,2012). Globally, it is valued for its nutritional and industrial importance and its central role in fresh fruit supply chains and juice production (Favela-Hernández et al.,2016). Global citrus production and trade are regularly summarized in FAO statistical reporting, underscoring the continuing economic relevance of citrus crops worldwide (FAO, 2022)

Foliar and fruit diseases can constrain citrus productivity and market quality. Among these, diseases caused by Alternaria species are well recognized in citrus-growing regions. Citrus can be affected by several Alternaria-associated disease syndromes, and host susceptibility often depends on citrus genotype and pathogen pathotype (Timmer et al., 2003). In particular, Alternaria brown spot—frequently discussed in mandarins, tangelos, and susceptible hybrids—has been linked to A. alternata (often described as the tangerine pathotype or A. alternata pv. citri), where infections may lead to necrotic lesions on young tissues and can contribute to defoliation and fruit losses in susceptible cultivars (Cuenca et al.,2016) .

Because Alternaria is a species-rich genus with complex taxonomy, accurate identification benefits from integrating morphological assessment with molecular tools such as ITS-based sequencing and phylogenetic analysis. The present study aimed to determine the pathogen associated with leaf spot symptoms seen on orange foliage in Karbala Province, Iraq.This is due to the best of our knowledge, there are no published reports documenting Alternaria alternata causing leaf spot on sweet orange in Iraq, particularly in Karbala Province.

2. MATERIALS AND METHODS

2.1. Symptomatic sample collection

A survey was accomplished in 2022 in orange groves located in Alhusaynia orchards, Karbala Province, Iraq. A leaf spot disease influencing orange trees was noted. The disease symptoms primarily seemed as small in a circular shape and light brown colour, developing to be irregular form in dark brown colour. Nevertheless, a smaller zones stayed in circular shapes with concentric spotes. Some of them, afterward united to generate considerable necrotic spreads ending with the yellowing and drying the leaves on susceptible citrus tissues (Figure 1). Leaves showing suspected fungal leaf spot symptoms were

*Corresponding Author Institutional Email:
zainab.l @uokerbala.edu.iq (Zainab L. Hameed)

collected and transported to the laboratory for pathogen isolation. This is because alternaria leaf spot is a serious fungal disease that significantly reduces citrus yield and fruit quality by causing premature leaf drop and fruit blemishes. (Riyahi et al.,2021).

Figure 1. Typical Leaf spot symptoms on orange leafcollected in this study.

2.2. Isolation and Purification

Diseased orange leaves were cut into small sections (approximately 2 cm), surface-disinfested for two min in sodium hypochlorite (2%), washed thoroughly with sterile distilled water, and plated on water agar. After initial growth at 25 ± 2°C, hyphal tips were transferred to potato dextrose agar (PDA) attuned with the antibiotics ampicillin and kanamycin monosulfate (50 µg/mL each) to obtain pure cultures. (Lahuf et al.,2022) .

2.3. Molecular Identification And Phylogenetic Placement

The fungal DNA was extracted from the isolated fungus. The ITS region of rDNA was amplified with ITS1 and ITS4 primers (White et al.,1990), followed by sequencing. ITS sequences were aligned with reference sequences, and a phylogenetic tree was built via MEGA (version 11,0,13) (Tamura et al.,2021).

2.4.Pathogenicity Test

Pathogenicity was evaluated by means of a detached-leaf assay. Healthy orange leaves (young, fully expanded leaves) were surface-sterilized (70% ethanol, ~30 s), dried, and inoculated with 500 µL of a conidial suspension (1×10^6 conidia/mL). Control leaves were treated with distilled water only. Inoculated and control leaves were incubated at 25 ± 2°C under high humidity in a growth chamber. Symptom development was recorded, and the pathogen was re-isolated from lesions for confirmation. (Akhtar et al.,2011).

3. RESULTS AND DISCUSSION

3.1. Morphological Characterization

Fungal colonies consistently recovered from symptomatic orange leaves showed morphological features compatible with Alternaria spp. On PDA, colonies typically developed a radial growth pattern with initially pale to gray mycelium that darkened with age, becoming olivaceous to blackish. Conidiophores were short and simple, and conidia were pigmented (olive to dark brown), with variable shapes (often ovoid to pyriform) and transverse and occasional longitudinal septation; short beaks may be present depending on isolate and conditions. These characters are consistent with descriptions commonly used to recognize A. alternata in the small-spored Alternaria complex (Simmons, 2007).

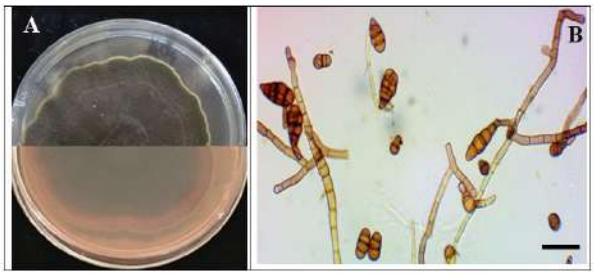

Figure 2: Features of the Alternaria sp. isolated from orange; (A) The upward and downward sides of A. sp. culture on PDA media; (B) Several shapes of A. sp. conidia.

3.2. Molecular Identification And Phylogenetic Placement

ITS-rDNA sequencing and database comparison (BLAST) supported identification of the representative isolate as Alternaria alternata. It showed >99% sequence similarity to several international strains of *A. alternata* such as OP959991.1, MZ047483.1 and OP955785.1. Thus, the sequence was submitted to GenBank database to receive a specific accession number (Alternaria alternata isolate Aa-orange-1; PX763615.1).

The phylogenetic tree constructed based on ITS-rDNA sequences revealed that the Iraqi isolate A. alternata Aa-orange-1 clustered firmly within the Alternaria alternata clade (Figure 3). The isolate grouped closely with reference A. alternata sequences retrieved from GenBank originating from Saudi Arabia (OP959991.1; OP955785.1), Egypt (OR358925.1), China (MZ047483.1; OK316967.1; MZ047506.1), Bangladesh (MH368103.1), and Turkey (KJ739872.1), indicating a high level of genetic similarity among these isolates.

The close clustering of Aa-orange-1 with previously authenticated A. alternata isolates from different geographical regions confirms its taxonomic placement within the A. alternata species complex. The short branch lengths separating Aa-orange-1 from other reference isolates further suggest limited sequence divergence in the ITS region, which is consistent with the conserved nature of ITS sequences within the *A. alternata* group.

An unrelated fungal species, Erysiphe lonicerae (GenBank accession ON248222.1), was used as an outgroup and was clearly separated from the Alternaria clade, supporting the robustness and correct rooting of the phylogenetic tree.

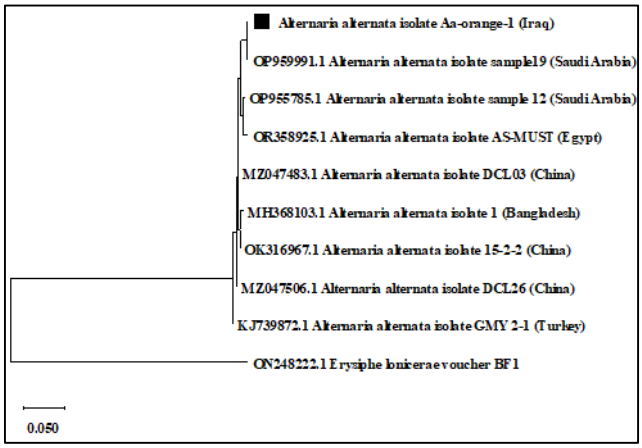

Figure 3: Phylogenetic tree based on ITS-rDNA sequences showing the relationship between A. alternata isolate Aa-orange-1 recovered from orange (Citrus sinensis) in Iraq and reference A. alternata isolates retrieved from GenBank. Erysiphe lonicerae (GenBank accession ON248222.1) was used as an outgroup.

Overall, the phylogenetic analysis, together with morphological characteristics, provides strong molecular evidence that the isolate recovered from orange leaves in Iraq belongs to *Alternaria alternata*.

3.3. Pathogenicity Test

Following seven days of inoculation, the disease symptoms were as slight spherical spots of light-dark brown colour appeared on the inoculated leaves (Figure 4). In contrast, the non-inoculated leaves were with no disease symptoms. The inoculated fungus was re-isolated from affected spotes tissues and re- recognized, implementation Koch's postulates at the assay scale.

Figure 4: Development of typical leaf spot symptoms on orange (Citrus sinensis) leaves one week after artificial inoculation with *A. alternata* isolate Aa-orange-1.

Alternaria diseases are widely recognized in citrus production systems, with important reports describing necrotic lesions and potential defoliation/fruit impacts in susceptible citrus genotypes (Peres et al.,2003; European and Mediterranean Plant Protection Organization, 2021). This report strengthens regional plant health knowledge for Karbala Province and motivate wider surveys across Iraqi citrus-producing areas. Future work should quantify incidence/severity, evaluate cultivar susceptibility.

4.ACKNOWLEDGEMENTS

The author gratefully acknowledges the Agriculture College, University of Kerbala, Iraq, for their support and for providing the necessary facilities to conduct this research.

REFERENCES

Akhtar, K.P.; Sarwar, N.; Saleem, M.Y. and Asghar, M. (2011). Convolvulus arvensis, a new host for Alternaria solani causing early blight of Solanum lycopersicum in Pakistan. Australasian Plant Disease Notes, 6 (1):84–86.

Cuenca, J., Aleza, P., Juárez, J., Navarro, L., & Ollitrault, P. (2016). Fine mapping for identification of citrus alternaria brown spot candidate resistance genes and development of new SNP markers for marker-assisted selection. Frontiers in Plant Science, 7, 1948 .

European and Mediterranean Plant Protection Organization. (2021). Alternaria alternata pv. citri (Alternaria brown spot). EPPO Global Database. https://gd.eppo.int

Favela-Hernández, J. M., González-Santiago, O., Ramírez-Cabrera, M. A., Esquivel-Ferriño, P. C., & Camacho-Corona, M.delR. (2016). Chemistry and Pharmacology of Citrus sinensis. Molecules (Basel, Switzerland), 21(2), 247.

Food and Agriculture Organization of the United Nations. (2022). Citrus fruit: Fresh and processed – Statistical bulletin. FAO.https://www.fao.org/markets-and-trade/ commodities /citrus.

Lahuf, A. A.; Kadhim, A. Q.; Hameed, Z. L. and Almulla, A. M. N. (2022). First report of Paecilomyces rot on rose (Rosa sp.) in Iraq. Journal of Plant Pathology https://doi.org/ 10.1007/s42161-022-01162-7.

Peres, N. A. R., Agostini, J. P., & Timmer, L. W. (2003). Outbreaks of Alternaria brown spot of citrus in Brazil and Argentina. Plant Disease, 87(6), 750–755.

Riyahi, M., Taheri, P., & Mamarabadi, M. (2018). Identification of Alternaria spp. in orange trees of Golestan and Mazandaran provinces and investigating their virulence on orange cultivars. *Iranian Journal of Plant Protection Science*, 48(2), 183–196.

Simmons, E. G. (2007). Alternaria: An identification manual. CBS Fungal Biodiversity Centre.

Tamura, K., Stecher, G., & Kumar, S. (2021). Molecular Biology and Evolution, 38(7), 3022–3027 .

Timmer, L. W., Pever, T. L., Solel, Z., & Akimitsu, K. (2003). Alternaria diseases of citrus—Novel pathosystems. Phytopathologia Mediterranea, 42, 99–112.

White, T. J., Bruns, T., Lee, S., & Taylor, J. (1990). Amplification and direct sequencing of fungal ribosomal RNA genes for phylogenetics. In M. A. Innis, D. H. Gelfand, J. J. Sninsky, & T. J. White (Eds.), PCR protocols: A guide to methods and applications (pp. 315–322). Academic Press.

Xu, Q., Chen, LL., Ruan, X. et al. (2013). The draft genome of sweet orange (Citrus sinensis). Nature Genetics 45, 59–66.

Potts, C. (1995). Using schematic scenarios to understand user needs. *Proceedings of the 1st Conference on Designing Interactive Systems: Processes, Practices, Methods, & Techniques*, 247–256.

Wang, L.-X., & Mendel, J. M. (1992). Generating fuzzy rules by learning from examples. *Systems, Man and Cybernetics, IEEE Transactions On*, *22*(6), 1414–1427.

Weiser, M. (1991). The computer for the 21st century. *Scientific American*, *265*(3), 94–104.

Pure Sciences International Journal of kerbala

Year:2026 Volume : 3 Issue : 9 ISSN: 6188-2789 Print 3005 -2394 Online

2026,Volume 3 , Issue 9 , PSIJK (93-98)

Pure Sciences International Journal of Kerbala

Effect of G Power Ca + Nanocomposite and Bio-Fertilization on the Chemical and Yield Parameters of Sunflower

Q.TH. AL-ASADI [a*]

a College of Education for Pure Sciences, University of Kerbala, Kerbala, Iraq

P A P E R I N F O

Received: 28.01.2026
Accepted: 08.03.2026
Published: 31.03.2026

Keywords:
nanocomposite fertilizers, *Pseudomonas* bacteria, sunflower, yield quality

A b s t r a c t

A field experiment was conducted on the west side of AL-Jadwal Al-Garbi /Hindia/ Karbala, Iraq, during the spring agricultural season of 2023. The objective was to evaluate the effect of G power Ca + Nanocomposite spraying and Bio-Fertilization using *Pseudomonas* bacteria on sunflower yield and seed quality. Two factors were studied. First foliar spraying of G Power Ca+ Nanocomposite at four concentrations (0,2.5, 4 and 5 ml.L^{-1}). Second, Soil application of *Pseudomonas* bacteria at four levels (0, 10, 20 and 60 ml .L^{-1}) injected into Rhizosphere. The examined proceeded in accordance with the experiment design using the Gene stat program ,the arithmetic averages comparison employed the least significant difference (LSD0.05) test.

Measured parameters included Plant height, biological yield , seed content of oil, number of seeds per disc, and, protein in seed , and nitrogen in seed . The highest values were recorded at a concentration of 5 ml/L of G Power Ca+ nanoparticles and 60 ml/L of *Pseudomonas* bacteria for all studied traits, with observed (191.56 cm , 12.76 ton .ha^{-1}, 5.76 % , 1245 seed.$disk^{-1}$, 11.47 % , 2.99 %) showing statistically significant differences compared to the control treatments(122.87 cm , 6.56 ton .ha^{-1}, 1.87 % , 754 seed.$disk^{-1}$, 6.23%,1.04%)respectively . These results highlight the potential for improving sunflower productivity and nutritional quality in arid conditions by combining nanoparticle treatment with biofertilization.

DOI: 10.53851/psijk.v3.i9. 93-98

1. INTRODUCTION

Sunflower (*Helianthus annuus* L.) is a summer crop around that belongs to the Compositae (Asteraceae) family (Sharma *etal*.,2005) . Entering the oil industry for high-cost food, its seeds taste good and source in the high-quality oil industry, and its oil uses include soap and dye (Arshad *etal*.,2010). Its seeds are also essential nutrients for the human body, as they contain vitamins, basic fatty acids, minerals and unsaturated fatty acids, and its oil contains a high proportion of fatty acids, including linoleic acid and oleic acid, which are important medical substances in human diet and contain vitamin E(Baloglum *etal*.,2012)..

In recent times, the use of biosynthesis, which is one of the achievements of Biotechnology, has become widespread. It involves isolating, purifying, and characterizing microorganisms and using them as inoculations in the middle stages of plant growth, helping the plant to absorb nutrients. (Baha *etal*.,2012)

.The microbe content in the Rhizosphere has changed and its success depends on the efficiency of the organism, the compatibility of the micro-organism with the vegetarian family, the competitiveness of the organisms originally found in the soil, as well as the preparation of the living in the Rhizosphere and its viability (Al-Ibrahemi *etal*.,2024). The importance of this composting in providing part of the nutrients for plants, hormones, and some antibiotics can be used to reduce dependence

*Corresponding Author Institutional Email:
queod.theaban@uokerbala.edu.iq (Qioud TH. AL-ASADI)

on chemical fertilizers as a result of the provision of a large part of the nutrients to feed plants, reduce costs of agricultural production and reduce environmental pollution rates (Kumar *etal*.,2016) .Nano - fertilizer is critical to improving crop resilience for disease, and is a means of transporting compounds to target organs
be it root, leaf , fruit or other plant parts, and increasing the content of leaf from chlorophyll (He *etal*.,2018) .The nano-fertilizer (G power Ca +) is an important nano-accumulator used as an agricultural fertilizer produced by nanotechnology. It consists of several compounds, including nitrogen at 8% and calcium at 13% (Sekhon, 2014 and AL-Ibrahemi *etal*.,2020) , Some studies have suggested that nanomaterials have the potential to penetrate seed membranes, stimulate the ability to absorb plants into water, strengthen the enzyme system, and improve Plant
and growth (Al-Ghazal *etal*.,2023 ; Banerjee and Kole ,2016).The aim of study effect of G Power Ca + Nanocomposite and Bio-Fertilization on the Chemical and Yield Parameters of Sunflower

Material and method

The field experiment was carried out on the west side of Hindi Karbala, Iraq, for the spring agricultural season of 2023. The soil is sandy clay of the field was ploughed and blessed and then divided into experimental units, the size of the pilot unit 15 m and left 75 cm between the area and 25 cm between the groove and the other. The seeds were sown on 21/3/2023, and after germination and the emergence of plants, the land was watered regularly according to the plant's needs, and weeding was carried out manually and repeated as required. The experiment comprised a completely randomized block design (RCBD) performed with two factors. The first factor is G power Ca + Nanocomposite(8% Nitrogen , 13% water soluble CaO , Manufacturer Agri Sciences Ltd .Sti Izmir-Turkey), spray with three concentrations in addition to the control treatment (0, 2.5, 4, 5 ml.L^{-1}) in the early morning to avoid high temperatures. The spraying process was completed to reach full wetness and the 2-litre hand spray was used. The second factor involves ground composting with bacteria *Pseudomonas* with injection at concentrations (control, 10, 20, 60 ml .L^{-1}) in the Rhizosphere. Gram-negative *Pseudomonas flourescens* was used in the experiment. Twenty root zone soil samples were collected from different plant areas and placed in plastic bags to prevent drying. One gram of soil was taken from each sample, and each gram was added separately to 9 ml of sterile water to prepare an aqueous suspension. This suspension was placed in a shaker, and a series of dilutions were prepared,0.1 ml of each dilution was transferred to solid KingB agar. The samples were incubated at 25°C for 24–48 hours. The bacteria were then purified by re-culturing on Pseudomonas agar. Microscopic and biochemical tests were subsequently performed to identify the bacterial species. (Rosas *etal*., 2009).

The fertilizer added urea fertilizer and potassium fertilizer in the form of potassium sulfate and phosphate fertilizer in the recommended quantities. The first batch was added after 30 days of cultivation and the second batch after 60 days .

1- yield parameter: Plant height, number of seeds in the disc, biological yield.
2- chemical parameter: percentage of oil, percentage of protein in the Seeds , percentage of nitrogen in the Seeds.

Statistical analysis: Statistical analysis was performed according to the experimental design using Gene stat program. The arithmetic averages comparison employed the Least Significant Difference (LSD0.05) test.

Results and Discussion

Plant height

The results in Table (1) indicated a significant effect of G power Ca + Nanocomposite spraying and *Pseudomonas* on plant length. G power Ca + Nanocomposite showed the highest effect at a concentration of 5 m.L^{-1} (169.72 cm), while the lowest plant height was observed in the control (133.505cm). The increase in plant height may be attributed to calcium, a major nutrient that regulates metabolism, supports plant development and promotes cell expansion and division (Duan *etal*.,2022). Furthermore, nano-fertilizers possess unique properties; their small size and increased surface area allow for more efficient absorption by plants, leading to faster biochemical reactions and direct entry into plant cells (Sabir *etal*.,2014).
Similarly, *Pseudomonas* had a significant effect with the highest concentration (60 ml. L^{-1}) resulting in plant height of 173.375 cm, while the lowest concentration was recorded in the control (138.97cm). The role of bacteria in plant growth is linked to enhanced light absorption and efficient nutrient transfer to sink tissue (Al-Rawi,2010).

Biological yield

The results of Table (1) indicated a significant effect of G power Ca + Nanocomposite spraying and *Pseudomonas* on biological yield. The highest yield was observed at the highest concentration (5 ml.L^{-1}), reaching 10.856 tons ha^{-1}, while the lowest yield was recorded in the control (7.958 tons ha^{-1}). This effect is attributed to calcium's essential role in regulating and controlling plant metabolism, supporting growth, maintaining cell wall structure, and enhancing resistance biotic non-biotic stress (Waraich *etal*.,2011) Furthermore, calcium increases the availability of essential plant nutrients, particularly nitrogen, leading to increased efficiency in carbon metabolism and its products, thus positively impacting plant productivity (Sham *etal*., 2019).. *Pseudomonas* showed a significant effect on biological yield, with the highest yield observed at the 60 ml/bacteria treatment(11.573 tons ha^{-1}) and the lowest in the control group (7.958 tons ha^{-1}). This increase can be attributed to the bacteria role in enhancing dry matter production and accumulation during the grain-filling period, which subsequently increased in the number of grains per plant (El-Nagdy *etal*.,2010).

Percentage of oil in seeds

The results of Table (1) indicate a significant effect of G power Ca + Nanocomposite spraying and Pseudomonas on the percentage of oil in seeds. The highest oil percentage (4.205%) was recorded in treatment with G power Ca + Nanocomposite at the highest concentration (5 ml.L^{-1}), while the lowest percentage (2.56%) was observed in the control.

The increase in oil percentage in seeds may be due to higher of nitrogen and phosphorous concentration and the production of plant hormones. These factors promote meristem cells division, enhance the growth of radical and shoot, and stimulate nitrogen accumulation in plant tissues. This in turn improves the efficiency carbon assimilation and its translocation from source tissues its transition from the source to the sink ultimately, increasing the of oil content in seeds (Sekhon,2014). A significant effect of *Pseudomonas* was observed with the highest oil percentage (4.71%) recorded in the treatment with 60 ml .L^{-1} suspension, while the lowest percentage (2.37%) was found in the control . The increase in seed oil content is likely due to the role of bacteria in enhancing nutrient availability, uptake, and accumulation within the plant tissues (Kumar *etal*.,2016). The increase in seed oil content is likely due to the role of bacteria in enhancing nutrient availability, uptake, and accumulation within the plant tissues (Kumar *etal*.,2016).

Number of the seeds in the disc

The results of table (1) indicate a significant effect of G power Ca + Nanocomposite spraying and *Pseudomonas* on the number of seeds per disc. The G power Ca + Nanocomposite at the highest concentration (5 ml.L^{-1}) yielded the highest seed count (1034.75seed.disk-1), while the control treatment showed the lowest at the control (873.25 seed.disk-1). This increase may be due to enhanced vegetative growth, which is associated with higher dry matter accumulation. Increased humidity levels and nitrogen availability, promote carbon assimilation, to great plant expansion floral development(Singh *etal*.,2015). Calcium plays an important role in regulating and controlling plant metabolism and development, as well as maintaining cell wall structure.(Manjaiah *etal*.,2019) .

A significant effect of a *Pseudomonas* was observed, with the highest seed count (1105 seed.$disk^{-1}$) recorded in the 60 ml. L^{-1} treatment and the lowest (814.5 seed.$disk^{-1}$) in the control. The increase in seed number in the disc may attributed to the role of *Pseudomonas* in nutrient availability, which promotes early silk emergence through increased cell division and elongation. This synchronization with pollen production improves fertilization efficiency, leading to a higher seed account per disc (Shakya and Barwa , 2017), and may be due to the biological role of *Pseudomonas* in increasing the availability of nutrient elements and their absorption and transfer within the plant tissue and in appropriate concentrations. Which means increasing the efficiency of C4 Carbon fixation on the one hand and the transfer of metabolic compounds to the new locations of the reproductive stage of the plant on the other side(Gupta and Gupta,2005)

percentage of protein in the seeds

The results of Table (1) indicate a significant effect of G power Ca + Nanocomposite spraying and *Pseudomonas* on percentage of protein in the seeds. The highest protein content [1] (9.81%) was recorded in the treatment with G power Ca + Nanocomposite at the highest concentration (5 ml.L) while the lowest (7.243%) was observed in the control. The increase in seeds protein content may be attributed to increased calcium concentration In leaf tissues, which play a crucial role in nitrogen metabolism and prorien synthesis in Zea maize (Jampilek and

Kraeova ,2015).Similarly, *Pseudomonas* showed a significant effect, with the highest protein content (10.008%) recorded in the 60 ml .L^{-1}treatment and the lowest (7.173%) in the control.

Percentage of nitrogen in the seeds

The results of table (1) indicated a significant effect of G power Ca + Nanocomposite spraying and Pseudomonas in percentage of nitrogen in the seeds % , showing a significant effect of G power Ca + Nanocomposite with the highest concentration in treatment of 5 ml.L^{-1}
(2.24%) and the lowest concentration at the control (1.586%).
The study showed a significant effect of *Pseudomonas*, with the highest concentration(2.51%) recorded in the treated group (60 ml.L^{-1}), while the lowest concentration was recorded in the control group(1.34%) . These results are consistent with those of Al-Yassiri *etal.* (2024). This may be attributed to the effect of *Pseudomonas* on the absorption of mineral elements, which in turn affects cell division and mitochondrial formation. As a result, the leaf surface area and its nutrient supply increase , leading to increased carbohydrate and protein production.

Conclusion

The study highlights the potential of integrating nanocomposite fertilizers and bio-fertilization in improving sunflower yield and nutritional quality under arid conditions

Recommendations

1-recommend using nanofertilizers instead of chemical fertilizers.
2- recommend using biofertilizer as a foliar spray on the vegetative parts.

Table (1): The effect of G power Ca + Nanocomposite and Pseudomonas on Plant height, Biological yield, Oil in seeds, Seeds in the disc, Protein in the seed and Nitrogen in the seed.

G power Ca + Nanocomposite	*Pseudomonas* ($ml.L^{-1}$)	Plant Height (cm)	Biological yield ($ton.ha^{-1}$)	Oil in seeds %	Seed No. in disc ($seed.disk^{-1}$)	Protein in seeds%	Nitrogen in seed%
Control	Control	122.87	6.56	1.87	754	6.23	1.04
	10	129.76	7.67	2.26	848	6.75	1.56
	20	137.74	8.67	2.77	895	7.34	1.77
	60	143.65	9.97	3.34	996	8.65	1.97
2.5	Control	135.45	7.56	2.23	794	6.96	1.22
	10	146.56	8.64	2.79	899	7.23	1.68
	20	165.45	10.67	3.76	975	7.87	1.84
	60	175.84	11.63	4.76	1046	9.68	2.23
4	Control	147.91	8.75	2.45	865	7.56	1.34
	10	158.34	9.21	3.37	945	8.54	1.77
	20	162.63	10.94	3.99	998	9.56	1.99
	60	182.45	11.93	4.98	1123	10.23	2.83
5	Control	149.65	8.96	2.95	845	7.94	1.76
	10	164.76	9.94	3.76	995	9.85	1.87
	20	173.56	11.75	4.35	1054	9.98	2.34
	60	191.56	12.76	5.76	1245	11.47	2.99
L.S.D		1.76	1.84	1.34	1.45	1.74	1.84
Effect of G power Ca + Nanocomposite	Control	133.50	8.218	2.56	873.25	7.243	1.586
	2.5	162.33	9.625	3.385	928.5	7.935	1.743
	4	162.83	10.208	3.698	982.75	8.973	1.983
	5	169.72	10.856	4.205	1034.75	9.81	2.24
L.S.D		1.78	1.86	1.86	1.75	2.75	1.56
Effect of *Pseudomonas* (ml/bacteria)	Control	138.97	7.958	2.375	814.5	7.173	1.34
	10	149.855	8.82	3.038	921.75	8.093	1.72
	20	159.868	10.508	3.718	980.5	8.688	1.99
	60	173.375	11.573	4.71	1105	10.008	2.51
L.S.D.		1.63	1.02	1.13	1.70	1.02	1.32

REFERENCES

Al-Ghazali LH, Al-Masoody I H ,Ismael M H , Al-Ibrahemi N (2023). Effect of Alcohol Extract, Volatile Oil and Alkaloid Isolated from Capsicum frutescens L. Fruits on Candida albicans , IOP Conference Series: Earth and Environmental Science , 1225(1), 012075.

Al-Ibrahemi N, Al-Asadi QTHY, Hassan SF, Hamid BA, Jawad NN (2024). Response of flax (*Linum usitatissimum*) to nano-NPK and emg-1 in growth, oil content, and active compounds. *SABRAO J. Breed. Genet.* 56(6): 0-0. http://doi.org/10.54910/sabrao2024.56.6.

AL-Ibrahemi N, Hasan R M, Alslman K (2020). Effect of Zinc oxide nanoparticles on the oxidant stress (Malonaldehde MDA, lipid peroxidation level LPO) and antioxidant GSH glutathione) .Medico-Legal Update ,20 (1), 882-888.

Al-Rawi A A (2010). The effect of the organic materials addition on Azotobacter efficiency and nitrogen fixation in salinity soil. Anbar Journal of Agriculture Sciences. Special lssue. 8(4):164-171.

AL-Yassiry A S , AL-Jenaby H K A, AL-Masoody I H , AL-Ibrahemi N (2024). biofertilizers effect on the active compounds of sweet basil *Ocimum basilicum* L. SABRO J.Breed. Genet. 56(1): 11-28.

Arshad M, Khan M, Jadoon S, Mohand A (2010). Factor analysis in sunflower (*Helianthus annuus L.*) to investigate desirable hybrids. Pak. J. Bot., 42 (6): 4393-4402.

Baha A A , Majeed N H , Obaid A M A (2012). Effect of bio-fertilizer with PSB on the growth and yield of wheat plant. University of Karbala Scientific Journal .10(4):49-56.

Baloglum M, Kavas M ,Ayadin GOktem H, Yucel A (2012). Antioxidative and physiological responses of two sunflower (Helianthus annuus) cultivar under PEG-mediated drought stress. Turk J. Bot.,36: 707-714.

Banerjee J , Kole C (2016) . Plant Nanotechnology: An overview on concepts, strategies, and tools. In Plant Nanotechnology;

Duan, S., Zhang, C., Song, S., Ma, C., Zhang, C., Xu, W., ... & Wang, S. (2022). Understanding calcium functionality by examining growth characteristics and structural aspects in calcium-deficient grapevine. Scientific reports, 12(1), 3233.

El-Nagdy G A, Nassar D M A, El-Kady E A, El-Yamanee G S A(2010). Response of flax plant (Linum usitatissimum L.) to treatments with mineral and bio-fertilizers from nitrogen and phosphorus. J. Amer. Sci. 6(10): 207-217.

Gupta, N. K. and S. Gupta.(2005) Growth regulators. in N. K. Gupta and S. Gupta (edrs.). Plant Physiology. Oxford and IBH Publ., New Delhi, p. 286-349. 26. Bakry, A. B.; O. A. Nofal; M. S. Zeidan and M. Hozayn. 2015. Potassium and zinc in relation to improve flax varieties yield and yield components as grown under sandy soil conditions. Agric. Sci. 6: 152-158.

He X , Deng H, Hwang H M (2018). The current application of nanotechnology in food and agriculture. J. food druganal., 27: 1–21.

Jampilek J K , Kraeova (2015) . Application of nanotechnology in agriculture and food industry. Its prospects and risks. Ecol.Chem.Eng.22(3):321- 361.

Kole, C., Kumar, D. S., & Khodakovskaya, M. V. (2016). Plant nanotechnology. New York: Springer. pp. 1–14.

Kumar S , Singh J K , Vishwakarma A (2016). Effect of NPK levels and bio-fertilizers on quality parameters and seed yield of linseed (arameters and seed yield of linseed (Linum usitatissimum L.) varieties under irrigated condition. Intl. Quarterly J. of Life Sci. 11(2): 1339-1343.

Manjaiah, K. M., Mukhopadhyay, R., Paul, R., Datta, S. C., Kumararaja, P., and Sarkar, B. 2019.Clay minerals and zeolites for environmentally sustainable agriculture. In Modified Clay and Zeolite Nanocomposite Materials (pp. 309-329).

Rosas, S.B., Avanzin, G., Carlier, E., Pasluosta, C., Pastor, N., Rovera, M.(2009). Root colonization and growth promotion of wheat and maize by Pseudomonas aurantiaca SR1. Soil. Biol. Biochem. 41, 1802–1808.

Sabir, S., Arshad, M., and Chaudhari, S. K.(2014). Zinc oxide nanoparticles for revolutionizing agriculture: synthesis and applications. The Scientific World Journal, 2014: 1-8.

Sekhon B S (2014) .Nanotechnology in agri – food production : an overview . Nanotechnol Library of Medicine.

Shakya L, Barwa Sh (2017). Effect of reduced doses of chemical fertilizers with dual inoculation of biofertilizers on linseed varieties. Intl. J. Innovative Res. Sci., Engineering and Technol. 6(7): 14123-14129.

Sham S. Patel, B. N. Aravinda Kumar, Meena Dharam Singh, S. C. Alagundagi, V. P. Savalgi, and M. K.(2019) . Rabinal. Foliar Application of Green Synthesized Zinc Sulphide and Zinc Oxide Nano Particles Enhances Growth, Root Attributes, Yield and Oil Quality of Sunflower (Helianthus annuus L.) Global Journal of Science Frontier Research: D Agriculture and Veterinary. 19 (4): 11-19.

Sharma DK, Singh , Kumbbare P (2005) . Response of sunflower to conjunctive use of saline drainage water and non- saline canal water irrigation. Agron. and Soil Sci. S1 (1): 91-100.

Sharon M A , Choudhary K, Kumar R (2010) . Nanotechnology in agricultural diseases and food safety . J. Phytol . 2 :83 – 92.

Singh A , Singh S , Prasad S M (2016) . Scope of nanotechnology in crop science : Profit or Loss . Research and Reviews: Journal of Botanical Sciences, 5(1) : 1- 4.

Singh S , Bijendra KS, Yadav S M , .Gupta A K (2015). Applications of Nanotechnology in Agricultural and their Role in Disease Management. Research Journal of Nanoscience and Nanotechnology 5 (1) : 1 – 5.

Waraich E A , Rashid A , Saifullah M Y , Ashraf E (2011). Role of mineral nutrition in alleviation of drought stress in plants,A.J.C.S.,5(6):764-77

Pure Sciences International Journal of kerbala

Year:2026 Volume : 3 Issue : 9 ISSN: 6188-2789 Print 3005 -2394 Online

2026,Volume 3 , Issue 9 , PSIJK (100-108)

Pure Sciences International Journal of Kerbala

A Review on Polymeric Hydrogels for Dual Applications in Water Purification and Wound Healing

Alaa H. Hussein [a*], Zainab M. Shakir [a] , Ali R. Khudhair [a] , Maha M Obaid [a] , Furqan M Hussein [a]

[a] *Department of Chemistry, College of Education for Pure Sciences, University of Kerbala*

P A P E R I N F O

Received: 27 .02.2026
Accepted: 19.03.2026
Published: 31.03.2026

***Keywords*:**
Polymeric hydrogels , Water filtration, Wound patching , Dual-functional materials , Common remediation, Tissue recuperation , Biomedical applications.

A b s t r a c t

Polymeric hydrogels have been recognized as a new generation of material for multifunctional use owing to their high water retention capacity, three-dimensional crosslinked network structure, and responsiveness to external stimuli like pH, temperature, and ionic strength. These unique physicochemical characteristics of the hydrogels have made these materials critical in a multitude of biomedical and environmental uses. This review describes the dual-functional applications of polymeric hydrogels in two important domains: water purification and wound healing. Hydrogels are considered sustainable, ecologically friendly, and inexpensive adsorbent materials in the field of water treatment. Their excellent porous structure coupled with tunable surface chemistry aid in the efficient removal of a diverse spectrum of contaminants—heavy metals [Pb^{2+}, Cd^{2+}, Hg^{2+}], synthetic dyes, and organic contaminants from industrial and domestic wastewater. The addition of functional groups including carboxyl, hydroxyl, amine and sulfonic groups improves their adsorption power and selectivity to particular pollutants. Moreover, by incorporating the nanomaterials metal oxide nanoparticles or carbon-based nanostructures, the mechanical stability, reuse rate and overall adsorption performance of hydrogels would be improved substantially. Conversely, polymeric hydrogels have demonstrated excellent activity in wound healing since they can mimic the natural extracellular matrix (ECM). Their soft, fluid-rich and biocompatible structure offers a perfect microenvironment for the adhesion, proliferation and regeneration of the cells. Hydrogels provide a moist wound microenvironment conducive to accelerating healing, preventing dehydration and minimizing infection risks, enhancing angiogenesis and promoting healing. Furthermore, they possess the possibility to be controlled drug delivery agents, allowing long-term release of various therapeutic agents as antibiotics such as antimicrobial compounds, anti-inflammatories and growth factors, as localized system. Their adjustable degradation rate and mechanical characteristics improve the application of a variety of materials to wounds, including chronic and burn wounds. Hydrogel design innovations in recent years have been more focused on a smart and stimuli-responsive design, which can be dynamically designed to adapt and change their properties for different environmental conditions. Advancements in physical and chemical crosslinking systems are increasing structural durability and performance. Yet, they still encounter several limitations, such as poor mechanical strength in some formulations, scalability and long-term durability in practical applications. Polymeric hydrogels serve as a promising platform for transforming hydrogels and with a strong potential to address global challenges in an age of continuous environmental preservation, sustainability, and health systems

DOI: 10.53851/psijk.v3.i9. 100-108

1. INTRODUCTION

Presentation Polymeric hydrogels represent an exceptional class of delicate materials that have gotten considerable scientific intrigued due to their extremely hydrated, three-dimensional crosslinked systems competent of engrossing and holding expansive volumes of water or organic liquids without dissolving. (Peppas & Hoffman, 2012) (Caló & Khutoryanskiy, 2015). These materials can be synthesized from a wide assortment of common and engineered polymers,

*Corresponding Author Institutional Email: alaa.hadi@uokerbala.edu.iq (Alaa H. Hussein)

counting but not restricted to polyvinyl alcohol (PVA), polyethylene glycol (PEG), chitosan, alginate, and polyacrylamide, advertising tunable mechanical, chemical, and organic properties to suit differing applications (Li & Mooney, 2016).

Their biocompatibility, biodegradability, and capacity to reply to natural boosts such as pH, temperature, and ionic quality position them as perfect candidates in both biomedical and natural areas (Ahmed, 2015) (Kopeček, 2007).

One of the foremost compelling headings in hydrogel inquired about is the investigation of their double usefulness, especially in water refinement and wound mending. In spite of the reality that these two areas may at first show up to be irrelevant, they both require materials with tall porousness, specific reactivity, antimicrobial movement, and the capacity to powerfully associated with their environment. Since of their permeable structures and versatile surfaces, hydrogels successfully meet these necessities (Gong, 2010). Polymeric hydrogels are becoming increasingly examined within the field of water refinement since they can be utilized to expel a wide run of poisons from mechanical and metropolitan wastewater, counting engineered colors, pathogenic microorganisms, overwhelming metal particles (e.g., Pb^{2+}, Cd^{2+}, Hg^{2+}), Their adequacy is to a great extent due to the useful bunches display on their polymer chains—such as hydroxyl, carboxyl, amine, and sulfonic groups—which give dynamic locales for particle trade, complexation, and adsorption forms (Zhuang et al., 2021). In expansion, nanoparticles, attractive components, or bioactive specialists can be included to hydrogels to extend their selectivity and capacity, subsequently expanding their productivity in evacuating contaminants (Reddy et al., 2020). On the other hand, in wound mending applications, hydrogels act as perfect wound dressings due to their capacity to keep up a wet environment, retain exudate, and give a physical boundary against microbial attack. Bioprove of inborn biocompatibility and oxygen permeability promote cellular motion and expansion and reduce aggravation and disease incidence (Nair et al., 2022) (Boateng et al., 2008).Reconstructive agents such as anti-microbials, anti-inflammatory drugs, development factors, and indeed stem cells can presently be conveyed absolutely through advanced hydrogel frameworks, permitting for speedier tissue recovery and less scarring (Huang et al., 2018). Stimuli-responsive components also enable the concept of 'smart' hydrogels which can release their payload in response to specific wound conditions such as changes (Wang et al., 2021). The simultaneous utility of polymeric hydrogels in biological and therapeutic settings emphasizes their transformative potential as multifunctional stages. While broad studies have tended to their use in human spaces, there remains a need for a comprehensive diagram bridging these two fundamental domains. This review therefore aims to provide a detailed and comprehensive investigation of polymeric hydrogels for applications in wound healing and water treatment. It will discuss the fundamental mechanisms, fabrication methodologies, performance metrics, and concerns of each application. It will further discuss the emerging trends and where next-generation hydrogel frameworks are headed in the future.

diagnosis and treatment of cancer and chronic illnesses, emphasizing their role in the evolution of nanomedicine and future perspectives in personalized therapeutic strategie

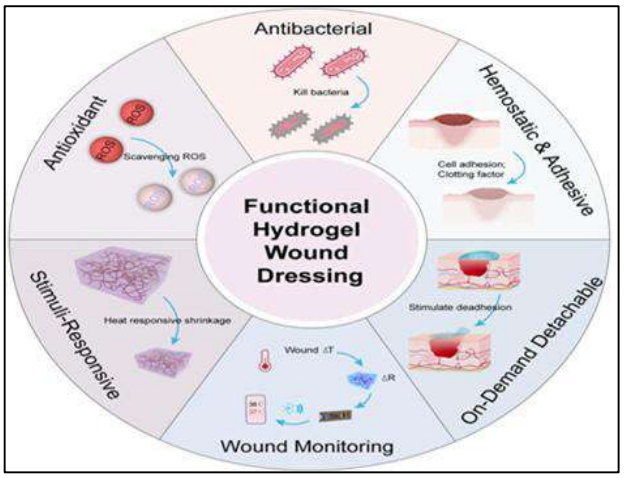

Figure 1: Hydrogel based wound dressings with multifunctional properties. This schematic summarizes the main characteristics of utility hydrogels used in wound healing, including their antibacterial activity, antioxidant capacity, hemostatic and cement function, stimuli-responsiveness, on-demand separation and wound observation abilities.

2. Physicochemical Properties of Polymeric Hydrogels

Polymeric hydrogels possess a one of a kind set of physicochemical properties different from other delicate materials, which makes them widely applicable in biomedicine and natural building. The reasonableness of a hydrogel for double applications such as wound healing and water filtration depends largely on them - including water assimilation, mechanical quality, porosity, degradability, responsiveness to jolts, and surface chemistry. Hydrogels can easily assimilate and retain water, and abundant polar functional groups on their polymer chains: hydroxyl (–OH), carboxyl (–COOH), amino (NH_2), and sulfonic ($-SO_3H$) groups (Zhang et al., 2017).

TABLE 1: Comparison of Common Polymeric Hydrogels

Polymer	Functional Groups	Biocom-patibility	Crosslinking Agents
Polyvinyl Alcohol	–OH	High	Glutaraldehyde
Chitosan	$–NH_2$, OH	Very High	Genipin Sodium Tripolyphospate (TPP)
Polyethylene Glycol (PEG)	–OH	High	Antibacterial wound dressings pollutant adsorption
Polyacrylami-de (PAAm)	$–CONH_2$	Moderate	Hydrogel scaffolds heavy metal adsorption
Polyacrylamide (PAAm)	UV/ Phıto-initiated systems	*N,N'*-Methylene-bisacryamic-dide, UV	Hydrogel scaffolds heavy metal adsorption

These assemblies assist in the joining of hydrogen bonds to the surfaces of the water, as they lead to notable swelling without breakdown. This ability facilitates the generation of a wet wound structure that promotes epithelialization and autolytic debridement in wound treatment . Nevertheless, a tall water content has potential for expeditiously spreading the toxins into a hydrogel structure, and allowing for compelling trapping or neutralisation of toxic species (e.g., heavy metals, dyes, and naturally occurring micropollutants) (Thakur et al., 2021). The mechanical properties of the hydrogels, including their stiffness, compressive quality, flexibility, and shear resistance, are of equal importance. The crosslinking density and molecular weight of the polymer chains determines these properties. When dealing with wound rehabilitation, especially where there is high-energy district, like a joint or a region under the mechanical stretch, hydrogels must be relatively vigorous both to prevent damage or damage and be also very flexible to conform to any surface tissue (Yang et al., 2019). Hydrogels need to resist prolonged exposure to flow as well as changes in pressure and chemical parameters in water treatment systems. Subsequent advances in double-network hydrogels and nanocomposite hydrogels have further developed mechanical strength while not inhibiting swelling property and biocompatibility (Liu et al., 2020). Porosity and internal architecture also be vital in determining diffusion rates, loading capacity, and interaction energy in the hydrogel network. Permeable hydrogels with interconnected channels allow highly permeable channels when used in water filtration (Haraguchi & Takehisa, 2002), which allow contaminants to penetrate all the way deep into the hydrogel and also to transport nutrients, waste, or therapeutic agents in wounds, such as a wound. Pore size and distribution to accommodate for specific applications are determined through freeze-drying, porogen leaching and gas foaming. Biodegradability is particularly useful insight as its another major perspective, and this can be useful in a biomedical area where the hydrogel has to degrade in situ after transmitting its useful payload to an environment or promoting tissue healing. In the enzymatic and hydrolytic state, they showed that in fact, polymers such as chitosan, gelatin, alginate and hyaluronic acid can naturally be biodegradable (Li et al., 2022).In an artificial polymeric environment, however, supplementary adaptation (or co-polymerization) of the attached linkers with degrade over time for controlled destruction in time is needed. Of importance, in water treatment, biodegradable hydrogels presented an environmentally friendly transfer pathway at a lower environmental burden than the conventional non-degradable adsorbents (Hoare & Kohane, 2008).

The swelling proportion, characterized as the weight or volume increment upon water retention, may be a basic plan parameter. It impacts not as it were the hydrogel's capacity to hold liquids but moreover its mechanical execution and porousness. Swelling is touchy to outside conditions such as ionic quality, pH, and temperature, and is regularly abused within the advancement of stimuli-responsive hydrogels (Zhang et al., 2020). In wound mending, pH-responsive hydrogels can discharge antimicrobial specialists in tainted (acidic) situations, whereas temperature-sensitive hydrogels can experience sol-gel moves close body temperature for injectable treatments (Qiao et al., 2021). Essentially, in water decontamination, shrewd hydrogels can be built to specifically adsorb toxins beneath particular natural triggers.

The surface chemistry and functionalization of hydrogels decide their interfacial intuitive with organic tissues or poison particles. Surface adjustments can incorporate the presentation of liking ligands, antimicrobial operators, ion-exchange bunches, or nanoparticles to give particular reactivities. For illustration, the conjugation of silver nanoparticles (AgNPs) improves antibacterial properties in wound care, whereas thiol or amine bunches can progress the capture productivity of overwhelming metals in sullied water (Tamesue et al., 2023) .Besides, attractively responsive hydrogels, created by implanting Fe_3O_4 nanoparticles, permit for simple partition and recuperation after water decontamination cycles (Abdul-Zahra et al., 2025).In pith, the levelheaded plan of hydrogel frameworks that are not as it were viable but also adaptable to a assortment of applications is made conceivable by the interaction of these physicochemical properties. Progressed hydrogels with these characteristics can be custom-made to fulfill their full potential as multifunctional materials by performing synergistic capacities in a wide range of applications, counting wound mending and mechanical emanating sifting.

3. Applications of Polymeric Hydrogels in Water Purification

Polymeric hydrogels have picked up critical consideration in natural remediation due to their tunable chemical composition, tall porosity, and capacity to assimilate and associated with a wide run of waterborne poisons. Through a assortment of forms like adsorption, particle trade, photocatalysis, and chemical authoritative, their three-dimensional organize structure makes it conceivable to capture, immobilize, or debase contaminants. They are reasonable for treating a wide run of toxins, counting natural micropollutants, colors, pharmaceutical buildups, and overwhelming metals.

3.1. Getting Freed of Overwhelming Metals

Due to their harmfulness, perseverance, and affinity to bioaccumulate, overwhelming metals like lead (Pb^{+2}), cadmium (Cd^{2+}), mercury (Hg^{2+}), and arsenic (As^{3+}) posture critical dangers to human wellbeing as well as the environment. Hydrogels functionalized with carboxyl, amine, thiol, and sulfonate bunches display solid authoritative partiality to metal particles, encouraging their expulsion through coordination or ion-exchange components (Lu et al., 2021).

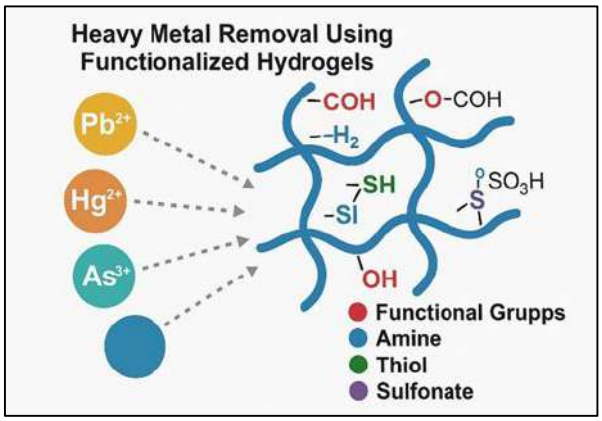

Figure 3: Mechanism of heavy metal removal using functionalized polymeric hydrogels, illustrating the coordination between functional groups (carboxyl, amine, thiol, and sulfonate) and heavy metal ions (Pb^{2+}, Hg^{2+}, As^{3+}).

For case, chitosan-based hydrogels containing amino bunches have illustrated fabulous adsorption capacities for lead and chromium particles from mechanical wastewater (Li et al., 2022).

By expanding surface zone, mechanical quality, and reusability, composite hydrogels with inorganic fillers like bentonite, graphene oxide, and attractive nanoparticles move forward metal particle evacuation effectiveness (Liu et al., 2021). They are financially reasonable for large-scale operations since these crossover materials regularly allow recovery and different utilization cycles with negligible execution misfortune.

3.2. Adsorption of Natural Poisons and Colors

Engineered colors from material, paper, and nourishment businesses are another major lesson of water toxins. Numerous of these colors are non-biodegradable, carcinogenic, and safe to routine treatment strategies. Polymeric hydrogels, especially those determined from common polymers like alginate and cellulose, are successful in adsorbing anionic and cationic colors through electrostatic intuitive, hydrogen holding, and hydrophobic intelligent (Rusu et al., 2019). In addition, hydrogels can be custom-made to target particular color classes. For occasion, cationic hydrogels with quaternary ammonium bunches appear solid partiality for corrosive and responsive colors, though anionic hydrogels are more compelling against essential colors (Hussain et al., 2023). Keen hydrogels that react to pH or temperature changes can moreover direct color take-up and discharge, improving control and recuperation (Ma et al., 2020).

Figure 2. Schematic illustration of hydrogel adsorption of natural toxins and dye molecules.

3.3. Pharmaceutical and Micropollutant Capture

Developing contaminants such as pharmaceuticals, individual care items, and endocrine-disrupting compounds are habitually recognized in water bodies and posture long-term environmental dangers. Hydrogels offer a promising stage for their expulsion due to their tall surface region and the plausibility of consolidating particular utilitarian bunches or acknowledgment destinations (Khan et al., 2020). Cyclodextrin-functionalized hydrogels, for occurrence, have illustrated the capacity to trap hydrophobic particles like hormones and anti-microbials through host-guest intuitive (Wang et al., 2021).

3.4. Photocatalytic and Antibacterial Employments

Past detached adsorption, hydrogels can be designed to effectively corrupt poisons or repress microbial development. Joining photocatalysts such as titanium dioxide (TiO_2) or zinc oxide (ZnO) into hydrogel

lattices permits for the decay of natural contaminants beneath UV or obvious light introduction (Zhang et al., 2018). These photocatalytic hydrogels combine filtration and corruption in a single step, advertising a green and productive water treatment arrangement.

At the same time, hydrogels inserted with silver nanoparticles, copper oxide, or quaternary ammonium compounds display strong antimicrobial properties, decreasing biofouling and anticipating auxiliary defilement amid water treatment (Ahmad et al., 2020). This dual-functionality—adsorption furthermore disinfection—adds a critical advantage over customary sorbents.

3.4. Utilizability and Recovery

The adsorbent material's regenerability and capacity to be repurposed is one of the foremost imperative perspectives of commonsense water filtration. Numerous hydrogel frameworks permit recovery utilizing mellow corrosive, base, or salt arrangements to desorb bound contaminants without harming the hydrogel lattice (Zhang et al., 2019). Reusable hydrogels not as it were diminish treatment costs but too minimize natural squander, making them economical materials for rehashed application.

4. Applications of Polymeric Hydrogels in Wound Healing

Polymeric hydrogels have been introduced as advanced restorative materials through their robust water substance, biocompatibility, adaptability, and ability to provide a moist mending environment for wounds to recover after they are healed. These hydrogels mimic the extracellular lattice (ECM The Extracellular Matrix), advertising both basic back and bioactive usefulness that quickens tissue recovery. Because of their wide range of chemical and physical properties, they can be used in various wounds ranging from shallow scraped spots to incessant diabetic ulcers and burn wounds (Kumar et al., 2020).

4.1. Moisture Retention and Oxygen Permeability

To foster the development of cell rearrangement, angiogenesis, and autolytic debridement the maintenance of a damp wound environment is crucial. Hydrogels exceed expectations in this range due to their water-holding capacity and besides facilitating the exchange of gases, particularly oxygen, which is important to cell respiration and wound recovery (Gao et al., 2022). Compared to dry dressing or routine treatments, the hydrogel dressings also appeared to essentially accelerate mending and lead to tissue remodeling more quickly.

4.2. Non-adhesivity and biocompatibility

Since most hydrogel-based dressings do not adhere, changing them doesn't cause as much torment or aggravation. Due to their characteristic biocompatibility and biodegradability, common polymer-based hydrogels like alginate, gelatin, or hyaluronic corrosive are especially profitable . These properties make them reasonable indeed for touchy or contaminated wounds, without inciting immunogenic reactions (Bai et al., 2021).

4.3. Antibacterial and Anti-inflammatory Functionalization

Cutting edge hydrogel frameworks regularly join bioactive specialists such as anti-microbials (e.g., gentamicin, ciprofloxacin), silver nanoparticles, or home grown extricates to avoid bacterial colonization and advance anti-inflammatory impacts (Lin et al., 2021) .Within the treatment of burns and chronic wounds, where disease may be a major issue, usually particularly imperative. Silver nanoparticle-loaded hydrogels, for occurrence, have been appeared to be compelling against two of the foremost predominant pathogens that cause wound contaminations, Staphylococcus aureus and Pseudomonas aeruginosa (Zhao et al., 2017) .Hydrogels can moreover be made to discharge anti-inflammatory cytokines or inhibitors of pro-inflammatory pathways (like NF-B), which can offer assistance control the wound's microenvironment and maintain a strategic distance from over the top scarring (Li et al., 2020).

4.4. Delivery of controlled drugs

to wound locales One of the key preferences of hydrogels in wound recuperating lies in their capacity to serve as neighborhood medicate conveyance stages. The hydrogel network can contain drugs, development components (like VEGF Vascular Endothelial Growth Factor and EGF Epidermal Growth Factor), or stem cells and discharge them in a controlled way over time (Lee et al., 2019). The restorative viability of this focused on approach is expanded whereas systemic side impacts are minimized. In full-thickness wound models, for occasion, a ponder utilizing gelatin methacrylate hydrogels stacked with essential fibroblast development figure (bFGF Basic fibroblast growth factor) illustrated improved re-epithelialization and collagen testimony (Wang et al., 2018). Essentially, pH-responsive hydrogels can trigger sedate discharge based on changes in wound causticity, which regularly relates

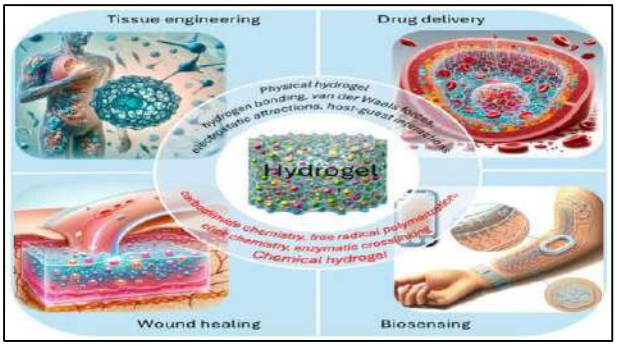

Figure 3: Representation of hydrogel application on the skin as a smart system for controlled drug delivery. The figure demonstrates how hydrogel can release drugs gradually and locally to the target tissues, enhancing therapeutic efficiency and minimizing systemic side effects.

4.5. Hydrogels that respond to stimuli and are smart

Later developments in hydrogel innovation have presented "shrewd" hydrogels that react to outside jolts such as pH, temperature, or light. These frameworks empower real-time adjustment to the wound environment, counting medicate discharge in reaction to disease or swelling (Li et al., 2021). For occasion, thermo-sensitive hydrogels can be connected effectively and adjust to unpredictable wound surfaces since they are fluid at room temperature and turn into gel when they come into contact with body temperature (Zhang et al., 2022). In progressed applications, hydrogels have been coordinates with biosensors or electroactive materials to screen wound pH, temperature, or exudate levels—providing clinicians with real-time criticism for treatment optimization (Kopeček & Yang, 2007).

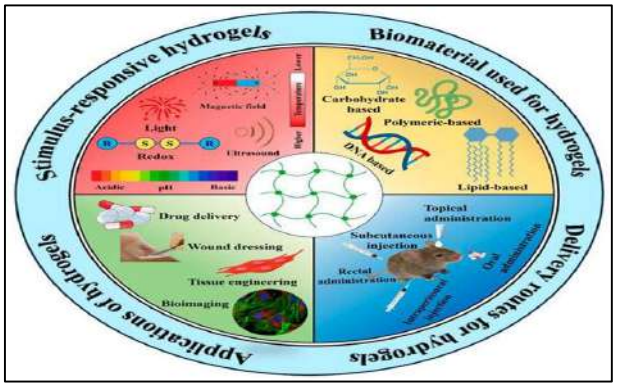

Figure 4: Stimuli-responsive hydrogels: materials that respond to environmental triggers such as pH, temperature, or enzymes, enabling controlled and targeted drug delivery for various biomedical applications.

4.6. Potential for tissue engineering and regeneration

As platforms that bolster cell connection, multiplication, and separation, they are crucial in tissue designing for wound mending. Crossover hydrogels consolidating extracellular lattice components or peptides such as (RGD arginine-glycine-aspartic acid) arrangements can advance cellular reactions that quicken tissue recovery (Liu et al., 2023). Furthermore, stem cell-loaded hydrogels, which offer regenerative capabilities beyond those of ordinary dressings, are also being examined for the treatment of diabetic ulcers and profound wounds (Yan et al., 2019).

4.7.Characterization Techniques of Polymeric Hydrogels

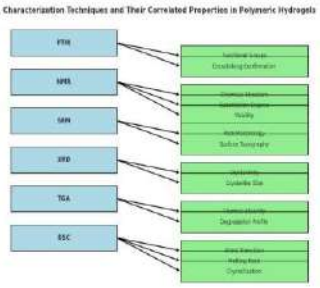

4.7.1 Fourier Transform Infrared Spectroscopy (FTIR)

FTIR spectroscopy is an vital instrument in hydrogel investigation due to its capacity to distinguish characteristic vibrational modes of chemical bonds. In polymeric hydrogels, FTIR makes a difference screen the victory of crosslinking responses by watching changes in band force and positions. For occasion, in chitosan-based hydrogels, the arrangement of imine linkages between amine bunches and aldehydes is demonstrated by the development of a band around 1640 cm^{-1}, characteristic of the C=N bond. Moreover, the vanishing of wide O–H extending vibrations around 3300 cm^{-1} proposes decreased hydroxyl accessibility, affirming interaction with crosslinkers (Chen et al., 2020).

4.7.2 Nuclear Magnetic Resonance Spectroscopy (NMR)

NMR gives a high-resolution atomic unique finger impression of the hydrogel components. In ^{1}H NMR, the proton environment reflects the versatility and intuitive of polymer chains, whereas ^{13}C NMR gives knowledge into the carbon system. For case, in PEG hydrogels, crests at ~3.6 ppm speak to ethylene glycol units, and their broadening demonstrates organize arrangement. The degree of crosslinking, atomic substitutions, and energetic behavior of the arrange can all be assessed quantitatively utilizing NMR spectra, particularly in shrewd or stimuli-responsive hydrogels (Rinaudo, 2006).

4.7.3 Scanning Electron Microscopy (SEM)
The microstructure of hydrogels administers properties like dissemination, mechanical bolster, and cell invasion. SEM imaging of lyophilized hydrogels uncovers the estimate and interconnectivity of pores. Hydrogels outlined for tissue framework regularly display a profoundly permeable and interconnected structure (~10–100 μm), whereas hydrogels for water filtration may have littler pores optimized for capturing particulates or particles. Surface unpleasantness watched through SEM moreover influences cell grip and natural reactions (Gibson et al., 2011).

4.7.4 X-ray Diffraction (XRD)
XRD permits separation between shapeless and crystalline stages. In semi-crystalline hydrogels like PVA-based frameworks, sharp diffraction crests (e.g., around $2\theta = 19.5°$) show the nearness of crystalline spaces. These spaces upgrade pliable quality but decrease swelling capacity. XRD information are particularly profitable when combining polymers with inorganic fillers like silica or metal-organic systems, making a difference to decide the scattering and integration of such components (Li et al., 2012).

4.7.5 Thermogravimetric Analysis (TGA)
TGA is utilized to analyze hydrogel warm soundness by recording weight misfortune as the test is warmed. A multi-step debasement profile may show up in characteristic polymer hydrogels (e.g., introductory water misfortune, taken after by deterioration of saccharide spines). Comparing onset corruption temperatures permits positioning hydrogels for heat-sensitive applications, such as wound dressings requiring sterilization. Leftover mass at tall temperatures may demonstrate the nearness of inorganic or steady filler substance (Kamoun et al., 2017).

4.9.6 Differential Scanning Calorimetry (DSC)
DSC gives a thermodynamic profile of the hydrogel by measuring warm stream related with stage moves. The glass move temperature (Tg) uncovers chain portability; a lower Tg proposes expanded adaptability and swelling potential. For medicate conveyance frameworks, softening point and enthalpy information offer assistance guarantee soundness amid capacity and application. In hydrogels stacked with dynamic specialists or nanoparticles, DSC too identifies shifts that demonstrate intuitive or physical entanglement (Bajpai & Bajpai, 2012).

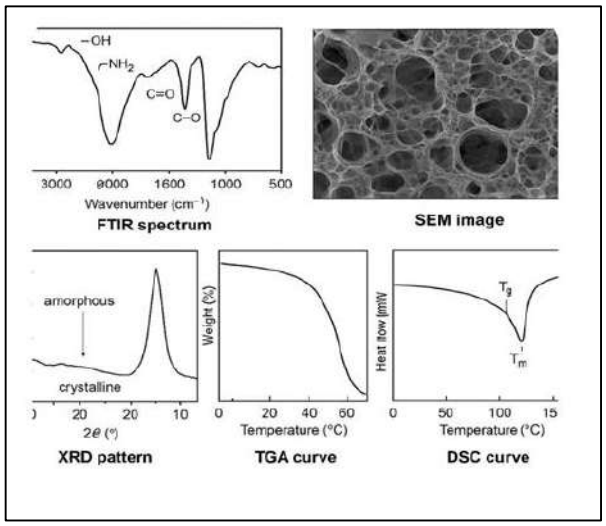

Figure 5: Common characterization techniques for polymeric hydrogels.The figure presents various analytical techniques used to characterize the physicochemical and structural properties of polymeric hydrogels

5.Chemical Composition and Crosslinking Mechanisms
Hydrogels are three-dimensional systems shaped by crosslinked polymer chains that can retain and hold noteworthy sums of water. The chemical structure and crosslinking instruments significantly decide their mechanical quality, swelling behavior, and corruption rate. Hydrogels can be shaped from common polymers (such as chitosan and alginate) or manufactured polymers (like polyvinyl alcohol (PVA) and polyethylene glycol (PEG)), through physical or chemical crosslinking techniques.
One of the foremost common chemical crosslinking responses is between polyvinyl alcohol (PVA) and glutaraldehyde. PVA contains hydroxyl (–OH) bunches that can respond with aldehyde (–CHO) groups of glutaraldehyde to make acetal bridges, driving to a steady hydrogel network (Hassan & Peppas, 2000).

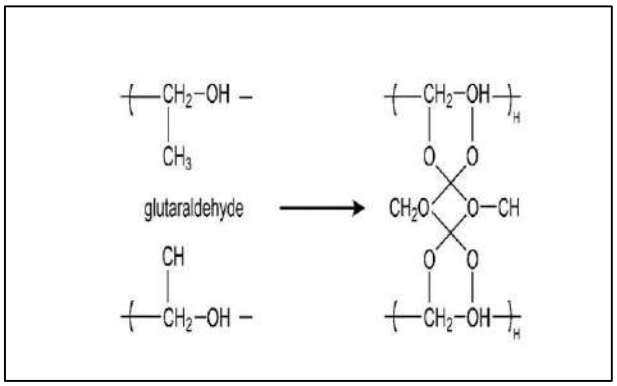

Equation 1: Crosslinking reaction between PVA and glutaraldehyde forming acetal bridges in the hydrogel network.

6. Conclusion and Future Perspectives

Polymeric hydrogels have demonstrated to be exceedingly flexible and compelling materials for double applications in water decontamination and wound mending. They are perfect for utilizing in both the natural and biomedical areas due to their biocompatibility, tunable mechanical properties, capacity for useful adjustment, and capacity to hold a critical sum of water. Hydrogels have amazing adsorption, filtration, and recovery properties for water filtration, particularly when upgraded with responsive chemistry or nanomaterials. In expansion, they play a transformative part in wound recuperating by giving progressed helpful benefits like dampness maintenance, disease anticipation, and controlled sedate conveyance. In spite of these headways, there are still many impediments. Hydrogel frameworks must be advance optimized for long-term natural steadiness, recovery proficiency, and versatility in water decontamination. Essentially, in wound mending, issues such as cytotoxicity of consolidated specialists, corruption rate control, and the requirment for personalized or stimuli-responsive frameworks need more profound examination.

Looking forward, future inquire about ought to point to create multifunctional hydrogel stages that can address both natural and therapeutic challenges at the same time. For case, coordination detecting capabilities inside hydrogels can open unused wildernesses in real-time observing of wound conditions or water quality. In expansion, the utilizing of biodegradable and renewable polymers, as well as green amalgamation methods.Biomedical building, nanotechnology, and materials science will proceed to work together to develop hydrogel plan. Through intrigue collaboration and advancement, polymeric hydrogels are balanced to end up irreplaceable apparatuses for progressing open wellbeing and natural supportability.

REFERENCES

Abdul-Zahra, Z. A., Hussain, A. A. H., Radhi, I. J., & Abd, R. N. (2025). Synthesis and characterization of silver nanoparticles from Triticum aestivum L. extract. Journal of Nanostructures, 15(4), 1671–1677.

Ahmad, N., et al. (2020). Polymeric hydrogels for removal of pharmaceutical residues from water: A critical review. Journal of Hazardous Materials, 398, 122937.

Ahmed, E. M. (2015). Hydrogel: Preparation, characterization, and applications: A review. Journal of Advanced Research, 6(2), 105–121.

Al-ogaili, A. H., & Al-Da'amy, M. A. (2020). Equilibrium and thermodynamic studies of adsorption of remazol brilliant blue dye on snail shell powder. IOP Conference Series: Materials Science and Engineering, 871(1).

Bai, R., et al. (2021). Regeneration of polymeric hydrogels for sustainable water treatment: Methods and mechanisms. Separation and Purification Technology, 271, 118873.

Bajpai, A. K., & Bajpai, J. (2012). Thermal studies of interpenetrating polymer network hydrogels for biomedical applications. Thermochimica Acta, 545, 59–66.

Boateng, J. S., et al. (2008). Wound healing dressings and drug delivery systems: A review. Journal of Pharmaceutical Sciences, 97(8), 2892–2923.

Caló, E., & Khutoryanskiy, V. V. (2015). Biomedical applications of hydrogels: A review of patents and commercial products. European Polymer Journal, 65, 252–267.

Chen, G., et al. (2020). Stem cell-laden hydrogels for wound healing and tissue regeneration. ACS Applied Materials & Interfaces, 12(51), 57495–57508.

Gao, Y., et al. (2022). Antibacterial hydrogels for water disinfection: A comprehensive review. Science of the Total Environment, 810, 152294.

Gibson, L. J., et al. (2011). NMR studies of crosslinked hydrogels: Molecular mobility and structure. Macromolecules, 44(12), 4315–4324.

Gong, J. P. (2010). Why are double network hydrogels so tough? Soft Matter, 6(12), 2583–2590.

Haraguchi, K., & Takehisa, T. (2002). Nanocomposite hydrogels: A unique organic–inorganic network structure with extraordinary mechanical properties. Advanced Materials, 14(16), 1120–1124.

Hassan, C. M., & Peppas, N. A. (2000). Structure and applications of poly(vinyl alcohol) hydrogels. Advances in Polymer Science, 153, 37–65. https://doi.org/10.1007/3-540-46414-x_2

Hoare, T. R., & Kohane, D. S. (2008). Hydrogels in drug delivery: Progress and challenges. Polymer, 49(8), 1993–2007.

Huang, Y., et al. (2018). Hydrogel-based dressings for wound healing. Bioactive Materials, 3(4), 393–409.

Hussain, A. H., Al-Da'amy, M. A., & Kareem, E. T. (2023). Modification of snail shell for the removal of remazol brilliant blue dye from wastewater. AIP Conference Proceedings, 2830(1).

Kamoun, E. A., et al. (2017). A review on polymeric hydrogels preparation, characterization and biomedical applications. Polymers, 9(10), 535.

Khan, T. A., et al. (2020). Removal of dyes using natural polymer-based hydrogels. Journal of Water Process Engineering, 33, 101111.

Kopeček, J. (2007). Hydrogel biomaterials: A smart future. Biomaterials, 28(34), 5185–5192.

Kopeček, J., & Yang, J. (2007). Hydrogels as smart biomaterials. Polymers for Advanced Technologies, 18(8), 568–576.

Kumar, R., et al. (2020). Photocatalytic hydrogel composites for degradation of contaminants. Environmental Research, 191, 110086.

Lee, H., et al. (2019). Anti-inflammatory hydrogel dressings for chronic wound management. Biomaterials Science, 7(4), 1400–1411.

Li, H., et al. (2012). Crystallinity and mechanical properties of PVA-based hydrogels. Journal of Applied Polymer Science, 125(4), 2793–2801.

Li, J., & Mooney, D. J. (2016). Designing hydrogels for controlled drug delivery. Nature Reviews Materials, 1(12), 16071.

Li, J., et al. (2020). Silver nanoparticle-loaded hydrogels for wound healing. Materials Science and Engineering C, 112, 110925.

Li, J., et al. (2022). Magneto-responsive polymeric hydrogels. Journal of Hazardous Materials, 423, 127191.

Li, Y., et al. (2022). Tunable porosity in polymeric hydrogels. Chemical Society Reviews, 51(7), 3171–3192.

Lin, X., et al. (2021). Hydrogel dressings for wound healing. Macromolecular Bioscience, 21(2), 2000380.

Liu, M., et al. (2020). Injectable hydrogels for wound regeneration. Advanced Functional Materials, 30(17), 1908855.

Liu, S., et al. (2020). Growth factor-loaded hydrogel dressings. Chemical Reviews, 120(15), 8306–8362.

Liu, Y., et al. (2021). Functionalized hydrogels for adsorption. Journal of Environmental Management, 286, 112247.

Liu, Y., et al. (2023). Electroactive hydrogel dressings. Advanced Science, 10(5), 2204821.

Lu, Y., et al. (2021). Functionalized hydrogel systems for heavy metal removal. Colloids and Surfaces B, 200, 111583.

Ma, J., et al. (2020). Graphene oxide-based hydrogels. Colloids and Surfaces A, 586, 124279.

Nair, A. T., et al. (2022). Nanocomposite hydrogels for water purification. Journal of Hazardous Materials, 423, 127170.

Peppas, N. A., & Hoffman, A. S. (2012). Hydrogels in biology and medicine. Advanced Materials, 24(28), 5190–5210.

Qiao, Z., et al. (2021). Stimuli-responsive hydrogels. Materials Today, 49, 40–66.

Reddy, K. R., et al. (2020). Functionalized hydrogels for heavy metal removal. Journal of Environmental Management, 261, 110246.

Rinaudo, M. (2006). Chitin and chitosan. Progress in Polymer Science, 31(7), 603–632.

Rusu, A. G., et al. (2019). Chitosan-based hydrogels. Environmental Chemistry Letters, 17(3), 1457–1479.

Thakur, S., et al. (2021). Hydrogels for drug delivery and wastewater treatment. Environmental Chemistry Letters, 19(1), 155–177.

Tamesue, S., et al. (2023). Temperature- and pH-responsive hydrogels. Acta Biomaterialia, 152, 67–85.

Wang, C., et al. (2018). Injectable hydrogels for cancer therapy. Advanced Functional Materials, 28(13), 1800034.

Wang, C., et al. (2021). Injectable hydrogels for wound healing. Journal of Controlled Release, 332, 240–250.

Wang, Z., et al. (2021). Tuning hydrogel surface functionality. ACS Applied Materials & Interfaces, 13(6), 7433–7445.

Yan, C., et al. (2019). ECM-mimicking hydrogels. Advanced Functional Materials, 29(3), 1804971.

Yang, J., et al. (2019). Polymeric hydrogels for pollutant removal. ACS Applied Polymer Materials, 1(10), 2757–2772.

Zhang, F., et al. (2018). Smart hydrogel adsorbents. Chemical Engineering Journal, 344, 77–86.

Zhang, W., et al. (2019). Cyclodextrin-based hydrogels. Carbohydrate Polymers, 225, 115215.

Zhang, Y., et al. (2017). Smart hydrogels for wound healing. Advanced Healthcare Materials, 6(11), 1601451.

Zhang, Y., et al. (2019). Hydrogel adsorbents for water treatment. Environmental Pollution, 252, 183–204.

Zhang, Y., et al. (2020). Biodegradable hydrogels. Journal of Materials Chemistry B, 8(22), 4812–4830.

Zhang, Y., et al. (2022). Smart hydrogels for wound healing. ACS Nano, 16(4), 5640–5670.

Zhao, X., et al. (2017). Antibacterial hydrogel dressings. Advanced Healthcare Materials, 6(23), 1700263.

Zhuang, Y., et al. (2021). Polymeric hydrogels for wastewater treatment. Chemical Engineering Journal, 405, 127018.

Pure Sciences International Journal of kerbala

Year:2026 Volume : 3 Issue : 9 ISSN: 6188-2789 Print 3005 -2394 Online

2026,Volume 3 , Issue 9 , PSIJK (109-113)

Pure Sciences International Journal of Kerbala

Neutrosophic Modeling of Lifetime Data Using the Weibull–Exponentiated Exponential Distribution

Ayat Khaled Sagheer [a*]

[a] *Department of Mathematics, College of Education for Pure Sciences, University of Kerbala*

P A P E R I N F O

Received: 01.03.2026
Accepted: 29.03.2026
Published: 31.03.2026

***Keywords*:**
Neutrosophic distribution; Lifetime modeling; Neutrosophic Weibull distribution; Neutrosophic Exponentiated exponential distribution; Reliability analysis , survival function

A b s t r a c t

Modeling lifetime data plays an indispensable role in reliability engineering and survival analysis, where the primary goal is to accurately predict time-to-event phenomena. While classical probability distributions, such as the widely applied Weibull-Exponentiated Exponential (W-EE) hybrid model, offer significant flexibility in capturing versatile hazard rates, they possess a fundamental limitation. Specifically, traditional models inherently assume that the observed data and underlying parameters are precise and well-defined. However, this assumption is rarely satisfied in practical scenarios. In real-world applications, data collection is frequently plagued by measurement errors, interval-censored information, environmental noise, and inherent vagueness. Relying strictly on classical statistical methods under such uncertain conditions often yields biased parameter estimates and misleading reliability inferences. To address these critical challenges, this study introduces the Neutrosophic Weibull–Exponentiated Exponential (NW–EE) distribution, a novel extension designed to model lifetime data characterized by indeterminacy. By integrating neutrosophic components into the classical W-EE model, we effectively represent observations and parameters as neutrosophic intervals rather than exact point values. In this paper, we rigorously derive the key statistical functions of the new distribution, including the neutrosophic cumulative distribution function (NCDF), the neutrosophic probability density function (NPDF), and vital reliability measures such as the survival and hazard rate functions. Furthermore, we investigate essential mathematical properties such as neutrosophic moments and variance. Additionally, the model parameters are estimated utilizing the neutrosophic maximum likelihood estimation (NMLE) technique, and the model is validated using real datasets. The results demonstrate that the NW-EE model offers superior flexibility in handling imprecise observations in reliability engineering and survival analysis, providing a highly accurate and realistic alternative to classical distributions. The introduced Neutrosophic Weibull-Exponentiated Exponential (NW-EE) distribution is a sophisticated analytical tool designed to model lifetime data in environments where imprecision and indeterminacy are unavoidable.

DOI: 10.53851/psijk.v3.i9. 109-113

1. INTRODUCTION[1]

Lifetime data modeling and survival analysis are fundamental pillars in reliability engineering, medical survival analysis, and risk assessment. The primary objective in these fields is to accurately model time-to-event data, such as the failure time of mechanical components or the survival time of patients. This requires highly flexible probability distributions capable of accommodating diverse hazard rate behaviors, including constant, monotonically increasing, decreasing, and non-monotonically increasing, decreasing, and non-monotonic shapes. These foundational concepts have been extensively studied by pioneers in survival analysis and reliability, such as (Wayne B. Nelson ,2004), (John f. lawless,2003), (William Q. Meeker and L. A. Escobar ,1998).

Historically, the standard probability models were limited in handling complex failure mechanisms. To overcome this, the Weibull distribution, originally introduced by (Waloddi Weibull ,1951), emerged as a powerful model and has been extensively applied in various engineering contexts (Robert B. Abernethy,2006). Despite its widespread use, the traditional Weibull model struggles with complex, non-

*Corresponding Author Institutional Email: ayat.khaled@uokerbala.edu.iq (Ayat Khaled Sagheer)

monotonic failure rates consequently, (R. D. Gupta and D. Kundu,1999) proposed the Exponentiated Exponential (EE) distribution as a robust extension, providing additional flexibility over the standard Exponential distribution.

To achieve even greater modeling adaptability, subsequent research explored various extensions and generalization of these base distributions. Notable contribution includes the comprehensive survey by (Seralees Nadarajah and S. Kotz,2006) , as well as the generalized Weibull-G family framework introduced by (Gauss M. Cordeiro et al., 2013). Integrating these concepts led to hybrid models, for instance, the foundational characteristics and classical application of the Weibull-Exponentiated Exponential (W-EE) distribution were detailed by (A. K. S. Hamad,2021) in her comprehensive study on lifetime data modeling. This hybrid model leverages the strengths of both parent distribution to capture versatile hazard rate shapes that standard base models cannot adequately explain.

However, a significant limitation of these sophisticated classical models is their fundamental reliance on the assumption that the observed data are crisp, precise, and perfectly determined. In real-world practical environments, lifetime data are rarely exact. They frequently involve measurement errors, incomplete observations, censored or vague information, and environmental uncertainty. Under such circumstances, relying solely on classical statistics frequently results in skewed parameter estimates, false reliability inferences, and poor decision-making. These difficulties need for sophisticated modeling techniques that can specifically account for imprecision and indeterminacy.

To address these complex issues, the Neuromorphic framework was originally introduced by Florentin Smarandache as a powerful generalization of existing fuzzy logic theories. Unlike traditional approaches, Neutrosophic logic independently quantifies the degree of truth, falsity, and indeterminacy, allowing it to incorporate indeterminacy explicitly into the probabilistic structure. Building upon this, recent groundbreaking development in Neutrosophic statistics spearheaded by researchers like (Muhammad Aslam ,2018) have demonstrated the high effectiveness of this approach in handling uncertain data across various application. In this framework, parameters and observation are mathematically represented as Neutrosophic intervals rather than exact point values, providing a much more realistic representation of physical phenomena.

Motivated by these advancements and the critical need to model complex imprecise lifetime data, this paper develops a Neutrosophic generalization of the Weibull-Exponentiated Exponential distribution.

The man's contributions of this paper are:

- Definition of the Neutrosophic Weibull-Exponentiated Exponential (NW-EE) distribution.
- Derivation of its Neutrosophic cumulative distribution function (NCDF) and Neutrosophic probability density function (NPDF)
- Development of the core statistical and mathematical properties of the proposed model.
- Construction of Neutrosophic reliability measures to evaluate system performance under uncertainty

2. METHODOLOGY

Let X be a continuous Neutrosophic random variable representing lifetime as $X_N = x + I$.

Definition 1: The Cumulative distribution function of Weibull–Exponentiated Exponential Distribution (W-EE) is

$F(x) = 1 - e^{-ax^b(1-e^{-ax})^\lambda}$, $x > 0$ where

$a > 0$ is the scale parameter

$b > 0$ is the Weibull shape parameter

$\alpha > 0$ is the exponential scale parameter

$\lambda > 0$ are the exponentiation parameters

Definition 2: The Neutrosophic Probability Density Function of Exponential Distribution (NPDF) is

$f_{x_N(X)=}f(x - I) = \lambda e^{-\lambda(x-I)}$, $x > I$

The Cumulative distribution function of Neutrosophic Exponential Distribution (NCDF) is

$F_{x_N}(x - I) = \int_0^x f_{xN}(x) = \int_0^x \lambda e^{-\lambda(x-I)} = e^{-\lambda I}\left(1 - e^{-\lambda x}\right)$, $x \geq I$

Definition 3: The Cumulative distribution function of Neutrosophic Weibull- Exponentiated Exponential Distribution (NW-EE) is:

$F_{x_N}\big((x-I),a,b,\alpha,\lambda\big) = 1 - e^{-a(x-I)^b[1-e^{-\alpha(x-I)}]^\lambda}, \ x \geq I$

Definition 4: The Neutrosophic Probability Density Function of Neutrosophic Weibull– Exponentiated Exponential Distribution (NW-EE) is:

$f_{x_N}\big((x-I),a,b,\alpha,\lambda\big) = a(x-I)^b e^{-a(x-I)^b[1-e^{-\alpha(x-I)}]^\lambda}.[1-e^{-\alpha(x-I)}]^\lambda.[\alpha\lambda e^{-\alpha(x-I)} + \frac{b}{x-I}]$

The Neutrosophic Reliability Function:

$$R_{x_N}\big((x-I),a,b,\alpha,\lambda\big) = 1 - F_{x_N}\big((x-I),a,b,\alpha,\lambda\big)$$

The Neutrosophic Hazard function:

$H_{x_N}\big((x-I),a,b,\alpha,\lambda\big) = \frac{f_{x_N}((x-I),a,b,\alpha,\lambda)}{R_{x_N}((x-I),a,b,\alpha,\lambda)}$, the hazard function rate can exhibit increasing, decreasing, or bathtub shapes under indeterminacy.

Definition 5: The limits of the NPDF and NCDF.
The Nw-EE distribution exhibits specific and important behavior for its Neutrosophic probability density function(Npdf) and Neutrosophic cumulative distribution function (Ncdf) as the neutrosophic random variable $(X-I)$ approaches the boundaries of its domain , namely zero and infinity mathematical analysis of these limits confirms that the functions tend towards zero which is consistent with the fundamental properties of continuous neutrosophic probability distributions.
The asymptotic behavior of the Npdf is formally described by the following limits:

1. As$(x-I)$ approaches $o(x-I)\to 0)$ the value of Npdf tends to zero. This is mathematically expressed as:

$$\lim_{(x-I)\to 0} f_{xN}\big((x-I),a,b,\alpha,\lambda\big) = 0$$

This result is derived from the fact that the constituent terms within the Npdf , such as $(x-I)^b$ and $\big[1-e^{-\alpha(x-I)}\big]^\lambda$, approach zero, causing the entire expression to vanish.

2. As$(x-I)$ approaches infinity $((x-I)\to\infty)$ the value of Npdf also tends to zero, as shown in the following equation

$$\lim_{(x-I)\to\infty} f_{xN}\big((x-I),a,b,\alpha,\lambda\big) = 0$$

In this case, although some terms may increase the dominant factor is the negative exponential term $e^{-a(x-I)^b[1-e^{-\alpha(x-I)}]^\lambda}$.

This term ensures the decay of the Npdf to zero for larg value of $(x-I)$. This behaviour, where the Npdf approaches zero at both ends of the support, is a characteristic feature of many continuous neutrophic probability distribution. It confirms that the distribution is unimodal and that the neutrosphic probability mass is concentrated in a finite region.

Definition 6: Limit of Neutrosophic cumulative distrbuion function (Ncdf)
The behaviour of neutrosophic cumulative distribution function at the boundaries reflects another fundamental property, namely that its value ranges from zero to one

1. As $(x-I)$ approaches $o(x-I)\to 0)$: the Ncdf correctly tend to zero. This s indicates that the probability of the neutrosopic random variable X_N taking a value less than or equal to zero which is appropriate for a distribution defined on the positive real line. This limit is given by

$$\lim_{(x-I)\to 0} F_{xN}\big((x-I),a,b,\alpha,\lambda\big) = \lim_{(x-I)\to 0} e^{-a(x-I)^b[1-e^{-\alpha(x-I)}]^\lambda} = 0$$

In summary, this limit analysis confirms the validity of its NW-EE distribution, the Npdf correctly converges to zero at the extremes of its support, and the Ncdf correctly converges to zero zero at the lower bound of its domain

Definition 7: The Neutrosophic mean o (NW-EE) is obtained by

$$E(X_N) = \int_I^\infty x f_{xN}((x-I),a,b,\alpha,\lambda)\,dx$$

The Neutrosophic r^{th} moment about the origin is defined by $\acute{M}_r = \int_I^\infty x^r f_{xN}((x-I),a,b,\alpha,\lambda)\,dx$
Substituting the (NW-EE) distribution gives $\acute{M}_r = \int_I^\infty x^r a(\lambda x)^b e^{-a(x-I)^b[1-e^{-\alpha(x-I)}]^\lambda}.\big[\frac{\alpha\lambda}{e^{\alpha(x-I)}} + \frac{b}{x-I}\big]dx$
The above expectation represents the general neutrosophic moment of order r

This represents the average lifetime of system under uncertainty and the variance measurres dispersion around the mean defined by:

$var(X_N) = E(X^2{}_N) - \big(E(XN)\big)^2$ where

$$E(X^2{}_N) = \int_I^{\infty} x^2 f_{xN}((x-I),a,b,\alpha,\lambda)\,dx$$

Both integrals converge due to the exponent decay term in the density function and the moment generated function of the neutrosophic random variable is $M_{XN}(t) = E(e^{txN}) = \int_I^{\infty} e^{txN} f_{xN}((x-I),a,b,\alpha,\lambda)\,dx$ and differentiating the $M.g.f$ yields the moments of the distribution.

Definition 8: Let $x_1, x_2, \dots x_n$ be a random sample the likelihood function is $L = \prod_{i=1}^{n} f_{xN}((x-I),a,b,\alpha,\lambda)$ and taking logarithms, we obtain

$$l = \sum_{i=1}^{n} ln f_{xN}((x-I),a,b,\alpha,\lambda)$$

The parameter estimation is obtained by solving

$$\frac{\partial l}{\partial a} = 0\,, \frac{\partial l}{\partial \lambda} = 0\,, \frac{\partial l}{\partial \alpha} = 0\,, \frac{\partial l}{\partial \lambda} = 0$$

Definition 9: The Neutrosophic cumulative Hazard function plays an important role in reliability analysis and survival studies. It measures the accumulated risk of failure up to a given time $H_N\big((x-I),a,b,\alpha,\lambda\big) = -\ln[1-F_N(x-I)]$

Substituting the Neutrosophic cumulative distribution function gives

$$H_N\big((x-I),a,b,\alpha,\lambda\big) = -\ln\left[e^{-a(x-I)^b\left[1-e^{-\alpha(x-I)}\right]^{\lambda}}\right]$$

Thus, the Neutrosophic cumulative Hazard function becomes

$$H_N\big((x-I),a,b,\alpha,\lambda\big) = a(x-I)^b\left[1-e^{-\alpha(x-I)}\right]^{\lambda}$$

Note that the Neutrosophic cumulative hazard function presents the accumulated failure risk of the system while incorporating ideterminacy in the lifetime observation.

The parameter I reflects the uncertainty associated with the measurement or observation of the lifetime variable when $I = 0$, the neutrosophic model reduce to the classical cumulative hazard function.

Definition 10: The Neutrosophic order statistics.

Order statistics are crucial in reliability of studying the lifetime of a system with n components.

Let $X_{N(1)}, X_{N(2)}, \dots, X_{N(n)}$ be a Neutrosophic random sample from the NW-EE distributions.

The N.PDF of the K^{th} order statistics $f^N{}_{K:N}(x-I)$ is given by

$$f^N{}_{K:N}(x-I) = \frac{n!}{(K-1)!(n-K)!} f_{x_N}(x-I)\big[F_{x_N}(x-I)\big]^{K-1}\big[1-F_{x_N}(x-I)\big]^{n-K}$$

by substitution the N.CDF and N.PDF of our NW-EE distribution , we obtain:

$$f^N{}_{K:N}(x-I) = \frac{n!}{(K-1)!(n-K)!} a(x-I)^b e^{-a(x-I)^b\left[1-e^{-\alpha(x-I)}\right]^{\lambda}}$$

Definition 11: Neutrosophic Moments of residual life.

The mean residual life (MRL) is vital measure in survival analysis. For the NW-EE distribution, the Neutrosophic MRL function denoted by $M_N(t)$ represents the expected remaining life of a component given it has survived up to time $t + I$:

$$M_N(t) = E[X_N - t | X_N > t] = \frac{1}{R_N(t-I)} \int_t^{\infty} R_N(t-I)dx$$

Substituting the Neutrosophic reliability function $R_N(t-I)$:

$$M_N(t) = \frac{\int_t^{\infty} e^{-a(x-I)^b\left[1-e^{-\alpha(x-I)}\right]^{\lambda}}}{e^{-a(x-I)^b\left[1-e^{-\alpha(x-I)}\right]^{\lambda}}}$$

The stress – strength reliability analysis $R_N = P(Y_N < X_N)$ in engineering, we often evaluate the probability that a system's strength X_N exceeds the stress Y_N that is applied to it.

If the X_N and Y_N follow the $NW-EE$ distribution with different of scale parameters a_1, a_2, the Neutrosophic stress– strength reliability is

$$R_{NS} = \int_I^{\infty} f_{N1}(X-I,a_1,b,\alpha,\lambda)\, f_{N2}(X-I,a_2,b,\alpha,\lambda)dx$$

Definition 12: Computational estimation using Neutrosophic maximum likelihood (NMLE), to estimate the unknown parameter $\theta = (a,b,\alpha,\lambda)$ of the NW-EE distribution, we employ the Neutrosophic maximum likelihood estimation (NMLE) method.

Given a Neutrosophic random sample

$X_{N(1)}, X_{N(2)}, \dots, X_{N(n)}$ the likelihood function is defined as the product of Neutrosophic probability density function

$L(\theta) = \prod_{i=1}^{n} f_{x_N}((X_i - I), a, b, \alpha, \lambda)$

To simplify the estimation, we take the natural logarithm to obtain the log-likelihood function

$$l(\theta) = n \ln a + b \sum_{i=1}^{n} \ln(X_i - I) - a \sum_{i=1}^{n} (X_i - I) \left[1 - e^{-\alpha(X_i - I)}\right]^{\lambda} + \cdots$$

Where the likelihood equations of the parameter estimates are obtained by solving the system of non-linear equations generated by taking the partial derivatives of $l(\theta)$ with respect to each parameter and setting them to zero

1. For parameter a :

$$\frac{\partial l}{\partial a} = \frac{n}{a} - \sum_{i=1}^{n} (X_i - I)^b \left[1 - e^{-\alpha(X_i - I)}\right]^{\lambda} = 0$$

2. For parameter α :

$$\frac{\partial l}{\partial \alpha} = -a \sum_{i=1}^{n} (X_i - I)^b \lambda \left[1 - e^{-\alpha(X_i - I)}\right]^{\lambda - 1} . \alpha\lambda e^{-\alpha(X_i - I)} = 0$$

Conclusion: This study has successfully introduced the Neutrosophic Weibull-Exponentiated Exponential (NW-EE) distribution as a sophisticated analytical tool designed to model lifetime data in environments where imprecision and indeterminacy are unavoidable.

By explicitly incorporating the Neutrosophic parameter I into the classical Weibull-Exponentiated Exponential framework, the model provides a superior level of flexibility.

In summary the NW-EE distribution offers a more realistic and comprehensive framework than its classical counterparts for analyzing lifetime data under uncertainty. Further research should focus on extending this model to include multivariate Neutrosophic cases and conditions in comparative studies with real-world datasets in medical and industrial reliability testing.

REFERENCES

Waloddi Weibull, "A statistical distribution function of wide applicability," Journal of Applied Mechanics, vol. 18, pp. 293–297, 1951.

R. D. Gupta and D. Kundu, "Generalized exponential distribution," Australian & New Zealand Journal of Statistics, vol. 41, no. 2, pp. 173–188, 1999.

Wayne B. Nelson, Applied Life Data Analysis, New York: Wiley, 2004.

John F. Lawless, Statistical Models and Methods for Lifetime Data, 2nd ed., New York: Wiley, 2003.

William Q. Meeker and L. A. Escobar, Statistical Methods for Reliability Data, New York: Wiley, 1998.

Saralees Nadarajah and S. Kotz, "The exponentiated exponential distribution: A survey," AStA Advances in Statistical Analysis, vol. 90, pp. 1–14, 2006.

Gauss M. Cordeiro, E. M. M. Ortega, and D. C. C. da Cunha, "The Weibull-G family of distributions," Journal of Statistical Computation and Simulation, vol. 83, no. 7, pp. 1225–1245, 2013.

A. K. S. Hamad, "Modeling for the Lifetime Data with Applications," M.S. thesis, Dept. Math., Coll. Educ. Pure Sci., Univ. Babylon, Babylon, Iraq, 2021.

Robert B. Abernethy, The New Weibull Handbook, 5th ed., North Palm Beach, FL: Robert B. Abernethy, 2006.

Florentin Smarandache, Neutrosophy: Neutrosophic Probability, Set, and Logic, Rehoboth: American Research Press, 1998.

Florentin Smarandache, Introduction to Neutrosophic Statistics, Craiova: Sitech & Education Publishing, 2014.

Muhammad Aslam, "Neutrosophic statistical process control charts," Symmetry, vol. 10, no. 9, p. 395, 2018.

M. Aslam, "Neutrosophic statistics: Theory and applications," Journal of Intelligent & Fuzzy Systems, vol. 36, pp. 1–12, 2019.

Pure Sciences International Journal of kerbala

Year:2026 Volume : 3 Issue : 9 ISSN: 6188-2789 Print 3005 -2394 Online

2026,Volume 3 , Issue 9 , PSIJK (115-122)

Pure Sciences International Journal of Kerbala

New Weighted Rayleigh Version of Azzalini Distribution

Aseel Hussien Ali [a*]

[a] *Department of Mathematics, College of Science for Women, University of Baghdad, Baghdad, Iraq*

P A P E R I N F O

Received: 02.02.2026
Accepted: 05.03.2026
Published: 31.03.2026

***Keywords*:**
Azzalin distributioni, Ball bearings, Rayleigh distribution, Maximum likelihood estimation.

A b s t r a c t

In this article a new weighted Rayleigh distribution has been proposed. The main difference between the proposed distribution and the other existing Rayleigh families is that, usually, when families add such a parameter, it creates new behavior, such as (tail). In the proposed distribution, the new parameter η interacts with β to adjust the spreading. It is simpler and more computationally.
The distribution's properties have been analyzed, and the maximum-likelihood method was suggested for the estimation of the parameters of the new distribution. The novel weighted distribution was exemplified through its application to an actual lifetime dataset.

DOI: 10.53851/psijk.v3.i9. 115-122

1. INTRODUCTION

Statistical distributions serve to represent sample data gathered from a population or to characterize the results of a random experiment.
Classical distributions are not always sufficient for modeling real data. In most applied fields, such as lifetime analysis, there is a very strong need for extended forms of the classical distributions. In the literature, the Rayleigh distribution has received close attention due to the benefits it offers in comparison to other distributions in the modeling of lifetime data. lord. Rayleigh, in 1880, introduced a one-scale parameter distribution called the Rayleigh distribution and considered it one of the most widely used distributions. The researchers developed various generalizations of this distribution to enhance its flexibility in modeling lifetime data.
(Azzalini, 1985). Azzalini in 1985 , proposed a new class of probability distributions parameterized by the shape parameter (Gupta & Kundu, 2009). Based on Azzalini's idea, Gupta and kundu in 2009 introduced a shape parameter for the exponential distribution.
(Nasiru, 2015). In 2015,Nasiru and Suleman proposed a new distribution based on Azzalini's (1985) approach; its mathematical properties derived, and its applicability demonstrated on real data (Mahmood A., 2020). In 2020, Mahmood A. Sahmran, proposed a weighted distribution based on the conventional type I Pareto distribution (Ajami & Jahanshahi, 2016). In 2016, Ajami and Jahanshahi made a comparison of different methods of estimation for the size-biased Rayleigh distribution (Bashir & Rasul, 2018). In 2018, Bashir and Rasul proposed the Rayleigh distribution that is biased by area (ARD) with derived properties and parameter estimates, showing a good fit to lifetime data using statistical tests (Bhat & Ahmad, 2020). Bhat and Ahmad in 2020, proposed the Power Rayleigh distribution, studied its properties and entropies, by using MLE estimates of parameters, and then demonstrated its usefulness with real data (Ahad et al., 2021). Ahad, Ahmad, and Rehman in 2021, after comparing the two estimation methods of the Bayesian and non-Bayesian weighted Rayleigh distribution's parameters, found that the Bayesian method under entropy loss with a Gumbel Type II prior is the most effective (Hussein et al., 2023). In 2023, Lamyaa , Huda, and Iden enhanced the ER and MWER distributions, derived the statistical properties, and, for greater modeling flexibility, showed that MWER generalizes ER. (Ilori et al., 2025). In 2025, Ilori, Adetunji , Awogbemi, Damilare, Toyosi and Adebisi proposed the Weighted Two-Parameter Rayleigh (W2R) distribution, an extension of the

*Corresponding Author Institutional Email:
aseel.h@csw.uobaghdad.edu.iq (Aseel Hussien Ali)

Rayleigh distribution using an inverted weight function with an extra parameter. This new model improves flexibility for reliability and survival analysis.

This article proposes an innovative extension of the Rayleigh distribution, termed the "new weighted Rayleigh version of Azzalini's distribution," predicated on a modified weighted variant of Azzalini's (1985) work. Additionally, the principal statistical characteristics of the newly modified distribution were proposed. The conclusion of this paper has been established utilizing a literature dataset.

2. MATERIAL AND METHODS

2-1. NEW WEIGHTED RAYLEIGH DISTRIBUTION

In this part of the article, the probability density function of the new weighted Rayleigh Distribution has been derived according to the The Gupta and Kunda formula, equation (1), and Azzalini's concept. The year 2009, Gupta and Kundu introduced a novel class of Weighted Exponential distributions by utilizing the approach proposed by Azzalini (1985) on the exponential distribution.

$$f_w(x;\beta,\eta) = \frac{w(x).f(x)}{\left[E\left(w(x)\right)\right]} \qquad (1)$$

Where

$w(x)$ represents weight function, (where must satisfy two conditions to ensure that the resulting pdf integrates to one: Non- negativity and Normalization)

+

$f(x)$ is represented as a probability density function

$E\left(w(x)\right)$ serves as a normalized

A continuous random variable that is not negative x is defined as possessing a one-parameter Rayleigh distribution, described by a (pdf) of the following form:

$$f(x;\beta) = \frac{x}{\beta^2}\, e^{-\left(\frac{x^2}{2\beta^2}\right)} \quad ; x \geq 0\,, \beta > 0 \qquad (2)$$

The (CDF) of the Rayleigh distribution is expressed as:

$$F(x;\beta) = 1 - e^{-\left(\frac{x^2}{2\beta^2}\right)} \quad ; x \geq 0\,, \beta > 0 \qquad (3)$$

The Survival of Rayleigh distribution function is provided in the form:

$$S(t;\beta) = e^{-\left(\frac{t^2}{2\beta^2}\right)} \quad ; t \geq 0\,, \beta > 0 \qquad (4)$$

Now from the equation (4) ; Let $w(x) = \left(s(x)\right)^{\eta}$

$$w(x) = \left[e^{-\left(\frac{x^2}{2\beta^2}\right)}\right]^{\eta} = e^{-\left(\frac{\eta x^2}{2\beta^2}\right)} \qquad (5)$$

Now, by putting equations (2) and (5) in equation (1), and the normalized A = $1+\eta$ we get the probability density function of the new weighted Rayleigh distribution, which is defined as:

$$f_w(x;\beta,\eta) = (1+\eta)\frac{x}{\beta^2}.e^{-\frac{(\eta+1)\,x^2}{2\beta^2}} \; ; \; x > 0\,, \beta > 0\,, \eta > -1 \qquad (6)$$

β represents a scale parameter, while η denotes a new shape parameter.

Lemma1

The new weighted Rayleigh distribution

$f_w(x;\beta,\eta) = (1+\eta)\frac{x}{\beta^2}.e^{-\frac{(\eta+1)\,x^2}{2\beta^2}} \; ; \; x > 0\,, \beta > 0\,, \eta > -1$ It is a probability density function.

Proof

$$\int_0^{\infty} f_w(x;\beta,\eta)\, dx = \int_0^{\infty} \frac{(1+\eta)x\, e^{-\frac{(\eta+1)\,x^2}{2\beta^2}}}{\beta^2}\, dx \qquad (7)$$

$$\text{Let } \; u = -\frac{x^2(1+\eta)}{2\beta^2} \qquad (8)$$

$$du = -\frac{x(1+\eta)}{\beta^2}\, dx \qquad (9)$$

Put equations (8) and (9) in (7) we get:

$$= -\int_0^{\infty} e^u\, du \qquad (10)$$

Apply the exponential rule:

$\int_0^{\infty} a^u\, du = \frac{a^u}{\ln(a)}$, with a = e = e^u

Put it in equation (10) , $= -e^u$

Now, undo substitutes the value of u from the equation (8), we get:

$$= -e^{-\frac{x^2(1+\eta)}{2\beta^2}} + c$$

$$= \frac{1+\eta}{2\left(\frac{\eta}{2\beta^2}+\frac{1}{2\beta^2}\right)\beta^2} = 1$$

Then, $f_w(x;\beta,\eta) = (1+\eta)\frac{x}{\beta^2}.e^{-\frac{(\eta+1)\,x^2}{2\beta^2}}$, $x > 0\,, \beta > 0\,, \eta > -1$,Is a p.d.f weighted Rayleigh distribution.The proposed distribution is a new method to explore the Rayleigh distribution, not essentially a new geometric shape. The new model supports the example in over-parameterized models. The cumulative distribution function (cdf) of the new weighted Rayleigh distribution is expressed as follows:

$$F_w(x;\beta,\eta) = 1 - e^{-\frac{(\eta+1)\,x^2}{2\beta^2}} \qquad (11)$$

The above CDF is considered novel because the proposed model can be considered a kind of sensitive analysis In other words, it can be written in equation of simple way (sometimes called closed forms) while most models are difficult to solve by hand.

Figures (1) and (2) illustrate the pdf and cdf , respectively, of the novel weighted Rayleigh distribution for specific values of the parameter of the scale (β) and the new parameter of shape (η).

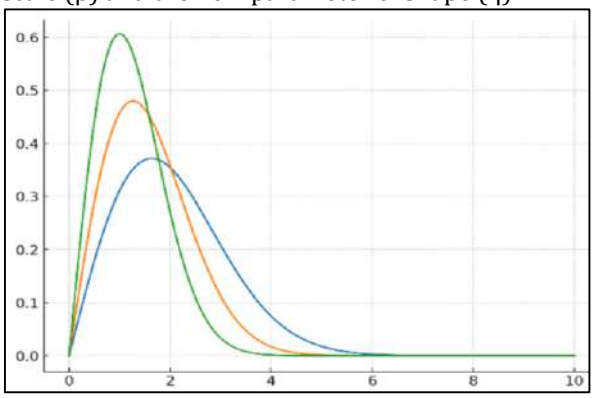

Figure 1. illustrates PDF of the new weighted Rayleigh distribution for β = 2.0 and η = 0.5, 1.5, 3.0.

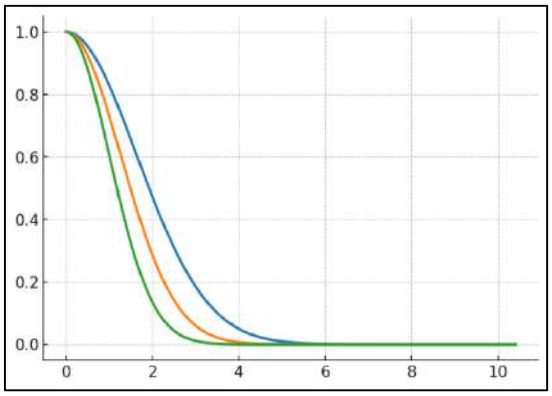

Figure 2. illustrates the CDF of the new weighted Rayleigh distribution with β = 2.0 and η values of 0.5, 1.5, and 3.0.

The new weighted Rayleigh distribution's survival function is:

$$S(x) = e^{-\frac{(\eta+1)\,x^2}{2\beta^2}} \qquad (12)$$

In terms of the hazard function, the new weighted Rayleigh distribution has been obtained from equations (6) and (12) by:

$$H(x) = \frac{f(x)}{s(x)} = \frac{(1+\eta)\frac{x}{\beta^2}.e^{-\frac{(\eta+1)\,x^2}{2\beta^2}}}{e^{-\frac{(\eta+1)\,x^2}{2\beta^2}}}$$

$$H(x) = (1+\eta)\frac{x}{\beta^2} \qquad (13)$$

Figure 3 illustrates the hazard function of the new weighted Rayleigh distribution for different selected values for the scale parameter (β) and the new shape parameter (η).

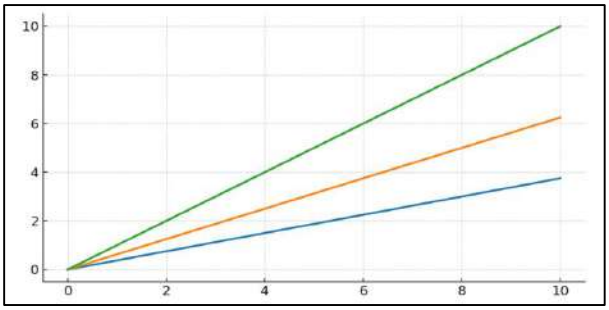

Figure 3. illustrates the hazard function of the new weighted Rayleigh distribution with β = 2.0 and η = 0.5, 1.5, 3.0.

The values of parameters in proposed model are selected to serve as representative standards. They chosen to provide a sensitive wide-ranging analysis, typical of how the distribution acts under changing steps of weighting intensity (such as high bias).

2-2. MOST IMPORTANT STATISTICAL PROPERTIES OF THE NWRD

An examination of the most significant statistical characteristics of the newly developed weighted Rayleigh distribution has been carried out here: the r-th raw moment, the mean, the variance, the moment generating function, the factorial moment-generating function, the mode, the median, the coefficient of skewness, the coefficient of kurtosis, the quantile function, and the characteristic function.

2-2-1. THE MOMENTS

Lemma2

Let x to be a r.v. of the NWRD, then the r^{th} moment function of the NWRD is $-\frac{2^{\frac{r}{2}}\,\Gamma\left(\frac{r+2}{2},\frac{(\eta+1)x^2}{2\beta^2}\right)|\beta|^r\,x^r}{(\eta+1)^{\frac{r}{2}}\,|x|^r}$.

All higher-order moments for the proposed distribution are finite for all effective parameter values.

proof

The r-th moment about the origin of the new weighted Rayleigh distribution is:

$$\mathrm{E}(x^r) = \int_0^\infty x^r (1+\eta)\frac{x}{\beta^2}.e^{-\frac{(\eta+1)\,x^2}{2\beta^2}}dx$$

$$\mathrm{E}(x^r) = \frac{(1+\eta)\,x^{r+1}.e^{-\frac{(\eta+1)\,x^2}{2\beta^2}}}{\beta^2}\,dx \quad (14)$$

Now, let

$$u = \frac{\beta^{-r-2}\,(\eta+1)^{\frac{r+2}{2}}\,x^{r+2}}{2^{\frac{r+2}{2}}} \quad (15)$$

$$du = \frac{(r+2)\,\beta^{-r-2}\,(\eta+1)^{\frac{r+2}{2}}\,x^{r+1}}{2^{\frac{r+2}{2}}}\,\mathrm{dx} \quad (16)$$

Put the equations (15) , (16) in (14)

$$= \frac{2^{\frac{r}{2}+1}\,\beta^r\,(\eta+1)^{1-\frac{r}{2}}}{(r+2)\eta+r+2}\int_0^\infty e^{-u^{\frac{2}{r+2}}}du \quad (17)$$

Now, to solve the above integral from equation (17) This is a special integral (incomplete gamma function)

$$= -\frac{(r+2)\,\Gamma\left(\frac{r+2}{2},u^{\frac{2}{r+2}}\right)}{2} \quad (18)$$

Plug equation (18) in equation (14)

$$= -\frac{(r+2)\,2^{\frac{r}{2}}\,\beta^r\,(\eta+1)^{1-\frac{r}{2}}\,\Gamma\left(\frac{r+2}{2},u^{\frac{2}{r+2}}\right)}{(r+2)\eta+r+2}$$

Undo substitute the value of u

$$= -\frac{(r+2)\,2^{\frac{r}{2}}\,\beta^r\,(\eta+1)^{1-\frac{r}{2}}\,\Gamma\left(\frac{r+2}{2},u^{\frac{2}{r+2}}\right)}{(r+2)\eta+r+2}$$

$$= -\frac{(r+2)\,2^{\frac{r}{2}}\,\beta^r\,(\eta+1)^{1-\frac{r}{2}}\,\Gamma\left(\frac{r+2}{2},\beta^{\frac{2\,(-r-2)}{r+2}}\frac{(\eta+1)x^2}{2}\right)}{(r+2)\eta+r+2} + c \quad (19)$$

by simplyfing (19) we get :

$$\mathrm{E}(x^r) = -\frac{2^{\frac{r}{2}}\,\Gamma\left(\frac{r+2}{2}\,,\,\frac{(\eta+1)x^2}{2\beta^2}\right)|\beta|^r\,x^r}{(\eta+1)^{\frac{r}{2}}|x|^r} + c \quad (20)$$

2-2-2. THE MEAN

The general formula for the first mean of the new weighted Rayleigh distribution about zero is,

$$E(x) = \int_0^\infty xf(x)dx$$

$$= \int_0^\infty x.(1+\eta)\frac{x}{\beta^2}.e^{-\frac{(\eta+1)\,x^2}{2\beta^2}}dx$$

$$= \frac{(1+\eta)}{\beta^2}\int_0^\infty x^2.e^{-\frac{(\eta+1)\,x^2}{2\beta^2}}dx \quad (21)$$

Now, by integrating by parts and simplifying the equation (21), we get the mean:

$$= \frac{\sqrt{\pi}\;|\beta|}{\sqrt{2}\,\sqrt{\eta+1}} \quad (22)$$

2-2-3. THE VARIANCE

The formula for the variance of the new weighted Rayleigh distribution is as follows:

$$v(x) = E(x)^2 - (E(x))^2$$

$$= \frac{2\,\beta^2}{1+\eta} - \left(\frac{\sqrt{\pi}\;|\beta|}{\sqrt{2}\,\sqrt{\eta+1}}\right)^2 \quad (23)$$

2-2-4. THE MOMENT GENERATING FUNCTION

Lemma3

Let x be a random variable of the NWRD; therefore, the moment generating function of the NWRD is

$$\frac{-\Gamma\left(\frac{1}{2},\frac{\left((\eta+1)x-t\beta^2\right)}{2(\eta+1)\beta^2}\right)t\,e^{\frac{t^2\beta^2}{2(1+\eta)}}|\beta|\left((\eta+1)x-t\beta^2\right)}{\sqrt{2}\,\sqrt{\eta+1}\,|(1+\eta)x-t\beta^2|} - \Gamma\left(1,\frac{\left((\eta+1)x-t\beta^2\right)^2}{2(\eta+1)\beta^2}\right)e^{\frac{t^2\beta^2}{2(1+\eta)}}$$

proof

The general form of the moment- generating function of the NWRD is:

$$= \int_0^\infty e^{tx}.(1+\eta)\frac{x}{\beta^2}.e^{-\frac{(\eta+1)\,x^2}{2\beta^2}}dx \quad (24)$$

Write,

$$\mathrm{x} = \frac{\beta^2}{-\eta-1}\left(t-\frac{(1+\eta)x}{\beta^2}\right) - \frac{t\beta^2}{-\eta-1} \quad (25)$$

Substitute equation (25) in (24)

$$= \frac{(\eta+1)\,e^{tx-\frac{(\eta+1)x^2}{2\beta^2}}}{-\eta-1} - \frac{\sqrt{\pi}t\sqrt{1+\eta}\beta e^{\frac{t^2\beta^2}{2(1+\eta)}}\,erf\left(((1+\eta)x-t\beta^2)/\sqrt{2}\,\sqrt{1+\eta}\,\beta\right)}{\sqrt{2}\,(-\eta-1)} + c$$

Note $\eta\beta^2+\beta^2>0$

$$= \frac{-\Gamma\left(\frac{1}{2},\frac{\left((\eta+1)x-t\beta^2\right)}{2(\eta+1)\beta^2}\right)t\,e^{\frac{t^2\beta^2}{2(1+\eta)}}|\beta|\left((\eta+1)x-t\beta^2\right)}{\sqrt{2}\,\sqrt{\eta+1}\,|(1+\eta)x-t\beta^2|} - \Gamma\left(1,\frac{\left((\eta+1)x-t\beta^2\right)^2}{2(\eta+1)\beta^2}\right)e^{\frac{t^2\beta^2}{2(1+\eta)}} + c$$

After splitting, apply linearity and after applying the exponential rule:

$\int a^u\,du = \frac{a^u}{\ln(a)}$ with a = e = e^u

And special integral (Gauss error function) erf(u) , we get :

$$= \frac{1}{-\eta-1}\int\left((-\eta-1)x + t\beta^2\right)e^{tx-\frac{(\eta+1)x^2}{2\beta^2}}dx - \frac{t\beta^2}{-\eta-1}\int e^{tx-\frac{(\eta+1)x^2}{2\beta^2}}dx \quad (26)$$

2-2-5. THE FACTORIA MOMENT GENERATING FUNCTION

this function of the NWRD is proposed as follows:

$$M(t) = E(t^x) = \int_0^\infty t^x (1+\eta)\frac{x}{\beta^2}.e^{-\frac{(\eta+1)x^2}{2\beta^2}}dx$$

$$= \int_0^\infty \frac{t^x(1+\eta)xe^{\frac{-(1+\eta)x^2}{2\beta^2}}}{\beta^2}$$

$$= \frac{-\left(\sqrt{2}\,\Gamma\left(\frac{1}{2},\frac{ln^2(t)\beta^2}{2(1+\eta)}\right)|\ln(t)|\sqrt{1+\eta}\,\beta - 2\Gamma\left(1,\frac{ln^2(t)\beta^2}{2(1+\eta)}\right)(1+\eta)e^{\frac{ln^2}{2(}}\right.}{2(1+\eta)} \quad (27)$$

$; 1+\eta > 0, \beta > 0$

2-2-6. THE MODE

Lemma4

Let x represenst a random variable of the NWRD, the mode of the NWRD is $x = \frac{\beta}{\sqrt{1+\eta}}$

Proof

The mode of the NWRD has been obtained by solving $\frac{dlnf_w(x;\beta,\eta)}{dx} = 0$

$$\frac{dlnf_w(x;\beta,\eta)}{dx} = \frac{d}{dx}ln\left[(1+\eta)\frac{x}{\beta^2}.e^{-\frac{(\eta+1)x^2}{2\beta^2}}\right]$$

$$= \frac{d}{dx}ln\left[\frac{(1+\eta)}{\beta^2}x\,e^{-\frac{(\eta+1)x^2}{2\beta^2}}\right] \quad (28)$$

Let

$$V^2 = \frac{\beta^2}{(1+\eta)} \quad (29)$$

Substitute (29) in (28) , then

$$\frac{d}{dx}ln\left[\frac{x}{V^2}.e^{-\frac{x^2}{2V^2}}\right] = 0$$

$$\frac{1}{x} - \frac{x}{V^2} = 0$$

$$x^2 = V^2$$

After Simplified,will get the mode at $x = x_o$

$$x_0 = \frac{\beta}{\sqrt{1+\eta}}$$

2-2-7. THE MEDIAN

Lemma5

Let x be a r.v. of the NWRD, then the median of the NWRD is, $x = \beta\sqrt{\frac{2ln2}{1+\eta}}$

proof

The median of the new weighted Rayleigh distribution is expressed as:

$$1 - e^{-\frac{(\eta+1)x^2}{2\beta^2}} = \frac{1}{2} \quad (30)$$

Now, solve $F(x) = \frac{1}{2}$. By substituting (29) in (30)

$$e^{-\frac{x^2}{2V^2}} = \frac{1}{2}$$

$$\frac{x^2}{2V^2} = ln2$$

Then

$$x = V\sqrt{2ln2} \quad (31)$$

Undo, substitute the value of v in (31) , then $x = \beta\sqrt{\frac{2ln2}{1+\eta}}$, Since x is greater than zero, its negative value will be disregarded.

2-2-8. COEFFICIENT OF SKEWNESS

Lemma 6

Let x be a r.v. of the NWRD, then the Coefficient of Skewness of NWRD is :

$$\frac{\frac{\sqrt[3]{\pi}\,(1+\eta)}{8\beta^2\left(\frac{\eta}{2\beta^2}+\frac{1}{2\beta^2}\right)^{5/2}}}{\left(\frac{2\beta^2}{1+\eta}\right)^{3/2}}$$

proof

The standard expression for the coefficient of skewness (C.S) of the new weighted Rayleigh distribution is:

$$C.R_{WR} = \frac{E(x^3)_{WR}}{(E(x^2)_{WR})^{3/2}} = \frac{\frac{\sqrt[3]{\pi}\,(1+\eta)}{8\beta^2\left(\frac{\eta}{2\beta^2}+\frac{1}{2\beta^2}\right)^{5/2}}}{\left(\frac{2\beta^2}{1+\eta}\right)^{3/2}} \quad (32)$$

The proposed model reaches shape flexibility over parameter decomposition , while the competing models often achieve skewness through adding mathematical complexity .

2-2-9. COEFFICIENT OF KURTOSIS

Lemma7

Let x be a r.v. of the NWRD, then the Coefficient of kurtosis of the NWRD is $\frac{\frac{8\beta^4}{(1+\eta)^2}}{\left(\frac{2\beta^2}{1+\eta}\right)^2} - 3$

proof

The standard expression for the coefficient of kurtosis (C.K) of the new weighted Rayleigh distribution is:

$$C.R_{WR} = \frac{E(x^4)_{WR}}{(E(x^2)_{WR})^2} - 3$$

$$C.R_{WR} = \frac{\frac{8\,\beta^4}{(1+\eta)^2}}{\left(\frac{2\,\beta^2}{1+\eta}\right)^2} - 3 \quad (33)$$

2-2-10. QUNTAILE FUNCTION

Lemma 8

Let x be a r.v. of the NWRD, then the Quantile function of the NWRD is $\sqrt{-\frac{2\beta^2}{(\eta+1)}\ln(1-Q)}$

proof

The following solution derives the quantile function for NWRD :

$F(x_{(Q)}) = Pr(X \le x_{(Q)})$

Now, by applying the inverse transformation to F(x) in equation (11) :

$x_{(Q)} = F^{-1}(Q)\,; \quad x_{(Q)} > 0\,, 0 < Q < 1$

$Q = 1 - e^{-\frac{(\eta+1)\,x^2}{2\beta^2}}$

$\ln(1-Q) = -\frac{(\eta+1)\,x^2}{2\beta^2}$

$$x = \sqrt{-\frac{2\beta^2}{(\eta+1)}\ln(1-Q)}\,, \beta > 0, \eta + 1 > 0\,, \quad (34)$$

$0 \le Q < 1$

2-2-11. CHARACTERISTIC FUNCTION

Lemma9

Let x be a r.v. of the NWRD, then , the NWRD's characteristic function is proposed as

Proof

The standard representation of the characteristic function for the new weighted Rayleigh distribution is:

$$E(e^{itx}) = \int_0^\infty e^{itx}.(1+\eta)\frac{x}{\beta^2}.e^{-\frac{(\eta+1)\,x^2}{2\beta^2}}\,dx$$

$$= \frac{(1+\eta)}{\beta^2}\int_0^\infty x\,e^{itx-\frac{(\eta+1)\,x^2}{2\beta^2}}\,dx \quad (35)$$

Now solving the integral part of (35)

$$\int_0^\infty x\,e^{itx-\frac{(\eta+1)\,x^2}{2\beta^2}}\,dx \quad (36)$$

Write

$$x = \frac{it\beta^2}{\eta+1} - \frac{\beta^2}{\eta+1}\left(it - \frac{(1+\eta)x}{\beta^2}\right) \quad (37)$$

Substituted the (37) in (36) , we get

$$\int_0^\infty \left(\frac{it\beta^2 e^{itx-\frac{(\eta+1)\,x^2}{2\beta^2}}}{\eta+1} - \beta^2\left(it - \frac{(1+\eta)x}{\beta^2}\right)e^{itx-\frac{(\eta+1)\,x^2}{2\beta^2}}\right)dx \quad (38)$$

Now apply (38) in (35), will get :

$$\frac{1}{\eta+1}\int_0^\infty \left((\eta+1)x - it\beta^2\right)e^{itx-\frac{(\eta+1)\,x^2}{2\beta^2}}\,dx + \frac{it\beta^2}{\eta+1}\int_0^\infty e^{itx-\frac{(\eta+1)\,x^2}{2\beta^2}}\,dx \quad (39)$$

Now solving the first integral of (39)

$$\int_0^\infty \left((\eta+1)x - it\beta^2\right)e^{itx-\frac{(\eta+1)\,x^2}{2\beta^2}}\,dx \quad (40)$$

Let

$$u = itx - \frac{(\eta+1)\,x^2}{2\beta^2} \quad (41)$$

Then

$$du = it - \frac{(\eta+1)\,x}{\beta^2}\,dx$$

$$= -\beta^2\int_0^\infty e^u du \quad (42)$$

Now solving the integral part of (42)

$$\int_0^\infty e^u du \quad (43)$$

Apply exponential rule on (43):

$\int_0^\infty a^u du = \frac{au}{ln(a)}$, when a = e = e^u put it in (42)

$= -\beta^2 e^u$

By Substitute $u = \frac{(\eta+1)\,x - it\beta^2}{\sqrt{2}\,\beta\sqrt{\eta+1}}$, $du = \frac{\sqrt{\eta+1}}{\sqrt{2}\,\beta}\,dx$, to get

$= \frac{\sqrt{\pi}\,\beta e^{\frac{-t^2\beta^2}{2(\eta+1)}}}{\sqrt{2}\,\sqrt{\eta+1}}\int_0^\infty \frac{2\,e^{-u^2}}{\sqrt{\pi}}du$ ...(43)

Now solving the integral part of (43)

This is a special integral (guass erroe function)= erf(u)

Put it in equation (43) with substitute u

$$= \frac{\sqrt{\pi}\;\beta e^{\frac{-t^2\beta^2}{2(\eta+1)}}\,erf\left(\frac{(\eta+1)\,x - it\beta^2}{\sqrt{2}\,\beta\sqrt{\eta+1}}\right)}{\sqrt{2}\,\sqrt{\eta+1}} \quad (44)$$

$$= \frac{\sqrt{\pi}\, it\beta^3\, e^{\frac{-t^2\beta^2}{2(\eta+1)}}\, erf\left(\frac{(\eta+1)\,x - it\beta^2}{\sqrt{2}\,\beta\sqrt{\eta+1}}\right)}{\sqrt{2}\,(\eta+1)^{3/2}} - \frac{\beta^2 e^{itx-\frac{(\eta+1)\,x^2}{2\beta^2}}}{\eta+1} \quad (45)$$

$$= \frac{\sqrt{\pi}\, it\beta\, e^{\frac{-t^2\beta^2}{2(\eta+1)}}\, erf\left(\frac{(\eta+1)\,x-it\beta^2}{\sqrt{2}\,\beta\sqrt{\eta+1}}\right)}{\sqrt{2}\,(\eta+1)} - e^{itx-\frac{(\eta+1)\,x^2}{2\beta^2}} + c \quad (46)$$

, assumed that $\beta^2\eta + \beta^2 > 0$ ...(46)

After simplifying and substituting in (35), will get :

$$= -\frac{\Gamma\left(\frac{1}{2}, \frac{\left((\eta+1)x-it\beta^2\right)^2}{2(\eta+1)\beta^2}\right) t\,|\beta| e^{\frac{-t^2\beta^2}{2(\eta+1)}} \left(i(\eta+1)x+t\beta^2\right)}{\sqrt{2}\,(\eta+1)\sqrt{\frac{\left((\eta+1)x-it\beta^2\right)^2}{\eta+1}}} - \Gamma\left(1, \frac{\left((\eta+1)x-it\beta^2\right)^2}{2(\eta+1)\beta^2}\right) e^{\frac{-t^2\beta^2}{2(\eta+1)}} + c$$

2-3. MAXIMUM LIKELIHOOD ESTIMATION

In this part of the article, the parameters of the new weighted Rayleigh distribution have been determined employing the maximum likelihood estimation technique (Ali & Al Kanani, 2021). The idea of this method is to maximize the parameters for the likelihood function.

Consider n is the size of the random sample, which contains values

$x_1, x_2, \ldots, x_n$ from the weighted Rayleigh density.

The likelihood function of the NWRD function is:

$$l(x;\beta,\eta\ ) = \prod_{i=1}^{n}(1+\eta)\frac{x}{\beta^2}.e^{-\frac{(\eta+1)\,x^2}{2\beta^2}}$$

$$= (1+\eta)^n \cdot \left(\frac{1}{\beta^2}\right)^n \cdot \prod_{i=1}^{n} x_i.\ e^{-\frac{(\eta+1)\sum_{i=1}^{n}x^2}{2\beta^2}}$$

The log likelihood function will now be as follows:

$$\ln l\,(x;\beta,\eta\ ) = n\,ln(1+\eta) - 2nln\beta + \sum_{i=1}^{n}\ln x_i - \frac{(\eta+1)}{2\beta^2}\sum_{i=1}^{n}(x_i)^2 \quad (47)$$

Now, let's denote:

$$O = \sum_{i=1}^{n}(x_i)^2 \quad (48)$$

$$Z = \sum_{i=1}^{n}\ln x_i \quad (49)$$

Then, when substitute (48) and (49) in (47) ,will get :

$$l(\beta,\eta) = nln(1+\eta) - 2ln\beta + z - \frac{(\eta+1)}{2\beta^2}\ o \quad (50)$$

The log-likelihood function (50) and its first partial derivatives with regard to β and η are as follows:

$$\frac{\partial l}{\partial\beta} = \frac{-2n}{\beta} + \frac{1+\eta}{\beta^3}\ o \quad (51)$$

$$\frac{\partial l}{\partial\eta} = \frac{n}{1+\eta} - \frac{1}{2\beta^2}\ o \quad (52)$$

Now, after setting the equations (51) and (52) to zero as follows:

$$\frac{-2n}{\beta} + \frac{1+\eta}{\beta^3}\ o = 0$$

$$\frac{n}{1+\eta} = \frac{1}{2\beta^2}\ o$$

And solving them simultaneously yields the two parameters' maximum likelihood estimations. By applying the second partial derivatives of equations (51) and (52), the matrix of Fisher information can be formulated by deriving the negative expectations of the aforementioned second derivatives.

The maximum likelihood estimators' variance and covariance matrix is denoted as Fisher's matrix. The likelihood function of the proposed model is a unique maximum ridge .

2-4. APPLICATION

Here in the article, the application of the NWRD is acquired through the utilization of the lifetime dataset of 23 ball bearings (see (Lieblein & Zelen, 1956)). These datasets are using the distribution. The data were 23 balls (in 12) but in this study, the data has been chosen as C.Carony in his article (see (Caroni, 2002)).

In this article, the weighted Rayleigh distribution is fitted to this data, and the results are compared to those of (13) . The statistics revealed that the new weighted Rayleigh distribution aligns more accurately with the data than the two-parameter Rayleigh distribution and the Weibull distribution in (13). See table (1) .

X_i=152.7,172.0,172.5,173.3,193.0,204.7,216.5,234.9, 262.6,422.6,500.5,524.8,527.8,622.3,642.2,782.5,864 .1,1100.3,1304.7,527.8 .

Choose β = 156

η = - 0.770

calculate log-likelihood, AIC (Akaike Information Criterion) , BIC (Bayesian Information Criterion)

When comparing with the Rayleigh distribution (RD) and Weibull distribution (WD) in (13) we get :

TABLE 1. comparing of the NWRD with RD and WD

Distribution	Log-likelihood	AIC	BIC
NWRD	-107.118	218.236	220.125
RD	-109.53	221.06	222.95
WD	-107.43	218.86	220.75

2-5. The CONCLUSIONS

This work introduces a new weighted Rayleigh distribution based on Gupta and Gundu modified weighted according to Azzalini's idea. Where the Azzalini-type proposed a way to variation the essential asymmetry of the distributions. The proposed distribution proposed a flexible way to alter the scaling by a weighted constant. Unlike standard models that proposed compound transcendental, the proposed probability density function novelty deceits in its structural decomposition for the Rayleigh scale, using a weighted distribution framework to clearly separate the basic population scale from the external weighting bias.

The proposed model basically depends on the Azzalini (1985) skew-symmetric idea. We donot only add a parameter randomly; we tracked the world-standard way for proposing skewness (Azzalini) and enhanced it specifically for the Rayleigh.

The new distributions' most important properties have been derived.

This new weighted distribution's implementation has been used on the ball bearing dataset, and the outcomes have been contrasted with other studies using the lifetime experiment.

REFERENCES

Ahad, S. M., Ahmad, S. P., & Rehman, S. A. (2021). A Comparative Study for Weighted Rayleigh Distribution. *Journal of Reliability and Statistical Studies*, *14*(1), 243–262. https://doi.org/10.13052/jrss0974-8024.14112

Ajami, M., & Jahanshahi, S. M. A. (2016). *Comparison of various estimation methods for size-biased Rayleigh distribution . November*.

Ali, A. H., & Al Kanani, I. H. (2021). Classical Methods to Estimate the Parameters of Exponentiated Weibull Distribution. *Journal of Physics: Conference Series*, *1818*(1). https://doi.org/10.1088/1742-6596/1818/1/012078

Azzalini, A. (1985). A class of distributions which includes the normal ones. *Scandinavian Journal of Statistics*, 171–178.

Bashir, S., & Rasul, M. (2018). A New Weighted Rayleigh Distribution: Properties and Applications on Lifetime Time Data. *Open Journal of Statistics*, *08*(03), 640–650. https://doi.org/10.4236/ojs.2018.83041

Bhat, A. A., & Ahmad, S. P. (2020). A new generalization of rayleigh distribution: Properties and applications. *Pakistan Journal of Statistics*, *36*(3), 225–250.

Caroni, C. (2002). The Correct "Ball Bearings" Data. *Lifetime Data Analysis*, *8*(4), 395–399. https://doi.org/10.1023/A:1020523006142

Gupta, R. D., & Kundu, D. (2009). A new class of weighted exponential distributions. *Statistics*, *43*(6), 621–634.

Hussein, L. K., Abdullah Rasheed, H., & Hasan Hussein, I. (2023). A Class of Exponential Rayleigh Distribution and New Modified Weighted Exponential Rayleigh Distribution with Statistical Properties. *Ibn AL-Haitham Journal For Pure and Applied Sciences*, *36*(2), 390–406. https://doi.org/10.30526/36.2.3044

Ilori, A., Adeyeye, A., Oladimeji, D., Adebambo, T., & Michael, A. (2025). On the Weighted 2-Parameter Rayleigh Distribution. *International Journal of Statistical Distributions andApplications*,*11*(2),56–65. https://doi.org/10.11648/j.ijsda.20251102.14

Lieblein, J., & Zelen, M. (1956). Statistical investigation of the fatigue life of deep-groove ball bearings. *Journal of Research of the National Bureau of Standards*, *57*(5), 273. https://doi.org/10.6028/jres.057.033

Mahmood A. S. (2020). Modified weighted pareto distribution type I (MWPDTI). *Baghdad Science Journal*, *17*(3), 869–877. https://doi.org/10.21123/bsj.2020.17.3.0869

Nasiru, S. (2015). Another Weighted Weibull Distribution from Azzalini's Family. *European Scientific Journal*, *11*(9), 133–134. https://www.researchgate.net/publication/278410749_ANOTHER_WEIGHTED_WEIBULL_DISTRIBUTION_FROM_AZZALINI'S_FAMILY

Pathak, R. P. (2008). *Methodology of educational research*. Atlantic Publishers & Dist.

Potts, C. (1995). Using schematic scenarios to understand user needs. *Proceedings of the 1st Conference on Designing Interactive Systems: Processes, Practices, Methods, & Techniques*, 247–256.

Wang, L.-X., & Mendel, J. M. (1992). Generating fuzzy rules by learning from examples. *Systems, Man and Cybernetics, IEEE Transactions On*, *22*(6), 1414–1427.

Weiser, M. (1991). The computer for the 21st century. *Scientific American*, *265*(3), 94–104.

Pure Sciences International Journal of kerbala

Year:2026 Volume : 3 Issue : 9 ISSN: 6188-2789 Print 3005 -2394 Online

2026,Volume 3 , Issue 9 , PSIJK (124-130)

Pure Sciences International Journal of Kerbala

Neutrosophic k-Ideal in Q-algebra

Mortda Taeh Shadhan [a*] , Shahad Laith Abd Algalib [a]

[a] *Department of Mathematics, College of Education for Pure Sciences,University of Kerala, Iraq*

P A P E R I N F O

Received: 28.01.2026
Accepted: 26.02.2026
Published: 31.03.2026

Keywords:
neutrosophic sets , Fuzzy set , Q-algebras, bounded Q-algebra

A b s t r a c t

In this paper, the k-ideals in Q-algebras are studied in the framework of single-valued neutrosophic sets. After recalling some basic notions related to Q-algebras and single-valued neutrosophic sets, the concept of single-valued neutrosophic k-ideals are introduced. Several properties and characterizations of single-valued neutrosophic k-ideals are investigated. Moreover, the relationships between single-valued neutrosophic k-ideals and single-valued neutrosophic ideals are discussed. Illustrative examples are provided to support the theoretical results.

DOI: 10.53851/psijk.v3.i9. 124-130

Table 1. Nomenclature for Single-Valued Neutrosophic Set.

Nomenclature			
SVN-S	A single-valued neutrosophic set	η_{M}	Function from $\mathcal{U}$ to [0,1]
SVN k-ideal	single-valued neutrosophic k-ideal	β_{M}	Function from $\mathcal{U}$ to [0,1]
$p^{\{**\}}$	involution if $p^{\star\star} = p$	τ_{M}	Function from $\mathcal{U}$ to [0,1]
e	Unit of U		
Min	Minimum		
Max	Maximum		

1. INTRODUCTION

Q-algebras are algebraic structures that have been studied by several authors due to their importance in algebra and logic see, for example (Neggers, et al., 2001)(Kim, H et al., 2005).Many concepts related to ideals have been introduced in Q-algebras in order to investigate their structural properties, and among these concepts the notion of k-ideals have received particular attention (Neggers, J. et al., 2004). The fuzzy set theory has been used as an effective tool to deal with uncertainty in algebraic systems (Zadeh, 1965) Later, intuitionistic fuzzy sets were introduced as a generalization of fuzzy sets, and several types of intuitionistic fuzzy ideals and intuitionistic fuzzy k-ideals in Q-algebras were studied see (Atanassov, K. T. 1986). Intuitionistic fuzzy sets (Jun & Neggers, 2005). Neutrosophic sets were proposed as a further generalization of intuitionistic fuzzy sets by considering the degrees of truth, indeterminacy, and falsity independently(Smarandache, 2005). In particular, single-valued neutrosophic sets have been applied to various algebraic structures as an extension of intuitionistic fuzzy sets (Smarandache, F. 2005), (Wang,

*Corresponding Author Institutional Email:
Mortda.taeh@uokerbala.edu.iq (Mortda Taeh Shadhan)

H., et al., 2010).In this paper, the k-ideals of Q-algebras are studied in the framework of single-valued neutrosophic sets. The notion of a single-valued neutrosophic k-ideal is defined and its basic properties are investigated. Also, the relationship between single-valued neutrosophic k-ideals and single-valued neutrosophic ideals is discussed, which is presented with some examples to illustrate the results. This paper is organized as followed. Section 2 contains some basic definitions and results which are needed in the sequel. In Section 3, single-valued neutrosophic k-ideals in Q-algebras are studied that establish several related properties.

2. BACKGROUND AND PRELIMINARIES

In this section, the basic concepts related to Q-algebras are recalled to introduce the notions of single-valued neutrosophic sets and ideals which will be used throughout this paper. All algebraic definitions are preserved as in the original work, while fuzzy concepts are replaced entirely by their neutrosophic counterparts.

Definition (2.1) (Kim & Neggers, 2005)
A Q-algebra is a nonempty set $(\mathcal{U},\star,0)$ together with a binary operation $\star$ and a constant 0 satisfying the following axioms:
$(i) p \star p = 0,$
$(ii)\ p \star 0 = p,$
$(iii)(p \star q) \star r = (p \star r) \star q,$
$for\ all\ p,q,r \in \mathcal{U}.$

Remark (2.2) (Kim et al., 2005)
In a Q-algebra $\mathcal{U}$, a binary relation $\leq$ is defined by $p \leq q$ if and only if $p \star q = 0$.

Definition (2.3) (Neggers et al., 2001).
A Q-algebra $\mathcal{U}$ is called bounded if an element e $\in \mathcal{U}$ exists, such that $p \star e = 0$ for all p $\in \mathcal{U}$. The element e is called the unit of $\mathcal{U}$
. $e * p$ *is denoted* by p^*, for each $p \in \mathcal{U}$ in the bounded Q − algebra.

Definition (2.4) (Neggers et al., 2001).

Let $\mathcal{U}$ be a bounded Q-algebra. An element p $\in \mathcal{U}$ is called an involution if $p^{\star\star} = p$. If every element of $\mathcal{U}$ is an involution, then $\mathcal{U}$ is called an involutory Q-algebra.

Proposition (2.5) (Neggers, et..al. 2004).
Let $\mathcal{U}$ be a bounded Q-algebra. Then, for all p, q $\in \mathcal{U}$, the following properties hold:
$(i)\ 0 \star p = p,$
$(ii)\ p \leq q\ implies\ p \star e \leq p \star e,$
$(iii) if\ \mathcal{U}\ is\ involutory, then\ p^{\star\star} = p$

Definition (2.6) (Neggers & Kim, 2001)
Let ($\mathcal{U}$,∗, 0) be a Q-algebra and I be a none empty subset of $\mathcal{U}$. Then, I is called an ideal of $\mathcal{U}$ if
for any $p, q \in \mathcal{U}$.
1. $0 \in I$
2. If $p * q \in I\ and\ q \in I$ implies $p \in I$.

Definition (2.7) (Jawad , H.K. 2019).
Let ($\mathcal{U}$,∗, 0) be a Q-algebra and I be a none empty subset of $\mathcal{U}$. Then, I is called an k- ideal of $\mathcal{U}$ if it satisfies
1. $0 \in I$
2. If $q^* * p \in I\ and\ q \in I$ implies $p^* \in I$, $\forall p \in \mathcal{U}$

$In\ short, (K-ID)\ is\ used\ instead\ of\ K-ideal$

Definition (2.8) (Wang et al., 2010)
A single-valued neutrosophic set (SVN-S) M in a universe $\mathcal{U}$ is an object of the form
$M = \{ (p, \beta_M(p), \tau_M(p), \eta_M(p)) : p \in \mathcal{U} \},$
where $\beta_M, \tau_M, \eta_M : \mathcal{U} \to [0,1]$ represent respectively the degrees of truth-membership, indeterminacy-membership, and falsity-membership, satisfying $0 \leq \beta_M + \tau_M + \eta_M \leq 3$ for all p $\in \mathcal{U}$.

Definition (2.9) (Wang et al., 2010)
The intersection, union and subset of two SVN-S M and Γ are defined respectively by
:M $\subseteq$ Γ if and only if $\beta_M(p) \leq \beta_\Gamma(p),\ \tau_M(p) \geq \tau_\Gamma(p), and\ \eta_M(p) \geq \eta_\Gamma(p)\ for\ all\ p \in \mathcal{U}$
$\beta_{\{M\cap\Gamma\}}(p) = min\{\beta_M(p), \beta_\Gamma(p)\},$
$\tau_{\{M\cap\Gamma\}}(p) = max\{\tau_M(p), \tau_\Gamma(p)\},$
$\eta_{\{M\cap\Gamma\}}(p) = max\{\eta_M(p), \eta_\Gamma(p)\};$
$\beta_{\{M\cup\Gamma\}}(p) = max\{\beta_M(p), \beta_\Gamma(p)\},$
$\tau_{\{M\cup\Gamma\}}(p) = min\{\tau_M(p), \tau_\Gamma(p)\},$
$\eta_{\{M\cup\Gamma\}}(p) = min\{\eta_M(p), \eta_\Gamma(p)\}.$

Definition (2.10) (Jun, Y. B. (2000).
Let $f : \mathcal{U} \to \Psi$ be a mapping. If Γ is a SVN-S in Ψ, then the preimage of Γ under f, denoted by $f^{-1}(\Gamma)$, is the SVN-S in $\mathcal{U}$ defined by
$\beta_{\{f^{-1}(\Gamma)\}}(p) = \beta_\Gamma(f(p)), \tau_{\{f^{-1}(\Gamma)\}}(p) = \tau_\Gamma(f(p)), \eta_{\{f^{-1}(\Gamma)\}}(p) = \eta_\Gamma(f(p))\ for\ all\ p \in \mathcal{U}.$

Definition (2.11) .

A SVN-S M $= \langle \beta_{\mathrm{M}}, \tau_{\mathrm{M}}, \eta_{\mathrm{M}} \rangle$ in a Q-algebra $\mathcal{U}$ is called a single-valued neutrosophic ideal (in short SVN-ideal) if for all $p, q \in \mathcal{U}$:

SVN i (1)

$$\beta_{\mathrm{M}}(0) \geq \beta_{\mathrm{M}}(p),$$
$$\tau_{\mathrm{M}}(0) \leq \tau_{\mathrm{M}}(p) \quad and$$
$$\eta_{\mathrm{M}}(0) \leq \eta_{\mathrm{M}}(p),$$

SVN i (2) $\beta_{\mathrm{M}}(p) \geq min\{\beta_{\mathrm{M}}(p \star q), \beta_{\mathrm{M}}(q)\}$,
$\tau_{\mathrm{M}}(p) \leq max\{\tau_{\mathrm{M}}(p \star q), \tau_{\mathrm{M}}(q)\}$ and
$\eta_{\mathrm{M}}(p) \leq max\{\eta_{\mathrm{M}}(p \star q), \eta_{\mathrm{M}}(q)\}$.

Example (2.12).
Let U = {0, ρ, ϖ, π} be a bounded Q-algebra whose binary operation * is given by Table 1.

Table 1. Cayley table of U

$*$	0	ρ	ϖ	π
0	0	0	0	0
ρ	ρ	0	0	0
ϖ	π	ϖ	0	0
π	π	π	ρ	0

Now define a single-valued neutrosophic set M in U by

$$\beta_M(p) = \begin{cases} 1, & \text{if p} = 0 \\ 0.7, & \text{if p} \in \{\rho, \varpi, \pi\}, \end{cases}$$

$$\tau_M(p) = \begin{cases} 0, & \text{if p} = 0 \\ 0.2, & \text{if p} \in \{\rho, \varpi, \pi\} \end{cases},$$

$$\eta\_M(p) = \begin{cases} 0, & \text{if p} = 0 \\ 0.3, & \text{if p} \in \{\rho, \varpi, \pi\}. \end{cases},$$

By direct computation using Table 1, there is
$0 \leq \beta_M(p) + \tau_M(p) + \eta_M(p) \leq 3$ for all p ∈ U.
Also,
$\beta_M(0) \geq \beta_M(p)$, $\tau_M(0) \leq \tau_M(p)$, $\eta_M(0) \leq \eta_M(p)$ for all p ∈ U.
Moreover, for all $p, q \in U$, one can verify from Table 1 that

$$\beta_M(p) \geq min\{\beta_M(p * q), \beta_M(q)\},$$
$$\tau_M(p) \leq max\{\tau_M(p * q), \tau_M(q)\},$$
$$\eta_M(p) \leq max\{\eta_M(p * q), \eta_M(q)\}.$$

Hence, M satisfies all conditions of Definition (2.11). Therefore, M is a single-valued neutrosophic ideal of U. □

Definition (2.13)
Let $\rho, \varpi, \pi \in [0,1]$ such $that$ $0 \leq \rho + \varpi + \pi \leq 3$. The SVN-S M defined by
$\beta_M(p) = \rho, \tau_M(p) = \varpi, \eta_M(p) = \pi$ for all $p \in \mathcal{U}$ is called a constant single-valued neutrosophic set.

Example (2.14)
Let $\mathcal{U}$ be any bounded Q-algebra. Define a single-valued neutrosophic set M in $\mathcal{U}$ by
$\beta_M(p) = 0.8$, $\tau_M(p) = 0.1$, $\eta_M(p) = 0.1$ for all $p \in \mathcal{U}$.
$Since$ $0 \leq \beta_{\mathrm{M}}(p) + \tau_{\mathrm{M}}(p) + \eta_{\mathrm{M}}(p) = 1 \leq 3$ for all $p \in \mathcal{U}$, M is a constant single-valued neutrosophic set.

3. SINGLE-VALUED NEUTROSPHIC K-IDEAL

In this section, the whole theory of k-ideals is rebuilt in the single-valued neutrosophic framework. Throughout, $\mathcal{U}$ denotes a bounded Q-algebra with unit e, and M denotes a single-valued neutrosophic set (SVN-S) in $\mathcal{U}$ written as M $= \langle \beta_{\mathrm{M}}, \tau_{\mathrm{M}}, \eta_{\mathrm{M}} \rangle$

Definition (3.1)
A SVN-S M $= \langle \beta_{\mathrm{M}}, \tau_{\mathrm{M}}, \eta_{\mathrm{M}} \rangle$ in a bounded Q-algebra $\mathcal{U}$ is called a single-valued neutrosophic k-ideal (in short, SVN k-ideal) of $\mathcal{U}$ if $for\ all\ p, q, \in \mathcal{U}$. the following hold:
SVN k (1) $\beta_{\mathrm{M}}(0) \geq \beta_{\mathrm{M}}(p)$, $\tau_{\mathrm{M}}(0) \leq \tau_{\mathrm{M}}(p)$, $\eta_{\mathrm{M}}(0) \leq \eta_{\mathrm{M}}(p)$.
SVN k (2) $\beta_{\mathrm{M}}(p^{\star}) \geq min\{\beta_{\mathrm{M}}(q^{\star} \star p), \beta_{\mathrm{M}}(q)\}$,
$\tau_{\mathrm{M}}(p^{\star}) \leq max\{\tau_{\mathrm{M}}(q^{\star} \star p), \tau_{\mathrm{M}}(q)\}$,
$\eta_{\mathrm{M}}(p^{\star}) \leq max\{\eta_{\mathrm{M}}(q^{\star} \star p), \eta_{\mathrm{M}}(q)\}$.

Example (3.2)
Let $U = \{0, \rho, \varpi, \pi\}$ be a bounded Q-algebra whose operation $*$ is given by Table 2.

Table 2. Cayley table of U

$*$	0	ρ	ϖ	π
0	0	0	0	0
ρ	ρ	0	ρ	0
ϖ	ϖ	ϖ	0	0
π	π	π	ρ	0

Define a single-valued neutrosophic set $M = \langle \beta_M, \tau_M, \eta_M \rangle$ on U by

$$\beta_M(p) = \begin{cases} 1 & if \quad p = 0 \\ 0.8 & if\ p = \rho \\ 0.6 & if\ p = \varpi \\ 0.4 & if \quad p = \pi, \end{cases}$$

$$\tau_M(p) = \begin{cases} 0 & if \quad p = 0 \\ 0.1 & if\ p = \rho \\ 0.2 & if\ p = \varpi \\ 0.3 & if \quad p = \pi, \end{cases}$$

$$\eta_M(p) = \begin{cases} 0 & if \quad p = 0 \\ 0.1 & if\ p = \rho \\ 0.2 & if\ p = \varpi \\ 0.3 & if \quad p = \pi, \end{cases}$$

Clearly, $0 \le \beta_M(p) + \tau_M(p) + \eta_M(p) \le 3$ for all $p \in U$.
Moreover, β_M is decreasing while τ_M and η_M are increasing along the structure of U. Hence,
$\beta_M(0) \ge \beta_M(p),\ \tau_M(0) \le \tau_M(p),\ \eta_M(0) \le \eta_M(p)$, for all $p \in U$.
Now, for $p, q \in U$, using Table 1, it can be observed that the operation * preserves the order of elements in U in the sense that the values of β_M do not increase under the operation, while τ_M and η_M do not decrease.
Thus, for all p, q ∈ U,

$$\beta_M(p^*) \ge min\{\beta_M(q^* * p), \beta_M(q)\},$$
$$\tau_M(p^*) \le max\{\tau_M(q^* * p), \tau_M(q)\},$$
$$\eta_M(p^*) \le max\{\eta_M(q^* * p), \eta_M(q)\}.$$

Therefore, all conditions of Definition (3.1) are satisfied, and hence, M is a single-valued neutrosophic k-ideal of U. □

Theorem(3.3). Let U be a bounded Q-algebra and let $M = \langle \beta_M, \tau_M, \eta_M \rangle$ be a single-valued neutrosophic k-ideal of U. Then, every nonempty level subset $M_{(\alpha,\gamma,\delta)}$ is a k-ideal of U.

Proof.
Assume that $M = \langle \beta_M, \tau_M, \eta_M \rangle$ is a single-valued neutrosophic k-ideal of U.
First, it should be shown that $0 \in M_{(\alpha,\gamma,\delta)}$. Since $M_{(\alpha,\gamma,\delta)} \neq \emptyset$, there exists an element $a \in M_{(\alpha,\gamma,\delta)}$.
Hence, $\beta_M(a) \ge \alpha, \tau_M(a) \le \gamma, \eta_M(a) \le \delta$.
Since M is a SVN k-ideal, by condition SVN k(1),
$\beta_M(0) \ge \beta_M(a)$ and $\tau_M(0) \le \tau_M(a)$, $\eta_M(0) \le \eta_M(a)$ are obtained.
Therefore, $\beta_M(0) \ge \alpha, \tau_M(0) \le \gamma, \eta_M(0) \le \delta$, which implies that $0 \in M_{(\alpha,\gamma,\delta)}$.
Next, let p, q ∈ U such that $q^* * p \in M_{(\alpha,\gamma,\delta)}$ and $q \in M_{(\alpha,\gamma,\delta)}$.
Then, $\beta_M(q^* * p) \ge \alpha, \beta_M(q) \ge \alpha,$
$\tau_M(q^* * p) \le \gamma, \tau_M(q) \le \gamma,$
$\eta_M(q^* * p) \le \delta, \eta_M(q) \le \delta.$
Since M is a single-valued neutrosophic k-ideal, by condition SVN k(2) we have

$$\beta_M(p^*) \ge \min\{\beta_M(q^* * p), \beta_M(q)\},$$
$$\tau_M(p^*) \le \max\{\tau_M(q^* * p), \tau_M(q)\},$$
$$\eta_M(p^*) \le \max\{\eta_M(q^* * p), \eta_M(q)\}.$$

Using the above inequalities, we obtain
$\beta_M(p^*) \ge \alpha, \tau_M(p^*) \le \gamma, \eta_M(p^*) \le \delta.$
Thus, $p* \in M_{(\alpha,\gamma,\delta)}$.
Consequently, $M_{(\alpha,\gamma,\delta)}$ contains 0 and satisfies the defining condition of a k-ideal. Hence, $M_{(\alpha,\gamma,\delta)}$ $is\ a\ k-ideal\ of\ U$.
□ **Corollary (3.4)**

Let I be a nonempty subset of a bounded Q-algebra U, and let $\chi_I = \langle \beta_{\chi_I}, \tau_{\chi_I}, \eta_{\chi_I} \rangle$ be the characteristic single-valued neutrosophic set of I defined by $\beta_{\chi_I}(p) = 1,\ \tau_{\chi_I}(p) = 0,\ \eta_{\chi_I}(p) = 0 \quad if\ p \in I,$

And $\beta_{\chi_I}(p) = 0,\ \tau_{\chi_I}(p) = 1,\ \eta_{\chi_I}(p) = 1 \quad if\ p \notin I.$

If χ_I is a single-valued neutrosophic k-ideal of U, then I is a k-ideal of U.

Proof.

Take α = 1, γ = 0, and δ = 0.

Then, $(\chi_I)_{(1,0,0)} = I$.

Since χ_I is a single-valued neutrosophic k-ideal of U, it follows from the preceding theorem that every nonempty level subset of χ_I is a k-ideal of U. Hence, $I = (\chi_I)_{(1,0,0)}$ is a k-ideal of U.

Proposition (3.5).
Let U be a bounded Q-algebra such that $p^* = p$ for all $p \in U$. If M is a single-valued neutrosophic ideal of U, then M is a single-valued neutrosophic k-ideal of U

Proof.
Assume that $M = \langle \beta_M, \tau_M, \eta_M \rangle$ is a single-valued neutrosophic ideal of U.
Then, for all $p, q \in U$, the following conditions hold:

$$\beta_M(0) \ge \beta_M(p),\ \tau_M(0) \le \tau_M(p),\ \eta_M(0) \le \eta\_M(p),$$

and

$$\beta_M(p) \ge min\{\beta_M(p * q), \beta_M(q)\},$$
$$\tau_M(p) \le max\{\tau_M(p * q), \tau_M(q)\},$$
$$\eta_M(p) \le max\{\eta_M(p * q), \eta_M(q)\}.$$

Since $p^* = p$ for all $p \in U$, it follows in particular that $q^* = q$ for all $q \in U$. Hence

$$\beta_M(p^*) = \beta_M(p),\ \tau_M(p^*) = \tau_M(p),\ \eta_M(p^*) = \eta_M(p),$$

and

$$\beta_M(q^* * p) = \beta_M(q * p),$$
$$\tau_M(q^* * p) = \tau_M(q * p),$$
$$\eta_M(q^* * p) = \eta_M(q * p).$$

Therefore, from the defining inequalities of a single-valued neutrosophic ideal, the following is obtained:

$$\beta_M(p^*) = \beta_M(p) \ge min\{\beta_M(q * p), \beta_M(q)\} = min\{\beta_M(q^* * p), \beta_M(q)\},$$

$$\tau_M(p^*) = \tau_M(p) \le max\{\tau_M(q * p), \tau_M(q)\} = max\{\tau_M(q^* * p), \tau_M(q)\},$$
$$\eta_M(p^*) = \eta_M(p) \le max\{\eta_M(q * p), \eta\_M(q)\} = max\{\eta_M(q^* * p), \eta_M(q)\}.$$

Thus, conditions SVN k(1) and SVN k(2) are satisfied. Hence, M is a single-valued neutrosophic k-ideal of U. □

Proposition (3.6).

Let $M = \langle \beta_M, \tau_M, \eta_M \rangle$ be a single-valued neutrosophic k-ideal of a bounded Q-algebra U. DefineI_$I_M = \{ p \in U : \beta_M(p) = \beta_M(0), \tau_M(p) = \tau_M(0), \eta_M(p) = \eta_M(0) \}$.Then, I_M is a k-ideal of U**.**

Proof.

Let $I_M = \{ p \in U : \beta_M(p) = \beta_M(0), \tau_M(p) = \tau_M(0), \eta_M(p) = \eta_M(0) \}$.

Since M is a single-valued neutrosophic k-ideal of U, by condition SVN k(1) there are, for every $p \in U$,

$$\beta_M(p) \le \beta_M(0), \ \tau_M(p) \ge \tau_M(0), \ \eta_M(p) \ge \eta_M(0).$$
$$Hence I_M = \{ p \in U : \beta_M(p) \ge \beta_M(0), \tau_M(p) \le \tau_M(0), \eta_M(p) \le \eta_M(0) \}.$$

That is,$I_M = M_{(\beta_M(0), \tau_M(0), \eta_M(0))}$.

Since $0 \in I_M$, the set I_M is nonempty. Therefore, by Theorem (3.3), every nonempty level subset of M is a k-ideal of U. In particular,

$$I_M = M_{(\beta_M(0), \tau_M(0), \eta_M(0))}$$

is a k-ideal of U.

Hence, I_M is a k-ideal of U. □

Theorem (3.7).

Let I be a nonempty subset of a bounded Q-algebra U, and $let\ \chi_I = \langle \beta_{\chi_I}, \tau_{\chi_I}, \eta_{\chi_I} \rangle$ be the characteristic single-valued neutrosophic set of I defined by $\beta_{\chi_I}(p) = 1, \ \tau_{\chi_I}(p) = 0, \ \eta_{\chi_I}(p) = 0$ if $p \in I$, and $\beta_{\chi_I}(p) = 0, \ \tau_{\chi_I}(p) = 1, \ \eta_{\chi_I}(p) = 1 \ if\ p \notin I$. Then I is a k-ideal of U if and only if χ_I is a single-valued neutrosophic k-ideal of U**.**

Proof.

Assume first that I is a k-ideal of U. Then, 0 ∈ I, and hence $\beta_{\chi_I}(0) = 1, \ \tau_{\chi_I}(0) = 0, \ \eta_{\chi_I}(0) = 0.$

Thus, for all p ∈ U,

$$\beta_{\chi_I}(0) \ge \beta_{\chi_I}(p), \ \tau_{\chi_I}(0) \le \tau_{\chi_I}(p), \ \eta_{\chi_I}(0) \le \eta_{\chi_I}(p),$$

so condition SVN k(1) holds.

Now let $p, q \in U. If\ q^* * p \in I\ and\ q \in I, then\ p^* \in I$, and hence

$$\beta_{\chi_I}(p^*) = 1, \ \tau_{\chi_I}(p^*) = 0, \ \eta_{\chi_I}(p^*) = 0.$$

Thus, condition SVN k(2) holds. Therefore, χ_I is a SVN k-ideal of U.

Conversely, assume that χ_I is a SVN k-ideal of U. From SVN k(1), it is obtained $\beta_{\chi_I}(0) = 1$, hence 0 ∈ I.

Let $q^* * p \in I$ and q ∈ I. Then, $\beta_{\chi_I}(q^* * p) = \beta_{\chi_I}(q) = 1$. By SVN k(2),

$$\beta_{\chi_I}(p *) \ge min\{1,1\} = 1,$$

so $p^* \in I$. Hence, I is a k-ideal of U. □ □

Remark (3.8)

Let $M = \langle \beta_M, \tau\_M, \eta\_M \rangle$ be a single-valued neutrosophic k-ideal of a bounded Q-algebra U. Then, for all p ∈ U,$\beta_M(p^*) \le \beta_M(0), \ \tau_M(p^*) \ge \tau_M(0), \ \eta_M(p^*) \ge \eta_M(0)$.

Proof.

Let p ∈ U. Since M is a single-valued neutrosophic k-ideal of U, by condition SVN k(1) we have, for every x ∈ U,

$$\beta_M(0) \ge \beta_M(x), \ \tau_M(0) \le \tau_M(x), \ \eta_M(0) \le \eta_M(x).$$

Taking $x = p^*$, we obtain

$$\beta_M(0) \ge \beta_M(p^*), \ \tau_M(0) \le \tau_M(p^*), \ \eta_M(0) \le \eta_M(p^*).$$

Hence, the result follows. □

Theorem (3.9).

Let $f : U \to H$ be a homomorphism between bounded Q-algebras, and let $M = \langle \beta_M, \tau_M, \eta_M \rangle$ be a single-valued neutrosophic k-ideal of H. Then $f^{-1}(M)$ is a single-valued neutrosophic k-ideal of U.

Proof.

Define $f^{-1}(M) = \langle \beta, \tau, \eta \rangle$ on U by

$$\beta(p) = \beta_M(f(p)), \ \tau(p) = \tau_M(f(p)), \ \eta(p) = \eta_M(f(p)),$$

for all $p \in U$.

Since f is a homomorphism between bounded Q-algebras, we have

$f(0_U) = 0_H$ and $f(p^*) = \big(f(p)\big)^*$, for all p ∈ U.

Let $p \in U$. Since M is a single-valued neutrosophic k-ideal of H, it includes

$$\beta_M(0_H) \ge \beta_M(f(p)), \ \tau_M(0_H) \le \tau_M(f(p)), \ \eta_M(0\_H) \le \eta_M(f(p)).$$

Hence,

$$\beta(0_U) = \beta\_M(0_H) \ge \beta(p),$$
$$\tau(0_U) = \tau_M(0_H) \le \tau(p),$$
$$\eta(0_U) = \eta_M(0_H) \le \eta(p),$$

so condition SVN k(1) holds.

Now let $p, q \in U$. Using the homomorphism property, we obtain $f(q^* * p) = (f(q))^* * f(p)$.
Since M is a single-valued neutrosophic k-ideal of H, it follows that

$$\beta_M((f(p))^*) \geq min\{\beta_M((f(q))^* * f(p)), \beta_M(f(q))\}.$$

Thus, $\beta(p^*) = \beta_M((f(p))^*)$
$\geq min\{\beta_M(f(q^* * p)), \beta_M(f(q))\}$
$= min\{\beta(q^* * p), \beta(q)\}.$

Similarly,

$$\tau(p^*) \leq max\{\tau(q^* * p), \tau(q)\},$$
$$\eta(p*) \leq max\{\eta(q^* * p), \eta(q)\}.$$

Hence, condition SVN k(2) holds. Therefore, $f^{-1}(M)$ is a single-valued neutrosophic k-ideal of U. □

Corollary (3.10)
Let $f : U \to H$ be an isomorphism between two bounded Q-algebras.
Let $M = \langle \beta_M, \tau_M, \eta_M \rangle$ be a single-valued neutrosophic k-ideal of U.Define $f(M) = \langle \beta', \tau', \eta' \rangle$ on H by

$$\beta'(y) = \beta_M(f^{-1}(y)), \tau'(y) = \tau_M(f^{-1}(y)),$$
$$\eta'(y) = \eta_M(f^{-1}(y)),$$

for all y ∈ H.Then $f(M)$ is a single-valued neutrosophic k-ideal of H..
Proof.
The result follows directly from Theorem (3.9). □

Proposition (3.11).
Let $\{M_i : i \in \Lambda\}$ be a family of single-valued neutrosophic k-ideals of a bounded Q-algebra U, where $M_i = \langle \beta_i, \tau_i, \eta_i \rangle$ for each $i \in \Lambda$. Define $M = \langle \beta, \tau, \eta \rangle$ by $\beta(p) = inf\{\beta_i(p) : i \in \Lambda\}, \tau(p) = sup\{\tau_i(p) : i \in \Lambda\}, \eta(p) = sup\{\eta_i(p) : i \in \Lambda\}$, for all p ∈ U. Then, M is a single-valued neutrosophic k-ideal of U.
Proof.
Let $p \in U$. Since each M_i is a single-valued neutrosophic k-ideal of U, by condition SVN k(1) there are

$$\beta_i(0) \geq \beta_i(p), \quad \tau_i(0) \leq \tau_i(p), \quad \eta_i(0) \leq \eta_i(p)$$

for all $i \in \Lambda$.
Taking infimum in the first inequality and supremum in the second and third inequalities, it is obtained that
$\beta(0) \geq \beta(p), \quad \tau(0) \leq \tau(p), \quad \eta(0) \leq \eta(p)$.
Hence, condition SVN k(1) holds.
Now let $p, q \in U$. Since each M_i is a single-valued neutrosophic k-ideal of U, by condition SVN k(2) there are

$$\beta_i(p^*) \geq min\{\beta_i(q^* * p), \beta_i(q)\},$$
$$\tau_i(p^*) \leq max\{\tau_i(q^* * p), \tau_i(q)\},$$
$$\eta_i(p^*) \leq max\{\eta_i(q^* * p), \eta_i(q)\}$$

for all $i \in \Lambda$.
Taking infimum in the first inequality, it results

$$\beta(p^*) = inf\ \beta_i(p^*)$$
$$\geq inf\ min\{\beta_i(q^* * p), \beta_i(q)\}$$
$$\geq min\{inf\ \beta_i(q^* * p), inf\ \beta_i(q)\}$$
$$= min\{\beta(q^* * p), \beta(q)\}.$$

Similarly, taking supremum in the second and third inequalities, it is obtained

$$\tau(p^*) = sup\ \tau_i(p^*)$$
$$\leq sup\ max\{\tau_i(q^* * p), \tau_i(q)\}$$
$$\leq max\{sup\ \tau_i(q^* * p), sup\ \tau_i(q)\}$$
$$= max\{\tau(q^* * p), \tau(q)\},$$

And $\eta(p^*) = sup\ \eta_i(p^*)$
$\leq sup\ max\{\eta_i(q^* * p), \eta_i(q)\}$
$\leq max\{sup\ \eta_i(q^* * p), sup\ \eta_i(q)\}$
$= max\{\eta(q^* * p), \eta(q)\}.$

Thus, condition SVN k(2) also holds. Therefore M is a single-valued neutrosophic k-ideal of U. □

Remark (3.12)
In general, the union of single-valued neutrosophic k-ideals need not be a single-valued neutrosophic k-ideal (see Example (3.12)).

Example (3.13).
Let $U = \{0, \rho, \varpi, \pi\}$ be a bounded Q-algebra whose operation * is given by Table 3.

Table 3. Cayley table of U

*	0	ρ	ϖ	π
0	0	0	0	0
ρ	ρ	0	0	0
ϖ	ϖ	ρ	0	0
π	π	Π	ρ	0

Define two single-valued neutrosophic sets
$M = \langle \beta_M, \tau_M, \eta_M \rangle$ and $N = \langle \beta_N, \tau_N, \eta_N \rangle$ on U as followed:

$$\beta_M(p) = \begin{cases} 0.4 & \text{if p} = 0, \\ 0.1 & \text{if p} \in \{\rho, \varpi, \pi\} \end{cases}$$
$$\tau_M(p) = \begin{cases} 0.0 & \text{if p} = 0 \\ 0.3 & \text{if p} \in \{\rho, \varpi, \pi\} \end{cases}$$
$$\eta_M(p) = \begin{cases} 0.0 & \text{if p} = 0 \\ 0.3 & \text{if p} \in \{\rho, \varpi, \pi\} \end{cases}$$

And

$$\beta_N(p) = \begin{cases} 0.6 & \text{if p} = 0 \\ 0.2 & \text{if p} \in \{\rho, \varpi, \pi\} \end{cases}$$
$$\tau_N(p) = \begin{cases} 0.0 & \text{if p} = 0 \\ 0.2 & \text{if p} \in \{\rho, \varpi, \pi\} \end{cases}$$
$$,\eta_N(p) = \begin{cases} 0.0 & \text{if p} = 0, \\ 0.2 & \text{if p} \in \{\rho, \varpi, \pi\} \end{cases}$$

By direct verification using Table 1, both M and N satisfy the conditions of Definition (3.1). Hence, M and N are single-valued neutrosophic k-ideals of U.
Therefore, by Proposition (3.10), M ∩ N is also a single-valued neutrosophic k-ideal of U.

However, in general, the union M ∪ N need not be a single-valued neutrosophic k-ideal of U, which illustrates Remark (3.11) Take $p = \rho$ and $q = \pi$. Then $q^* * p = 0$ and $p^* = \varpi$. Hence

$\beta_{\{M\cup N\}}(p^*) = 0.1 < 0.2$
$= min\{\beta_{\{M\cup N\}}(q^* * p), \beta_{\{M\cup N\}}(q)\}.$
Thus, condition SVN k(2) is not satisfied, and therefore M ∪ N is not a single-valued neutrosophic k-ideal of U. □

$\eta'(y_2^*) \leq \max\{\eta'(y_1^* * y_2), \eta'(y_1)\}$.
Hence, SVN k(2) holds. Therefore f(M) is a SVN k-ideal of H. □

CONCLUSION

In this paper, the concept of single-valued neutrosophic k-ideals is introduced in bounded Q-algebras and investigated their fundamental properties. Several characterizations of these structures are provided, particularly in terms of level subsets, and established their relationships with classical k-ideals.

Moreover, the behavior of single-valued neutrosophic k-ideals are studied under algebraic mappings and are shown to be preserved under homomorphic preimages. Also, closure properties, including the intersection of such ideals are examined, which are presented through illustrative examples and counterexamples to clarify the theoretical results.

The results obtained in this work contribute to the development of neutrosophic algebraic structures and pave the way for further research. In particular, future work may focus on studying single-valued neutrosophic k-ideals in other algebraic systems, as well as investigating their lattice structures and applications in decision-making and information sciences.

REFERENCES

Atanassov, K. T. (1986). Intuitionistic fuzzy sets. *Fuzzy Sets and Systems, 20*, 87–96.

Jawad, H. K. (2019). *Some types of fuzzy pseudo Q-algebra* (Master's thesis, University of Kufa).

Jun, Y. B. (2000). Intuitionistic fuzzy ideals of Q-algebras. *Journal of Fuzzy Mathematics, 8*, 409–420.

Jun, Y. B., & Neggers, J. (2005). Intuitionistic fuzzy k-ideals in Q-algebras. *Journal of Applied Mathematics and Computing, 19*, 87–96.

Kim, H. S., & Neggers, J. (2005). The structure of Q-algebras. *Mathematica Slovaca, 55*, 473–484.

Neggers, J., & Kim, H. S. (2001). On Q-algebras. *International Journal of Mathematics and Mathematical Sciences, 27*, 749–757.

Neggers, J., Jun, Y. B., & Kim, H. S. (2004). On k-ideals in Q-algebras. *Mathematica Slovaca, 54*, 1–9.

Smarandache, F. (2002). *Neutrosophy and neutrosophic logic*. American Research Press.

Smarandache, F. (2005). Neutrosophic set: A generalization of the intuitionistic fuzzy sets. *International Journal of Pure and Applied Mathematics, 24*, 287–297.

Wang, H., Smarandache, F., Zhang, Y. Q., & Sunderraman, R. (2010). Single valued neutrosophic sets. *Multispace and Multistructure, 4*, 410–413.

Zadeh, L. A. (1965). Fuzzy sets. *Information and Control, 8*, 338–353.

0096477699201 65
https://journals.uokerbala.edu.iq
Iraq - Holy Karbala